PH.D. DISSERTATION

UNIVERSIDAD
DE GRANADA

Programa de Doctorado en Física y Ciencias del Espacio

Synergetic use of active and passive remote sensing techniques to retrieve vertical profiles of atmospheric aerosol properties during day- and night-time

Jose Antonio Benavent Oltra

Grupo Física
de la Atmósfera

IISTA
Instituto Interuniversitario de Investigación
del Sistema Tierra en Andalucía

Unidad de
Excelencia
UGR

UNIVERSIDAD DE GRANADA

DEPARTAMENTO DE FÍSICA APLICADA
GRUPO DE FÍSICA DE LA ATMÓSFERA

TESIS DOCTORAL

Synergetic use of active and passive remote sensing techniques to retrieve vertical profiles of atmospheric aerosol properties during day- and night-time

Tesis presentada por D. Jose Antonio Benavent Oltra para optar al grado de Doctor.

Directores de la Tesis:

Dr. Lucas Alados Arboledas
Catedrático de la UGR
Departamento Física Aplicada
Universidad de Granada

Dr. Roberto Román Diez
Investigador de la UVA
Grupo de Óptica Atmosférica
Universidad de Valladolid

Granada, febrero 2019

Editor: Universidad de Granada. Tesis Doctorales
Autor: José Antonio Benavent Oltra
ISBN: 978-84-1306-174-0
URI: http://hdl.handle.net/10481/55500

El trabajo de investigación que se expone en la presente memoria, titulado: ***Synergetic use of active and passive remote sensing techniques to retrieve vertical profiles of atmospheric aerosol properties during day- and night-time***, para aspirar al grado de Doctor en Física que presenta D. Jose Antonio Benavent Oltra, ha sido realizado en la Universidad de Granada gracias a la ayuda concedida por el Ministerio de Economía y Competitividad para la formación de doctores 'Formación de Personal Investigador' 2014 (BES-2014-068893), bajo la dirección de:

Directores de la Tesis:

Dr. Lucas Alados Arboledas

Dr. Roberto Román Diez

Doctorando

Fdo.: D. Jose Antonio Benavent Oltra

El doctorando / *The doctoral candidate* D. Jose Antonio Benavent Oltra y los directores de la tesis / *and the thesis supervisors* Dr. Lucas Alados Arboledas y Dr. Roberto Román Diez.

Garantizamos, al firmar esta tesis doctoral, que el trabajo ha sido realizado por el doctorando bajo la dirección de los directores de la tesis y hasta donde nuestro conocimiento alcanza, en la realización del trabajo, se han respetado los derechos de otros autores a ser citados, cuando se han utilizado sus resultados o publicaciones.

Guarantee, by signing this doctoral thesis, that the work has been done by the doctoral candidate under the direction of the thesis supervisor/s and, as far as our knowledge reaches, in the performance of the work, the rights of other authors to be cited (when their results or publications have been used) have been respected.

Granada, febrero de 2019

Directores de la Tesis / *Thesis supervisors*

Fdo.: Dr. Lucas Alados Arboledas

Fdo.: Dr. Roberto Román Diez

Doctorando / *Doctoral candidate*

Fdo.: D. Jose Antonio Benavent Oltra

A la meua família

“If you want to go fast
go alone,
if you want to go far
go together”

African proverb

Agradecimientos

En primer lugar, me gustaría dar las gracias a mis directores de tesis, el Catedrático Lucas Alados y el doctor Roberto Román. A Lucas le tengo que agradecer la confianza que depositó en mí desde el primer día para que realizara esta tesis, nunca es fácil aceptar a una persona ajena al grupo. Gracias por abrirme las puertas del GFAT y permitirme que conociera a grandes científicos y, sobre todo, grandes personas. A Roberto, agradecerle que me enseñara por primera vez los entresijos del GRASP, gracias por aguantarme en todos los congresos/campañas y darme los ánimos necesarios siempre que los necesité.

Aunque por burocracia sólo se permite que aparezcan dos directores, en esta tesis debería aparecer un tercer director. Esa persona es Dani, gracias por haber estado dispuesto a ayudarme siempre y sin tu ayuda esta tesis hubiera costado mucho más en salir adelante. Luego está Hassan, una de las mejores personas que hay en el CEAMA, gracias por todo lo que me has enseñado de ciencia, por nuestras 'discusiones' por todo y por ayudarme desde el primer día. Y como no, el 'picha', Juan Andrés, al cual considero un gran amigo, aunque siempre está criticando todos mis trabajos, gracias por tus consejos y ayuda. También agradecer a María Jose (la cual me 'cedió' su sitio) por todo su apoyo y ánimos a lo largo de estos años, espero que hayamos terminado con tu amado ChArMEx.

También quiero dar las gracias a Paco Pepe por su amabilidad, por toda su ayuda que me ofreció desde que llegué a Granada. Quiero dar las gracias al resto del GFAT, esa gente que ha estado dispuesta a ayudarme desde el primer día y me ha enseñado un poco más lo que es la investigación. Si tuviera que agradecer a cada uno de los que formamos este grupo, esto terminaría siendo más largo incluso que la tesis, por lo que sólo puedo agradeceros todos los buenos momentos que hemos

pasado, ya hayan sido en la Cabaña, comida de Navidades o en la feria. También me toca agradecer al personal del CEAMA que me ha ayudado y dado ánimos todos estos años. De fuera del CEAMA, pero que sabe todo de aquí, tengo que agradecer a Juan por todos los buenos momentos que me has hecho pasar y por tus sabios consejos.

No me iba a olvidar de mis compañeros de tesis, Pablo y Andrés. En los próximos meses les tocará a ellos terminar con este sufrimiento y estoy seguro de que les irá muy bien. Hemos pasado muchas noches de sufrimiento y peleas con el lidar, ese gran enemigo, pero también pasamos muy buenos tiempos, como el viaje a Holanda junto a Fátima y Caro. Agradecer a Andrés, al cual considero un hermano, y a Caro su hospitalidad en Colombia al adoptarme como uno más de su familia, nunca olvidaré lo que hicisteis por mí. Hablando de gente que va a terminar la tesis este año, no me podía olvidar de Marisel, gracias por aguantar mis altibajos durante estos años.

También agradecer a todos los investigadores que han pasado por el CEAMA un corto periodo pero que han dejado huella. Como son Manuela con su mala leche que al final se le cogía cariño, y Cristian, el cual no tenía fondo alguno y nos 'tumbaba' a todos. Y agradecer a los brasileños Marcelo y Anderson su paso por el CEAMA, sois muy buena gente con la cual espero volver a compartir una buena cerveza.

De brasileños tampoco puedo olvidarme de toda la gente que me ayudó y me brindó su amistad durante mi estancia en São Paulo. A Eduardo por aceptarme en su grupo, a Fabio por ayudarme con todo lo que he necesitado, y a Antonio y Jonatan por esas *quartas-feiras de pipocas*. Y, por último, la persona más buena de este mundo, Gregori, gracias por todo y sabes que te esperamos siempre de vuelta, sobre todo, para tomarnos unos zumos de tomate. I switch to English to thank to people of Laboratoire d'Optique Atmosphérique for offering me the opportunity to join his

group for a few months. Especially, thanks to Oleg, Anton, Benja and David for teach me and helping me with GRASP. Hablando de GRASP, me toca agradecer todo su apoyo, ánimos y ayuda que me ha ofrecido Milagros estos últimos meses, eres una de las mejores personas que he conocido y espero que no cambies nunca.

Per últim, toca parlar de la gent de la meua terreta. Primer agrair als físics Juanjo, Gemma, Oreto i Loleta per tots el bons moments que hem passat i encara que ens vegem cada molt de temps sempre serem bons amics. I parlant d'amics, no podia oblidar-me de la 'Cerda Pinta', bona gent allí on estiga sense cap dubte, gràcies per seguir sempre junts. Per al final, dedique aquesta tesis a la meua família, en especial aquells que hui en dia no segueixen entre nosaltres. Com no agrair als meus pares, Mª Carmen i Pepe, per tot l'esforç que han fet durant aquesta vida per a que haja pogut arribar aquest dia, es mereixeu el millor. També agrair a les meues germanes, Maria i Lucia, a Salva i a la xicotiua i més bonica de casa, Areliza, gràcies per tot de veritat.

Espero no haberme olvidado de nadie, si así es, espero que no se lo tome a mal. Muchas gracias a toda la gente que ha hecho posible esta tesis.

Contents

Abstract

This PhD dissertation focuses on the characterization of atmospheric aerosols properties during day- and night-time combining active and passive remote sensing measurements. The study provides both column-integrated and vertically resolved aerosol properties.

The key for this thesis is the combination of advanced ground-based remote sensing instrumentation. By one hand, it is used a multiwavelength Raman lidar that which measures both elastic and Raman signals, therefore, independent backscatter and extinction profiles can be calculated. The system operates twice a week in the frame of ACTRISE - ARLINET (Aerosols, Clouds, and Trace gases Research InfraStructure Network - European Aerosol Research LIdar NETwork) and more intensively during special field campaigns. But due to the low signal-to-noise ratio Raman measurements are only available during night-time, being the daytime measurements based on the use of multiwavelength elastic measurements. Additionally, continuous measurements during the entire year have been registered with a ceilometer in the infrared range. Finally, sun/sky photometry was used to obtain direct estimation of aerosol optical properties during daytime and lunar photometry for direct estimation of spectral aerosol optical depths during night-time.

Experimental measurements used were collected during ChArMEx/ADRIMED (Chemistry-Aerosol Mediterranean Experiment/Aerosol Direct Radiative Impact on the regional climate in the MEDiterranean region) field campaign in 2013, and during SLOPE I (Sierra Nevada Lidar AerOsol Profiling Experiment) field campaign in 2016. Both field campaigns were developed at the Andalusian Global ObseRvatory of the Atmosphere (AGORA) that deployed instrumentation at three different sites at different altitudes near the city of Granada

(Southeastern Spain): the UGR station located at Andalusian Institute for Earth System Research (IISTA-CEAMA) in the city at 680 m a.s.l.; and two mountain stations located at short distance in Sierra Nevada mountains: Cerro Poyos (CP) station at 1820 m a.s.l. and Sierra Nevada Station (SNS) at 2500 m a.s.l..

The atmospheric aerosol properties analyzed in this thesis are mainly retrieved by Generalized Retrieval of Aerosol and Surface Properties algorithm (GRASP), which was developed in the Laboratoire d'Optique Atmosphérique, Lille (France). GRASP is a versatile and flexible algorithm for the retrieval of aerosol microphysical properties from their optical properties, and in this thesis, it uses the combination of sun/sky photometer with lidar measurements to retrieve enhanced columnar aerosol microphysical properties that allow the separation between fine and coarse mode properties, and also vertically-resolved microphysical properties.

The retrievals from GRASP algorithm are evaluated versus in-situ airborne measurements during ChArMEx/ADRIMED field campaign for a desert dust episode. GRASP was run using as inputs lidar and sun/sky photometer measurements acquired either in UGR or CP stations to explore the effect of incomplete overlap associated with lidar measurements. The extinction profiles at 532 nm retrieved by GRASP present differences less than 20% with respect the in-situ measurements on board the ATR-42 aircraft by CAPS (Cavity Attenuated Phase Shift). In the case when the dust layer was coupled to the aerosol layer close to surface, the total volume concentration differences between airborne in situ data and GRASP retrievals are 15% or 36%, depending on the use of the sun/sky measurements at UGR or at CP for the retrievals. In contrast, in the case when dust layer was decoupled from the aerosol layer close to the surface the differences are around 17% for both retrievals.

GRASP algorithm is also used for retrieving continuous day- and night-time aerosol properties during a dust event registered during the SLOPE I campaign. For

extending the use of GRASP to night-time, three different schemes have been proposed in this thesis. The first one assumes that there is no change in the aerosol column-integrated properties along the night, in this way the retrieval is done combining the night time elastic lidar measurements with the closest sun/sky measurements registered the day before or the day after. The second approach considers that the aerosol load in the vertical column can be monitored by lunar photometry, but assumes that there are no changes in the aerosol column-integrated intensive properties, that is this approach considers that there are no changes in the aerosol type. In this way, the night-time elastic lidar signal is combined with the aerosol optical depth measured by lunar photometer, fixing the aerosol complex refractive index and spherical particle fraction to the values retrieved from the closest daytime retrieval. The last approach uses night-time elastic lidar signals and aerosol optical depth measurements retrieved from a lunar photometer in combination with relative sky radiances at the lunar aureole, retrieved from a Sky images. The different approaches are applied to the evolution of a Saharan dust outbreak registered during SLOPE I field campaign. The dust plume evolution has been monitored and the results discussed with the different approaches. Furthermore, considering the availability of independent measurements of some aerosol properties at SNS station, GRASP retrievals at 2500m a.s.l. are compared with in-situ measurements obtained at SNS station, assuming that the proximity of this station allow us to consider that it is in the same vertical column explored by the lidar system operated at UGR. GRASP retrievals show coherent values when compared with AERONET retrievals, being observed a smooth and coherent day-to-night evolution. GRASP and Raman retrieved values agrees quite well, with differences below 30%. Generally, both GRASP retrievals and in-situ measurements follow the same patterns and are sensitive to the arrival of Saharan dust particles.

Finally, it is presented a novel approach for the estimation of vertically-resolved aerosol concentrations from GRASP retrievals using combined

measurements of ceilometer and sun/sky photometer measurements. Sensitivity tests for this configuration are performed with synthetic data to show the performance of this new methodology, especially for coarse particles. This new configuration is applied to measurements at UGR station and the retrievals are compared with in-situ airborne measurements acquired during the ChArMEx/ADRIMED field campaign. This study shows that the retrieved aerosol volume concentration profiles agree well with in-situ airborne measurements, being the mean differences within the uncertainty of GRASP retrievals. An additional validation of the methodology is based on the use of in-situ aerosol volume concentration registered at SNS station during the SLOPE I field campaign station. In this sense, the aerosol volume concentration retrieved at 2500m a.s.l. from the combination of ceilometer and sun/sky photometer present a high correlation with some trends to overestimation of the in-situ measurements obtained at SNS station.

Resumen

Esta tesis doctoral se centra en la caracterización de las propiedades de los aerosoles atmosféricos durante el día y la noche, combinando medidas de teledetección activas y pasivas. El trabajo presentado proporciona propiedades del aerosol atmosférico tanto integradas en columna como resueltas verticalmente.

La clave para esta tesis es la combinación de diferentes instrumentos de teledetección. Por un lado, se utiliza un lidar Raman multiespectral que mide tanto señales elásticas como Raman, por lo tanto, se pueden calcular los perfiles de retrodispersión y extinción de manera independiente. Este sistema mide dos veces por semana en el marco de ACTRIS-EARLINET (*Aerosols, Clouds, and Trace gases Research InfraStructure Network - European Aerosol Research LIdar NETwork*) y más intensamente durante el desarrollo de campañas. Debido a la baja relación señal-ruido, las mediciones Raman solo están disponibles durante la noche. Durante el día, el lidar Raman mide la señal elástica retrodispersada en tres longitudes de onda, desde el rango ultravioleta al infrarrojo. Además, también se utilizan las medidas de retrodispersión elástica en el rango infrarrojo de manera continua realizadas con un ceilómetro. Finalmente, los fotómetros solares se utilizan para realizar una estimación directa de las propiedades ópticas del aerosol durante el día, pero en los últimos años se han desarrollado los fotómetros lunares (miden tanto empleando el sol como la luna) los cuales permiten estimar el espesor óptico del aerosol a distintas longitudes de onda durante la noche.

Las medidas experimentales utilizadas a lo largo de esta tesis fueron tomadas durante la campaña de medidas ChArMEx/ADRIMED (*Chemistry-Aerosol Mediterranean Experiment/Aerosol Direct Radiative Impact on the regional climate in the MEDiterranean region*) en 2013, y durante la campaña SLOPE I (*Sierra*

Nevada Lidar AerOsol Profiling Experiment) en el verano de 2016. Ambas campañas se desarrollaron en el *Andalusian Global ObseRvatory of the Atmosphere* (AGORA) que desplegó instrumentación en tres sitios diferentes a diferentes altitudes cerca de la ciudad de Granada (sureste de España): la estación UGR ubicada en el Instituto Andaluz para la Investigación del Sistema Terrestre (IISTA-CEAMA) en la ciudad de Granada a 680 m s.n.m.; y dos estaciones de montaña ubicadas en las montañas de Sierra Nevada: la estación de Cerro Poyos (CP) a 1820 m s.n.m. y la estación de Sierra Nevada (SNS) a 2500 m s.n.m..

Las propiedades de los aerosoles atmosféricos analizadas en esta tesis se obtienen principalmente mediante el algoritmo GRASP (Generalized Retrieval of Aerosol and Surface Properties) desarrollado por el Laboratoire d'Optique Atmosphérique (LOA), Lille (Francia). GRASP es un algoritmo versátil y flexible que permite el cálculo de las propiedades ópticas y microfísicas del aerosol atmosférico. En esta tesis, GRASP se utiliza combinando las medidas de un fotómetro con las medidas de lidar para obtener las propiedades ópticas y microfísicas de aerosol en columna como los perfiles verticales separando en modo fino y grueso.

Se ha realizado una evaluación de las propiedades que proporciona el algoritmo GRASP mediante la comparación con medidas in situ realizadas desde un avión durante la campaña ChArMEx/ADRIMED para un episodio de polvo desértico. En este estudio, GRASP se ha utilizado empleando como variables de entrada las medidas del lidar en la estación UGR, pero también medidas del espesor óptico del aerosol y las radiancias de cielo tomadas con el fotómetro de las estaciones UGR o CP para explorar el efecto del solapamiento asociado con las medidas lidar. Los perfiles de extinción a 532 nm calculados con GRASP presentan diferencias menores del 20% con respecto a las medidas in situ a bordo del avión ATR-42 medidas con CAPS (*Cavity Attenuated Phase Shift).* En el caso de que la

capa de polvo este acoplada a la capa de aerosol cercana de la superficie, las diferencias de concentración de volumen total entre GRASP y los valores in situ son del 15% o 36%, dependiendo de si se usa el fotómetro de UGR o de CP para los cálculos de GRASP. Por otro lado, cuando la capa de polvo estaba desacoplada de la capa de aerosol cercana a la superficie, las diferencias entre los valores obtenidos con GRASP y las medidas in situ son en torno al 17%, usando tanto el fotómetro de UGR como el de CP.

El algoritmo GRASP también se ha utilizado para inferir las propiedades del aerosol tanto de día como a la noche durante un evento de polvo desértico registrado durante la campaña SLOPE I. En esta tesis se han propuesto tres esquemas diferentes para calcular las propiedades del aerosol durante la noche mediante el uso de GRASP. El primer esquema supone que las propiedades integradas en columna del aerosol no cambian a lo largo de la noche, por lo tanto, las inversiones GRASP utilizan como datos de entrada la combinación de las medidas nocturnas del lidar con las medidas diurnas del fotómetro más cercanas. El segundo esquema considera que la carga de aerosol en la columna se puede calcular mediante fotometría lunar, pero supone que no hay cambios en las propiedades intensivas integradas en la columna de aerosol, es decir, este enfoque considera que no hay cambios en el tipo de aerosol. De este modo, el segundo esquema combina la señal lidar elástica nocturna con la profundidad óptica del aerosol medida por el fotómetro lunar y fijando el índice de refracción del aerosol y la fracción de partículas esféricas a los valores obtenidos de la inversión diurna más cercana. El último esquema utiliza las señales lidar elásticas nocturnas, el espesor óptico del aerosol obtenido del fotómetro lunar y la radiancia relativa del cielo, medida con de una cámara de cielo, en torno a la aureola lunar. Se ha monitoreado la evolución de la nube de polvo y se han discutido los resultados con los diferentes esquemas. Además, los valores de las propiedades obtenidas por GRASP a 2500 m s.n.m. se han comparado con los valores medidos in situ en la estación de SNS, asumiendo la proximidad de esta

estación. Las inversiones de GRASP muestran valores coherentes en comparación con los valores de AERONET, observándose una evolución suave y coherente de día a noche. Los valores de GRASP coinciden bastante bien, con los de Raman, mostrando diferencias por debajo del 30%. En general, tanto los valores de GRASP como las medidas in situ siguen los mismos patrones y son sensibles a la llegada de partículas de polvo del Sahara.

Finalmente, se presenta un nuevo esquema para la estimación de los perfiles de concentración del aerosol a partir de las inversiones de GRASP combinando las medidas de ceilómetro con las del fotómetro solar. El rendimiento de esta metodología se ha comprobado mediante pruebas de sensibilidad con datos sintéticos. Posteriormente, esta configuración se ha aplicado a las medidas de la estación UGR y los valores obtenidos se comparan con las medidas in situ obtenidas en la campaña ChArMEx/ADRIMED. Este estudio muestra que los perfiles de concentración calculados con GRASP concuerdan con las medidas in situ, siendo las diferencias inferiores a la incertidumbre de las inversiones de GRASP. Una última validación de esta metodología se ha realizado comparando la concentración en volumen del aerosol obtenida con GRASP a 2500 m s.n.m. con las medidas in situ en la estación SNSN durante la campaña SLOPE-I. La combinación de las medidas de ceilómetro y fotómetro solar presenta una alta correlación, pero sobrestimando las medidas in situ obtenidas en la estación SNS.

1. Introduction

Atmospheric aerosols play an important role in the Earth–atmosphere radiative budget because they can scatter and absorb solar and terrestrial radiation. This is the well-known aerosol direct effect and its sign (warming or cooling) depends on aerosol properties and on their vertical distribution [e.g. Boucher et al., 2013]. On the other hand, aerosol particles can act as cloud condensation and ice nuclei and thus can modify the development, microphysical properties and lifetime of clouds [e.g. Andreae et al. 2004]. Although the uncertainties associated with the aerosol direct effect have been reduced in the last years, there is a large uncertainty in aspects related to their absorption properties and how they can affect cloud developments [IPCC, 2013]. The atmospheric aerosol properties can present large variations between the free troposphere and the atmospheric boundary layer, and even within this last one. In this sense, a better understanding of the aerosol vertical distribution, and more specifically the vertical profiling of its microphysical properties, is a current challenge. Furthermore, aerosol profiling is also relevant in practical aspects like the management of aviation traffic, especially during a volcanic eruption [Prata, 2009; Flentje et al., 2010].

The column-integrated optical and microphysical aerosol properties can be gathered with passive remote sensing instruments. Satellites with this kind of instrumentation (e.g. MODIS, MISR, POLDER or OMI) usually provide global coverage of atmospheric aerosol properties, but with a lack of temporal resolution. On the contrary, ground-based measurements from sun/sky photometers such as those from the Aerosol Robotic Network (AERONET) [Holben et al., 1998] and SKYNET [Takamura and Nakajima, 2004, Nakajima et al., 2007], provide aerosol column-integrated properties with high temporal resolution, but with limited spatial

coverage. A limitation of satellite and of the most ground-based passive remote sensing techniques is that only provide daytime measurements, but there is demand of night-time measurements for understanding the aerosol dynamic along the whole day [e.g. Pérez-Ramírez et al., 2012]. Furthermore, the characterization of aerosol properties at night-time is crucial in polar areas, where there is a lack of daytime measurements in winter [Stone et al., 2010; Tomasi et al., 2015]. Recent technological advances are allowing new achievements in night-time aerosol characterization through passive remote sensing measurements such as stellar photometry [e.g. Pérez-Ramírez et al., 2008, 2011; Baibakov et al., 2015], lunar photometry [e.g. Berkoff et al., 2011; Barreto et al., 2013, 2016], and VIIRS satellite through the measurements of radiance values above artificial light sources [e.g. McHardy et al., 2015]. However, all these techniques only provide column-integrated properties of aerosol particles, being the vertical characterization of aerosol properties a current challenge in evaluating aerosol impact on climate.

Active remote sensing measurements by lidar systems (from both space and ground) have been proven as a very useful technique to face issues related with aerosol vertical distribution. In this sense, several studies remarked that the direct radiative forcing of the aerosol is very sensitive to the aerosol vertical distribution [e.g. Meloni et al., 2006]. Space measurements from CALIPSO [Winker et al., 2010] or CATS [Yorks et al., 2016] satellites provide global coverage, while global networks such as MPLNET [Welton et al., 2002] are providing extended temporal coverage. These lidar systems only have information about the elastic signal which allows the calculation of vertical profiles of the backscatter coefficient (β) by the Klett-Fernald method [Fernald et al., 1972; Fernald, 1984; Klett, 1981] (described in Section 4.1.1) and the corresponding aerosol extinction coefficient (α) by assuming the extinction-to-backscattering ratio, the so-called lidar ratio (LR), as constant.

There are two kinds of lidar systems, the basic lidar systems which only have information on the elastic scattered signal and which allows the retrieval of the vertical profiles of the aerosol backscatter coefficient by the Klett-Fernald method. Among these systems are the ceilometers, which usually works with a wavelength in the infrared region. The main advantages of ceilometers are cheap, easily deployable and capable of operating continuously. On the other hand, the advanced multiwavelength lidar systems, which measure the elastic and non-elastic (Raman signal) scattered signals at different wavelengths. The signals measured by this kind of systems can be used to calculate independently backscatter and extinction coefficients [Ansmann et al., 1992] (described in Section 4.1.2). In this sense, the EARLINET (European Aerosol Research LIdar NETwork) [Pappalardo et al., 2014] and LALINET (Latin American LIdar NETwork) [Guerrero-Rascado et al., 2016] networks, which provide vertical distribution of aerosols over Europe and Latin America, respectively, implement networks based on multiwavelength Raman systems for more accurate vertical profiling of aerosol properties.

Current challenges to improve our knowledge about the aerosol effects on Earth-atmosphere radiative budget call for a better vertical characterization of aerosol optical and microphysical properties. In this sense, in recent years different inversion algorithms have been developed based on the regularization technique to retrieve vertical profiles of aerosol microphysical properties using three backscatter and two extinction coefficients (the so-called $3\beta + 2\alpha$ configuration) [e.g. Müller et al., 1999; Böckmann et al., 2001; Veselovskii et al., 2002]. Only a limited number of stations fulfil the requirements of the $3\beta + 2\alpha$ configuration while a larger number of lidar stations included in the observational network operate elastic lidar with up to 3β configuration. For that, additional retrieval schemes have been developed in the framework of EARLINET that combine elastic lidar measurements (by far more frequent than Raman) with ground-based AERONET photometers. Here, it is highlighted the LIdar-Radiometer Inversion Code (LIRIC) [Chaikovsky

et al., 2016] and the Generalized Retrieval of Atmosphere and Surface Properties algorithm (GRASP) [Dubovik et al., 2014], which includes the Generalized Aerosol Retrieval from Radiometer and Lidar Combined data algorithm (GARRLiC) [Lopatin et al., 2013].

The main algorithm used throughout this thesis is GRASP, which is described in detail in Section 4.2.2. GRASP consists of several modules that can be used in different ways according to the needs of the user. Its versatility allows the retrieval of aerosol optical and microphysical properties by combining different remote sensing measurements. Actually, GRASP was successfully used for the retrieval of the vertical aerosol properties using different configurations and measurements: as the combination of aerosol optical depth, sky radiances and elastic lidar [Lopatin et al., 2013; Bovchaliuk et al., 2016; Tsekeri et al., 2017]; polar nephelometer data [Espinosa et al., 2017]; satellite images [Kokhanovsky et al., 2015]; aerosol optical depth and sky radiances (including polarization) [Fedarenka et al., 2016]; spectral aerosol optical depth and sky camera images [Román et al., 2017a] and even only spectral aerosol optical depth measurements [Torres et al., 2017].

The research activities of this thesis are in the framework of advancing in the understanding of aerosol vertical distribution, more specifically in aerosol microphysical properties. In this sense, the main objective of this thesis is the implementation of new schemes in GRASP algorithms that allows continuous day-to-night aerosol vertical profiles characterization, with focus on aerosol microphysical properties. To this end, in this thesis is studied the potential of GRASP algorithm to retrieve vertically-resolved aerosol properties by means of the synergic use of lidar and sun/sky photometer data, the combination of different passive and active remote sensing measurements for continuous day- and night-time retrievals. Finally, in this thesis is studied the potential of GRASP to combine the

ceilometer and sun/sky measurements for obtaining aerosol properties using single-wavelength lidar systems.

This thesis is structured in eight chapters. The first chapter presents an overview of current research in atmospheric aerosols followed by the objectives and outline of this thesis. The second chapter focus on the theoretical fundaments needed to follow this thesis and include a discussion of the Earth's atmosphere structure and aerosol definitions including their sources, impacts and properties. The third chapter is for detailed descriptions of the experimental stations and of the remote sensing and in-situ instrumentations used.

The fourth chapter is devoted to the description of the methodologies and inversion schemes used. First the lidar inversions, both Klett and Raman inversion methods, are presented. Secondly, the LIRIC and GRASP algorithms are described, with an extended description of GRASP due to its extensive use in this thesis.

The fifth chapter compares aerosol properties retrieved by GRASP with in-situ airborne measurements acquired during the ChArMEx/ADRIMED field campaign. Here, GRASP combines the lidar and the sun/sky photometer data for retrieving both vertically-resolved and column-integrated aerosol properties. GRASP is used to investigate its potential for studying aerosol properties by comparing its retrievals with airborne measurements, AERONET and LIRIC products.

The sixth chapter presents the results of day and night aerosol microphysical properties retrieved by GRASP during an intense Saharan dust event that occurred during SLOPE I field campaign. The different schemes and instrumentations used for night-time retrievals are discussed. Evaluations of retrieved parameters are done versus in-situ measurements at the high mountain Sierra Nevada station.

The seventh chapter is focused on the retrieval of vertical profiles of aerosol microphysical properties using low-cost lidar systems such as ceilometers combined with sun/sky photometers. The accuracy of this approach is evaluated using synthetic data. The results of this approach are discussed using measurements collected in ChArMEx/ADRIMED and SLOPE I field campaigns.

Finally, the eighth chapter presents the summary and main conclusions of this thesis, and also an outline of future research.

2. Fundamentals

2.1. Earth's atmosphere structure and properties

The Earth's atmosphere is a layer of the planet retained by its gravity and mainly composed by clouds, gases and suspended particles. The life at Earth can be developed thanks in part to the atmosphere because of its contribution to modulate the planetary temperature (greenhouse effect) and to absorb harmful ultraviolet solar radiation. Figure 2.1 shows the layering structure of the Earth's atmosphere based on its thermal structure, characterized by the presence of different temperature gradients along the vertical profile. It should be noted that 75% of the atmospheric mass is located within the first 12 km from ground and the atmosphere does not has an abrupt end, in fact, it slowly becomes thinner and fades into space [Seinfeld and Pandis, 1998].

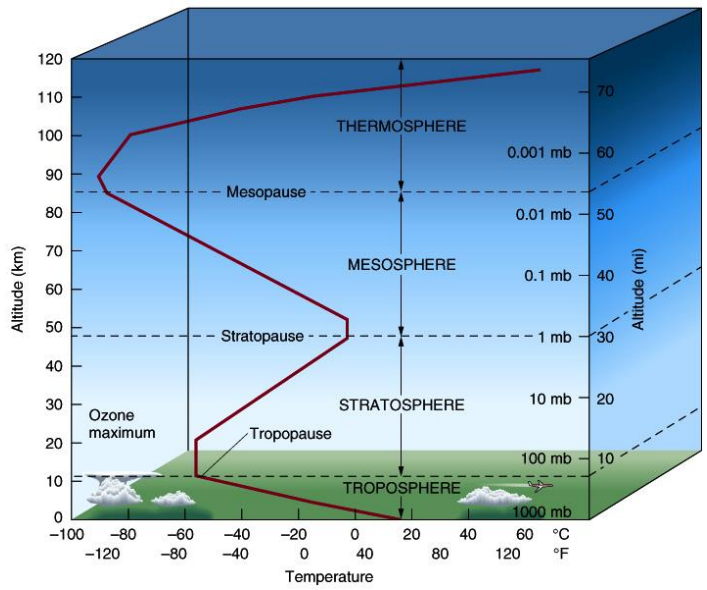

Figure 2.1. Atmosphere structure and temperature profile (source: http://unilaggeography2012.blogspot.nl/p/gry-101-introduction-to-physical.html).

The regions of the atmosphere are summarized as follows:

- *Troposphere* is the lowest layer of the atmosphere which extends from Earth's surface up to ~12 km (depending on latitude and time of year) and where all activities and aspects related with weather occurs. In this layer the temperature decreases with the altitude at a mean rate of 6.5ºC/km (in normal conditions) and there is an active vertical mixing. On top of the troposphere there is an isothermal layer known as tropopause.

- *Stratosphere* is the layer from above tropopause up to 50 km. The presence of atmospheric aerosol in this layer is usually related to volcanic injection where the time residence varies between several months to few years [Alados-Arboledas and Olmo, 1997; Seinfeld and Pandis, 1998]. In this region, in contrast to the troposphere, the vertical mixing is weak and the temperature increases with the altitude due to absorption of UV radiation by the ozone. The maximum temperature occurs in the stratopause, located at the top of the stratosphere.

- *Mesosphere* is the layer extending from stratopause up to 80 km. In this region, the temperature gradient with altitude is negative again and at mesopause, the upper boundary of mesosphere, the temperature reaches up to -80ºC.

- *Thermosphere*, which height extends from 80 to 640 km. The radiation at shortest wavelengths is absorbed by N_2 and O_2 and causes the increasing of temperature with height.

- *Exosphere* is the outermost layer of atmosphere where only He and H_2 are found.

Earth's atmosphere is mainly composed by two groups of gases. The first group includes the permanent gases with percentages almost constant, among which are the nitrogen, oxygen and several noble gases. The second group consists of gases

with variable concentrations and account for about one tenth percent of the atmosphere. Among other atmospheric components atmospheric aerosol particles, which are highly variable in space and time, are included. Table 2.1 shows the percentage in volume of the gases in the atmosphere.

Table 2.1. Average composition of the dry atmosphere below 25 km [Barry and Chorley, 1987].

Constant gases		**Variable gases**	
Gas	**Volume (%)**	**Gas**	**Volume (%)**
Nitrogen (N_2)	78.08	Water vapor (H_2O)	0-4
Oxygen (O_2)	20.95	Carbon dioxide (CO_2)	$3.94x10^{-2}$
Argon (Ar)	0.93	Methane (CH_4)	$1.5x10^{-4}$
Neon (Ne)	$1.8x10^{-3}$	Nitrous oxide (NO_2)	$3.25x10^{-5}$
Helium (He)	$5.2x10^{-4}$	Carbon monoxide (CO)	$0.19\ x10^{-4}$
Krypton (Kr)	$1.1x10^{-4}$	Ozone (O_3)	$0\text{-}12x10^{-4}$
Xenon (Xe)	$8.9x10^{-5}$		

2.2. Atmospheric aerosol

2.2.1. Atmospheric aerosol definition and origins

The atmospheric aerosol is defined as the suspension of solid and/or liquid particles in a gaseous medium such as atmospheric air [Seinfeld and Pandis, 2006]. The atmospheric aerosols can be mainly classified by their origin, source, shape and size. Aerosols sources can be split into natural and anthropogenic. Also, aerosols particles can be divided into primary or secondary depending on the origin. Primary aerosols account for that emitted directly to the atmosphere in the particulate phase, whereas secondary aerosols undergo a more complex formation pathway, produced by gas-to-particle conversion of aerosol precursors.

Primary natural aerosol particles include sea salt from the oceans, volcanic ash, biogenic particles (e.g. pollen or other plant material), smoke from fires, and wind-blown mineral dust. Mineral dust is produced by wind erosion of soil in arid and semi-arid regions (e.g. Sahara Desert) and is injected into the atmosphere under favorable weather conditions, being one of the major aerosols of the Earth's atmosphere. Once lifted into the air, mineral dust can be transported over several thousands of kilometers [Hamonou et al., 1999; Goudie and Middleton, 2001; Ansmann et al., 2003], therefore it is not only a regional phenomenon that has a global climate effect. On the other hand, natural sources of secondary aerosols can be the biosphere and volcanoes that emit sulfur (e.g. in form of dimethyl sulfide, DMS, and sulfur dioxide into the atmosphere) which through oxidation to sulphate forms new particles. The biosphere can also emit volatile organic compounds (VOCs) that can be oxidized and are able to form new particles [Ehn et al. 2014].

Primary anthropogenic aerosol particles mainly include black carbon (BC) and organic carbon (OC). The origin of BC and OC are mainly from biomass burning (e.g. land clearing and land-use) and fossil fuel combustion by traffic and industry processes. The mineral dust emissions are also assumed anthropogenic when the origin is agricultural or industrial practices [Prospero et al., 2002; Rodríguez et al., 2011]. Secondary anthropogenic aerosol particles are generated from precursor gases (e.g. SO_2, NO, NH_3 and VOCs) emitted through domestic heating systems based on coal or wood combustion, industrial plants, vehicle emissions and agricultural activities.

The lifetime of aerosol particles can generally span from a few days to a few weeks and are removed from the atmosphere by wet deposition through incorporation into precipitation or dry deposition through sedimentation. The combination of specific sources and lifetimes of aerosol particles explains their highly non-uniform distribution around the globe. The shape of aerosol particles is

very variable and may be irregular as shown Figure 2.2. The size of aerosol particles is also highly variable, ranging from a few nanometers to several hundreds of micrometers. Indeed, the aerosol size distribution is characterized by different size modes, which are specific concerning their sources and their different transformation.

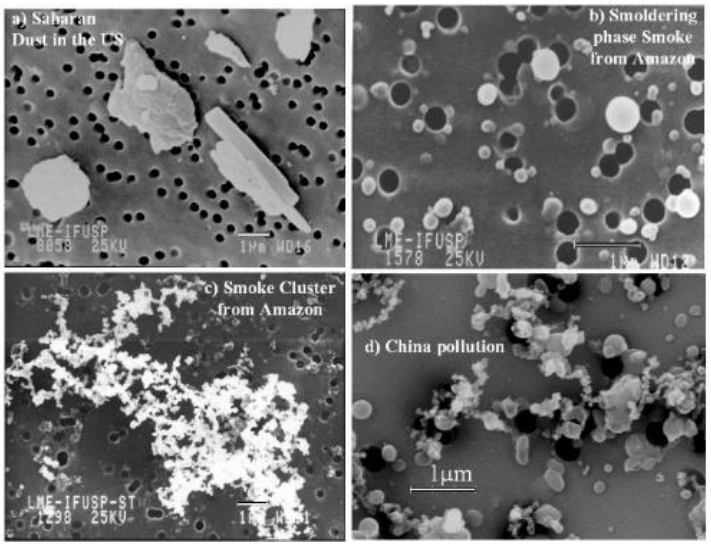

Figure 2.2. Aerosol particles analyzed by the scanning electron microscope (source: http://alg.umbc.edu/usaq/archives/001044.html).

Figure 2.3 shows a schematic of aerosol particle size distribution (PSD) with an overview of the relevant processes that affect different size of particles and lead to changes in the size distribution of particles [Zieger, 2011]. Generally, four groups of atmospheric particles can be defined based on the diameter of aerosol particles. The first group is nucleation mode with diameters not exceeding 0.025 μm. They are thought to be generated by gas-to-particle conversion processes and have a very short lifetime. The second group is the Aitken mode particles which have diameters between 0.025 and 0.1 μm. These particles are formed from gas-to-particle conversion of hot vapors and are transformed through coagulation into particles of the accumulation mode. The accumulation mode is the third group, which the

particles have diameters from 0.1 to 1 μm. These three particle modes are collectively referred to as fine particles. The last group is defined as the coarse mode and it includes particles with diameters larger than 1 μm. These particles are introduced directly into the atmosphere, from both natural and anthropogenic sources, and due to their large size and mass, the more important removal process is sedimentation.

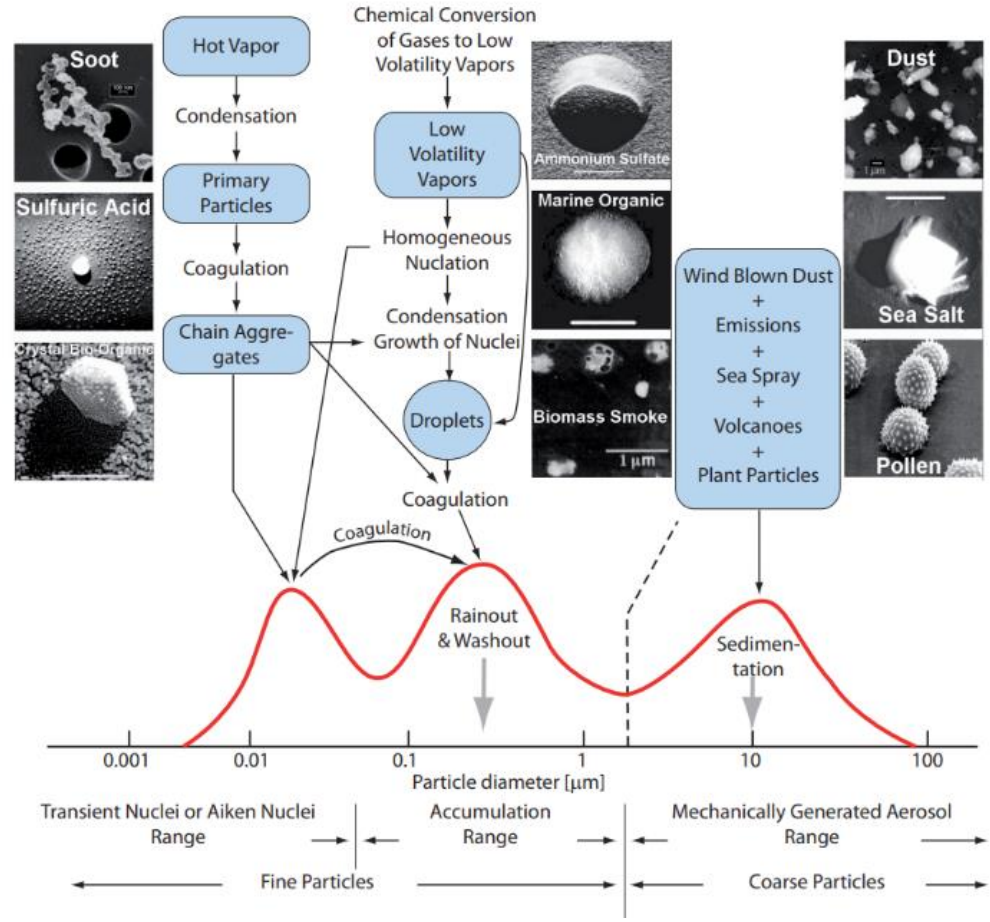

Figure 2.3. Idealized scheme of the distribution of particle surface area of an atmospheric aerosol Whitby et al. [1976]. Principal modes, sources and particle formation and removal mechanisms are also indicated (Figure taken from Zieger [2011], originally adapted from Whitby and Cantrell [1976]; Seinfeld and Pandis [1998]; Heintzenberg et al. [2003]).

2.2.2. Aerosol effects on climate

The study of atmospheric aerosols is important because affect directly human health, ecosystems, materials, visibility and Earth's budget. The atmospheric aerosols climate effect is associated to their influence on the radiative budget of the Earth. The two main roles of atmospheric aerosols within the Earth-atmosphere energy budget are its interaction with the solar and terrestrial radiation and its interaction with clouds [IPCC, 2013]. Figure 2.4 gives a scheme of aerosol-radiation (ARI) and aerosol-cloud interactions (ACI).

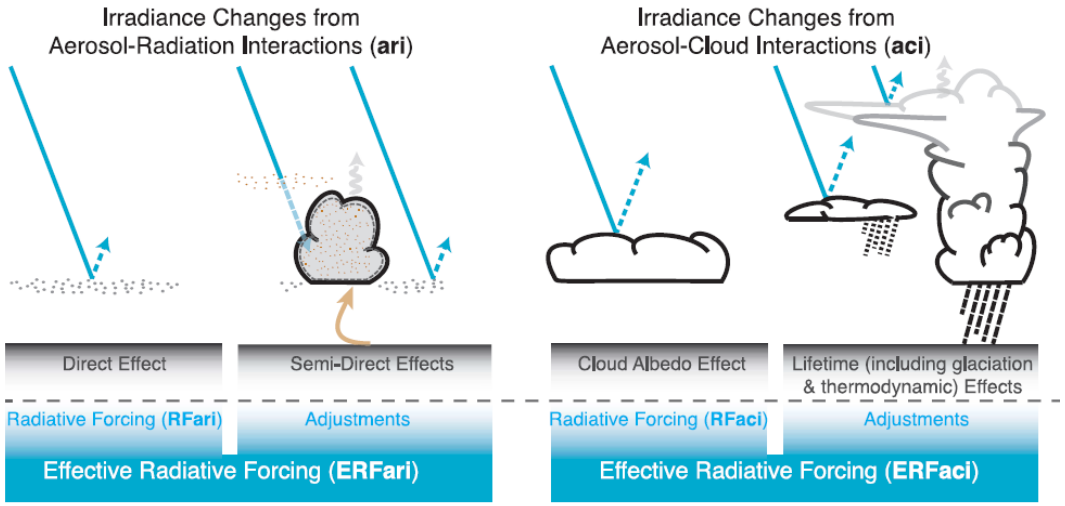

Figure 2.4. Schematic of the aerosol-radiation and aerosol-cloud interactions. The blue arrows depict solar radiation, the grey arrows terrestrial radiation and the brown arrow symbolizes the importance of couplings between the surface and the cloud layer for rapid adjustments. Adapted from Boucher et al. [2013] (Source: IPCC, 2013).

The ARI is mainly associated with the aerosol direct effect: extinction of incoming solar through scattering and absorption mechanisms. The aerosol radiative forcing (the difference in the incoming and outgoing radiation in the Earth-atmosphere system caused by aerosols) due to the direct effects may be both positive and negative and depends on the absorption both from the aerosol and the underlying surface albedo (e.g. oceans, desert, snow, clouds) [Chylek and Wong, 1995; Haywood and Shine, 1995; Haywood and Boucher, 2000].

The ACI is based on the modifications of cloud properties due to the role of some aerosol particles as cloud condensation nuclei (CCN) and/or ice forming nuclei (IN). The aerosol affects clouds in several possible pathways, as is catalogued by Denman and Brasseur [2007]. All radiative consequences of aerosol-cloud interactions are included in the "effective radiative forcing due to aerosol-cloud interactions" (ERFaci). ERFaci explains the aerosol-related microphysical modifications of the cloud albedo [Twomey, 1974, 1977], as well as any secondary effects from clouds adjustments to changes in their environment [Pincus and Baker, 1994].

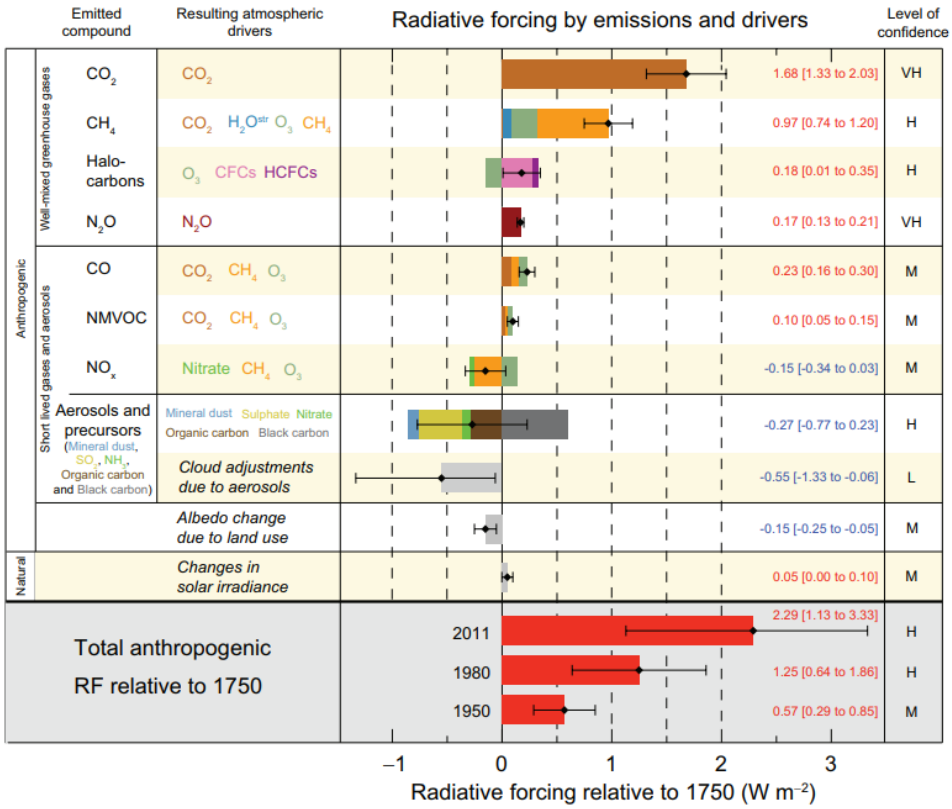

Figure 2.5. Radiative forcing estimates in 2011 relative to 1750 and aggregated uncertainties for the main drivers of climate change taken from IPCC [2013]. Values are global average radiative forcing. The best estimates of the net radiative forcing are shown as black diamonds with corresponding uncertainty intervals; the numerical values are provided on the right of the figure, together with the confidence level in the net forcing (VH – very high, H – high, M – medium, L – low, VL – very low). Total anthropogenic radiative forcing is provided for three different years relative to 1750.

The aerosol-radiation and aerosol-cloud interactions still have associated an uncertainty that, together with the scarce knowledge of the spatial and temporal distribution of the atmospheric aerosol, cause a large uncertainty in the estimation of the radiative forcing due to atmospheric aerosol [Boucher et al., 2013]. Figure 2.5 shows the main components of the climate radiative forcing. The atmospheric aerosol distribution is highly non-uniform around the globe due to combination of specific sources and their lifetimes. The quantification of radiative forcing by the aerosol effect is more complex compared with the greenhouse gases due to their short lifetime, which usually can span from a few days to a few weeks.

2.3. Interactions of light with aerosol particles

The light crossing the atmosphere is attenuated due to scattering and absorption of radiation by particles and gas molecules. The extinction of light caused by particles is the sum of the absorption and scattering processes.

Absorption is a process where the incident radiative energy becomes part of the internal energy of the particles or gases interacting with radiation. The fundamental idea of the absorption process lies in the exchanges of energy between the electromagnetic field and the molecules in the atmosphere. For gases, this process depends on the molecule energy state that at the same time depends on the rotational, vibrational or electronic energies. The gas absorption process is selective because the absorption occurs only at discrete wavelengths, having in mind that the energy levels associated with these different kinds of energy are quantized. The absorption that may take place over a number of wavelengths very close to each other is called absorption band [Iqbal, 1983]. In contrast with gases absorption, which is spectrally selective, the absorption by aerosols does not vary abruptly with wavelength, at least from ultraviolet to near infrared wavelengths [Dubovik et al.,

2002a]. In general, the absorption processes produce an increase of atmospheric components internal energy and therefore of their temperature.

Scattering is a process where the incident energy transported by an electromagnetic wave is scattered in other directions as a result of the interaction of the gases or particles with this electromagnetic wave. For gas molecules, due to their small size, the scattering cross section depends on the λ-wavelength as λ^{-4} [Nicolet, 1984; Bodhaine et al., 1999], phenomenon called as Rayleigh scattering and being responsible of the blue-sky color in cloud-free sky. On the other hand, due to the bigger size of the aerosols, the aerosol scattering is explained by the Mie theory, which predicts weaker dependence of scattering cross section on wavelength. Due to the high variability of real particles shapes, the exact solutions describing the interaction between the electromagnetic field and particles have been calculated only for a few selected geometrical shapes [Mishchenko et al., 2000, 2002]. Hence, one of the main difficulties in remote sensing of atmospheric aerosols is the modelling of light scattering by non-spherical particles [Dubovik et al., 2006]. Mishchenko et al. [1997] noted that non-spherical particles assumed as mixture of randomly-oriented spheroids with different sizes and axis ratios can reproduce the phase function of desert dust. This spheroid model is applied in different aerosol retrieval using remote sensing data [Dubovik et al., 2002b, 2006; Veselovskii et al., 2010; Lopatin, 2013].

The scattered light mostly preserves the frequency of the incident light (elastic scattering), but sometimes the scattering has a shift of frequency (Raman scattering). The Raman scattering allows variations in the quantum state of the molecule, changing its vibrational, rotational and/or vibrational-rotational energy level. If scattered radiation energy decreases due to absorption of energy by the molecule, then the wavelength of the scattered radiation is shifted towards higher values and the process is called Stokes Raman scattering. On the other hand, anti-

Stokes Raman scattering happens when the frequency of the scattered radiation increases and the wavelength is shifted towards lower values due to the loss of energy by the scattered molecule. It should be noted that the intensity of the Raman scattered electromagnetic radiation is three orders of magnitude lower than the intensity of the elastic scattering [Kovalev and Eichinger, 2004].

The scattering process strongly depends on the size parameter, x, defined as the relation between the particle radius and the wavelength of the incident wave ($x=2\pi r/\lambda$) and also on the complex refractive index (CRI) which depends on the particle chemical composition [Bohren and Huffmann, 1998]:

- For $x < 0.6/n$, where n the real part of the CRI of the particles, the scattering process is described by Rayleigh theory. The Rayleigh's theory describes the scattering of solar radiation by air molecules and it is based on the assumption that the scattering particles are spherical with radii less than 0.2 times the wavelength of the incident radiation.
- For $0.6/n < x < 5$, the scattering is explained by Mie theory. It is applied when the size of the particles is comparable to the incident wavelength ($x \sim 1$). This scattering produces interference patterns with the partial waves emitted by multipoles of the particles having phase differences. Therefore, there is a strong angular dependency which increases in the forward scattering (compared to Rayleigh pattern) and the spectral dependence of the scattering is smaller.

More detail on Lorentz-Mie scattering theory can be found in Born and Wolf [2013]. Figure 2.6 shows the angular pattern for Rayleigh and Mie scattering theories. Rayleigh scattering is symmetric respect to the plane perpendicular to the propagation with maxima at $\Theta = 0^o$ and, hence, $\Theta = 180^o$, being its minima at $\Theta = \pm 90^o$. By other hand, Mie scattering presents an asymmetry pattern, with a strong forward scattering compared to Rayleigh pattern. The angular distribution of

scattered radiation can be described by the phase function, which is well known for gases (Rayleigh phase function), while it varies for particles with the aerosol type. The phase function, $P(\Theta)$, is a variable which describes the angular distribution of the scattered energy as function of the scattering angle Θ. Usually the aerosol phase function is approximated by the Henyey-Greenstein phase function [Henyey and Greenstein, 1941], which depends on a parameter called "asymmetry parameter" that quantifies the scattered radiation fraction in the hemispherical forward direction.

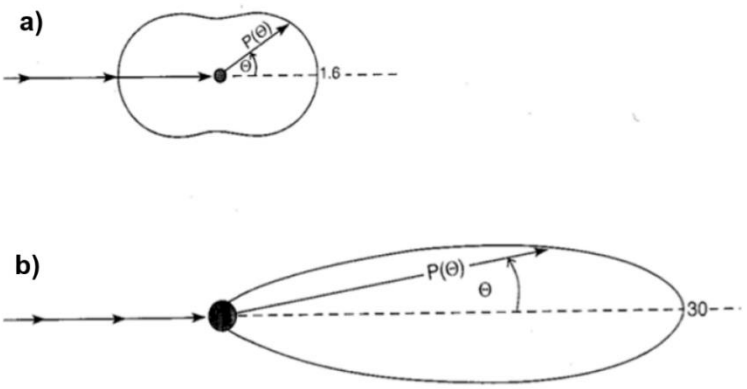

Figure 2.6. Rayleigh (**a**) and Mie (**b**) scattering processes.

According to Beer-Lambert-Bouguer law, a well collimated beam of monochromatic light with radiant flux L_λ will be attenuated by dL_λ which passes a heterogeneous medium of length ds (Figure 2.7).

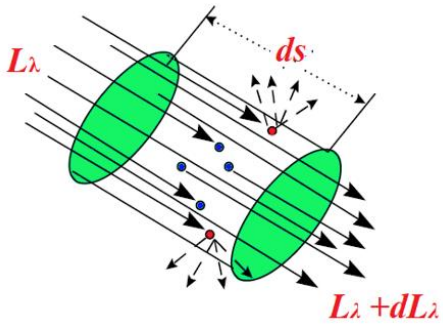

Figure 2.7. Schematic drawing of the radiance variation observed when a radiant flux beam travels through a distance in the medium.

The dL_λ is defined as:

$$dL_\lambda = -L_\lambda \alpha_{tot}(s,\lambda) ds \qquad \text{Eq. 2.1}$$

where α_{tot} is the total extinction coefficient, which is the attenuation of light by atmosphere due to a combination of scattering (σ_{sca}) and absorption (σ_{abs}) processes both aerosols and molecules; it is the sum of molecules and particles extinction coefficients. The relation for the attenuated beam through a medium of length R is obtained by integrating the Equation 2.1:

$$F_\lambda = F_{0,\lambda} e^{-\int_0^R \alpha_{tot}(s,\lambda) ds} \qquad \text{Eq. 2.2}$$

where $F_{0,\lambda}$ is the incident light beam.

2.4. Optical and microphysical aerosol properties

The measurements of atmospheric aerosol properties are necessary for the study of the atmospheric aerosol impact on the Earth's climate. Aerosol optical and microphysical properties are used as input data for the atmospheric aerosol models [Thomas and Stamnes, 2002]. The main aerosol properties used for the discussion of the obtained results in this dissertation are described in the following subsections.

2.4.1. Aerosol optical properties

From the Equation 2.2, the optical thickness (OT) is defined as the integrated extinction coefficient between two points located at s_1 and s_2:

$$OT(\lambda) = \int_{s_1}^{s_2} \alpha_{tot}(s,\lambda)\, ds \qquad \text{Eq. 2.3}$$

By the other band, in atmospheric science it is used the total optical depth, τ_{tot}, or normal optical thickness as the optical thickness measured in the vertical direction between the h_1 and h_2 altitudes:

$$\tau_{tot}(\lambda) = \int_{h_1}^{h_2} \alpha_{tot}(h, \lambda)\, dh \qquad \text{Eq. 2.4}$$

The relationship between optical thickness and optical depth is

$$OT(\lambda) = \tau_{tot}(\lambda) \cdot m_0 \qquad \text{Eq. 2.5}$$

where m_0 is the relative optical air mass. The Equation 2.6 shows the relative optical air mass, m_0, as a function of the solar zenith angle (SZA; θ) defined as the angle between the zenith (the vertical direction) and the direct solar irradiance path:

$$m_0 = \frac{1}{\cos(\theta)} \qquad \text{Eq. 2.6}$$

The Equation 2.6 is valid for a uniform atmosphere with refractive index equal to one is assumed, a plane-parallel atmosphere is considered, and values of θ smaller than 80º [Iqbal, 1983]. Otherwise, a different approximation has to be used [i.e. Kasten and Young, 1989].

The atmospheric total optical depth is usually defined from ground up to the top of the atmosphere (TOA) and it includes the scattering and absorption processes of the different atmospheric components:

$$\tau_{tot}(\lambda) = \tau_g(\lambda) + \tau_c(\lambda) + \tau_a(\lambda) \qquad \text{Eq. 2.7}$$

where τ_g refers to the optical depth of gases absorption such as by water vapor, nitrogen, dioxide and ozone, and also refers to the gases scattering contribution by the Rayleigh scattering; τ_c represents the optical depth of absorption and scattering of light by clouds (this optical depth will be neglected using only cloud-free absorption and scattering); τ_a is the aerosol optical depth (AOD). Hereafter, it will refer to τ_a as τ since in the results presented in this thesis it will focus mainly in this term.

The spectral dependence of the aerosol optical depth is parameterized by means of the Ångström law [Ångström, 1964]:

$$\tau(\lambda) = \tau_{1\mu m} \cdot \lambda^{-AE} \qquad \text{Eq. 2.8}$$

where λ units are microns, $\tau_{1\mu m}$ is the turbidity parameter which corresponds with AOD at 1 μm, and AE is the Ångström exponent which characterizes the spectral features of aerosols and is linked to the size of the particles [Shifrin, 1995]. Large AE values are related with the prevalence of fine particles (e.g. anthropogenic pollution) and low values indicate the presence of coarse particles (e.g. desert dust and marine aerosols) [Dubovik et al., 2002a].

The complex refractive index is also an optical property of the aerosol that is involved in the extinction of light:

$$m(\lambda) = n(\lambda) + i\kappa(\lambda) \qquad \text{Eq. 2.9}$$

where n and κ are the real and imaginary part of the complex refractive index, m, respectively. The real refractive index (RRI) is related with the scattering efficiency of particles which depends on the size and shape of particles. On the other hand, the imaginary refractive index (IRI) is related with the absorption efficiency of particles which depends on the particles chemical composition.

Single scattering albedo (SSA; ω_0) determines the relation between the processes of scattering and absorption occurring simultaneously when the radiation interacts with particles:

$$\omega_0(\lambda) = \frac{\sigma_{sca}(\lambda)}{\sigma_{sca}(\lambda) + \sigma_{abs}(\lambda)} = \frac{\sigma_{sca}(\lambda)}{\alpha(\lambda)} \qquad \text{Eq. 2.10}$$

The SSA is a key parameter for the estimation of the direct radiative impact of aerosols. It depends on the relative source strengths of the various aerosol

substances. Purely scattering particles (e.g. sulphates) exhibit values of 1, while very strong absorbers (e.g. black carbon) can have values of 0.2 [Schnaiter et al., 2003].

2.4.2. Aerosol microphysical properties

As commented in the Section 2.2, the size of atmospheric aerosols ranges from a few nanometers to several hundreds of micrometers which can be described by the number size distribution $\mathrm{n}(r)$ as:

$$\mathrm{n}(r) = \frac{dN}{d\ln r} \qquad \text{Eq. 2.11}$$

representing the number of particles with radius in the logarithmic interval $[\ln r, \ln r + d\ln r]$. From the $\mathrm{n}(r)$, the equivalent surface size distribution $s(r)$ is defined as:

$$s(r) = \frac{dS}{d\ln r} = 4\pi r^2 \frac{dN}{d\ln r} = 4\pi r^2 \mathrm{n}(r) \qquad \text{Eq. 2.12}$$

and the volume size distribution $v(r)$ is expressed as:

$$v(r) = \frac{dV}{d\ln r} = \frac{4\pi r^3}{3}\frac{dN}{d\ln r} = \frac{4\pi r^3}{3}\mathrm{n}(r) \qquad \text{Eq. 2.13}$$

These relations of the surface and volume distributions with number distribution can only be used assuming spherical particles.

The particle size distributions often present certain behavior allowing their modelling. The log-normal distribution function is a mathematical expression which allows an analytical representation of these size distributions, especially for the smaller particles, in clean and polluted areas [Hegg et al., 1993]:

$$v(r) = \frac{dV}{d\ln r} = \frac{VC}{\sigma_v\sqrt{2\pi}}\exp\left[-\frac{\ln^2(r/r_m)}{2\sigma^2}\right] \qquad \text{Eq. 2.14}$$

where VC is the total volume concentration of particles, r_m is the volume median radius which identifies the location of the peak in the curve (the center) of the size distribution, and σ_v is the standard deviation from volume median radius and it represents the width of this distribution. These parameters are calculated as follows:

$$\mathrm{VC} = \int_{r_{min}}^{r_{max}} \frac{dV}{d\ln r} d\ln r \qquad \text{Eq. 2.15}$$

$$\ln r_v = \frac{\int_{r_{min}}^{r_{max}} \ln r \frac{dV}{d\ln r} d\ln r}{\int_{r_{min}}^{r_{max}} \frac{dV}{d\ln r} d\ln r} \qquad \text{Eq. 2.16}$$

$$\sigma_v = \sqrt{\frac{\int_{r_{min}}^{r_{max}} (\ln r - \ln r_v)^2 \frac{dV}{d\ln r} d\ln r}{\int_{r_{min}}^{r_{max}} \frac{dV}{d\ln r} d\ln r}} \qquad \text{Eq. 2.17}$$

These three parameters for both fine and coarse modes describe a bimodal log-normal size distribution. In this thesis, also is used a secondary aerosol property as the effective radius (r_{eff}), which is the ratio between the third and second moments of aerosol number size distribution:

$$r_{eff} = \frac{\int_{r_{min}}^{r_{max}} r^3 \frac{dN}{d\ln r} d\ln r}{\int_{r_{min}}^{r_{max}} r^2 \frac{dN}{d\ln r} d\ln r} \qquad \text{Eq. 2.18}$$

3. Experimental sites and instrumentation

3.1. AGORA

The experimental part of this thesis has been developed at Andalusian Global ObseRvatory of the Atmosphere (AGORA), located in Southern Spain and including several experimental sites. AGORA is operated by the Atmospheric Physics Group (GFAT) being the main research activities focused on the study of the atmosphere, the Earth's surface and their interactions using remote sensing and in-situ techniques. AGORA combines complementary stations with different atmospheric conditions, high-degree of expertise and many facilities providing an ideal environment for a wide range of aerosol research, from urban to remote background conditions. AGORA favors integrated studies by using a broad range of instrumentation from active and passive remote sensing to a variety of in-situ methodologies.

The location of the installations, in the most meridian sector of the European continent near the African coast, allows a detailed analysis of the Saharan dust [e.g. Guerrero-Rascado et al., 2008; Cazorla et al., 2017] and the impact of the anthropogenic aerosol (originated at the metropolitan area of Granada) [e.g. Lyamani et al., 2010; Titos et al., 2017]. Due to its location at the slopes of Sierra Nevada Mountain range, AGORA offers a unique combination of remote sounding and in-situ techniques at different elevations, which is an added value for validation of vertical profiles of aerosol optical and microphysical properties retrieved by inversion of remote sensing data acquired at the valley level.

Figure 3.1 shows a scheme of the three different stations included in AGORA. The UGR station (37.16º N, 3.61º W, 680 m a.s.l.) is located at the

Andalusian Institute for Earth System Research (IISTA-CEAMA) in the city of Granada. The UGR station combines long-term monitoring of vertical distribution of atmospheric aerosol, based on active and passive remote sensing, with in-situ measurements for the characterization of aerosol particles at ground level, as well as the monitoring of atmospheric and solar radiation at several spectral ranges.

AGORA includes two additional stations in Sierra Nevada Mountain range: Cerro Poyos station (hereinafter called CP) at 1820 m a.s.l. (37.11º N, 3.49º W) and Sierra Nevada station (hereinafter called SNS) at 2500 m a.s.l. (37.10º N, 3.39º W) located about 12 and 25 km away (horizontally) from UGR. The SNS station can allows for characterization of regional and long-range transport episodes and the validation of inversion algorithms used to retrieve aerosol optical and microphysical properties.

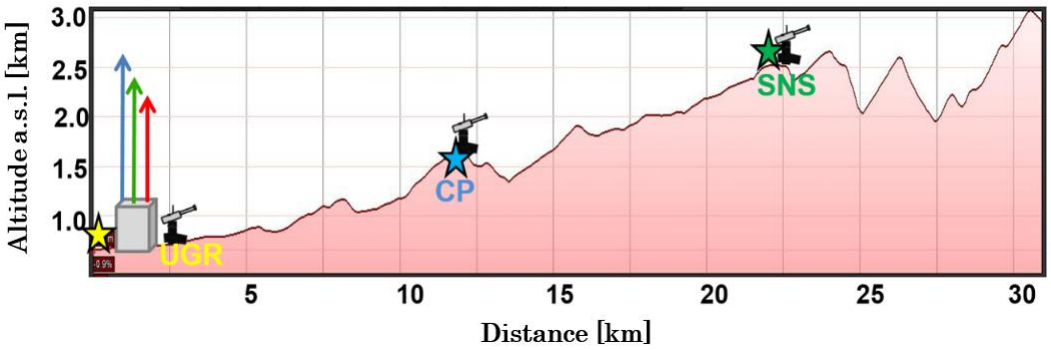

Figure 3.1. Spatial distribution of AGORA stations.

3.2. Remote sensing instrumentation

For the atmospheric aerosol characterization is commonly used both active and passive remote sensing. The active remote sensing systems include an emitting energy source and the system scan the atmosphere using a sensor that measure the energy that interacts with the atmosphere and come back towards the instrument; in the lidar systems the backscattered radiation from both gaseous molecules and atmospheric aerosol (under cloud-free conditions). On the other hand, the passive

remote sensing consists of a detection system that measures a natural light source after crossing the atmosphere. In the case of sun photometers, the natural source is the radiation emitted by the Sun that is transmitted by the aerosol and gaseous molecules in the atmosphere. The active and passive instrumentation used in this thesis are described in the following subsections.

3.2.1. Active remote sensing instruments

Lidar (Light Detection and Ranging) and ceilometer are examples of active remote sensing instruments which allow monitoring the vertical structure, composition and dynamics of atmosphere.

These systems emit short monochromatic light pulses into the atmosphere and measure the radiation scattered by atmospheric constituents in the backward direction at scattering angle of 180º. These systems usually emit pulses in the vertical direction pointing to the zenith. After a time, t, the backscattered light returned by the atmospheric layer is measured by the photodetectors of the system and therefore with the relation $h = c \cdot t/2$, the distance, h, between the scattering particle and the lidar system can be calculated knowing the speed of light, c.

In its simplest form, the detected lidar signal can be written as:

$$P(h,\lambda) = \frac{K \cdot O(h)}{h^2} \beta_{tot}(h,\lambda) \exp\left(-2 \int_0^h \alpha_{tot}(h',\lambda)\, dh'\right) \qquad \text{Eq. 3.1}$$

where $P(h,\lambda)$ is the received power, K is a parameter that depends on the geometry and characteristics of the system, $O(h)$ is a geometrical factor (overlap function), $\beta_{tot}(h,\lambda)$ and $\alpha_{tot}(h,\lambda)$ are the spectral backscatter and extinction coefficients of the atmospheric layer at altitude h. The $\beta_{tot}(h,\lambda)$ and $\alpha_{tot}(h,\lambda)$ are defined as:

$$\beta_{tot}(h,\lambda) = \beta_{aer}(h,\lambda) + \beta_{mol}(h,\lambda) \qquad \text{Eq. 3.2}$$

$$\alpha_{tot}(h,\lambda) = \alpha_{aer}(h,\lambda) + \alpha_{mol}(h,\lambda) \qquad \text{Eq. 3.3}$$

where de subscripts aer and mol are the aerosol and molecular components, respectively. Hereafter, it will refer to β_{aer} and α_{aer} as β and α, respectively, since in the results presented in this thesis it will focus mainly in these terms. The squared transmittance (due to travel back and forth), $T^2(h,\lambda)$, of the laser signal is defined as:

$$T^2(h,\lambda) = \exp\left(-2\int_0^h \alpha_{tot}(h',\lambda)\,dh'\right) \quad \text{Eq. 3.4}$$

For lidar and ceilometer applications is usual to use the so-called range corrected signal (RCS), which is defined as:

$$RCS(\lambda) = P(h,\lambda)\cdot h^2 \quad \text{Eq. 3.5}$$

3.2.1.1. Multiwavelength Raman lidar system

Figure 3.2 shows the lidar system operating at the UGR station which is a multiwavelength Raman lidar LR331D400 (*Raymetrics S.A.*).

Figure 3.2. Raman lidar system operated at UGR station.

The main characteristics of the system are presented in Table 3.1. It is configured in a monostatic biaxial alignment pointing vertically to the zenith. The transmission system consists of a pulsed Nd:YAG laser that emits at 1064 (110 mJ), 532 (65 mJ) and 355 nm (60 mJ) by means of the 2nd and 3rd harmonic generators.

Table 3.1. Technical characteristics of the UGR lidar system.

Emitter	
Pulsed laser source	Nd:YAG (Quantel CFR Series)
Wavelength	355, 532 and 1064 nm
Energy/pulse	60, 65, 110 mJ
Repetition rate	1, 2, 5 and 10 Hz
Laser beam diameter	6 mm
Laser beam divergence	<0.1 mrad
Receiver Optics	
Telescope	Cassegrain
Primary/secondary mirror diameter	400/90 mm
Focal length	3998 nm
Wavelengths	355, 387, 408, 532p, 532s, 607, 1064 nm
Full Width at Half Maximum	1.0, 2.7, 1.0, 0.5, 0.5, 2.7, 1.0
Detection Unit	
Transient Recorder	LICEL
Detectors	APD (at 1064 nm), PMT (other channels)
Detection mode	Analog and photon counting
Nominal spatial resolution	7.5 m

The receiving system has seven channels: three to measure the backscatter light at emission wavelengths plus one additional channel to measure cross-polarized light at 532 nm; two channels at 387 and 607 nm for the detection of Raman scattering from N_2 and an additional channel to detect the Raman scattering from water vapor at 408 nm. The vertical resolution of the system is 7.5 m. Due to incomplete overlap, atmospheric information up to 500 m above the system is limited [Navas-Guzmán et al., 2011]. The system is included in EARLINET network since 2005 and contributes to the ACTRIS research infrastructure. A detailed description of this multiwavelength lidar system can be found in Guerrero-Rascado et al. [2008].

3.2.1.2. Ceilometer

The ceilometer installed at UGR station is a CHM15k-Nimbus, manufactured by *Jenoptik* company (now these ceilometers are in charge of *Lufft* manufacturer). This instrument operates with a pulsed Nd:YAG laser which emits at 1064 nm and measures the backscatter signal by the atmosphere at the same wavelength. The spatial resolution is 15 m, reaching a maximum height around 15000 m a.g.l. The complete overlap is found around 1500 m a.g.l. [Heese et al., 2010] but with the overlap function provided by the manufacturer the 90% complete overlap is obtained between 555 and 885 m a.g.l.. The instrument directly provides NetCDF files with the RCS at 1064 nm every 15 seconds along all full day.

Figure 3.3. Ceilometer operated at UGR station.

In addition, the software also provides some products as the cloud base height and the total cloud cover. The ceilometer at UGR station is part of the Iberian Ceilometer Network (ICENET) [Cazorla et al., 2017]. Table 3.2 presents the main characteristics of the system, more information about it and its products can be found in the Jenoptik CHM15k user manual [Jenoptik, 2013].

Table 3.2. Technical characteristics of the UGR ceilometer system.

Emitter	
Pulsed laser source	Nd:YAG
Wavelength	1064 nm
Energy/pulse	8.4 μJ
Repetition rate	5-7 kHz
Laser beam divergence	<0.3 mrad
Detection Unit	
Transient Recorder	LICEL
Detectors	APD
Detection mode	Photon counting
Nominal spatial resolution	15 m

3.2.2. Passive remote sensing instruments

3.2.2.1. Sun/sky/lunar photometer

The automatic sun/sky photometer CIMEL CE318 (*Cimel Electronique*) is the standard instrument for the AERONET network. In this case, a CIMEL CE318-N installed at the UGR station (Figure 3.4a) was in operation since 2004 in a regular basis, but a CE318-NE model started to take measurements in 2011 and a CE318-T in 2016. At CP station, operated only from late spring to early autumn due to its remote location and snowfalls, a CIMEL CE318-NE is operated in a seasonal basis since 2011, being a CIMEL CE318-T since 2017. The calibration of these

photometers is annually performed by RIMA network (Red Ibérica de Medida fotométrica de Aerosoles, www.rima.uva.es) nowadays so-called GOA Calibration Facility, which is part of the European branch of AERONET (AERONET-EUROPE) in the framework of ACTRIS infrastructure. A complete description of the instrument and its measurements can be found in Holben et al. [1998]. Table 3.3 presents some characteristics and measurements of this system (CE318-NE).

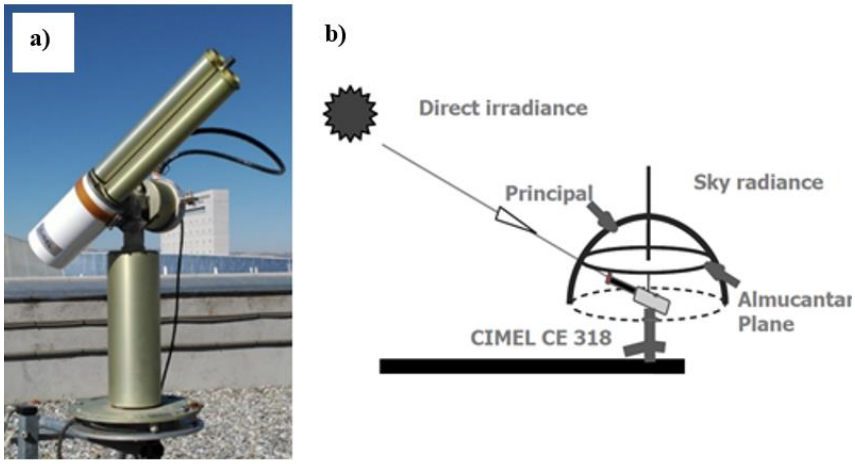

Figure 3.4. Sun/sky photometer CIMEL operated at UGR station (**a**). Scheme for measurement of direct irradiance, principal and almucantar plane (**b**).

The sun/sky (and lunar for CE318-T) photometer is equipped with 7-9 spectral channels (it depends on the photometer model) covering the spectral range between 340 and 1020-1640 nm. It performs direct sun (and lunar for CE318-T) irradiance measurements and sky radiance observations in both the almucantar and principal plane configurations at least at 440, 675, 870, and 1020 nm spectral channels (Figure 3.4b). Principal plane measurements are replaced by hybrid plane observations, a mix between principal and almucantar planes measurements, in CE318-T model. The direct sun irradiance measurements are made each 15 minutes, the almucantar and principle plane radiances are made hourly. For the almucantar radiance measurements, additional four sequences are also made, both in morning and afternoon, at optical airmasses of 4, 3, 2 and 1.7. In the principle plane, the

measurements are performed for different zenith angles with the azimuth angle constant and equal to the solar azimuth angle. On the other hand, for almucantar configuration, the zenith angle remains equal to the solar zenith angle and makes a scan clockwise and counter clockwise giving two measurements for each azimuth angle with respect to the sun position.

Table 3.3. Characteristics of photometer CIMEL CE318-NE.

Photometer CIMEL CE318-NE	
Detector	Si and InGaAs photodiodes
Wavelength	340, 380, 440, 500, 675, 870, 940, 1020 (with Si and also InGaAs) and 1640 nm
FOV	1.2º
Applications	Atmospheric aerosol Water vapor
Measurements	Direct sun irradiance Almucantar radiance Principal plane radiance

The CE318 measurements are automatically transferred in near real-time (every ~2 hours) to the GOA Calibration Facility, which resends after a first quality control the raw data to AERONET, where data are processed by the AERONET algorithm [Holben et al., 1998; Dubovik and King., 2000] to provide columnar aerosol optical and microphysical properties such as AOD, PSD, CRI and SSA. The data provided by AERONET (version 2 in this thesis) have various levels of quality: Level 1.0 hosts the unscreened data; Level 1.5 data are cloud-screened and Level 2.0 data are quality assured because they are reprocessed after calibration and manually inspected to fulfil a set of AERONET criteria [Holben et al., 2006]. In this thesis, the AERONET inversion products Version 2 Level 2.0 are used. However, in some cases, data of Version 2 Level 1.5 are used. The uncertainty of the

AERONET inversion products is described by Dubovik et al. [2000]. Errors in PSD retrievals are around 10–35 % for particles in the size range $0.1 < r < 7$ μm, while for sizes lower than 1 μm and higher than 7 μm retrieval errors rise up to 80–100%. For data products of Version 2 Level 2.0 ($AOD_{440}>0.4$ and $\theta>50^{o}$), the uncertainty in the retrieval of SSA is <0.03 and the errors are about 30–50% for the IRI. On the other band, the products Version 2 Level 1.5 provide accuracy levels drop down to 0.05–0.07 for the SSA, to 80% – 100% for the IRI, and to 0.05 for the RRI.

As mentioned before, the new sun/sky/lunar CIMEL CE318-T photometer (*Cimel Electronique*) was installed at UGR station since March 2016 and since 2017 at CP station. More details of the new CE318-T and its additional and enhanced operational functionalities are described by Barreto et al. [2016]. The most important feature of this new photometer is its capacity to measure the sun radiation reflected by the Moon during night-time providing valuable information of atmospheric aerosols during whole day. The new CE318-T characteristics are similar as CE318-NE sun/sky photometer (Table 3.3), taking measurements with a filter wheel (9 narrow filters) both with two detectors: Si for 340 to 1020 nm, and InGaAs (indium gallium arsenide) for 1020 and 1640 nm. During the day, the new instrument makes similar measurement to those described for the CE318-NE but replacing principal plane measurements by hybrid plane observation. For night-time, CE318-T makes multi-wavelength direct lunar irradiance measurements between first and third Moon quarters. CE318-T photometers (and the other models) used in this work were periodically calibrated following the standards of AERONET. The calibration of the CE318-T for AOD calculation at night-time has been done by the Lunar-Langley calibration method explained by Barreto et al. [2016].

3.2.2.2. Sky camera

The SONA sky camera ("Sistema de Observación de Nubosidad Automático": Automatic Cloud Observation System) is a device which provides hemispherical sky images along the whole day (Figure 3.5). The system is composed by a quartz dome with a shadow band in order to block the direct sun signal and a CCD camera with a fisheye lens inside of a waterproof case. The CCD camera provides RGB images with a resolution of 480x480 pixels. The camera takes images with an infrared (IR) cut-off filter which block IR light into the sensor which makes that the camera is not sensitive to infrared light above 700 nm. The CCD effective wavelengths for night moon scenarios were calculated by Román et al. [2017a], being 469 nm, 533 nm and 608 nm for blue, green and red channels, respectively. The main objective of the system was cloud cover detection identifying cloudy and cloud-free pixels, but it can be used with other purposes as to calculate the relative sky radiance near the Moon.

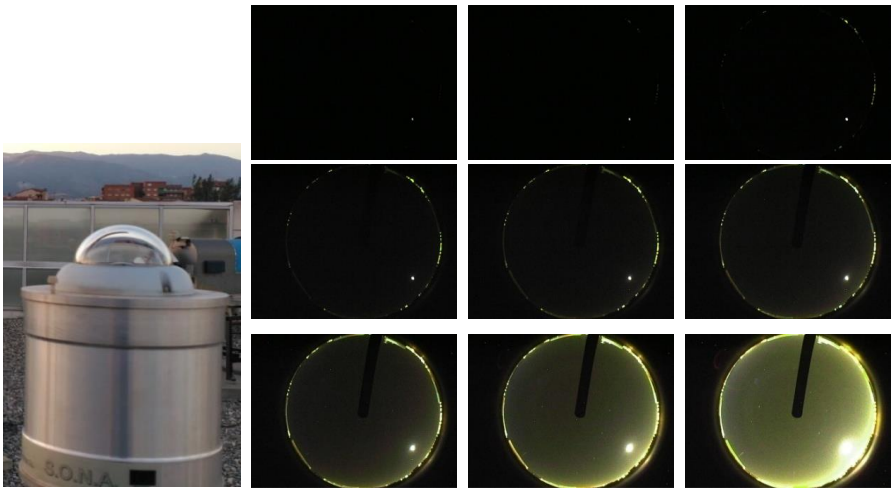

Figure 3.5. Sky camera SONA at UGR station and 9 sky images from the 16 images HDR multi-exposure sequence.

This camera was configured to take a multi-exposure sequence of sky images every 5 minutes. There is one sequence for daytime [Román et al., 2017b] and other

for night-time [Román et al., 2017a]. The night-time sequence consists of 16 consecutive sky images (9 of them are shown in Figure 3.5 as example) with exposure times following a doubling sequence. It allows obtaining a high dynamic range (HDR) image viewing the most illuminated parts of the sky in the low-exposure images and the darkest in the high-exposure ones. Using the pixel sensitivity function, that corrects linearity, calculated by Román et al. [2017a], an HDR image is calculated from the 16 images (dark frames are corrected previously in each individual image). This HDR is a linear image where every pixel signal is proportional to the incoming radiance, and the proportion is the same for every pixel (changes with the effective wavelength).

Once an HDR is calculated, the background light (previously calculated in Román et al. [2017a]) is removed in order to obtain the relative sky radiance at the lunar aureole. Then, the recorded relative irradiance in the HDR image is divided by the field of view (FOV) of each pixel to calculate the relative sky radiance (RSR). The RSR data points with same zenith angle of the Moon and different azimuth angles from 3° to 20° (1° steps) away from the Moon are chosen. The first azimuth is in agreement with the first angle of the almucantar measurements sequence used in the AERONET and the last azimuth is selected because beyond of it the camera signal does not significantly change. Both almucantar branches are averaged assuming the sky radiance is symmetric and finally, for each channel, the obtained signals are normalized giving as result the normalized camera radiance (NCR). A full description of this method is given by Román et al. [2017a], who quantified the uncertainty in NCR around 10% for the three channels.

3.3. In-situ instrumentation

The in-situ measurements presented in this study were mainly collected at SNS station. SNS station is part of the ACTRIS network and operates under ACTRIS

guidelines (http://actris2.nilu.no/). Air was sampled from the top of a stainless steel tube of 10 cm diameter and 4 m length located at about 15 m above the ground, on the roof of the building. Inside this main stack, there are several stainless steel pipes that drive the sampling air to the different instruments. A blower maintained a flow of 0.00167m^3 s^{-1} and the residence time of the air in the main pipe is 0.6 s. Thus, particles losses in the main pipe are considered negligible.

3.3.1. Nephelometer

The integrating nephelometer (model TSI 3563; Figure 3.6) measures the particle light scattering and backscatter coefficients, $\sigma_{sca}(\lambda)$ and $\beta(\lambda)$, at three wavelengths (450, 550 and 700 nm) with 5-min temporal resolution. A quartz-halogen lamp equipped with a built-in elliptical reflector illuminates over an angle of 7 to 170° the air sample (particle + gas) extracted by a small turbine blower at a constant flow of 30 l min^{-1}. The nephelometer underestimates the scattering and backscattering coefficients measurements due to the limits of the angular integration of the scattered light, since part of forward (0º–7º) and backward (170º–180º) signals are not measured. Nephelometer data were corrected for truncation and non-Lambertian illumination errors using the method described by Anderson and Ogren [1998].

Figure 3.6. Nephelometer TSI 3563.

A routine maintenance and calibration of the nephelometers was carried out periodically using CO_2 and filtered air. The nephelometer was zero adjusted using particle-free air every hour. The uncertainty in σ_{sca} is of 7% [Heintzenberg et al., 2006].

3.3.2. SMPS & APS

Figure 3.7. Scanning Mobility Particle Sizer.

The Scanning Mobility Particle Sizer (SMPS; Figure 3.7) composed of an Electrostatic Classifier (TSI Mod. 3080) and a Condensation Particle Counter (CPC; TSI Mod. 3772) measures the sub-micron particle number size distribution within the 12–615 nm particle mobility diameter range with 5-min temporal resolution. Aerosol and sheath flow rates were 1.0 and 5.0 lpm, respectively. SMPS data were corrected of internal diffusion losses and multiple charges with the AIM software (version 9.0.0, TSI, Inc., St Paul MN, USA). Following calibration procedures, uncertainty in the measured particle size distribution is within 10% and 20% for the size range 20-200 nm and 200-800 nm, respectively [Wiedensohler et al., 2017].

In addition, the coarse particle number size distribution within the 0.5–20 μm aerodynamic diameter range was measured by an Aerodynamic Particle Sizer (APS; TSI Mod. APS-3321; Figure 3.8). The APS measures number aerosol concentrations up to 1000 particles·cm^{-3} with coincidence errors inferior to 5% and 10% at 0.5 and 10 μm diameters, respectively. From these measurements, aerosol volume concentrations were obtained in the 0.05–10 μm radius range with 5-min time resolution. For that, Q-value=1 has been assumed for conversion from aerodynamic (APS) to mobility size distribution [Sorribas et al., 2015].

Figure 3.8. Aerodynamic Particle Sizer.

4. Methodology

4.1. Lidar inversion

There are two widely used techniques for retrieving the aerosol backscatter and extinction coefficients from lidar signals. The Raman inversion technique that uses both elastic and Raman signal [Ansmann et al., 1992] and Klett-Fernald inversion which only uses elastic signal [Fernald et al., 1972; Klett, 1981; Fernald, 1984]. Details on these inversion techniques are given in the following sections.

4.1.1. Elastic lidar technique

The Klett-Fernald method uses the elastic signal from lidar to retrieve the backscatter coefficient by the elastic lidar equation (Equation 3.1). The molecular terms are calculated using standard atmosphere conditions, usually tuned with the surface pressure and temperature measured in the lidar station or an atmospheric profile from radiosondes launched nearby, if it is available. Hence, to resolve the elastic lidar equation with two unknowns ($\beta_{aer}(h,\lambda)$ and $\alpha_{aer}(h,\lambda)$) is necessary to assume the aerosol extinction-to-backscatter ratio, which is called lidar ratio ($LR(h,\lambda)$). Aerosol lidar ratio is defined as:

$$LR(h,\lambda) = {\alpha(h,\lambda)}\Big/{\beta(h,\lambda)} \qquad \text{Eq. 4.1}$$

LR is a parameter that depends on the aerosol type and could vary with the height due to the variability of aerosol types with height. But under the assumption of constant lidar ratio with height, the equation for $\beta(h,\lambda)$ can be solved following the Klett-Fernald procedure as follows:

$$\beta(h,\lambda) + \beta_{mol}(h,\lambda) = \\ = \frac{RCS(h,\lambda)\exp\left\{-2\int_{h_0}^{h}[LR(h',\lambda) - LR_{mol}]\beta_{mol}(h',\lambda)\,dh'\right\}}{\frac{RCS(h_0,\lambda)}{\beta(h_0,\lambda) + \beta_{mol}(h_0,\lambda)} - 2\int_{h_0}^{h} LR(h',\lambda)RCS(h',\lambda)\,T_E(h',\,h_0)dh'}$$

Eq. 4.2

with:

$$T_E(h',\,h_0) = \exp\left\{-2\int_{h_0}^{h'}[LR(h'',\lambda) - LR_{mol}]\beta_{mol}(h'',\lambda)\,dh''\right\} \qquad \text{Eq. 4.3}$$

where the molecular extinction-to-backscatter ratio (LR_{mol}) is well determined by Rayleigh scattering with a value of $8\pi/3\ sr$.

In order to determine $\beta(h,\lambda)$ is necessary to estimate the aerosol backscatter coefficient at a specific reference height h_0 ($\beta(h_0,\lambda)$). The reference height is selected such that the aerosol backscatter coefficient at this height is negligible compared to the known molecular backscatter value. Such height is normally given for clear air conditions in the upper troposphere.

4.1.2. Inelastic lidar technique

The inelastic lidar technique, so-called Raman inversion, is based on the Raman scattering described in Section 2.3. The most important advantage is that this technique allows independent retrievals of aerosol backscatter and extinction coefficients without any assumption of lidar ratio. Due to the Raman scattering, the scattered light wavelength (λ_R) is shifted with respect to emitted laser wavelength (λ). This shift depends on the molecule that interacts with light. If the Raman scattering is due to a gas with known atmospheric density, as N_2 or O_2, the backscatter coefficient in the Raman lidar equation is known, therefore, only the

aerosol extinction and its wavelength dependence remain as unknowns [Ansmann et al., 1990]. The extinction coefficient is calculated as follows:

$$\alpha(h,\lambda) = \frac{\frac{d}{dh}\ln[N_R(h)/RCS(h,\lambda_R)] + \alpha_{mol}(h,\lambda) - \alpha_{mol}(h,\lambda_R)}{1 + (\lambda/\lambda_R)^k} \qquad \text{Eq. 4.4}$$

where $N_R(h)$ is the atmospheric number density of the reference gas and can be calculated using the pressure and temperature profile defined by a standard atmospheric model, usually tuned with the surface temperature and pressure measured at the lidar station, or from radiosonde measurements; k is the extinction Ångström exponent that consider the spectral changes between the elastic and Raman wavelengths.

The aerosol backscatter coefficient $\beta_{aer}(h,\lambda)$ can be expressed as:

$$\beta(h,\lambda) + \beta_{mol}(h,\lambda) = [\beta(h_0,\lambda) + \beta_{mol}(h_0,\lambda)]\cdot \cdot \frac{P(h_0,\lambda_R)P(h,\lambda)}{P(h_0,\lambda)P(h,\lambda_R)}\frac{N_R(h)}{N_R(h_0)} \cdot \frac{exp\left\{-\int_{h_0}^{h}[\alpha(h',\lambda_R) - \alpha_{mol}(h',\lambda_R)]\,dh'\right\}}{exp\left\{-\int_{h_0}^{h}[\alpha(h',\lambda) - \alpha_{mol}(h',\lambda)]\,dh'\right\}} \qquad \text{Eq. 4.5}$$

where $P(h,\lambda)$ and $P(h,\lambda_R)$ are the received elastic backscatter signal and the Raman signal, respectively. As in the Klett-Fernald retrieval, a reference height is selected in a region with clear air where $\beta(h_0,\lambda)$ can be approximated to 0. The molecular extinction and backscatter coefficients are calculated using Rayleigh scattering model [Bucholtz, 1995].

4.2. Combination of active and passive instruments

The first algorithms developed to retrieve vertically–resolved aerosol optical and microphysical properties use measurements of three aerosol backscatter and two extinction coefficients, as is mentioned in the Introduction chapter. However, these

measurements are scarce compared to the large database of elastic lidar measurements since multiwavelength Raman lidars are mostly capable of measuring only at night-time and the number of these kind of lidar is limited due to its high cost.

In this sense, different inversion methods have been recently developed within the European project ACTRIS and the EARLINET framework. These methods combine information of elastic lidar and sun/sky photometer measurements in order to retrieve vertical profiles of aerosol microphysical properties. Such kind of algorithms include the LIdar-Radiometer Inversion Code (LIRIC) developed in the Institute of Physics of Minsk (Belarus) and the Laboratoire d'Optique Atmosperique in Lille (France) [Chaikovsky et al., 2008] and also the Generalized Aerosol Retrieval from Radiometer and Lidar Combined data (GARRLiC; Lopatin et al., 2013). The last algorithm being nowadays a branch of the Generalized Retrieval of Aerosol and Surface Properties (GRASP; Dubovik et al., 2014) developed in the Laboratoire d'Optique Atmosperique (LOA) in Lille (France). A brief description of these algorithms is given in the following subsections.

4.2.1. LIRIC algorithm

LIRIC is described in detail in the literature [e. g. Chaikovsky et al., 2008, 2012, 2016; Granados-Muñoz et al., 2014]. The input information needed and the aerosol properties retrieved by LIRIC algorithm and used in this thesis are shown in Table 4.3. The inputs of LIRIC algorithm are the lidar elastic backscattered signals at three different wavelengths (355, 532 and 1064 nm; if available, the cross-polarized signal at 532 nm), together with the inversions of the sun/sky photometer measurements retrieved from AERONET (Version 2, Level 1.5). These data are put through an iterative procedure based on the Levenberg–Marquardt method, which is described in detail by Chaikovsky et al. [2016].

Table 4.1. General input and output data of LIRIC algorithm.

LIRIC		
INPUT	Sun/sky photometer	Lidar
	• Aerosol optical depth • Complex refractive index • Volume concentration • Spherical particle fraction	• Elastic backscatter signal at 355, 532 and 1064 nm • Cross-polarized signal at 532 nm
OUTPUT	Vertical profile	
	• Volume concentration for fine and coarse modes (spherical and spheroid if 532-cross is provided)	

This algorithm does not use directly the sun/sky photometer measurements, but assumes as true the column aerosol products from AERONET retrieved from sun/sky photometer measurements. LIRIC provides height-resolved aerosol volume concentration profile for the fine and coarse modes with a vertical resolution as high as the vertical resolution of the lidar system. Using information on the backscattered cross-polarized in a channel, 532 nm in our case, it is feasible to discriminate the contribution of the spherical and spheroid particles in the coarse mode. Additional products such as the aerosol extinction and backscatter coefficients or the lidar ratio for the different modes, among others, can be derived. In cases of good mixing within the boundary layer and low layering, the uncertainties of the retrieved vertical profiles of microphysical properties are below 10%, but they reach higher values (up to 30%) in cases of more complex structures [Granados-Muñoz et al., 2014].

4.2.2. GRASP/GARRLiC algorithm

GRASP algorithm is a versatile and open-source algorithm (www.grasp-open.com) which can retrieve vertical and columnar properties of atmospheric aerosols from a variety of remote sensing observations [Dubovik et al., 2014]. GARRLiC, which is part of GRASP algorithm, simultaneously inverts coincident elastic lidar and sun/sky photometer measurements to retrieve both vertical profiles and column-integrated optical and microphysical aerosol properties. In contrast to LIRIC, GARRLiC uses directly the sun/sky photometer measurements instead of the columnar AERONET products. GARRLiC algorithm applications and sensitivity tests are discussed in detail by Lopatin et al. [2013]. Hereafter, it will refer to GARRLiC directly as GRASP since it is run from GRASP in this thesis.

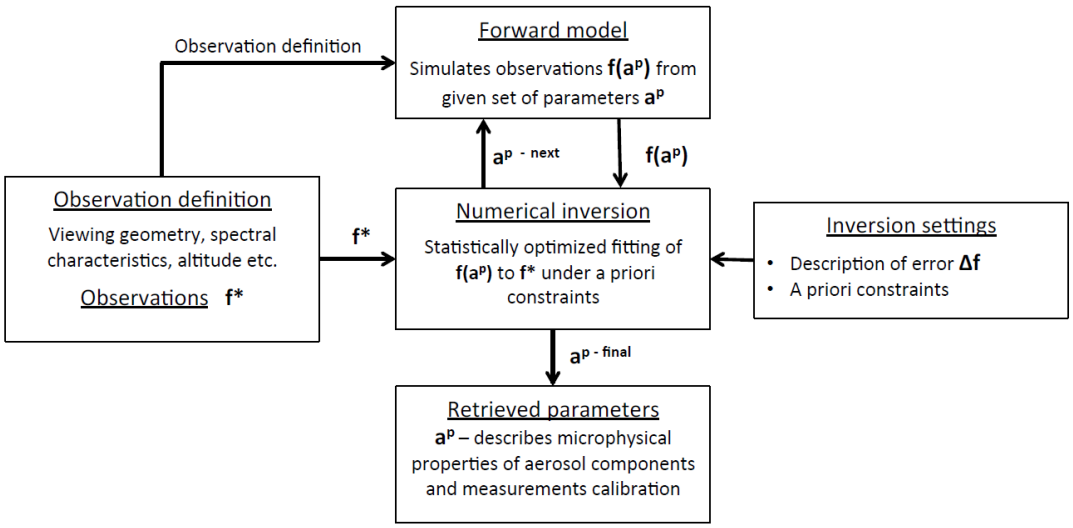

Figure 4.1. General structure of the GRASP algorithm (source: Lopatin et al., 2013).

GRASP is a modification of AERONET and POLDER/PARASOL algorithms [Dubovik et al., 2011] for inclusion of, among others, lidar data [Lopatin et al., 2013]. GRASP algorithm is divided in two main independent modules as shown in Figure 4.1: forward model and numerical inversion modules. The forward model is based on radiative transfer and aerosol models and it is capable of

generating the radiative measurements from a given set of parameters. The numerical inversion module is the main part of the core algorithm program which includes general mathematical operations based on multi-term least square method (LSM).

4.2.2.1. Forward model

The first versions of the retrieval algorithm [Dubovik and King, 2000; Dubovik et al., 2011] and its first modifications (which invert only passive observations by ground-based, satellite and airborne radiometers) [Sinyuk et al., 2007; Gatebe et al., 2010], were modified for modelling lidar observations [Lopatin et al., 2013]. Figure 4.2 shows a diagram of the main components of GRASP forward model module where elastic lidar measurements are simulated by lidar equation and sun/sky photometer observations are modelled by means of solving the vectorial radiative transfer equation [Lopatin et al., 2013].

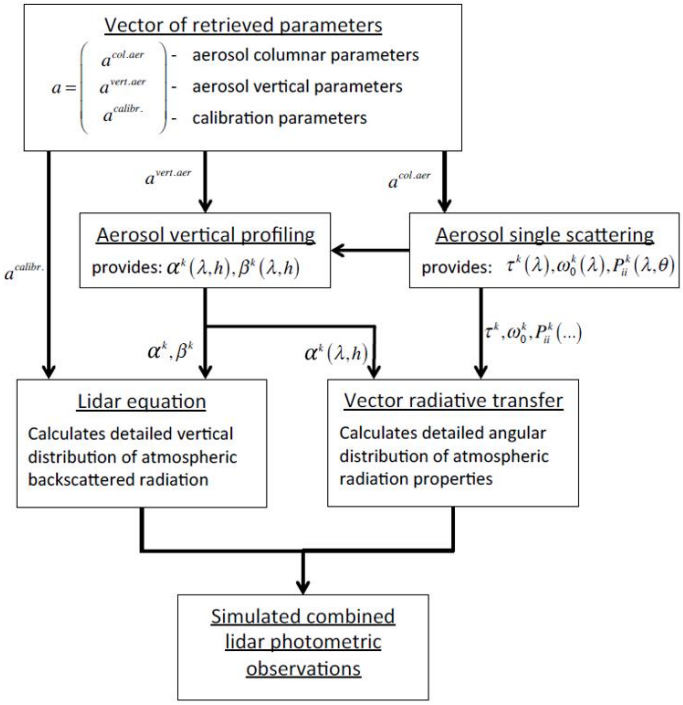

Figure 4.2. General scheme of the forward model of GRASP (from Lopatin, 2013).

The aerosol is defined as a mixture of several aerosol components (k) which have a different particle size distribution and a complex refractive index. Each aerosol component is a sum of spherical and non-spherical fractions. Sensitivity studies by Lopatin et al. [2013] demonstrated that a combination of multiwavelength lidar and ground-based sun/sky photometer measurements provides enough information to retrieve bi-component (k=2) aerosol mixture properties. Therefore, the extinction and scattering properties of the aerosol in whole atmospheric column can be modelled as:

$$\tau_{ext/sca}^{k}(\lambda) = \sum_{k=1,2}\left[\sum_{p=1,\dots,N_r}\left[C_{sph}^{k}K_{ext/sca}^{sph}(\lambda,\kappa,n,r_p) + \left(1-C_{sph}^{k}\right)K_{ext/sca}^{nons}(\lambda,\kappa,n,r_p)\right]\frac{dV(r_p)}{d\ln r_p}\right] \quad \text{Eq. 4.6}$$

$$\tau_{sca}^{k}(\lambda)P_{ij}^{k}(\lambda,\Theta) = \sum_{k=1,2}\left[\sum_{p=1,\dots,N_r}\left[C_{sph}^{k}K_{ij}^{sph}(\lambda,\Theta,\kappa,n,r_p) + \left(1-C_{sph}^{k}\right)K_{ij}^{nons}(\lambda,\Theta,\kappa,n,r_p)\right]\frac{dV(r_p)}{d\ln r_p}\right] \quad \text{Eq. 4.7}$$

where τ_{ext} and τ_{sca} are the columnar extinction and scattering optical depth, respectively, k is the number of aerosol components, the $P_{ij}(\lambda,\Theta)$ is the element of scattering matrix, C_{sph} is the fraction of the spherical particles, N_r is the number of size distribution bins and finally, $K_{ext/sca}$ and K_{ij} are the kernels of extinction, scattering and their properties. The detailed information of the calculation of the kernels was described by Dubovik et al. [2002b, 2006, 2011] and Volten et al. [2001].

On other hand, the atmospheric backscattering vertical profile is modelled as follows:

$$\beta(h,\lambda) = \frac{1}{4\pi}\sum_{k=1,2}\alpha^k(h,\lambda)\omega_0^k(\lambda)P_{11}^k(180º,\lambda) \qquad \text{Eq. 4.8}$$

where $\omega_0(\lambda)$ is the atmosphere single scattering albedo, $P_{11}(180º,\lambda)$ is the phase function at scattering angle Θ=180º and $\alpha^k(h,\lambda)$ is the aerosol extinction modelled as:

$$\alpha^k(h,\lambda) = \tau_k(\lambda)c_k(h) \qquad \text{Eq. 4.9}$$

where $\tau_k(\lambda)$ is the aerosol optical depth and $c_k(h)$ is the modelled vertical profiles of volume concentration where it is normalized to unity as:

$$\int_0^{h_{TOA}} c_k(h)dh = 1 \qquad \text{Eq. 4.10}$$

In the computations of volume concentrations, GRASP assumes that modal radius and complex refractive index do not changes with height. Due to incomplete overlap in the first meters above the ground, the volume concentration below a minimum altitude (h_{min}) fixed by the user is assumed constant and equals to the value on this h_{min}. For very high altitudes (above a maximum altitude, h_{max}) where it has very weak lidar measurements, GRASP assumes that aerosol load is negligible.

Finally, assuming the plane parallel approximation, the full radiative equation is solved using vertically dependent optical properties of the atmosphere:

$$\Delta\tau_i(\lambda) = \Delta\tau_i^{gas}(\lambda) + \Delta\tau_i^{mol}(\lambda) + \sum_{k=1,2}\Delta\tau_i^{aer,k}(\lambda) \qquad \text{Eq. 4.11}$$

$$\omega_0^i(\lambda) = \frac{\Delta\tau_i^{mol}(\lambda) + \sum_{k=1,2}\Delta\tau_i^{aer,k}(\lambda)\omega_0(\lambda)}{\Delta\tau_i(\lambda)} \qquad \text{Eq. 4.12}$$

$$P_{ij}^i(\Theta,\lambda) = \frac{\Delta\tau_i^{mol}(\lambda)P_{ij}(\Theta,\lambda) + \sum_{k=1,2}\Delta\tau_i^{aer,k}(\lambda)\omega_0(\lambda)P_{ij}^{aer,k}(\Theta,\lambda)}{\Delta\tau_i^{mol}(\lambda) + \sum_{k=1,2}\Delta\tau_i^{aer,k}(\lambda)\omega_0(\lambda)} \qquad \text{Eq. 4.13}$$

where $\Delta\tau_i(\lambda)$, $\omega_0^i(\lambda)$ and $P_{ij}^i(\Theta,\lambda)$ represent optical properties of i-th homogeneous layer of the atmosphere. More details about GRASP forward model module are described by Lopatin [2013].

GRASP forward module can also be independently run in order to simulate the optical observations for any aerosol scenario that users want. Particularly, forward model can also be used for generating measurements (e.g. lidar signals, sky radiances) for any given instrument.

4.2.2.2. Numerical inversion

The numerical inversion module is based on the multi-term LSM that solves the following system of equations [Dubovik and King, 2000; Dubovik, 2004; Dubovik et al., 2011]:

$$\begin{cases} \boldsymbol{f}^* = \boldsymbol{f}(\boldsymbol{a}) + \Delta\boldsymbol{f} \\ \boldsymbol{0}^* = \boldsymbol{S}\boldsymbol{a} + \Delta_S \\ \boldsymbol{a}^* = \boldsymbol{a} + \Delta\boldsymbol{a} \end{cases} \qquad \text{Eq. 4.14}$$

In the first formula of Equation 4.15, $\boldsymbol{f}^*$ is a vector of measurements f_i, $\boldsymbol{a}$ is the vector of unknowns to retrieve, $\boldsymbol{f}(\boldsymbol{a})$ denotes a physical forward model that allows adequate simulations of observations f_i from predefined parameters a_i, and $\Delta\boldsymbol{f}$ is the vector of measurements errors. The vector $\boldsymbol{a}$ includes the atmospheric aerosols properties: particles size distribution, spherical fraction of particles, real and imaginary part of refractive index and vertical profile of concentration.

The second formula in Equation 4.15 represents a priori smoothness parameters to constrain the variability of retrieved parameters. $\mathbf{0}^*$ is the vector of zeros which allows rejecting the solutions with strong oscillations and unrealistically high derivatives. The matrix $\boldsymbol{S}$ is composed of coefficients for calculating k-th differences of the retrieved parameters and Δ_S is the vector of the uncertainties characterizing the deviations of the differences from the zeros.

The third equation in Equation 4.15 represents the parameters to retrieve, $\boldsymbol{a}$, while $\boldsymbol{a}^*$ are the a-priori parameters to initialize the algorithm, $\Delta\boldsymbol{a}$ represents the uncertainty in these a priori estimates.

Assuming that the errors are normally distributed and using the multi-term LSM, it is possible to find the solution to the Equation 4.15 through the minimization of the following quadratic form:

$$\begin{aligned}\Psi(\boldsymbol{a}^p) &= \Psi_{\boldsymbol{f}}(\boldsymbol{a}^p) + \Psi_{\boldsymbol{S}}(\boldsymbol{a}^p) + \Psi_{\boldsymbol{a}}(\boldsymbol{a}^p) \\ &= \frac{1}{2}\left\{(\Delta\boldsymbol{f}^{\,p})^T\boldsymbol{W}_f^{-1}\Delta\boldsymbol{f}^{\,p} + \gamma_S(\boldsymbol{a}^p)^T\boldsymbol{\Omega}\boldsymbol{a}^p \right. \\ &\quad \left. + \gamma_a(\boldsymbol{a}^p - \boldsymbol{a}^*)^T\boldsymbol{W}_a^{-1}(\boldsymbol{a}^p - \boldsymbol{a}^*)\right\}\end{aligned} \qquad \text{Eq. 4.15}$$

where $\boldsymbol{\Omega}$ is the correspondent smoothness matrix and can be written as: $\boldsymbol{\Omega} = \boldsymbol{S}^T\boldsymbol{S}$, where $\boldsymbol{S}$ is the matrix of k-th differences. The p is the iteration index, and $\boldsymbol{W}$ and γ are the weighting matrices and Lagrange parameters, respectively, defined as follows:

$$\boldsymbol{W}_f = \frac{1}{\epsilon_{\boldsymbol{f}}^2}\boldsymbol{C}_{\boldsymbol{f}} \qquad \boldsymbol{W}_a = \frac{1}{\epsilon_{\boldsymbol{a}}^2}\boldsymbol{C}_{\boldsymbol{a}}$$

$$\gamma_S = \frac{\epsilon_{\boldsymbol{f}}^2}{\epsilon_{\boldsymbol{S}}^2} \qquad \gamma_a = \frac{\epsilon_{\boldsymbol{f}}^2}{\epsilon_{\boldsymbol{a}}^2} \qquad \text{Eq. 4.16}$$

where $\epsilon_{\boldsymbol{f}}$, $\epsilon_{\boldsymbol{S}}$ and $\epsilon_{\boldsymbol{a}}$ are the first diagonal elements of the corresponding covariance matrices $\boldsymbol{C}_f$ and $\boldsymbol{C}_a$, respectively. More details about the iterative process are described by Dubovik and King [2000], Dubovik [2004], Lopatin et al. [2013] and Torres et al. [2017].

GRASP estimates the errors of the retrieved parameters by means of formulations of multi-term LSM. The errors of the estimated parameters $\Delta\hat{\boldsymbol{a}}$ are normally distributed and have two components, random and systematic, that result from $\Delta\boldsymbol{f}_{ran}$ and $\Delta\boldsymbol{f}_{sys}$ in the measurements as:

$$\Delta\hat{\boldsymbol{a}} = \Delta\hat{\boldsymbol{a}}_{ran} + \Delta\hat{\boldsymbol{a}}_{sys} \qquad \text{Eq. 4.17}$$

Then, it is possible to derive the covariance matrix from the errors, which will also consist of two components, random and systematic, as follows:

$$C_{\hat{\boldsymbol{a}}} = C_{\Delta\hat{\boldsymbol{a}}_{ran}} + \hat{\boldsymbol{a}}_{bias}(\hat{\boldsymbol{a}}_{bias})^T \qquad \text{Eq. 4.18}$$

where,

$$\hat{\boldsymbol{a}}_{bias} = \left(\boldsymbol{K}^T\boldsymbol{W}_f^{-1}\boldsymbol{K} + \gamma_S\boldsymbol{\Omega} + \gamma_a\boldsymbol{W}_a^{-1}\right)^{-1}\left(\boldsymbol{K}^T\boldsymbol{W}_f^{-1}\boldsymbol{b_f} + \gamma_S\boldsymbol{\Omega}\boldsymbol{b}_S + \gamma_a\boldsymbol{W}_a^{-1}\boldsymbol{b}_a\right) \qquad \text{Eq. 4.19}$$

$$C_{\Delta\hat{\boldsymbol{a}}_{ran}} = \left(\boldsymbol{K}^T\boldsymbol{W}_f^{-1}\boldsymbol{K} + \gamma_S\boldsymbol{\Omega} + \gamma_a\boldsymbol{W}_a^{-1}\right)^{-1}\varepsilon_{\boldsymbol{f}}^2 \qquad \text{Eq. 4.20}$$

where **K** is the matrix corresponding to the first derivatives and $\boldsymbol{b_k}$ is the bias introduced by each data set.

In order to obtain the total error estimate, it is necessary to calculate:

$$\sigma_a = \sqrt{\sigma_{rand}^2 + \sigma_{bias}^2} \qquad \text{Eq. 4.21}$$

where it is important to note that σ_a is in log-scale.

On the other hand, GRASP return the retrieved parameters in normal scale. So, to express the parameter with its error estimate in the normal scale, it is necessary to write:

$$a' = \hat{a} \cdot \exp(\pm\sigma_a) \qquad \text{Eq. 4.22}$$

Therefore, the absolute error of the retrieved parameters can be written as follows:

$$\varepsilon_+ = \hat{a} \cdot (-1 + \exp(+\sigma_a))$$
$$\varepsilon_- = \hat{a} \cdot (1 - \exp(-\sigma_a)) \qquad \text{Eq. 4.23}$$

A detailed description of the error estimation can be found in Dubovik [2004].

4.2.2.3. Input data

GRASP retrieval starts from an assumed initial guess scenario followed by the iterative procedure, explained in the subsection 4.2.1.2, which allows to retrieve the characteristics of atmospheric aerosols; Figure 4.3 shows a diagram of this process.

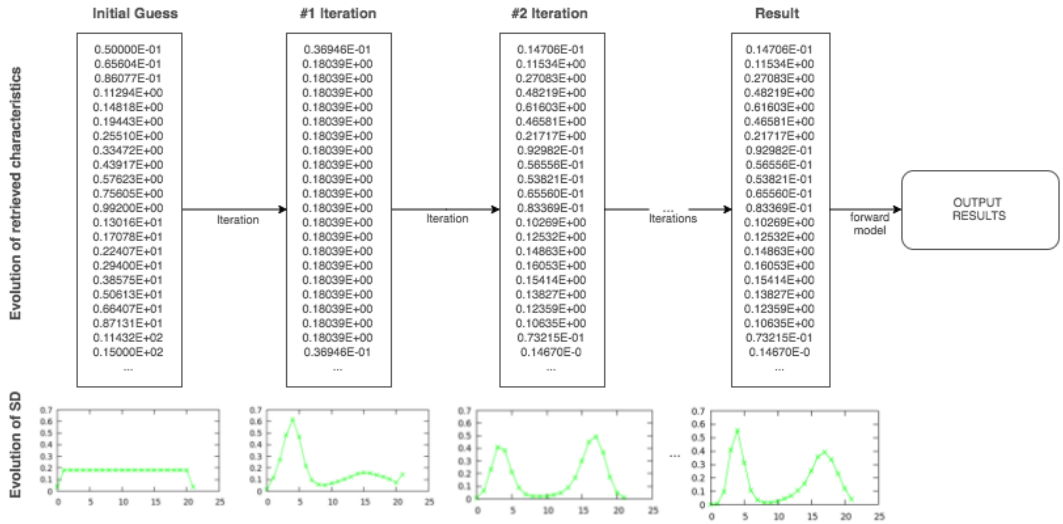

Figure 4.3. Evolution of retrieved characteristics during GRASP processing (source: https://www.grasp-open.com).

The initial guess is loaded as the first characteristic array to be retrieved, then GRASP provides the optical observations of the "initial guess scenario" and these observations are compared with the real measured observations (in the so-called SDATA file) and a new set of aerosol properties is obtained by the inversion module minimizing the differences between both set of observations. Iteratively, the forward module is run with the new aerosol properties obtained in the before iteration, providing a new set of observations that is compared with the real observations again in order to provide more realistic aerosol properties using the minimization equations. Finally, when the iterative process is stopped (when the residuals between consecutive iterations are lower than a fixed threshold by the user), the final array represents all the retrieved aerosol properties.

```
SDATA version 2.0
1 1 1 : NX NY NT

1 2016-07-18T16:32:00Z 680  0 0 : NPIXELS TIMESTAMP HOBS NSURF IFGAS
1 1 1 0 0 -3.61 37.16 680 100.00
7   0.355   0.440   0.532   0.675   0.870   1.020   1.064
1   2   1   2   2   2   1
31  12  41  31  12  41  12  41  12  41  31
60  1   26  60  1   25  1   26  1   25  60
0.0000  57.3169 0.0000  57.0815 56.8428 56.3619 0.0000
5758.3717   5509.2577   5270.9206   5042.8943   4824.7327   4616.0090   4416.3149
0.0000
122.6831    122.6831    122.6831    122.6831    122.6831    122.6831    122.6831
5758.3717   5509.2577   5270.9206   5042.8943   4824.7327   4616.0090   4416.3149
0.0000
122.9185    122.9185    122.9185    122.9185    122.9185    122.9185    122.9185
0.0000
123.1572    123.1572    123.1572    123.1572    123.1572    123.1572    123.1572
```

Figure 4.4. Part of a SDATA file example.

The SDATA file contains all information related to the measurements that can be inverted. This file is structured using the GRASP original input data format and it contains the measurements of sun/sky photometer and lidar or ceilometer (even sky camera when it is used). Figure 4.4 shows a piece of an example of SDATA file, where it is observed a simple structure: the first line contains the identifier SDATA followed by the version number; the second line contains the

spatial and temporal dimensions; and after an empty line, the information about the lidar and sun/sky photometer measurements are added. In this thesis, both the number of pixels in the SDATA and temporal dimension are considered one. A detailed description of the SDATA file is provided in www.grasp-open.com.

Table 4.2. General input and output data used by GRASP algorithm

GRASP		
	Sun/sky photometer	**Lidar**
INPUT	• Aerosol optical depth* • Normalized radiances* *at 440, 675, 870 and 1020 nm	• Range corrected profile normalized at 60 log-spaced bins at different heights at 355, 532 and 1064 nm** **for ceilometer only at 1064 nm
	Column-integrated	**Vertical profile**
OUTPUT	• Particle size distribution • Complex refractive index • Spherical particle fraction • Volume concentration • Single-scattering albedo • Lidar ratio	• Volume concentration • Extinction coefficient • Backscatter coefficient • Lidar ratio • Single-scattering albedo • Scattering coefficient • Absorption coefficient

Table 4.2 summarizes the sun/sky photometer and lidar data used in one SDATA file by GRASP. On the one hand, the sun/sky photometer measurements used are the aerosol optical depth and sky radiances at 440, 675, 870 and 1020 nm. In the case of sky radiances, a pre-processing of the data is necessary. Following the procedures applied by AERONET [Holben et al., 2006]: the data with azimuth angles from 3.5º to 160º are selected checking that the differences between both almucantar branches are below 20% and finally the data are normalized using the

"2000 ASTM Standard Extraterrestrial Spectrum Reference E-490-00" (http://rredc.nrel.gov/solar/spectra/am0).

On the other hand, the lidar data used corresponds to 30 minutes averages of the raw signals to which a preprocessing is applied to calculate a range corrected profile for each wavelength. This preprocessing includes at least background noise subtraction and altitude correction, but other corrections can also be applied as overlap correction, analog and photon-counting signals gluing and depolarization correction [Bravo-Aranda, 2014]. To reduce the number of retrieved parameters and remove the noise in lidar signals at higher altitudes a logarithmical altitude/range scale with 60 points between a minimum (h_{min}) and maximum (h_{max}) altitudes previously selected is used. The minimum altitude is selected as low as possible considering that the incomplete overlap is reliably corrected and the maximum altitude is selected in a region where the lidar measurements noise is acceptable and the amount of atmospheric aerosols is enough. Finally, the range corrected signal is normalized as follows:

$$NRCS(h,\lambda) = \frac{\frac{1}{N}\sum_{h=h_1}^{h=h_N} RCS(h,\lambda)}{\int_{h_{min}}^{h_{max}} RCS(h,\lambda)dh} \qquad \text{Eq. 4.24}$$

where $NRCS(h,\lambda)$ is the normalized range corrected signal at the h-bin (h ranges from 1 to 60), N is the number of RCS values between the h-bin and h_1, h_2, … and h_N is the N heights of the available RCS that are inside the h-bin.

4.2.2.3.a. BRDF data

A part of measured sky radiance has its source in the light reflected by the Earth surface. Therefore, the Bidirectional Reflectance Distribution Function (BRDF) is used to take into account this phenomenon. The BRDF is introduced in GRASP through the BRDF parameters of the Li–Ross model [Ross, 1981; Li and Strahler,

1992]. GRASP is capable to calculate BRDF parameters from satellite images [Dubovik et al., 2014] but the BRDF parameters used for this work are obtained from the V005 Collection MCD43C1 product (V005 MODIS Terra+Aqua BRDF/Albedo 16-Day L3 0.05Deg CMG) of MODIS (MODerate-resolution Imaging Spectroradiometer) with a spatial resolution of 0.05º [Schaff et al., 2011]. This product is generated every 8 days with 16 days of acquisitions at seven narrow bands, 470, 555, 659, 858, 1240, 1640 and 2130 nm. The available MCD43C1 data at the Granada coordinates from 2000 to 2014 have been averaged obtaining a table of BRDF parameters every 8 days for one representative year. The BRDF values are introduced in the settings of GRASP instead in the SDATA file.

4.2.2.4. Output data

GRASP output depends on the input settings and on the number of spectral channels of the lidar. In the case of single-wavelength lidar data (ceilometer case), the aerosol properties are retrieved for the whole aerosol load without discriminating between modes, while for multiwavelength lidar data, the algorithm provides separately the aerosol properties for fine and coarse modes [Bovchaliuk et al., 2016]. The list of products obtained by GRASP and used in this thesis is summarized in Table 4.2.

The column-integrated aerosol properties retrieved by GRASP are provided directly for total, fine and coarse modes, depending on whether the single- or multiwavelength lidar data is used. Properties as CRI, SSA and LR are wavelength dependent and therefore are provided for each wavelength.

For aerosol vertical-properties, GRASP provides the profiles of each mode assuming that modal radius and complex refractive index do not change with height. Thus, assuming retrievals of two modes, fine and coarse mode respectively, GRASP provides the profiles of fine (AVP_f) and coarse (AVP_c) mode respectively. From these profiles, GRASP computes the rest of properties vertically-resolved, which are

summarized in Table 4.3 (subscript f and c are again for fine and coarse mode, respectively).

Table 4.3. Equations to calculate the vertical profiles of aerosol properties

Property	Equation	
Volume concentration	$VC(h,\lambda) = VC_f * AVP_f(h) + VC_c * AVP_c(h)$	Eq. 4.25
Extinction coefficient	$\alpha(h,\lambda) = \tau_f(\lambda) * AVP_f(h) + \tau_c(\lambda) * AVP_c(h)$	Eq. 4.26
Backscatter coefficient	$\beta(h,\lambda) = \frac{\tau_f(\lambda) * AVP_f(h)}{LR_f(\lambda)} + \frac{\tau_c(\lambda) * AVP_c(h)}{LR_c(\lambda)}$	Eq. 4.27
Absorption coefficient	$\sigma_{abs}(h,\lambda) = \tau_f(\lambda) * AVP_f(h) * \left(1 - SSA_f(\lambda)\right) + \tau_c(\lambda) * AVP_c(h) * \left(1 - SSA_c(\lambda)\right)$	Eq. 4.28
Single-scattering albedo	$SSA(h,\lambda) = \frac{\alpha(h,\lambda) - \sigma_{abs}(h,\lambda)}{\alpha(h,\lambda)}$	Eq. 4.29
Scattering coefficient	$\sigma_{sca}(h,\lambda) = \tau_f(\lambda) * AVP_f(h) * SSA_f(\lambda) + \tau_c(\lambda) * AVP_c(h) * SSA_c(\lambda)$	Eq. 4.30
Lidar ratio	$LR(h,\lambda) = \frac{\alpha(h,\lambda)}{\beta(h,\lambda)}$	Eq. 4.31

5. Assessment of GRASP with airborne measurements

This chapter is adapted from "Comparative assessment of GRASP algorithm for a dust event over Granada (Spain) during ChArMEx-ADRIMED 2013 campaign" by Benavent-Oltra, J. A., Román, R., Granados-Muñoz, M. J., Pérez-Ramírez, D., Ortiz-Amezcua, P., Denjean, C., Lopatin, A., Lyamani, H., Torres, B., Guerrero-Rascado, J. L., Fuertes, D., Dubovik, O., Chaikovsky, A., Olmo, F. J., Mallet, M., and Alados-Arboledas, L. (2017) Published in Atmospheric Measurement Techniques, 10, 4439-4457, doi:10.5194/amt-2017-200.

This chapter presents the comparison of vertically-resolved and column integrated aerosol properties retrieved combining lidar and sun/sky photometer measurements into GRASP against in-situ airborne measurements as reference. Two scientific flights took place over Granada (Spain) on 16th and 17th June 2013 in the framework of the ChArMEx/ADRIMED field campaign. Data gathered during ChArMEx/ADRIMED campaign give us an excellent opportunity to evaluate the recently developed algorithms for retrieving aerosol microphysical and optical profiles. The GRASP configuration evaluated in this study is the one that combines lidar and sun/sky photometer data measured at UGR station. The same configuration but with different sun/sky photometer datasets are used: one co-located with the lidar system and the other in the CP station, at short horizontal distance of lidar system but at 1200 m height.

5.1. ChArMEx/ADRIMED campaign

The ADRIMED (Aerosol Direct Radiative Impact on the regional climate in the MEDiterranean region) field campaign, which was part of the international

cooperative research program Chemistry-Aerosol Mediterranean Experiment (ChArMEx) [Dulac et al., 2014], was carried out with the main objective of capturing the high complexity of the different aerosol types in the Mediterranean region [Mallet et al., 2016]. Several in-situ and remote sensing measurements, both at surface and onboard airborne platforms, were collected during this campaign. The measurements were performed at different stations over the western Mediterranean region during summer 2013, to gather an updated database of the physical, chemical and optical aerosol properties as well as the vertical distribution of the major "Mediterranean aerosols" [Mallet et al., 2016; Denjean et al., 2016].

During the period from 14th June to 4th July 2013, 16 flights were performed in the framework of ChArMEx/ADRIMED over the Mediterranean Basin with the ATR-42 aircraft of SAFIRE (French aircraft service for environmental research; http://www.safire.fr). These flights ascended or descended performing a spiral trajectory during 30 min.

5.1.1. Airborne instrumentation

The instrumentation onboard the ATR-42 airplane used in this chapter is summarized in Table 5.1. The SMPS with an accuracy of 5% [Wiedensohler et al., 2012] and the Ultra-High Sensitivity Aerosol Spectrometer (UHSAS) with an accuracy of 10% [Cai et al., 2008] are used for measuring aerosol number size distribution in the submicron range.

The wing-mounted Forward Scattering Spectrometer Probe, model 300 (FSSP-300) with an accuracy of 30% [Baumgardner et al., 1992] and the in-cabin GRIMM OPC (sky-OPC 1.129) with an accuracy of 10% [Denjean et al., 2016] were used to measure the optical size distributions in the diameter nominal size range between 0.28 and 20 µm and between 0.3 and 32 µm, respectively. The total particle volume concentrations in the diameter range 0.1 - 30 µm and volume

concentrations of fine (0.1 - 1 µm) and coarse (1 - 30 µm) modes were calculated from the measured aerosol number size distributions, assuming that aerosol particles are spherical.

Table 5.1. Instruments on board the ATR-42 aircraft. (*not applicable)

	Instrument	Abbreviation	Scientific objective	Nominal size range [µm]	λ [nm]
Size distribution	Forward Scattering Spectrometer Probe, Model 300, Particle Measuring Systems	FSSP-300	Coarse mode conc.	0.28 - 20	632.8
	Sky-Optical Particle Counter, model 1.129, Grimm Technik	GRIMM	Coarse mode conc.	0.25 - 32	655
	Ultra-High Sensitivity Aerosol Spectrometer Droplet Measurement Technologies	UHSAS	Aiken + accumulation mode conc.	0.04 - 1	1054
	Scanning mobility particle sizer, custom-built	SMPS	Aiken + accumulation mode conc.	0.03 - 0.4	n/a
Optical properties	3λ Integrated Nephelometer, Model 3563, TSI	Nephelometer	Scattering coefficient	n/a*	450, 550, 700
	Cavity Attenuated Phase Shift, Aerodyne Research Inc.	CAPS	Extinction coefficient	n/a*	530
	Photomètre Léger Aéroporté pour la Surveillance des Masses d'Air	PLASMA	Extinction coefficient AOD	n/a*	340-2250

In addition, the TSI (model 3563) nephelometer was used to measure particle scattering coefficients at three wavelengths (450, 550 and 700nm) with an accuracy of 5% [Müller et al., 2011] and a Cavity Attenuated Phase Shift (CAPS) was employed to obtain particle extinction coefficient at 530 nm with an accuracy of 3% [Massoli et al., 2010]. Also, the PLASMA (Photomètre Léger Aéroporté pour la Surveillance des Masses d'Air) system, which is an airborne sun-tracking photometer, was used to obtain AOD with wide spectral coverage (15 channels between 0.34 - 2.25 μm) with an accuracy of approximately 0.01 [Karol et al., 2013], as well as the particle extinction vertical profiles derived from these AOD measurements [Torres et al., 2017].

5.1.2. ChArMEx/ADRIMED flights over Granada

Two of these ChArMEx/ADRIMED flights took place over Granada on 16th (14:15 - 14:45 UTC) and 17th (07:15 - 07:45 UTC) June 2013. Figure 5.1 shows the spiral trajectory of the second flight, the first flight trajectory was similar to second flight, covering in both cases a similar atmospheric column. Flight details were described by Mallet et al. [2016] and Denjean et al. [2016].

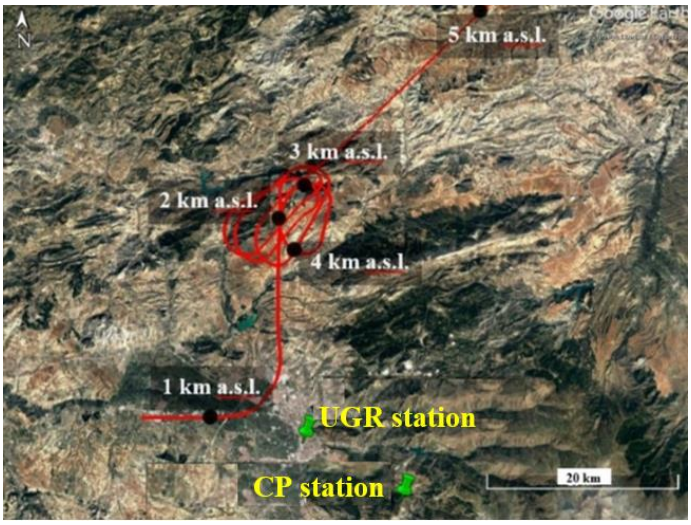

Figure 5.1. Map illustrating the UGR and CP stations. The red line indicates the trajectory and the black points the altitude of the aircraft on 17th June 2013.

Figure 5.2 shows the time series of the lidar RCS and the depolarization ratio (δ) at 532 nm measured at Granada station on both analyzed days. On the first day, a homogeneous layer is observed from the surface up to 5 km a.s.l., with an elevated aerosol layer coupled to the surface aerosol layer throughout the day. The next day this layer was decoupled from the aerosol layer close to surface and it disappeared around 13:00 UTC. The δ measurements evidence that there was an aerosol type below 2.7 km a.s.l. and another aerosol type above this altitude up to 5.5 km a.s.l..

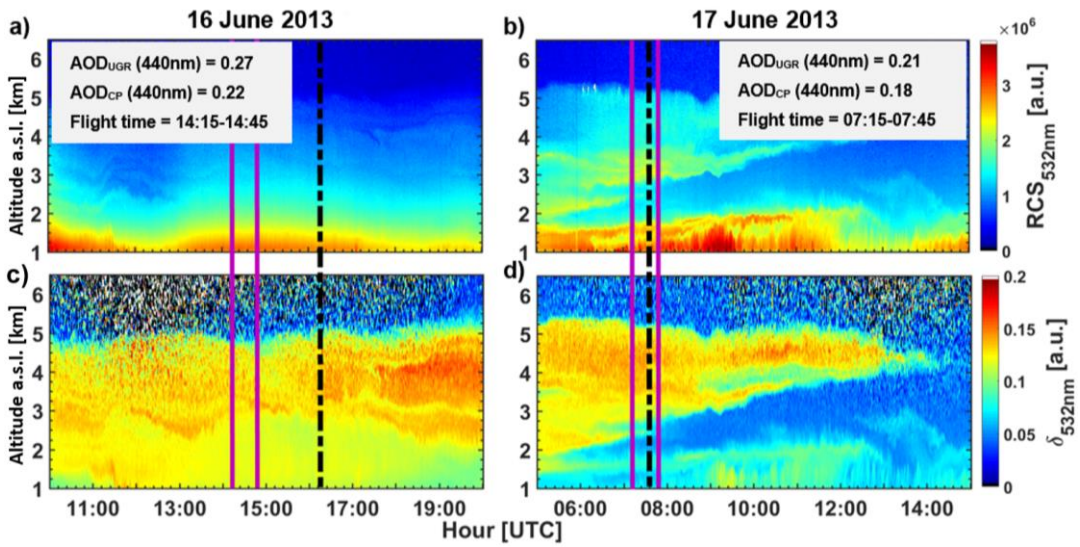

Figure 5.2. Temporal evolution of the lidar range corrected signal (**a, b**) and the depolarization ratio (**c, d**) at 532nm on 16th (**a, c**) and 17th (**b, d**) June, 2013. The two purple lines indicate the lidar analyzed time interval. The black dashed line indicates the time of the sun/sky photometer measurements. The AOD values at 440 nm obtained at UGR and CP stations are also included.

The time when the lidar and sun/sky photometer measurements used in GRASP were taken for both days are marked with purple lines and black dashed line, respectively, in Figure 5.2. On 16th June, the lidar measurements used were obtained during the first flight between 14:15 and 14:45 UTC, while the chosen sun/sky photometer measurements were collected at 16:22 UTC at UGR and CP stations. The selected sun/sky photometer measurements were the closest ones available in time to the first flight. On 17th June, the lidar measurements between

07:15 to 07:45 UTC and the sun/sky photometer measurements obtained at 07:40 UTC, for both UGR and CP stations, were selected for further analysis.

AERONET aerosol columnar products during these flights (shown in Figure 5.3) indicate the presence of dust particles in the atmosphere column. In fact, on 16th June; AOD at 440 nm (AOD_{440}) at 14:15 UTC was around 0.26 and 0.19 for UGR and CP stations, respectively, and 0.27 and 0.22 at 16:22 UTC. On this day, the $AE_{440\text{-}870}$ (AE calculated with AOD at 440 and 870 nm) was 0.30 - 0.26 (UGR-CP) at 14:30 UTC and 0.34 - 0.27 (UGR-CP) at 16:22 UTC, indicating moderate atmospheric aerosol load dominated by coarse particles. On 17th June, the AOD_{440} at 07:40 UTC was 0.21 and 0.18 and the $AE_{440\text{-}870}$ was 0.43 and 0.30 for UGR and CP stations, respectively, which also indicates the predominance of coarse particles in this day.

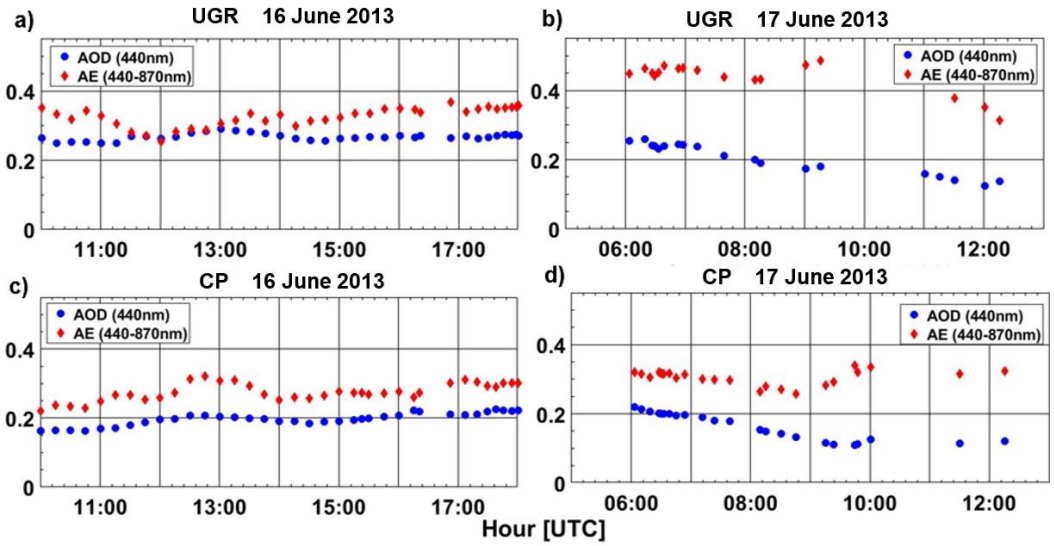

Figure 5.3. Temporal evolution of the AOD at 440 nm (blue) and AE (440-870 nm) (red) on 16th (**a, c**) and 17th (**b, d**) June, 2013 at UGR (**a, b**) and CP (**c, d**).

The presence of mineral dust over Granada region during both days is confirmed by the analysis of five-day back-trajectories obtained by HYSPLIT model (Hybrid Single-Particle Lagrangian Integrated Trajectory) [Stein et al.,

2015], which indicates that the relevant air masses came at Granada from the Saharan desert, specifically from Algeria and northern Morocco, at different heights (Figure 5.4).

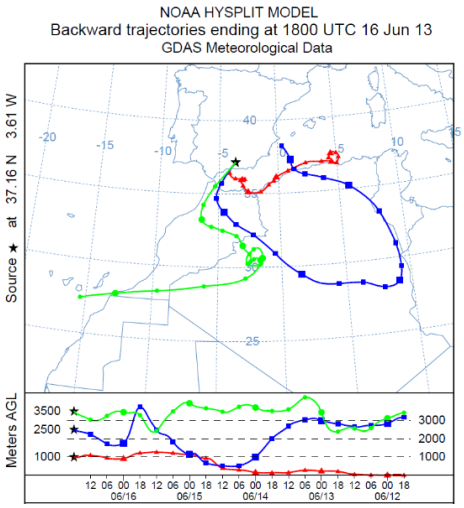

Figure 5.4. Five-day HYSPLIT backward trajectories arriving at Granada at 18:00 UTC on 16th June 2013.

5.2. Column-integrated aerosol properties

The aerosol columnar properties obtained from AERONET and retrieved by GRASP (combining lidar signals at 355, 532 and 1064 nm and sun/sky photometer measurements at 440, 675, 870 and 1020 nm) on 16th and 17th June at UGR and CP stations are shown in Figures 5.5 to 5.7 and summarized in Table 5.2.

Figure 5.5 shows the column-integrated particle size distribution, PSD, retrieved by both AERONET and GRASP algorithms on 16th and 17th June for UGR and CP stations. The retrieved PSDs evidence the predominance of coarse mode particles, as expected for dust events [Lyamani et al., 2005; Guerrero-Rascado et al, 2009]. Both AERONET and GRASP retrieved PSDs present a bimodal behavior, with the fine mode below 0.5 µm and the coarse mode above 0.5 µm. The differences between the PSD retrieved by GRASP and AERONET are mostly within uncertainties associated with both methods, being ±(10 - 35)% for the size range

from 0.1 µm to 7 µm and ±(35 - 100)% outside this range [Dubovik et al., 2000], except for the size range 5 - 8.7 µm where the differences are higher, especially at 6.64 µm (> 100%). Furthermore, the coarse mode retrieved by GRASP over both sites shows a clear shift towards higher radii in comparison to the AERONET retrievals (Figure 5.5). This shift was also observed by Lopatin et al. [2013] during dust and biomass burning events over Minsk, Belarus and by Bovchaliuk et al. [2016] during dust events over Dakar, Senegal. These authors attributed this coarse mode shift towards higher radii to the use of the lidar data in the GRASP retrievals. The lidar data provide additional information at scattering angles of 180º and further wavelengths compared to the only sun/sky photometer dataset, influencing the size distribution retrieved especially in the coarse mode.

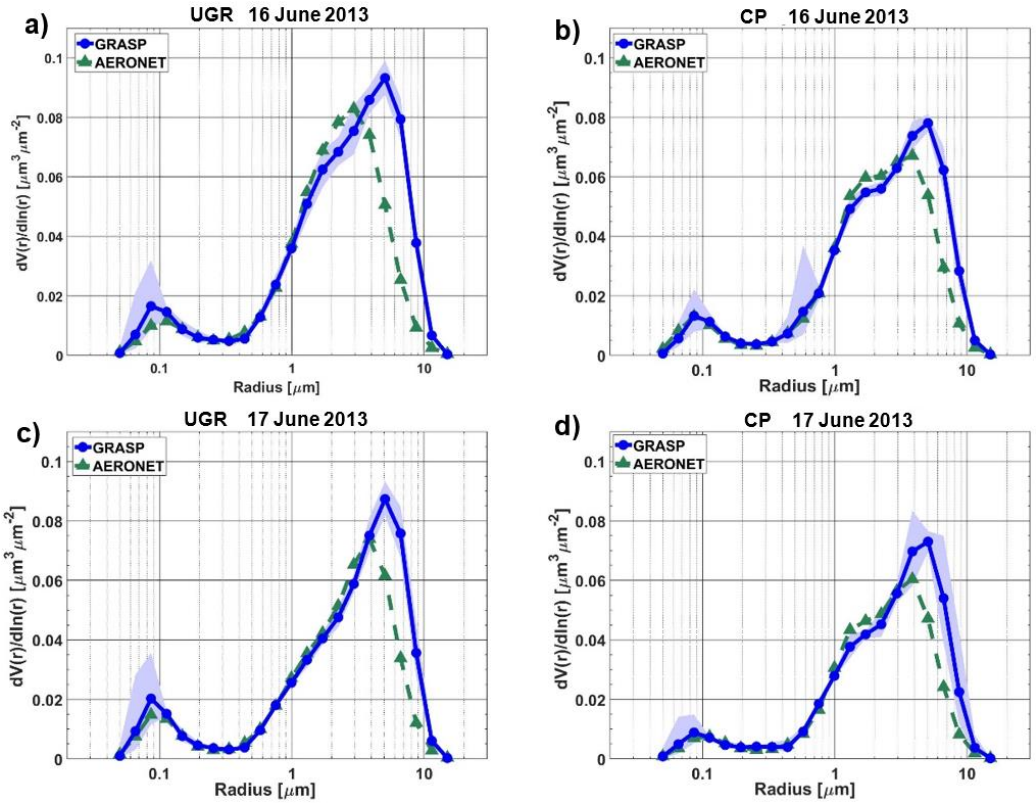

Figure 5.5. Size distribution retrieved by GRASP (blue) with its uncertainty (shaded area) and by AERONET (green) on 16th (**a, b**) and 17th (**c, d**) June 2013 at UGR (**a, c**) and CP (**b, d**).

Table 5.2 summarizes the columnar r_{eff} and VC of fine and coarse modes obtained at both stations by AERONET and GRASP algorithms on 16th and 17th June. The retrieved microphysical properties are similar to those typically obtained during African desert dust events over Granada [Valenzuela et al., 2012a]. The fine mode r_{eff} retrieved by both methods ranges between 0.10 and 0.13 µm. Differences between fine mode r_{eff} retrieved by GRASP and AERONET are below 0.02 µm, which are within the uncertainty of the inversions [Lopatin et al., 2013; Torres et al., 2014]. For the coarse mode, the r_{eff} values obtained by GRASP were 0.03 µm higher than those retrieved by AERONET but the differences are within the uncertainty range. A similar behavior is observed for the VC, with slightly larger values provided by GRASP for the fine and coarse modes (0.016 ± 0.003 $\mu m^3/\mu m^2$ and 0.148 ± 0.017 $\mu m^3/\mu m^2$) compared to AERONET (0.014 ± 0.003 $\mu m^3/\mu m^2$ and 0.125 ± 0.013 $\mu m^3/\mu m^2$), but differences are still within the uncertainties.

Table 5.2. Columnar effective radius and particle volume concentration for coarse and fine particles modes retrieved by GRASP and AERONET algorithms.

			16th June 2013		17th June 2013	
			UGR	CP	UGR	CP
r_{eff} [µm]	GRASP	Fine	0.12	0.13	0.10	0.12
		Coarse	2.2	2.2	2.4	2.2
	AERONET	Fine	0.12	0.11	0.11	0.12
		Coarse	1.9	1.9	2.1	1.9
VC [$\mu m^3/\mu m^2$]	GRASP	Fine	0.018	0.017	0.018	0.011
		Coarse	0.17	0.15	0.14	0.13
	AERONET	Fine	0.015	0.015	0.016	0.010
		Coarse	0.14	0.13	0.12	0.11

Figure 5.6 illustrates the retrieved columnar RRI and IRI for each day obtained by GRASP and AERONET at UGR and CP stations. Moreover, RRI and IRI at 530 nm estimated by Denjean et al. [2016] using airborne measurements over

Granada on 16th and 17th June, are added in the plot. AERONET provides RRI and IRI for the whole size distribution, while GRASP is able to provide RRI and IRI for fine and coarse modes separately. The RRI retrieved by GRASP and AERONET algorithms do not show any spectral wavelength variations, and the differences between RRI values retrieved by both inversion algorithms are within the uncertainties (differences below 5%). Because of the predominance of the coarse mode during the analyzed dust event, both the AERONET and airborne RRI values are close to the values retrieved by GRASP for coarse mode, with differences <0.03, on both days.

On the other hand, the IRI values retrieved by GRASP for the fine mode present a rather low spectral dependence while IRI values for the coarse mode presents a clear increase in the UV region. These results are coherent with those reported for different absorption species by Schuster et al. [2016] using AERONET data. At CP, the IRI values do not show the spectral dependence typically associated to mineral dust. The AOD_{440} were around 0.18 - 0.27 and the AERONET products used are Level 1.5, therefore, IRI values have large uncertainties (> 50%) [Dubovik et al., 2000]. The lack of IRI spectral dependence can be an artifact of the inversion. However, there is still discussion in the scientific community about dust refractive index and about the differences in dust particles between different sources [e.g. Colarco et al., 2014]. The results can suggest possible differences in dust refractive index between long range transported and mixture with local dust injections (the area is very dry in summer, thus favoring local mineral dust resuspension) and local pollution. The RRI and IRI values provided by AERONET show good agreement with GRASP retrievals for coarse mode, as expected due to the large predominance of dust particles. Better agreement between IRI retrieved by AERONET and by GRASP for coarse mode was found for CP, with differences ~ 10%, while for UGR these differences are between 35 - 80% (larger differences for shorter wavelengths). The high discrepancy between IRI retrieved by AERONET and by GRASP in the

case of UGR can be explained by the uncertainty associated to the incomplete lidar overlap. On the other hand, CP station is located above the lidar incomplete overlap height, and thus the effect of the incomplete overlap on the retrieval is negligible. On 16th June, IRI airborne values estimated at 530 nm are close to IRI retrieved by GRASP at 532 nm for coarse mode, and the differences are within the associated uncertainties. On the other hand, on 17th June, there are more differences between IRI values retrieved by GRASP at UGR station and those estimated from airborne measurements, with differences over 100%, whereas for the CP retrievals the differences are 50%.

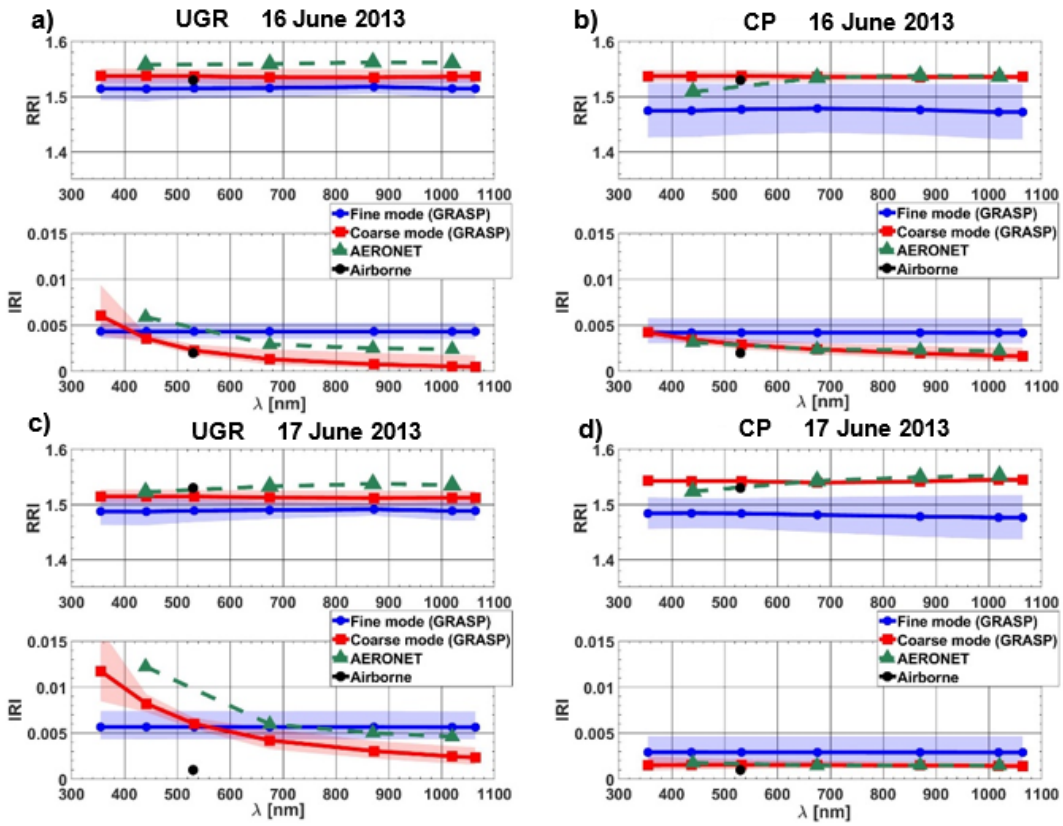

Figure 5.6. Spectral real (RRI) and imaginary (IRI) refractive indices retrieved by GRASP for the fine (blue) and coarse (red) modes with its uncertainty (shaded area); by AERONET (green) and airborne measurement (black) on 16th (**a, b**) and 17th (**c, d**) June 2013 in UGR (**a, c**) and CP (**b, d**).

Figure 5.7 shows the columnar SSA values retrieved by GRASP and AERONET on 16th and 17th June at UGR and CP. The SSA value at 530 nm calculated by Denjean et al. [2016] for dust layer using airborne measurements during the campaign was 0.95 ± 0.04. SSA retrieved by GRASP at 532 nm is close to this airborne value. Better agreement with this value is found for the retrievals from UGR on 16th June and at CP on 17th June. The differences from UGR on 17th June could be due the in-situ value was calculated for the dust layer whereas that GRASP and AERONET use sun/sky photometer data, which measures the total atmospheric column. Furthermore, in the case of UGR station, these measures could be influenced by injections of local pollution.

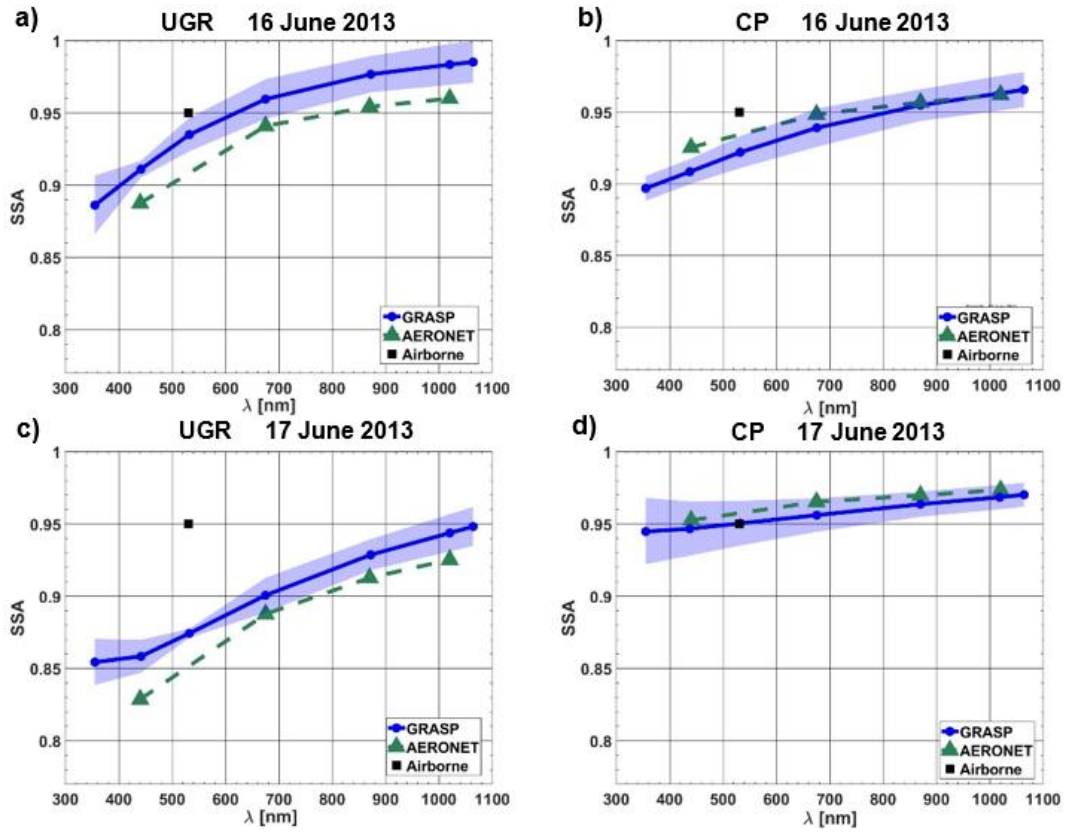

Figure 5.7. Single-scattering albedo retrieved by GRASP (blue) with its uncertainty (shaded area), AERONET (green) and airborne measurement (black) on 16th (**a, b**) and 17th (**c, d**) June 2013 at UGR (**a, c**) and CP (**b, d**).

The retrieved SSA values are in the range 0.85-0.98 (in the 355-1064 nm wavelength range) and are in the ranges of the typical values for dust aerosols [Dubovik et al., 2002; Toledano et al., 2011; Lopatin et al., 2013]. Both AERONET and GRASP retrievals follow the same pattern with wavelength, with increasing SSA as wavelength increases, which is a typical characteristic of dust aerosols [Dubovik et al., 2002; Valenzuela et al., 2012b]. Differences between SSA retrieved by AERONET and GRASP algorithms are below 0.03 at all wavelengths, which are within the uncertainties associated with each method. The small discrepancies between SSA retrieved by AERONET and GRASP algorithms are <1% for CP station in particular at 1020 nm, whereas for UGR retrievals the differences are bigger and the lowest discrepancies are obtained at 675 nm.

5.3. Vertically-resolved aerosol properties

Figure 5.8 shows particle total volume concentration profiles for the fine, coarse and total (fine+coarse) modes, retrieved by GRASP and LIRIC algorithms, together with the results obtained with airborne instrumentation. In general, there is a good agreement between the profiles retrieved by GRASP and LIRIC algorithms and those obtained by the airborne instrumentation, with both retrievals and the airborne data reproducing similar vertical structures on both days. The airborne data show a larger variability compared to GRASP and LIRIC mostly associated to their larger uncertainty and the fact that the airborne data are instantaneous measurements whereas the lidar data are an average over a 30-minute period.

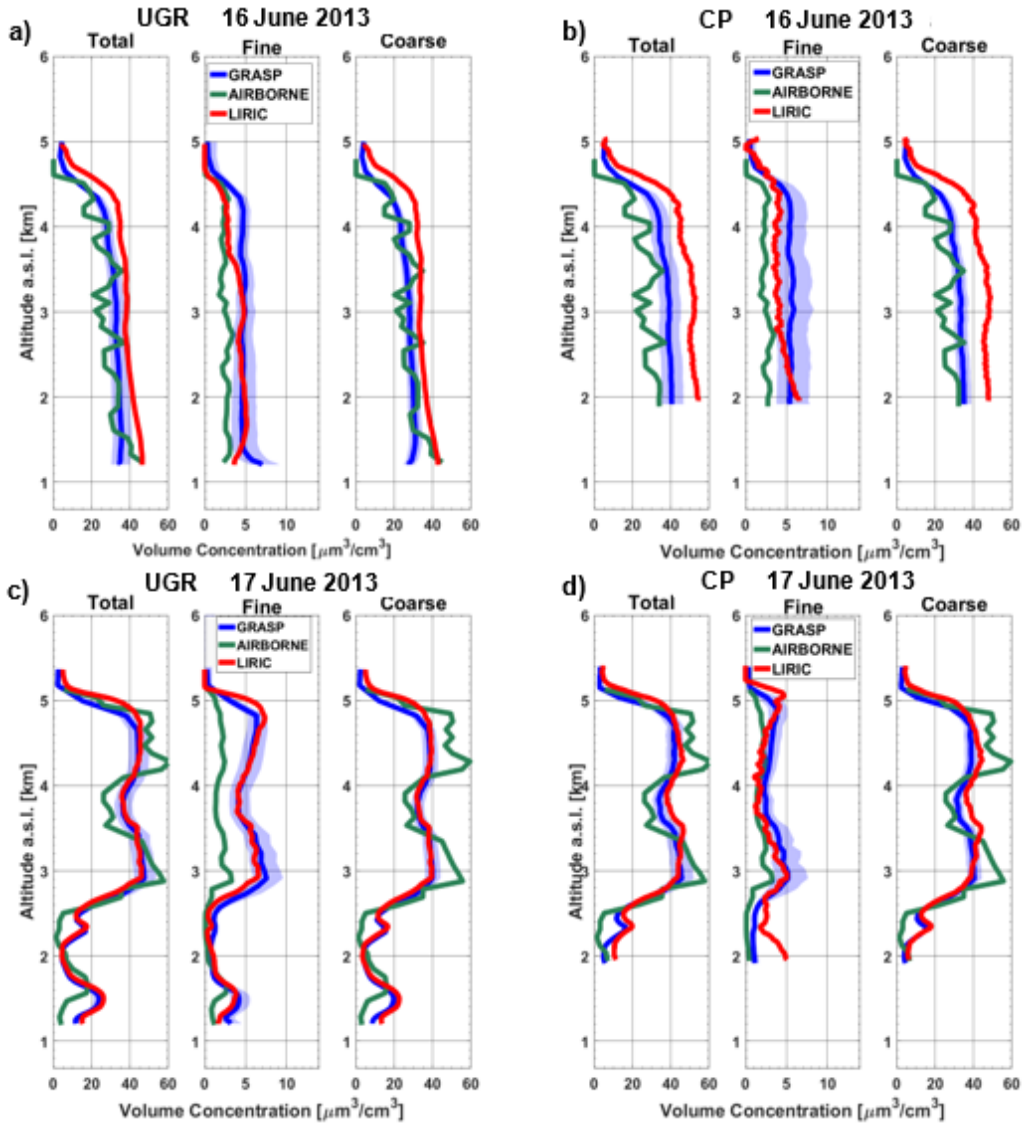

Figure 5.8. Volume concentration profile (total, fine and coarse mode) retrieved by GRASP (blue) with its uncertainty (shaded area), aircraft measurements (green) and LIRIC (red) on 16th (**a, b**) and 17th (**c, d**) June 2013 at UGR (**a, c**) and CP (**b, d**).

Both GRASP and LIRIC retrievals overestimate the airborne concentration data for the fine mode while they overestimate/underestimate the total mode on 16th/17th June using sun/sky photometer data at both UGR and CP stations. In the case of fine mode concentration, the differences between the airborne and the GRASP and LIRIC retrievals are lower than 5 μm^3/cm^3 (about 80%). The agreement

for the coarse mode is high with differences lower than 6 $\mu m^3/cm^3$ (25%), except for the LIRIC retrieval from CP on 16th June, where the difference is 19 $\mu m^3/cm^3$ (around 80%). Both algorithms show the largest differences for the retrievals from CP on 16th June, whereas the differences for the retrievals from UGR for total and coarse mode are around 15% and 25% using GRASP and LIRIC, respectively. On 17th June for UGR retrieval, the differences between both algorithms and airborne data below 2 km a.s.l. could be explained because the flight was not exactly over Granada city as shown in Figure 5.1 and in the first two kilometers of the atmosphere differences are expected because of the influence of the city. In the dust layer on 17th June, the differences are around 20% for coarse and total volume concentration by both algorithms for UGR and CP stations. Differences between GRASP and LIRIC retrievals are below 30%, being within the combined uncertainty from both retrievals.

Table 5.3. Comparison of fine, coarse and total mean volume concentration ($\mu m^3/cm^3$) retrieved by GRASP, measured by airborne and retrieved by LIRIC for dust layers on 16th (up to 4.5 km a.s.l.) and 17th (from 2.6 to 5.0 km a.s.l.) June.

VC [$\mu m^3/cm^3$]		**16th June 2013**		**17th June 2013**	
		UGR	**CP**	**UGR**	**CP**
Fine	GRASP	4.7 ± 0.6	5.5 ± 0.3	5.5 ± 1.3	3.5 ± 1.0
	AIRBORNE	2.6 ± 0.4	2.6 ± 0.4	1.9 ± 0.6	1.9 ± 0.6
	LIRIC	4.2 ± 0.8	4.6 ± 1.0	5.3 ± 1.3	2.8 ± 1.1
Coarse	GRASP	28 ± 4	32 ± 4	35 ± 7	36 ± 5
	AIRBORNE	31 ± 8	27 ± 5	41 ± 11	41 ± 11
	LIRIC	37 ± 4	46 ± 4	35 ± 5	38 ± 6
Total	GRASP	33 ± 4	38 ± 4	40 ± 8	39 ± 6
	AIRBORNE	33 ± 8	28 ± 5	42 ± 11	42 ± 11
	LIRIC	41 ± 5	50 ± 4	40 ± 6	41 ± 6

Table 5.3 summarizes the VC mean values and associated standard deviations retrieved from the in-situ airborne measurements, but also from GRASP and LIRIC profiles shown in Figure 5.8. Data are analyzed only for those layers with

total VC above 20 $\mu m^3/cm^3$ to avoid undesirable outliers for low aerosol loads. Hence, for 16th June it is analyzed the layer between 1.2 and 4.5 km a.s.l. and for 17th June, the analyzed layer is that from 2.6 to 5.0 km a.s.l.. There is a slight contribution of the fine mode to the dust layers on both days, with values between 3 $\mu m^3/cm^3$ for the airborne data and 5.3 $\mu m^3/cm^3$ for LIRIC. In general, it is observed that the coarse mode contributes the most to the total VC, as expected due to the predominance of mineral dust and the higher size of these particles. Coarse mode concentration averaged (± standard deviation) values are 28 ± 4 $\mu m^3/cm^3$ and 46 ± 4 $\mu m^3/cm^3$ on June 16th, and 35 ± 5 $\mu m^3/cm^3$ and 42 ± 11 $\mu m^3/cm^3$ on June 17th, depending on the dataset considered.

Figure 5.9 shows the aerosol β coefficient profiles at 355, 532 and 1064 nm retrieved by GRASP and the profiles calculated by Klett-Fernald method. The LR used in Klett method is assumed constant for the entire profile and was computed by fitting the integral of the different extinction profiles to the measured AOD. However, GRASP uses both sun/sky radiances and the RCS lidar data to retrieve LR values, both in column-integrated and vertical profiles. The GRASP LR values are close to the LR values used by Klett-Fernald method and are typical LR values of Saharan dust measured over the southeastern Spain [Guerrero-Rascado et al., 2009; Navas-Guzmán et al., 2013]. Below 1.6 km, the Klett retrieval at 355 showed unrealistic values probably associated with instrumental problems. However, for GRASP this problem does not appear and seems to be canceled due to the use of the combined data of lidar and sun/sky photometer. GRASP algorithm underestimates the β values obtained by Klett-Fernald method, except for CP retrieval on 17th June. Larger differences were observed for Granada β retrievals. Nevertheless, the differences are within the uncertainties claimed for our system (approximately 30%). The β differences at the ultraviolet channel reached 19% and around 9% for UGR and CP retrievals, respectively. The discrepancies between backscatter coefficient profiles at 532 nm retrieved by GRASP and Klett-Fernald are around

16% and 11% for UGR retrieval on 16th and 17th June, while for CP retrievals the discrepancies are around 11% on both days. In the case of backscatter coefficient profiles at 1064 nm, the differences between both retrievals are close to 24% for UGR on 16th June and CP on 17th June, while for the other two cases the differences are the lowest (6%).

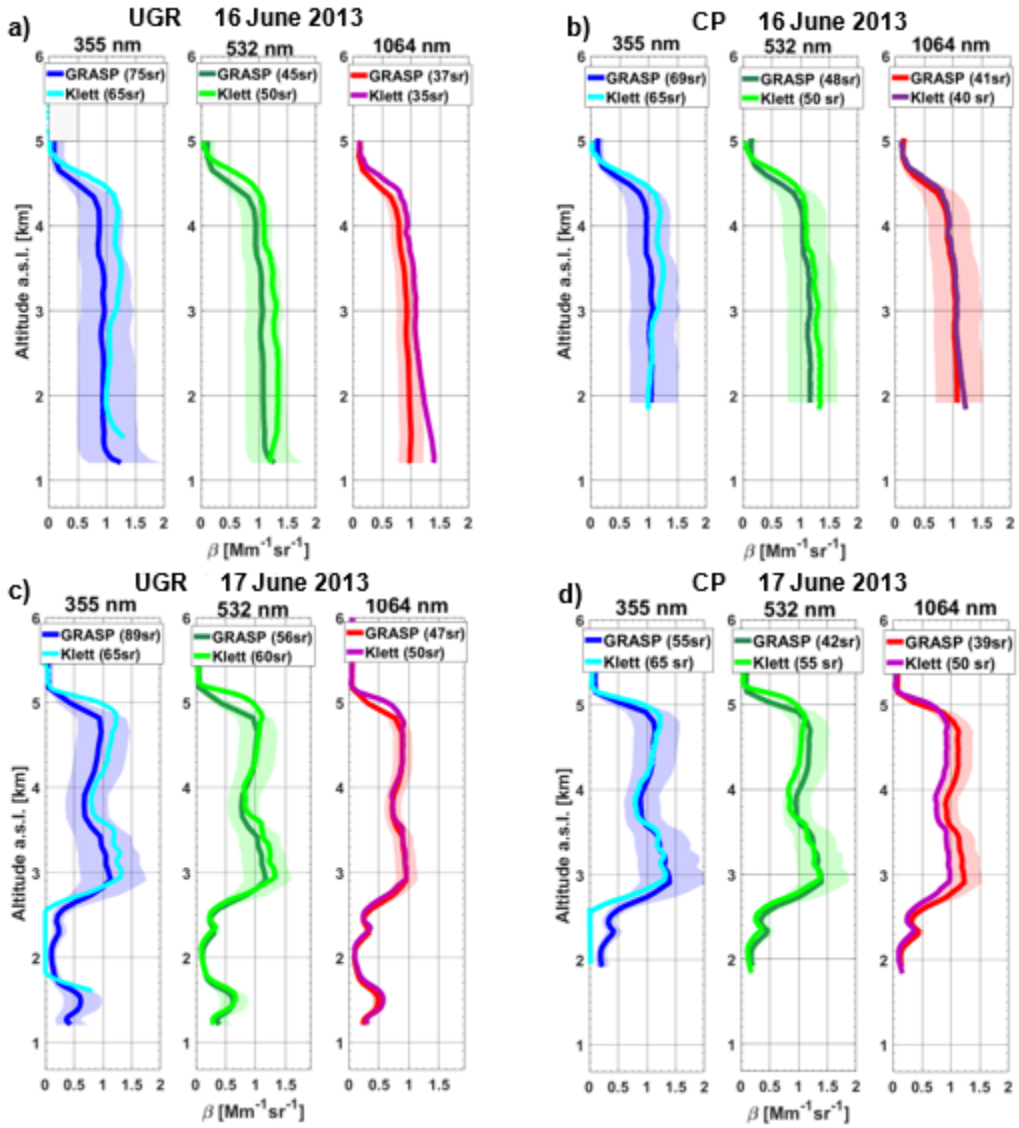

Figure 5.9. Aerosol backscatter coefficient profiles retrieved at 355, 532 and 1064 nm by GRASP with its uncertainty (shaded area) and Klett-Fernald on 16th (**a, b**) and 17th (**c, d**) June 2013 at UGR (**a, c**) and CP (**b, d**). LR values used in each inversion retrieval are also included in the figure.

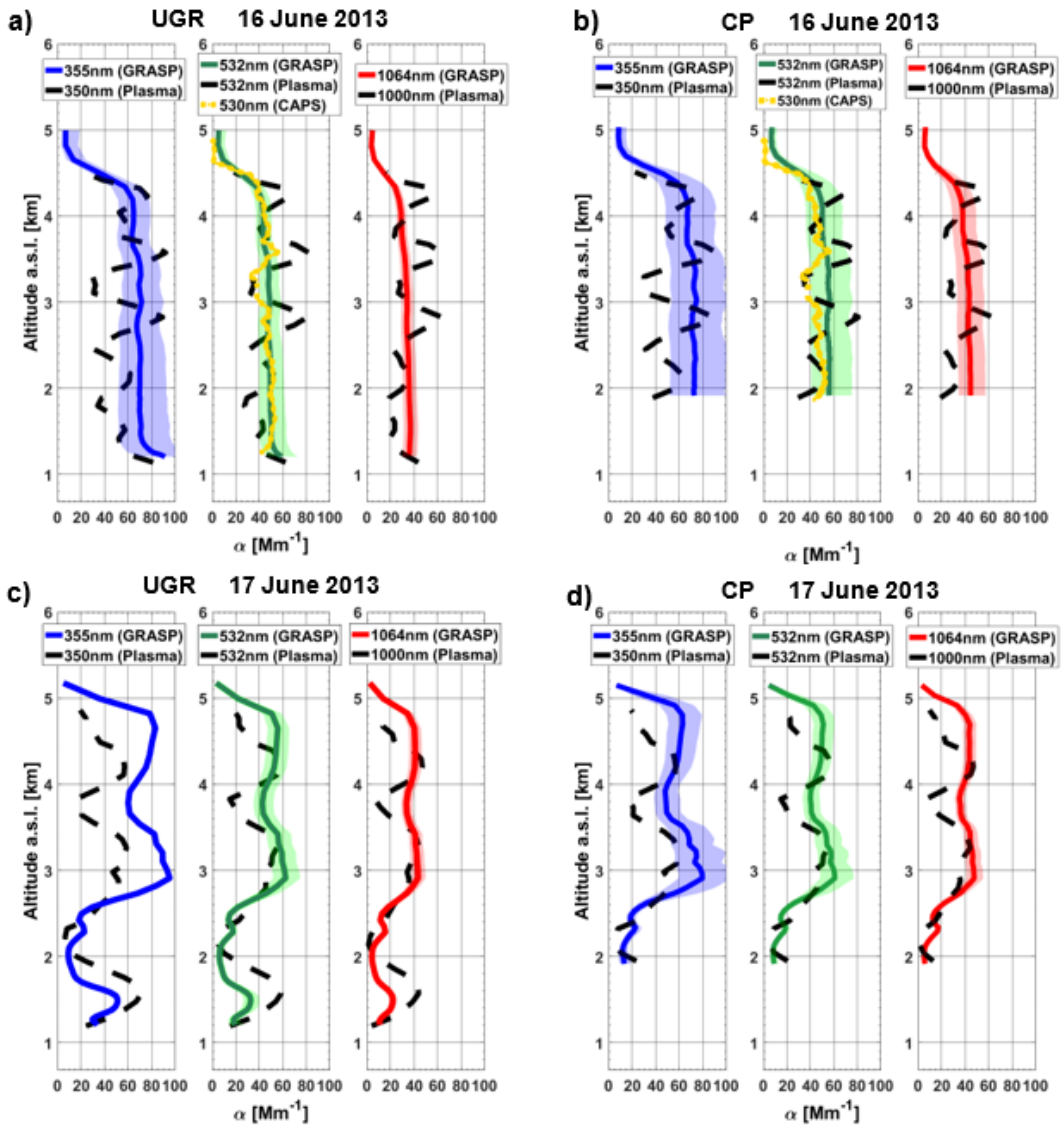

Figure 5.10. Aerosol extinction coefficient profiles retrieved by GRASP (355, 532 and 1064 nm) with its uncertainty (shaded area), PLASMA (350, 530 and 1000 nm) and CAPS (530 nm) on 16th (**a, b**) and 17th (**c, d**) June 2013 at UGR (**a, c**) and CP (**b, d**).

The comparison between aerosol α coefficient profiles retrieved by GRASP and those measured by airborne instruments (CAPS and PLASMA) is shown in Figure 5.10. Profiles retrieved by GRASP show good agreement with the CAPS data (measurements only on 16th June at 532 nm), even though with slightly higher values for GRASP of approximately 3 ± 3 Mm^{-1} (7%) and 9 ± 5 Mm^{-1} (18%) for the UGR

and CP retrievals, respectively. GRASP extinction coefficient retrievals were larger than PLASMA measurements at all wavelengths, with larger differences at the ultraviolet channel (~50%). On 16th June, the differences for the ultraviolet channel are 20 ± 11 Mm^{-1} (45%) and for the visible and infrared channels are 11 ± 8 Mm^{-1} (30% and 40%, respectively). These differences were similar or lower than those obtained by Karol et al. [2013] when comparing PLASMA with lidar data. On 17th June, α profiles obtained by PLASMA and GRASP show the same layers, but their differences are larger, reaching 50% for the visible channel and more than 60% for the ultraviolet and infrared channels. As GRASP and LIRIC reproduce the same layer structures for volume concentrations, these differences can be mainly associated with PLASMA due to the high fluctuations.

Vertical profiles of SSA obtained by GRASP at UGR and CP stations on 16th and 17th June are shown in Figure 5.11. As SSA is an intensive aerosol parameter, only SSA values for the layers with large aerosol loads are represented. On 16th June, there are no remarkable changes in SSA with altitude, which agrees with the extinction and backscatter coefficients profiles and with the particle volume concentrations. For 17th June, vertical profiles of SSA are sensitive to the different aerosol layers with different aerosol types illustrating the capabilities of GRASP for detecting different aerosol layers with different composition. Nonetheless, the values of SSA are also within those associated with dust aerosol in previous studies [Dubovik et al., 2002a; Toledano et al., 2011; Lopatin et al., 2013]. Differences are observed again between the SSA profiles obtained at UGR and CP stations. On 16th June SSA differences between both retrievals are lower than 2% while on 17th differences reach up to 10%. This result is again associated with overlap issues, although the influence of the city with injection of large amounts of particles confined below the altitude of CP cannot be neglected in sky radiance measurements. Orographic differences between UGR and CP could also partially explain the obtained results.

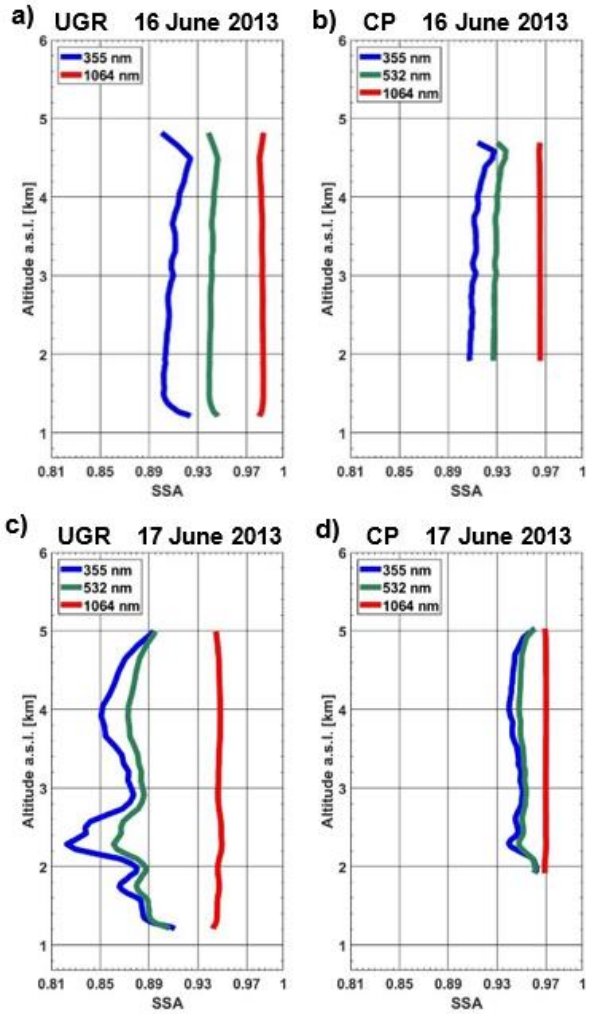

Figure 5.11. Single scattering albedo profiles at 355, 532 and 1064 nm retrieved by GRASP on 16th (**a, b**) and 17th (**c, d**) June 2013 at UGR (**a, c**) and CP (**b, d**).

Figure 5.12 shows scattering- Ångström Exponent computed between 450 and 700 nm, AE_{sca} (450-700), obtained by GRASP algorithm at UGR and CP stations together with those obtained from nephelometer airborne measurements. GRASP scattering coefficient profiles are calculated by multiplying the extinction coefficient by the SSA at the same wavelength. Despite the fact that the AE_{sca} (450-700) profiles from the airplane data are noisier than GRASP profiles, general good agreement is observed, with discrepancies within the uncertainties.

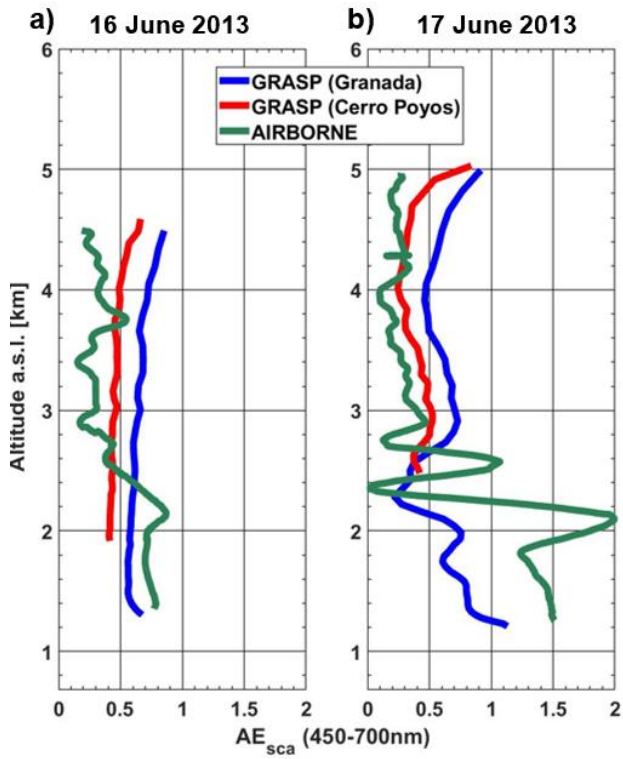

Figure 5.12. Scattering – Ångström Exponent (450 - 700 nm) retrieved by GRASP (blue and red) at UGR and CP, respectively, and aircraft measurements (green) on 16th (**a**) and 17th (**b**) June 2013.

In general, GRASP AE_{sca} (450-700) values are larger than the airborne data for altitudes above 2.5 km a.s.l.. Above this altitude, the AE_{sca} (450-700) values are close to zero on both days, which is typical of aerosols dominated by coarse particles [Bergstrom et al., 2007]. However, in the lower part of the profiles, the airborne AE_{sca} (450-700) values are larger (~0.7 and ~1.6 for the airborne data on 16th and 17th June, respectively) and GRASP AE_{sca} (450-700) profiles underestimate the airborne data. The values for these lower altitudes, including those retrieved by GRASP using the sun/sky photometer data measured at UGR and the airborne data, were similar to in-situ measurements at UGR station, with AE_{sca} (450-700) values around 0.70 ± 0.10 and 1.67 ± 0.07 on 16th and 17th June, respectively. GRASP profiles have similar values above and below 2.5 km a.s.l. with better agreement between airborne data and CP GRASP retrievals. UGR GRASP retrievals show

more differences on 17th June, the case with aerosol layers with different aerosol types. On 17th June, in the altitude range ~1.8 – 2.7 km a.s.l. the aerosol load was low (~5 $\mu m^3/cm^3$) and, hence, SSA and AE values could be less reliable in this layer. However, the layer up to 1.8 km a.s.l. showed a moderate aerosol concentration (~17 $\mu m^3/cm^3$) with a different composition to the layer above 2.7 km a.s.l. as shown by the SSA and AE profiles.

Finally, the Table 5.4 shows the mean values, with ±1 standard deviation, of backscatter-AE computed between 532 and 1064 nm, AE_β (532-1064), and color ratio (CR=$\beta(532\,nm)/\beta(1064\,nm)$) calculated with the obtained GRASP products in the layer between 1.8 and 4.5 km a.s.l. and between 2.8 and 5.0 km a.s.l. on 16th and 17th June, respectively. The values of AE_β and CR (0.5 ± 0.2 and 1.3 ± 0.3, respectively) are in the range of typical values of dust aerosols [e.g. Perrone et al., 2014].

Table 5.4. Mean value of backscatter - Ångström exponent (β-AE) and Color Ratio (CR) between 532 and 1064 nm, retrieved by GRASP for dust layers on 16th and 17th June 2013.

	16th June 2013		**17th June 2013**	
	UGR	**CP**	**UGR**	**CP**
AE_β	0.65 ± 0.07	0.46 ± 0.05	0.63 ± 0.12	0.40 ± 0.10
CR	1.15 ± 0.05	1.13 ± 0.05	1.09 ± 0.09	1.08 ± 0.04

5.4. Conclusions

The GRASP retrievals show a good agreement with AERONET column-integrated products, with discrepancies within the uncertainties. Total volume concentration profiles retrieved by GRASP and those obtained by airborne measurements show a good agreement with differences around 15% on 16th June using for the GRASP retrieval sun/sky photometer data measured at UGR station and on 17th June using for the GRASP retrieval sun/sky photometer data measured at CP station. The agreement between GRASP β profiles and those obtained using only lidar data and

Klett-Fernald algorithm are quite good using both station data, showing differences below 12% at 355 and 532 nm for CP station. In the case of the α profiles, good agreement was found between GRASP and the CAPS data (differences below 20%), while the comparison of GRASP retrievals with PLASMA data shows larger differences. The SSA profiles retrieved by GRASP show typical values of dust aerosols and the differences between GRASP retrievals using sun/sky photometer data measured at UGR and CP stations are below 10% at the lidar wavelengths. Other aerosol properties obtained with GRASP, like the CR and the AE_{β}, also show similar values to those reported in the literature for dust aerosols.

GRASP algorithm is quite robust as its retrievals show the good agreement with the optical and microphysical properties retrieved by AERONET and those obtained by airborne measurements. The results obtained here show that using GRASP algorithm by combining lidar and sun/sky photometer data can provide more complete column-integrated aerosol properties compared to AERONET retrieval. The GRASP algorithm can also provide reliable vertically-resolved aerosol properties such as the SSA, α or VC, improving the capabilities of previous algorithms such as LIRIC. Nonetheless, the AE_{sca} profiles retrieved by GRASP together with the better agreement found between CP retrievals and the aircraft measurements compared to UGR retrievals indicate that GRASP vertical distribution of some of the aerosol properties is still affected by considerable uncertainties.

6. Evaluation of day and night-time GRASP retrievals during an intense desert dust event

In this chapter, GRASP is applied to retrieve continuous day-to-night aerosol properties, both column-integrated and vertically-resolved. The study is focused on the evaluation of GRASP retrievals during an intense Saharan dust event that occurred during the Sierra Nevada Lidar aerOsol Profiling Experiment I (SLOPE I) field campaign. SLOPE I was held in the Andalusian Global ObseRvatory of the Atmosphere from May to September 2016 with the general objective of characterizing vertical variability of atmospheric aerosols combining in-situ and remote sensing measurements.

For daytime aerosol retrievals, GRASP is used, as described in Chapter 5, combining of elastic lidar signals and sun/sky photometer measurements, while for night-time retrievals three different combinations of active and remote sensing measurements are proposed. Evaluations of the columnar aerosol properties retrieved by GRASP are done versus standard AERONET retrievals. The coherence of day-to-night evolutions of the different aerosol properties retrieved by GRASP is also studied. The extinction coefficient profiles retrieved by GRASP are compared with the profiles calculated by Raman technique at night-time. Finally, GRASP aerosol retrievals at 2500 m a.s.l. are evaluated by in-situ measurements at this height at SNS station.

6.1. SLOPE I campaign

The objective of SLOPE I field campaign was the study of the vertical variability of the atmospheric aerosols in the region surrounding the city of Granada. SLOPE I uses a unique combination of active and passive remote sensing instruments at UGR

station (680 m a.s.l.) combined with in-situ measurements at the surrounding high mountain site of SNS station (2500 m a.s.l). The altitude difference between both stations (~1.8 km) and the short horizontal distance (less than 25 km) make SLOPE I ideal for fulfilling the objective of evaluating atmospheric aerosols vertical variability.

Active remote sensing instruments at UGR ran almost continuously during SLOPE I, particularly the multiwavelength Raman lidar. In this sense, several studies have been done using SLOPE I database: day-to-night evolution of atmospheric boundary layer [de Arruda Moreira et al., 2018] and its turbulence behavior [de Arruda Moreira et al., 2019], aerosol hygroscopic growth [Bedoya-Velásquez et al., 2018], the characterization of the angular scattering of the Sahara dust aerosol by means of polar nephelometry [Horvath et al, 2018] and the evaluation of the aerosol properties during daytime retrieved by GRASP by combining a ceilometer and sun/sky photometer measurements as will be demonstrated in Chapter 7. Here, the unique dataset of SLOPE I is used to evaluate GRASP aerosol retrievals during an intense desert dust event using different combinations of remote sensing instruments.

6.1.1 Dust event overview

This chapter is focused on an intense dust event that reached the southeastern of the Iberian Peninsula during SLOPE I field campaign from 18th to 21st July 2016. The analysis of five-day backward-trajectories computed by HYSPLIT model (Figure 6.1) shows that the air masses that arrived to Granada came from southwestern direction on 18th and 21st July 2016. These air masses originated from Sahara Desert area and passed along the south Morocco and Moroccan coast before reaching Granada. As shown hereafter, these Saharan air masses have transported large amounts of Saharan dust particles to the study area.

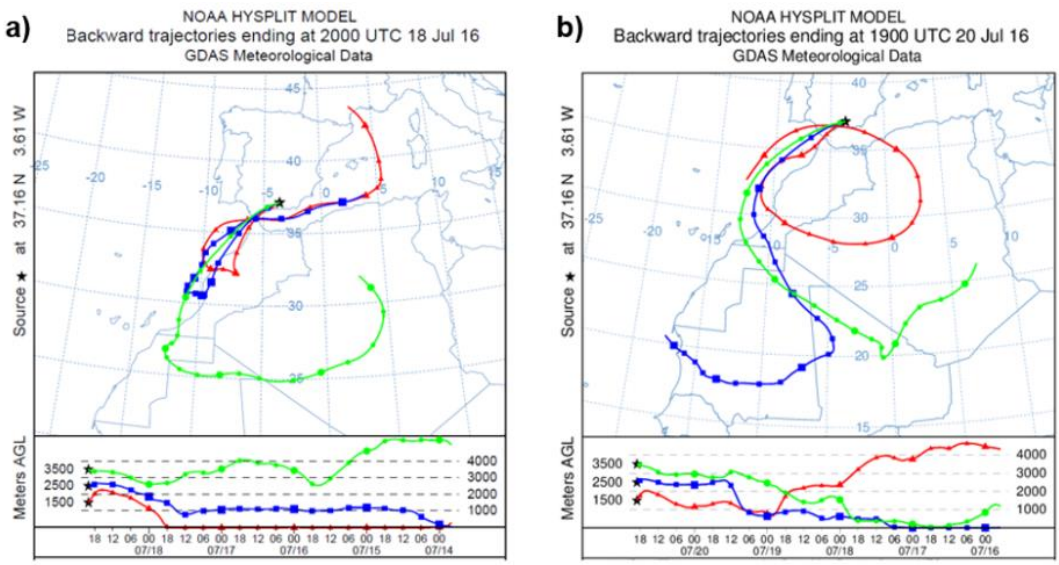

Figure 6.1. Five-day backward-trajectories computed using HYSPLIT reaching Granada at 20:00 UTC on 18th July (**a**) and at 19:00 UTC on 20th July 2016 (**b**).

Figure 6.2a and b show the day- and night-time AOD_{440} and the $AE_{440\text{-}870}$ at UGR station. Day-time values are provided by AERONET while night-time values are from lunar photometry measurements. Figure 6.2a and b reveal lower AOD_{440} on period 18th-19th July (hereinafter P1 period) than on 20th-21st July (hereinafter P2 period). Actually, AOD_{440} mean value and standard deviation during P2 (0.94 ± 0.08) is almost twice than on P1 (0.50 ± 0.03). The $AE_{440\text{-}870}$ shows a smooth behavior with no significant variations around the mean value of 0.17 ± 0.03, which is typical of Saharan dust intrusions over Granada region [e.g. Lyamani et al., 2006: Guerrero-Rascado et al., 2008]. Pérez-Ramirez et al. [2016] analyzed long-term record of AERONET measurements for Saharan dust outbreaks at Granada obtaining a mean AOD_{440} of 0.24 and mean $AE_{440\text{-}870}$ of 0.3. From Figure 6.2, AOD_{440} mean values obtained in P1 and P2 periods are two and four times higher than the AOD mean value reported by Perez-Ramirez et al. [2016] for desert dust intrusions over Granada, which make this Saharan dust event extraordinary.

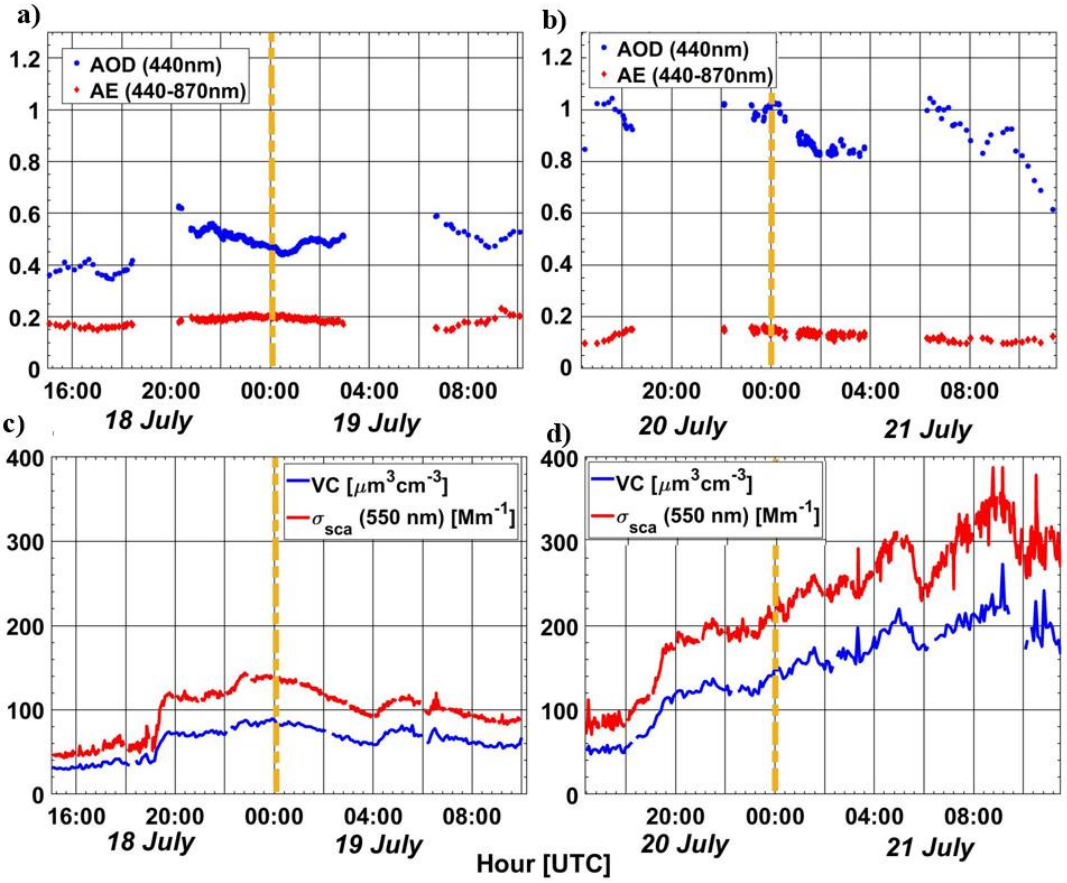

Figure 6.2. Day-to-night evolution of the AOD at 440 nm (blue) and AE (440-870 nm) (red) obtained at UGR station from 18th to 19th July 2016 (**a**) and from 20th to 21st July 2016 (**b**). Day-to-night temporal evolution of the total volume concentration (VC) and the scattering coefficient (σ_{sca}) at 550 nm measured at SNS station from 18th to 19th (**c**) and from 20th to 21st (**d**) July 2016.

Figure 6.2c and d show the day-to-night temporal evolution of σ_{sca} at 550 nm and the total VC obtained from in-situ instrumentation at SNS high mountain station, both from 18th to 21st July 2016. At a first sight, both VC and σ_{sca} show a monotonous increase starting with a minimum on 18th July (~50 Mm^{-1} for σ_{sca} and ~40 μm^3/cm^3 for VC), reaching the maximum values early in the morning on 21st July (~350 Mm^{-1} for σ_{sca} and ~250μm^3/cm^3 for VC). This large increase on these two extensive aerosol properties, especially on 20th-21st July, is associated with the

transport of Saharan dust particles and shows the drastic impact of this Saharan dust event on aerosol load at SNS remote station.

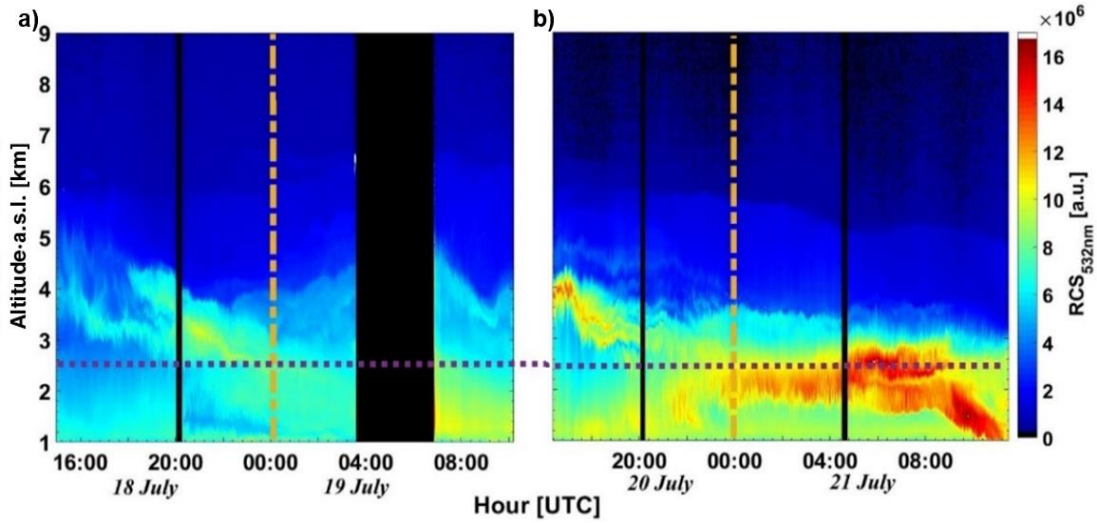

Figure 6.3. Temporal evolution of the lidar range corrected signal at 532nm from 18th to 19th (**a**) and from 20th to 21st(**b**) July 2016. The purple horizontal line indicates the SNS altitude.

Figure 6.3 shows the temporal evolution of the lidar RCS at 532 nm from lidar system at UGR station and gives detailed layers evolution during this Saharan dust event. Dashed horizontal purple line shows the height of SNS mountain station. Figure 6.3 clearly reveals important variability in the layer structures of the atmosphere. On 18th July evening two different and de-coupled aerosol layers are observed, one at 4 km a.s.l. and the other one near surface up to 1.2 km a.s.l., approximately. However, during the 18th - 19th night the upper aerosol layer went gradually down until it mixed up with the surface aerosol layer avoiding any clear layered vertical structure. On the following day, particularly after 08:00 UTC, two different aerosol layers can be observed again. From afternoon on 19th to noon on 20th, the clouds were present over the site and hence the RCS data obtained during this period are excluded from further analysis. After re-starting lidar measurements, on 20th July a de-coupled aerosol layer at approximately 4 km a.s.l. is observed again; this layer also went gradually down until it mixed up with the boundary layer early at night. But the most remarkable observation in this period is the very

different structure observed after 04:00 UTC on 21th July when two decoupled layers at ~2 - 3 km a.s.l. altitude appeared. Later, on 21st July morning, the upper layer collapsed and mixed-up with the surface layer.

The multi-layers aerosol evolution revealed in Figure 6.3 agrees with AOD and AE evolutions and with in-situ measurements at SNS. In fact, the increase in the intensity of RCS on 20th July agrees with the increase in AOD. Also, the increase of RCS at the altitude of 2500 m a.s.l. coincides with the increase in in-situ σ_{sca} and VC measured at SNS station. Furthermore, the collapse of the layer at 2500 m a.s.l. after 08:00 UTC on 21st July agrees with the decrease of σ_{sca} and VC at SNS.

Given the coherence among all measurements, hereafter, GRASP aerosol retrievals are evaluated using different combinations of these measurements as input to GRASP algorithm. In the following section, the different measurement combination used as input in GRASP algorithm for retrieving vertical and columnar aerosol optical and microphysical properties during this dust event are described in detail.

6.2. GRASP configurations

In this chapter GRASP algorithm is used for retrieving continuous day- and night-time aerosol properties. Table 6.1 summarizes the different GRASP input data used for day- and night-time retrievals. Daytime scheme (denoted as D) combines lidar and sun/sky photometer measurements, while night-time schemes uses three different configurations of passive and active remote sensing measurements (denoted as N0, N1 and N2).

Table 6.1. Data set used as input in GRASP algorithm for day and night-time retrievals. (*30 min of lidar range corrected signal at 355, 532 and 1064 nm). The number of the obtained converging retrievals for each scheme obtained during the first (P1) and second (P2) periods is also provided in the table.

		Input data	Nº Retrievals (P1/P2)
Daytime	**D**	• RCS* • AOD and sky radiances at 440, 675, 870 and 1020 nm (daytime).	10/7
Night-time	**N0**	• RCS* • AOD and sky radiances on the closest daytime measurements (daytime).	8/16
	N1	• RCS* • AOD at 440, 675, 870 and 1020 nm (night-time). • CRI and spherical particle fraction (daytime average values retrieved by GRASP using D scheme).	9/11
	N2	• RCS* • AOD at 469 (interpolated to camera canal), 675, 870 and 1020 nm (night-time). • Relative sky moon radiance at 469, 533 and 608 nm	6/7

Day-time GRASP retrieval (D scheme) of the microphysical properties of the atmospheric aerosol, both column-integrated and vertical profiles, requires as input the elastic lidar and the sun/sky photometer measurements. Available night-time measurements to be used as GRASP input are restricted, so the challenge is

how to manage the available information to run GRASP. In this thesis three different schemes have been proposed for extending the use of GRASP to night-time (see Figure 6.4). The first one (N0 scheme) assumes that there is no change in the aerosol column integrated properties along the night, in this way the retrieval is done combining the night-time elastic lidar measurements with the closest sun/sky measurements registered the day before or the day after. The second (N1 scheme) approach considers that the aerosol load in the vertical column can be monitored by lunar photometry, but assumes that there are no changes in the aerosol column-integrated intensive properties, that is this approach considers that there are no changes in the aerosol type. The last (N2 scheme) approach uses night-time elastic lidar signals and aerosol optical depth measurements retrieved from a lunar photometer in combination with relative sky radiances at the lunar aureole. Figure 6.4 schematizes the different combination of passive and remote sensing measurements proposed here for GRASP retrievals. Details about each configuration scheme are given in the following subsections.

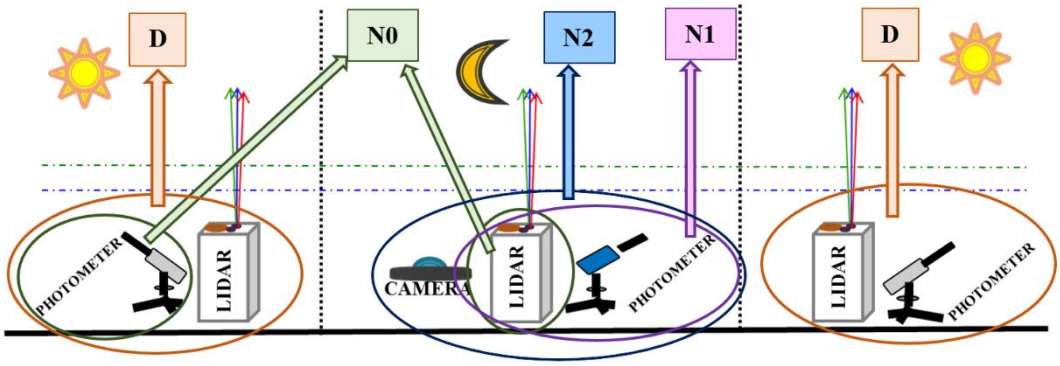

Figure 6.4. Diagram of different instrumentation used in each GRASP scheme for day- (D) and night- (N0, N1 and N2) time retrievals

6.2.1. Daytime GRASP configuration scheme

For daytime retrievals, the set of measurements used as input in GRASP are those recommended by Lopatin et al. [2013]: three wavelengths dependent lidar RCS and

four wavelengths dependent AOD and sky radiance measurements, covering the spectral range from the UV to the near-infrared region. In this approach, a bimodal log-normal size distribution is assumed, which allows the retrieval of fine (particles of radii below 0.5 μm) and coarse mode (particles of radii above 0.5 μm) aerosol properties respectively. The input data used by GRASP for this scheme is shown in Table 6.1.

6.2.2. Night-time GRASP configuration schemes

6.2.2.1. N0 scheme

AOD and sky radiance measurements during night-time are very scarce. Thus, the first night-time GRASP scheme (N0) uses the night-time RCS measured by lidar combined with the closest daytime measurements of AOD and sky radiances both at 440, 675, 870 and 1020 nm (Table 6.1). This scheme offers the possibility to retrieve aerosol vertical properties in stations where night-time photometer measurements are not available.

6.2.2.2. N1 scheme

Currently, night-time AOD measurements, taken with the recently developed sun/sky/lunar photometer CE318-T are available in some stations [e.g. Barreto et al., 2013, 2016, 2019]. GRASP scheme based on night-time AOD measurements alone was applied by Torres et al. [2017], showing the ability of GRASP to retrieve the total column aerosol properties at night-time using this configuration.

The N1 scheme proposed in this thesis attempts to go further and provide vertically-resolved aerosol properties at night-time by combining elastic lidar and the AOD at 440, 675, 870 and 1020 nm from lunar photometry measurements (Table 6.1). As in Torres et al. [2017] a bimodal log-normal size distribution is considered the CRI and the spherical particle fraction are not retrieved but are assumed as

known. Here, the CRI and the spherical particle fraction used as input in GRASP are the averaged GRASP values retrieved during the closest (after and before) daytime retrievals.

6.2.2.3. N2 scheme

The third scheme (N2) avoids any assumption about CRI and spherical particle fraction and uses the sky radiance near the Moon (lunar aureole) measured by sky camera as input in GRASP algorithm [Román et al., 2017a]. More specifically, the third scheme for night-time GRASP retrievals uses the lidar RCS, lunar aureole normalized sky radiances at 469, 533 and 608 nm derived by the SONA sky camera and the night-time AOD at 469, 675, 870 and 1020 nm from CE318-T (Table 6.1). The AOD at 469 nm is calculated by Ångström exponent interpolation computed in 440-675 nm wavelength range.

6.3. Evaluation of columnar aerosol properties retrieved by GRASP

For evaluating daytime columnar aerosol properties retrieved by GRASP (using D scheme) during the intensive observational period of 18th-21st July 2016, GRASP columnar aerosol retrievals were compared with those provided by AERONET operational algorithm. Generally, the data of Level 2.0 from AERONET Version 2 are used for this comparison, but for specific cases when retrieved SSA and CRI do not pass the thresholds imposed by AERONET Level 2.0 (see subsection 3.2.2.1) data of Level 1.5 from AERONET Version 2 are used.

There are not AERONET aerosol retrievals during night-time yet; thus, for evaluating columnar aerosol properties retrieved by GRASP at night-time an indirect approach is applied. In this sense, the results are discussed in terms of the smoothness and temporal coherence of the variation of the aerosol retrievals along the night and having as benchmarks the daytime retrievals (AERONET and/or GRASP) obtained the day before and the day after.

The selected study case presents, as previously shown, a situation with apparent smooth variation of the aerosol load (Figures 6.2 to 6.4) within a wide range of values but with the constancy of some of the intensive properties, identifying the type of aerosol, along the whole studied period, excluding the period with absence of remote sensing measurements. In this sense, the selected case offers an appropriate situation for testing the discussed night-time retrievals proposed, having in mind the smoothness of the aerosol evolution in spite of the ample change in the aerosol load. Hereafter, evaluations of the different GRASP aerosol parameter retrievals using different input data set are presented.

6.3.1. Columnar particle size distribution parameters

Table 6.2 summarizes the columnar aerosol properties retrieved by GRASP using different configuration schemes and those provided by AERONET. Due to the drastic change in aerosol load (as indicated by AODs) between 18th - 19th July (P1) and 20th - 21st July (P2) periods, the results of GRASP and AERONET retrievals are provided separately for these two periods.

The daytime aerosol parameters obtained by GRASP using scheme D are consistent with AERONET products, with differences being mostly within uncertainties. As in the case studied in Chapter 5, coarse modal radius retrieved by GRASP using scheme D is slightly larger than that provided by AERONET during both P1 and P2 periods. As commented in Chapter 5, this difference is attributed this to the use of the lidar data in the GRASP retrievals. The relative differences between GRASP and AERONET retrievals in the two analyzed periods are similar both for fine and coarse modes with mean relative differences around 8% (26%), 12% (35%) and 8% (10%) for VC_c (VC_f), r_{v_c} (r_{v_f}) and σ_{v_c} (σ_{v_f}), respectively (Table 6.2). It is noted that the coarse mode parameters obtained during the Saharan dust event analyzed here are the typical values obtained at Granada during dust events originating from Western Sahara [Valenzuela et al., 2012a].

Table 6 2. The average values (±standard deviations) of volume concentration (VC_f, VC_c [$\mu m^3/\mu m^2$]), volume modal radius (r_{v_f}, r_{v_c} [μm]) and standard deviation (σ_{v_f} and σ_{v_c}) for fine and coarse modes retrieved by GRASP using different configuration schemes and those provided by AERONET. The retrievals are provided for the first period 18th - 19th July (P1) and the second period 20th-21st July (P2). The subscript 'f' denotes fine mode and 'c' denotes coarse mode.

P1	AERONET	D	N0	N1	N2
VC_f	0.026 ± 0.007	0.023 ± 0.009	0.020 ± 0.002	0.020 ± 0.003	0.024 ± 0.002
r_{v_f}	0.146 ± 0.017	0.20 ± 0.03	0.202 ± 0.013	0.27 ± 0.04	0.193 ± 0.007
σ_{v_f}	0.67 ± 0.03	0.62 ± 0.06	0.63 ± 0.03	0.37 ± 0.10	0.552 ± 0.019
VC_c	0.23 ± 0.04	0.25 ± 0.05	0.28 ± 0.05	0.32 ± 0.02	0.27 ± 0.03
r_{v_c}	1.82 ± 0.08	2.06 ± 0.10	2.09 ± 0.18	2.32 ± 0.03	1.87 ± 0.14
σ_{v_c}	0.540 ± 0.018	0.58 ± 0.03	0.57 ± 0.02	0.60 ± 0.03	0.63 ± 0.03

P2	AERONET	D	N0	N1	N2
VC_f	0.046 ± 0.013	0.045 ± 0.014	0.037 ± 0.005	0.038 ± 0.002	0.031 ± 0.006
r_{v_f}	0.18 ± 0.04	0.19 ± 0.04	0.16 ± 0.02	0.26 ± 0.08	0.220 ± 0.009
σ_{v_f}	0.69 ± 0.06	0.70 ± 0.10	0.74 ± 0.07	0.39 ± 0.13	0.56 ± 0.04
VC_c	0.57 ± 0.07	0.60 ± 0.06	0.65 ± 0.04	0.62 ± 0.09	0.53 ± 0.04
r_{v_c}	1.86 ± 0.09	2.00 ± 0.09	2.03 ± 0.04	2.28 ± 0.02	1.93 ± 0.13
σ_{v_c}	0.507 ± 0.013	0.50 ± 0.04	0.51 ± 0.02	0.608 ± 0.008	0.617 ± 0.011

Nocturnal columnar aerosol properties retrieved by GRASP using different schemes show a good coherence and smooth variation when they are compared against daytime AERONET and GRASP retrievals (Table 6.2). In fact, the GRASP night-time retrievals using the N0 scheme present average values similar to those provided by GRASP daytime retrievals with discrepancies around 10% for both modes in the two periods. The values of aerosol properties of coarse mode retrieved by GRASP using N1 scheme are systematically slightly higher than those obtained during day time (by both D scheme and AERONET). The use of night-time AOD measurements in N1 scheme, which reveals change in AOD values (aerosol load) between day and night, can be behind these changes in the retrieved aerosol parameters revealed by N1 scheme. Finally, the values of aerosol parameters

retrieved by GRASP using the N2 scheme are almost similar to the values retrieved by AERONET the day before and after, especially for coarse mode where the discrepancies are around 12%, 3% and 20% for VC_c, r_{v_c} and σ_{v_c}, respectively. However, for fine mode properties (VC_f, r_{v_f} and σ_{v_f}) there are considerable differences between GRASP and AERONET retrievals mainly due to the low concentration of fine particles.

6.3.2. Columnar complex aerosol refractive indices

The RRI and IRI values obtained by GRASP and AERONET methods are not directly comparable because the GRASP configurations used here provide RRI and IRI for fine and coarse modes, separately, and AERONET provides only RRI and IRI equivalent values for the whole size distribution. Nevertheless, the RRI and IRI values provided by AERONET are used to study the consistency of GRASP retrievals. Retrievals of RRI are given in Table 6.3 while IRI are given in Table 6.4. In this case, the mean RRI and IRI values and their corresponding standard deviations correspond to the whole analyzed period. This is done because, in contrast to VC retrievals that showed a large change between P1 and P2 periods, RRI and IRI retrieved by GRASP (using different schemes) and AERONET were almost stable and showed a very small variation along the whole analyzed period, as indicated by the corresponding standard deviations. As can be seen in these tables, standard deviations were within and even below the uncertainties associated with the AERONET retrievals; ± 0.03 for RRI and ±50% for IRI [Dubovik et al., 2000]. On the other hand, it is important to remember that RRI and IRI values for the N1 scheme are not reported in Table 6.3 and 6.4 because in this case the average day values retrieved by GRASP during daytime were used as input for this GRASP configuration scheme.

Table 6.3. The average values (± standard deviation) of the real refractive indices (RRI) retrieved by GRASP (D, N0 and N2; both fine and coarse modes) and AERONET (for whole aerosol population) during 18th-21st July 2016.

RRI							
	GRASP						AERONET
	Fine			Coarse			
λ [nm]	D	N0	N2	D	N0	N2	
355	1.44 ± 0.02	1.47 ± 0.03	1.46 ± 0.01	1.45 ± 0.03	1.43 ± 0.03	1.43 ± 0.01	
440	1.44 ± 0.02	1.47 ± 0.03	1.46 ± 0.01	1.45 ± 0.03	1.43 ± 0.03	1.43 ± 0.01	1.46 ± 0.03
532	1.44 ± 0.02	1.47 ± 0.03	1.46 ± 0.01	1.45 ± 0.03	1.43 ± 0.03	1.43 ± 0.01	
675	1.44 ± 0.02	1.47 ± 0.03	1.47 ± 0.01	1.45 ± 0.03	1.44 ± 0.03	1.42 ± 0.01	1.47 ± 0.03
870	1.45 ± 0.02	1.48 ± 0.03	1.45 ± 0.01	1.45 ± 0.03	1.43 ± 0.03	1.41 ± 0.01	1.47 ± 0.03
1020	1.44 ± 0.02	1.47 ± 0.03	1.45 ± 0.01	1.45 ± 0.03	1.43 ± 0.03	1.41 ± 0.01	1.45 ± 0.03
1064	1.44 ± 0.02	1.47 ± 0.03	1.45 ± 0.01	1.45 ± 0.03	1.43 ± 0.03	1.41 ± 0.01	

RRI values retrieved by both GRASP (using different schemes) and AERONET show no remarkable spectral dependence, with maximum spectral variations of 0.03 which is below the uncertainties of the AERONET method. Also, no notable differences are observed between the retrieved values (using different GRASP schemes) or between the day and night retrievals. Retrieved RRI values agree with those reported in previous studies. In fact, using AERONET data, Dubovik et al. [2002a] reported a mean RRI value of 1.48 ± 0.05 for desert dust at Cape Verde (Republic of Cabo Verde). Also, using GRASP algorithm, Tsekeri et al. [2017] obtained an RRI value of 1.45 for a desert dust event at Finokalia (Crete). Nevertheless, the RRI values obtained here are lower than that (RRI of 1.53 for the visible spectral region) used for desert dust by several models [Shettle and Fenn, 1979, WMO, 1983, Koepke et al., 1997]. However, the differences between RRI values obtained here for desert dust event and those reported in literature can be explained by the differences in the chemical composition of dust [e.g., Patterson et al. 1977; Carlson and Benjamin, 1980, Sokolik et al., 1993, Sokolik and Toon, 1999].

Table 6.4. The average values (± standard deviation) of the imaginary refractive indices (IRI) retrieved by GRASP (D, N0 and N2; both fine and coarse modes) and AERONET (for whole aerosol population) during 18th-21st July 2016.

IRI ($x10^{-3}$)							
	GRASP						AERONET
	Fine			Coarse			
λ [nm]	D	N0	N2	D	N0	N2	
355	2.8 ± 0.4	3.2 ± 0.2	3.1 ± 0.1	10 ± 4	8 ± 5	12 ± 6	
440	2.8 ± 0.4	3.2 ± 0.2	3.1 ± 0.1	5.5 ± 2.0	5.0 ± 2.0	9 ± 3	5.2 ± 2.6
532	2.8 ± 0.4	3.2 ± 0.2	3.1 ± 0.1	3.4 ± 1.1	3.5 ± 1.1	6.1 ± 1.6	
675	2.8 ± 0.4	3.2 ± 0.2	3.1 ± 0.1	2.0 ± 0.6	2.2 ± 0.5	3.4 ± 0.8	1.5 ± 0.8
870	2.8 ± 0.4	3.2 ± 0.2	3.1 ± 0.1	1.2 ± 0.4	1.5 ± 0.4	2.5 ± 0.7	1.2 ± 0.6
1020	2.8 ± 0.4	3.2 ± 0.2	3.1 ± 0.1	0.9 ± 0.4	1.2 ± 0.4	2.2 ± 0.4	1.2 ± 0.6
1064	2.8 ± 0.4	3.2 ± 0.2	3.1 ± 0.1	0.8 ± 0.3	1.2 ± 0.4	2.1 ± 0.4	

For IRI, consistency during the whole analyzed period is observed again with smooth variations in the retrieved values. For fine mode, IRI values retrieved by GRASP (using different schemes) show neutral spectral dependence with wavelength and the differences between the three schemes (D, N0 and N2) are very small with mean difference values around 0.003. On the other hand, the spectral behavior of IRI retrieved by GRASP for coarse mode was similar to that of AERONET retrievals, showing a typical IRI spectral dependence of desert dust, characterized by higher IRI in the UV region [Patterson et al., 1977; Dubovik et al., 2002a; Wagner et al., 2012]. The mean IRI values retrieved using D and N0 schemes for coarse mode are almost similar to AERONET retrievals being the differences within the uncertainties (about 50%) associated with IRI provided by AERONET [Dubovik et al., 2000]. Although the discrepancy between IRI values retrieved using N2 scheme for coarse mode and those provided by AERONET is high, the IRI values of N2 scheme are consistent with IRI values around 0.008 at 675 nm obtained at night-time during a dust event in Dakar (Senegal) by Bovchaliuk et al. [2016].

Considering the success in this issue for daytime IRI retrievals, it can be concluded that accurate sky measurements combined with lidar measurements are required for accurately characterizing CRI, and particularly for separating the features of coarse and fine modes as discussed by Dubovik et al. [2000]. The approach proposed using additional relative radiance in the lunar aureole is also promising for the retrievals of IRI.

6.3.3. Columnar single-scattering albedo

Table 6.5 shows the average values of SSA and their corresponding standard deviations obtained by GRASP (using different schemes) and AERONET during entire dust event from 18th to 21st July 2016. As in the case of IRI and RRI retrievals, SSAs retrieved by both GRASP (using different schemes) and AERONET show very small temporal variation during the whole analyzed period, as confirmed by the low standard deviations of the SSAs values.

SSA retrieved by GRASP (using different schemes) and AERONET show a smooth variability between day and night for the total period. Actually, mean differences in SSAs retrieved by GRASP (using different schemes) and AERONET are below 0.03 which it is within uncertainty associated to AERONET retrieval for dust aerosol [Dubovik et al., 2000]. Also, SSAs retrieved by GRASP and AERONET present a common and remarkable spectral variability with SSA increasing from values around 0.85 at the UV to values around 0.99 in the near-infrared. Such SSA values and spectral dependence with wavelength is typically found in pure desert dust [Dubovik et al., 2002a; Valenzuela et al., 2012a].

Table 6.5. The average values (± standard deviation) of single-scattering albedo (SSA) retrieved by GRASP (using D, N0 and N2 schemes) and AERONET for the period 18th - 21st July 2016 (* 469 nm for N2 scheme).

	SSA				
	GRASP				AERONET
λ [nm]	D	N0	N1	N2	
355	0.85 ± 0.02	0.85 ± 0.03	0.83 ± 0.02	0.82 ± 0.05	
440*	0.89 ± 0.02	0.88 ± 0.02	0.88 ± 0.02	0.86 ± 0.03	0.89 ± 0.03
532	0.93 ± 0.01	0.92 ± 0.02	0.92 ± 0.01	0.89 ± 0.02	
675	0.96 ± 0.01	0.95 ± 0.01	0.96 ± 0.01	0.94 ± 0.01	0.97 ± 0.03
870	0.98 ± 0.01	0.97 ± 0.01	0.98 ± 0.01	0.96 ± 0.01	0.98 ± 0.03
1020	0.98 ± 0.01	0.98 ± 0.01	0.98 ± 0.01	0.97 ± 0.01	0.98 ± 0.03
1064	0.99 ± 0.01	0.98 ± 0.01	0.98 ± 0.01	0.97 ± 0.01	

6.4. Evaluation of vertical aerosol properties retrieved by GRASP

6.4.1. Aerosol extinction profiles at night-time

As commented in subsection 3.2.1.1, the multiwavelength lidar system used in this thesis has two channels that detect Raman scattering at 387 and 607 nm and thus Raman method was used here to independently obtain the extinction coefficient at 355 and 532 nm. An estimate of the extinction profile at 1064 nm is computed using the backscatter coefficient retrieved using the Klett-Fernald method with a constant LR for the entire profile of 50 sr; which is a representative value of desert dust [Guerrero-Rascado et al., 2009]. Because Raman measurements of this lidar system are noisy, the lidar signal is averaged ± 15 min around the GRASP retrieval time to get a high signal-to-noise ratio. Moreover, as commented in subsection 4.2.2.3, GRASP is currently optimized to provide aerosol vertical-properties at 60 levels altitude logarithmically spaced. However, Raman lidar profiles are obtained with a vertical resolution of 7.5 m after smoothing. Hence, the comparison presented

hereafter is made between the GRASP values and the Raman values obtained at the closest GRASP heights.

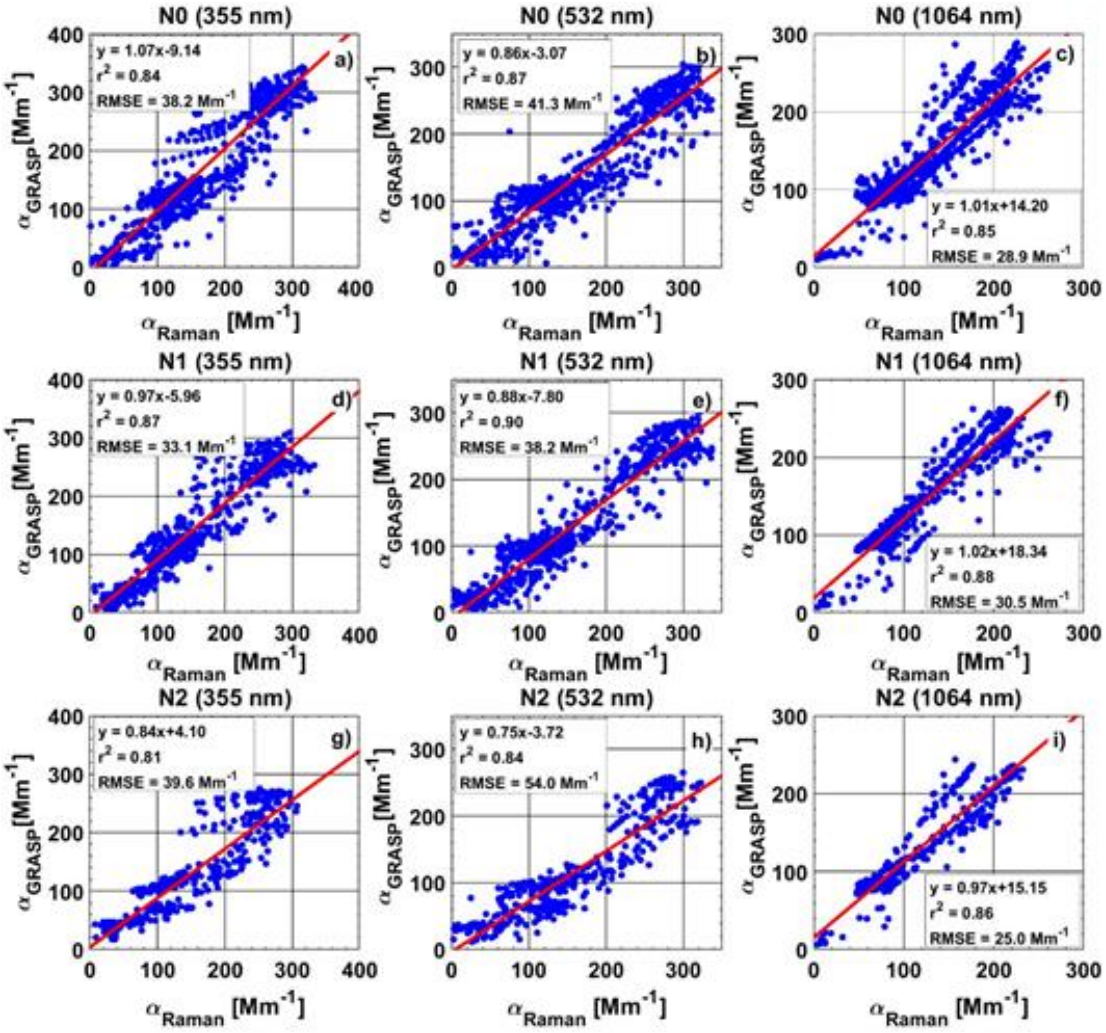

Figure 6.5. Aerosol extinction coefficient (α) retrieved by GRASP for N0 (**a, b and c**), N1 (**d, e and f**) and N2 (**g, h and i**) as a function of the α calculated by Raman technique at 355 (**a, d and g**) and 532 nm (**b, e and h**) and Klett-Fernald method at 1064 nm (**c, f and i**) during dust event observed over Granada during 18th-21st July 2016.

Figure 6.5 shows extinction coefficients at 355, 532 and 1064 nm retrieved by GRASP (N0, N1 and N2 schemes) at night-time versus the values obtained by multiwavelength Raman lidar measurements during dust event observed over

Granada in the period 18th - 21st July 2016. For all schemes and all wavelengths, extinction coefficients retrieved by GRASP and those obtained by Raman lidar measurements are highly correlated with a correlation coefficient (r^2) ranging from 0.8 to 0.9. The slopes of the regression lines varied between 0.75 and 1.07, indicating that in general GRASP underestimate the extinction coefficient obtained by Raman and Klett-Fernald methods. A statistical overview of the differences between GRASP retrievals and Raman measurements of extinction coefficient is given in Table 6.6. Particularly, mean differences given by $\Delta\alpha = \alpha_{GRASP} - \alpha_{Raman}$ and also relative absolute differences given by $\Delta\alpha(\%) = 100 \cdot |\alpha_{GRASP} - \alpha_{Raman}|/\alpha_{Raman}$ are shown. Error bars are the standard deviations of the statistics.

Table 6.6. Differences (± standard deviation) between the extinction values retrieved by GRASP (N0, N1 and N2 schemes) and Raman during dust event observed over Granada from 18th to 21st July 2016. The percentage differences are between parenthesis.

$\Delta\alpha(\lambda)$ [Mm^{-1}]	N0	N1	N2
355 nm	1.3 ± 40 (23%)	-11 ± 31 (23%)	-20 ± 30 (24%)
532 nm	-30 ± 30 (30%)	-30 ± 30 (30%)	-40 ± 40 (40%)
1064 nm	15 ± 24 (21%)	20 ± 23 (24%)	12 ± 22 (20%)

The relative differences at 355 nm between α values retrieved by GRASP and those obtained from Raman lidar measurements are around 23% for the three schemes. The lowest difference at 355 nm between values retrieved by GRASP (using different schemes) and those obtained from Raman lidar measurements is found for N0 scheme (1.3 ± 40 Mm^{-1}), while the highest absolute difference (20 ± 30 Mm^{-1}) is obtained for N2 schemes. However, for 532 nm, the differences between GRASP (using different schemes) and Raman lidar measurements are larger than those encountered at 355 nm and 1064 nm, being the relative differences of 30%, 30% and 40% for N0, N1 and N2 schemes, respectively. In addition, the mean biases are higher in this case, being of -30 ± 30 Mm^{-1}, -30 ± 30 Mm^{-1} and -40 ± 40 Mm^{-1}

for N0, N1 and N2 schemes, respectively. Finally, for 1064 nm the relative differences are between 20% and 24%.

Large part of the differences observed here can be associated to the different hypotheses used in GRASP retrievals being critical the assumption associated with the incomplete overlap region. Also, the rather broad assumption of constant lidar ratio used in the estimation of the extinction at 1064 nm, derived from the backscatter coefficient retrieved by Klett-Fernald retrieval, explains part of the discrepancies at 1064 nm. However, all these differences commented here are similar or lower than those encountered between GRASP retrievals and airborne photometer extinction coefficient measured by PLASMA (see Chapter 5).

6.4.2. Evaluation of GRASP retrievals versus in-situ measurements

Hereafter, $\sigma_{sca}(\lambda)$ and VC retrieved by GRASP are compared versus in-situ measurements obtained at SNS station (2.5 km a.s.l). For these comparisons the averaged values of GRASP retrievals at an altitude of 2.5 ± 0.2 km a.s.l. are used. In addition, in-situ measurements of scattering coefficient obtained by integrating nephelometer at SNS station are averaged ± 15 min around the GRASP retrieval time. Comparisons of σ_{sca} are made at 450, 550 and 700 nm and the Ångström exponent computed from GRASP retrievals is used to get the equivalent σ_{sca} at these wavelengths.

Figure 6.6 shows the temporal evolutions of the σ_{sca} at 550 nm obtained by GRASP (D, N0, N1 and N2 schemes) and integrating nephelometer at SNS station. Generally, both GRASP and in-situ measurements follow the same evolution pattern and are sensitive to the arrival of Saharan dust particles. Furthermore, differences between GRASP (using different schemes) and in-situ measurements are very small, being the differences less than 25 Mm^{-1} in 90% of the cases. Generally, the

differences are negligible for daytime. For night-time, the better agreement is found for the N1 scheme and the less accordance is obtained for the N2 scheme.

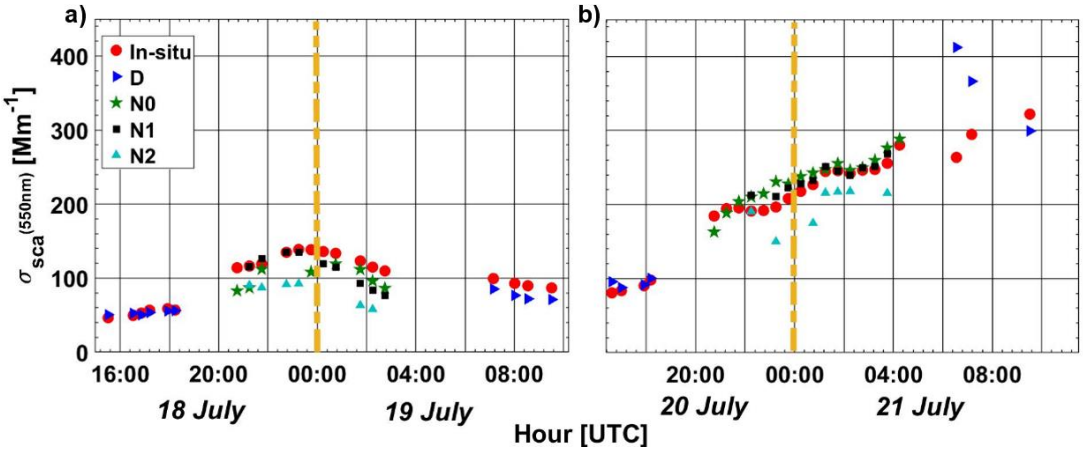

Figure 6.6. Temporal evolutions of σ_{sca} at 550 nm measured by integrating nephelometer at Sierra Nevada Station (red) and retrieved by GRASP (D: blue; N0: green; N1: black; N2: cyan) at 2.5 km a.s.l. from 18th to 19th (**a**) and from 20th to 21st(**b**) July 2016.

Figure 6.7 a, b and c show the scattering coefficients at 450, 550 and 700 nm retrieved by GRASP versus those measured at SNS. As can be seen these figures, the correlation coefficient (r^2) between the measured and the retrieved values is very high with values between 0.87 and 0.97. In general, the slopes of the linear fits indicate that the GRASP overestimates the in-situ scattering coefficient measurements at SNS.

An overview of the statistical analysis of the differences between GRASP retrievals and in-situ scattering coefficient measurements is given in Table 6.7 that shows the mean ($\Delta\sigma_{sca} = \sigma_{sca}^{GRASP} - \sigma_{sca}^{SNS}$) and relative differences $\Delta\sigma_{sca} = 100 \cdot |\sigma_{sca}^{GRASP} - \sigma_{sca}^{SNS}|/\sigma_{sca}^{SNS}$ for each scheme. Due to the drastic change in the scattering coefficient between P1 and P2 periods, this statistical analysis is provided separately for these two periods. For the P1 period, GRASP algorithm underestimates the in-situ scattering coefficient measurements both at day and night and at all wavelengths. The highest differences are found for N2 scheme with differences

between 30% (at 700 nm) and 35% (at 550 nm). However, for the others schemes (D, N0 and N1) the differences are less than 20%. Again, the uncertainties associated with IRI and with the incomplete overlap assumption as well as the particles losses in sampling inlet can be behind these differences. However, for P2 period, the differences are considerably small and even in some cases are one half than the differences observed in P1 period.

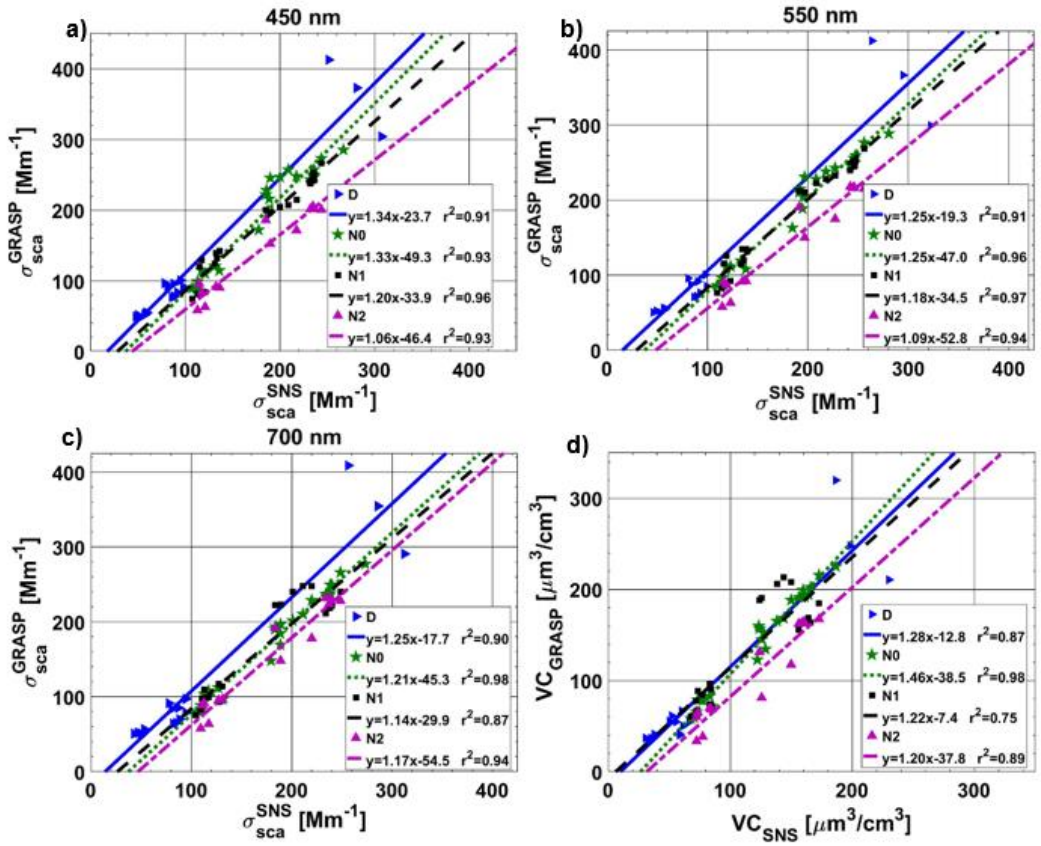

Figure 6.7. Scattering coefficient, σ_{sca}, at 450, 550 and 700 nm **(a, b, c)** and volume concentration, VC, **(d)** retrieved by GRASP (D: blue; N0: green; N1: black; N2: purple) at SNS station height versus in-situ scattering coefficient and volume concentration measurements at SNS during dust event over Granada in the period 18th-21st July 2016.

Table 6.7. Differences (± standard deviation) between the scattering values retrieved by GRASP (N0, N1 and N2 schemes) and in-situ measurements at SNS.

$\Delta\sigma_{sca}$ [Mm^{-1}]	λ [nm]	D	N0	N1	N2
P1	450	-5 ± 4 (8%)	-17 ± 10 (14%)	-9 ± 19 (13%)	-40 ± 14 (30%)
	550	-7 ± 8 (10%)	-20 ± 9 (17%)	-14 ± 15 (13%)	-43 ± 13 (40%)
	700	-5 ± 11 (12%)	-21 ± 9 (19%)	-21 ± 11 (17%)	-36 ± 14 (30%)
P2	450	40 ± 60 (21%)	26 ± 17 (13%)	9 ± 8 (5%)	-31 ± 16 (14%)
	550	30 ± 60 (16%)	11 ± 13 (7%)	8 ± 7 (4%)	-32 ± 17 (13%)
	700	30 ± 60 (16%)	1.3 ± 12 (4%)	6 ± 30 (12%)	-17 ± 19 (9%)

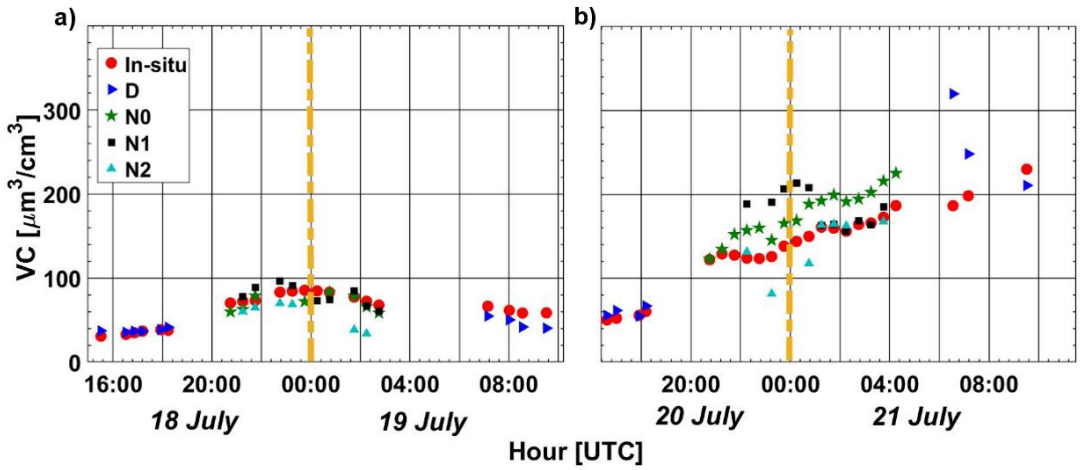

Figure 6.8. Temporal evolution of VC measured in-situ at Sierra Nevada Station (red) and the values retrieved by GRASP (D: blue; N0: green; N1: black; N2: cyan) at 2.5 km a.s.l. from 18th to 19th (**a**) and from 20th to 21st(**b**) July 2016.

On the other hand, Figure 6.8 shows the temporal evolutions of the VC retrieved by GRASP at 2500 m a.s.l. and those measured at SNS station. As for the scattering coefficient, the VC retrieved by GRASP and the measured at SNS follow the same evolution pattern both being sensitive to the increase of dust event intensity. Differences at daytime are negligible, while at night-time the differences

depend on the GRASP scheme used, being the differences in the P1 period much smaller than in P2 period indicating that the differences increase with increasing aerosol load. Figure 6.7d shows the VC values retrieved by GRASP (using different schemes) versus those measured at SNS station. The correlation between the measured and the retrieved values is very high with r^2 between 0.75 and 0.98. As in the case of the scattering coefficient, the slopes of the linear fits generally indicate an overestimation by GRASP.

Table 6.8 presents an overview of the statistical analysis of the VC comparisons. Particularly, in the table mean $\Delta VC = VC_{GRASP} - VC_{SNS}$ and absolute relative differences $\Delta VC(\%) = 100 \cdot |VC_{GRASP} - VC_{SNS}|/VC_{SNS}$ are shown. It is clearly observed that GRASP overestimates the measured values low than 15% for D, N0 and N1 schemes during P1 period, while for N2 scheme is observed an underestimation of 30%. However, for P2 period, the GRASP underestimates the in-situ measurements with differences around 20% for D, N0 and N1 schemes; while for N2 scheme, GRASP overestimates the in-situ measurements again but with lower differences than P1 period. Again, the different assumption in GRASP algorithm and the particles losses in sampling inlet (which increase with increasing aerosol load) can be behind the observed differences between GRASP retrievals and in-situ measurements.

Table 6.8. Differences (± standard deviation) between the volume concentration values retrieved by GRASP (N0, N1 and N2 schemes) and in-situ measurements at SNS.

ΔVC [µm³/cm³]	**D**	**N0**	**N1**	**N2**
P1	-4 ± 9 (14%)	-5 ± 7 (9%)	1.6 ± 10 (12%)	-21 ± 14 (30%)
P2	30 ± 50 (20%)	29 ± 12 (20%)	31 ± 32 (23%)	-9 ± 21 (10%)

6.5. Conclusions

The use of GRASP algorithm to retrieve vertical profiles and column-integrated optical and microphysical aerosol properties at night-time combining elastic lidar measurements with different passive remote sensing measurements has been explored.

The experimental measurements used were acquired during a Saharan dust event that took place during SLOPE I campaign at Granada (Spain) from 18th to 21st July 2016. This event was an extraordinary dust event because the aerosol load registered doubled the typical values registered during ordinary Saharan dust events that reach the study area. Moreover, during the dust event the aerosol extensive properties were more or less stable – e.g. Ångström exponent value which was around 0.2, points out that the coarse particles dominates in the atmosphere. That allows to evaluate GRASP retrievals using continuous measurements of multiwavelength lidar, sun/sky/lunar photometer during day- and night-time and sky camera images.

For column-integrated aerosol optical and microphysical AERONET inversion products were used as reference to evaluate the robustness of GRASP retrievals. Daytime GRASP retrievals used the same inputs as AERONET and also additionally elastic lidar signals. Consequently, GRASP retrieve a bi-modal size distribution with the capacity of separating aerosol CRI between fine and coarse mode. Comparisons of PSD between AERONET and GRASP retrievals do not show significant discrepancies in radii, widths and volume concentration for each mode. Slight differences are explained because the use of additional information about aerosol vertical distribution in GRASP. Retrieved RRI by AERONET and GRASP are quite similar, with no spectral dependences, being the values obtained typical for Saharan dust outbreaks. Comparisons between AERONET and GRASP for IRI remarked that AERONET values are very similar to the obtained by GRASP for

coarse mode, being identified the typical spectral dependence associate to dust particles with increasing absorption in the UV. Similar results were found for SSA. Thus, the results obtained verify the coherence of GRASP retrievals and show the potentiality to retrieve fine and coarse mode properties.

AERONET inversion products were also used to study the coherence of night-time retrievals and of the continuous day-to-night aerosol evolution when the combination of active and passive remote sensing is used at night-time. For the parameters derived from PSD, GRASP retrievals show coherent values when compared with AERONET retrievals, being observed a smooth and coherent day-to-night evolution. Similarly happens for CRI and SSA, although more variability is observed, particularly for the N2 scheme due to the large uncertainties in relative sky radiance measurements at lunar aureole and the higher freedom degrees assumed than in N1 scheme. Spectral dependencies in IRI and SSA agree again with typical values for mineral dust from Western Sahara measured at Granada in previous studies [Olmo et al., 2006; Valenzuela et al., 2014].

Generally, GRASP and Raman retrieved values agrees quite well, with differences below 30%. Nevertheless, these imply that some issues remain: The way of how the incomplete overlap area is analyzed in GRASP can yield to some incorrect values. Also, the uncertainties in IRI are behind these differences. But with the experimental data used here the study can not go further because a-priori aerosol optical and microphysical properties are not known. Additional studies are needed in this sense to investigate the accuracy of GRASP retrievals, particularly these with synthetic data from global models.

SLOPE I field campaign provided a unique opportunity of evaluating high-altitude GRASP retrievals versus in-situ measurements thanks to the correlative in-situ measurements at SNS station (2500 m a.s.l). Here, the evaluation of aerosol scattering coefficient and volume concentrations retrieved by GRASP is performed.

Generally, both GRASP retrievals and in-situ measurements follow the same patterns and are sensitive to the arrival of Saharan dust particles. Differences between GRASP and in-situ measurements are negligible for daytime. For night-time, however, some differences were observed. It is remarkable that no homogeneity was observed between the three night-time scheme, being GRASP retrievals larger for N0 and N1 schemes while the opposite was observed for N2. The use of relative sky radiances from lunar measurements can be behind these differences due to the large uncertainties associated with these lunar measurements [e.g. Román et al., 2017a].

7. Ceilometer and sun/sky photometer retrieval

This chapter is adapted from "Retrieval of aerosol profiles combining sunphotometer and ceilometer measurements in GRASP code" by Román, R., Benavent-Oltra, J. A., Casquero-Vera, J. A., Lopatin, A., Cazorla, A., Lyamani, H., Denjean, C., Fuertes, D., Pérez-Ramírez, D., Torres, B., Toledano, C., Dubovik, O., Cachorro, V. E., de Frutos, A. M., Olmo, F. J., and Alados-Arboledas, L. (2018) Published in Atmospheric Research, 204, 164-177, doi: 10.1016/j.atmosres.2018.01.021.

This chapter presents the sensitivity test performed with synthetic data to verify the capability of the GRASP to derive the aerosol properties from coincident ceilometer and sun/sky photometer observations. This method is applied to real data acquired during the ChArMEx/ADRIMED and SLOPE I campaigns. In the case of ChArMEx/ADRIMED campaign, the profiles of volume concentration are compared with airborne measurements whereas for SLOPE I campaign, the volume concentration values retrieved at 2500 m a.s.l. are compared with in-situ measurements obtained at SNS station.

7.1. Sensitivity test

As commented in the subsection 4.2.2, GRASP has been designed to distinguish the aerosol properties between fine and coarse modes separately in the case where multiple wavelength lidar data are used. In contrast, the use of sun/sky photometer and single wavelength lidar by GRASP can only retrieve the aerosol properties for the total amount of aerosols, since aerosol modes cannot be discerned in the vertical with a single wavelength.

In this chapter it is used the ceilometer which provides RCS profiles at only one single wavelength (1064 nm), therefore, for the retrieval constraining, intensive aerosol properties such as CRI, SSA, or lidar ratio are assumed equal for fine and coarse mode in the retrieval. Column-integrated properties obtained by GRASP using this method are shown in Table 4.2. However, the hypothesis of vertically constant aerosol intensive parameters allows changes in extensive properties and, therefore, vertical profiles of aerosol volume concentration and of extinction, backscatter, absorption and scattering coefficients at 5 wavelengths (440, 675, 870, 1020 and 1064 nm) are provided.

GRASP needs an initial aerosol scenario, also known as initial guess (described at subsection 4.2.2.3), to initialize each retrieval. The initial guess of each parameter has been assumed the same for all retrievals except for the size distribution, which has been assumed as a trapezoidal distribution proportional to the measured AOD at 440 nm wavelength. The minimum and maximum altitudes in the used RCS signal are 250 and 7000 m a.g.l..

7.1.1. Synthetic data

A sensitivity study with synthetic data is done in order to observe the capability of the GRASP to retrieve aerosol properties combining ceilometer and sun/sky photometer data. To this end, two kinds of aerosol are considered: Smoke and Dust, including different mixtures among them. Smoke and Dust typical PSD and CRI values are assumed the shown by Dubovik et al. [2002] for biomass burning in the African savanna (Zambia) and for desert dust at the Arabian Peninsula (Saudi Arabia), respectively. Figure 7.1 shows the typical PSD for these two aerosol types (Figure 7.1a) and their vertical distribution (Figure 7.1b), RRI (Figure 7.1c), and IRI (Figure 7.1d) according to values reported in the bibliography.

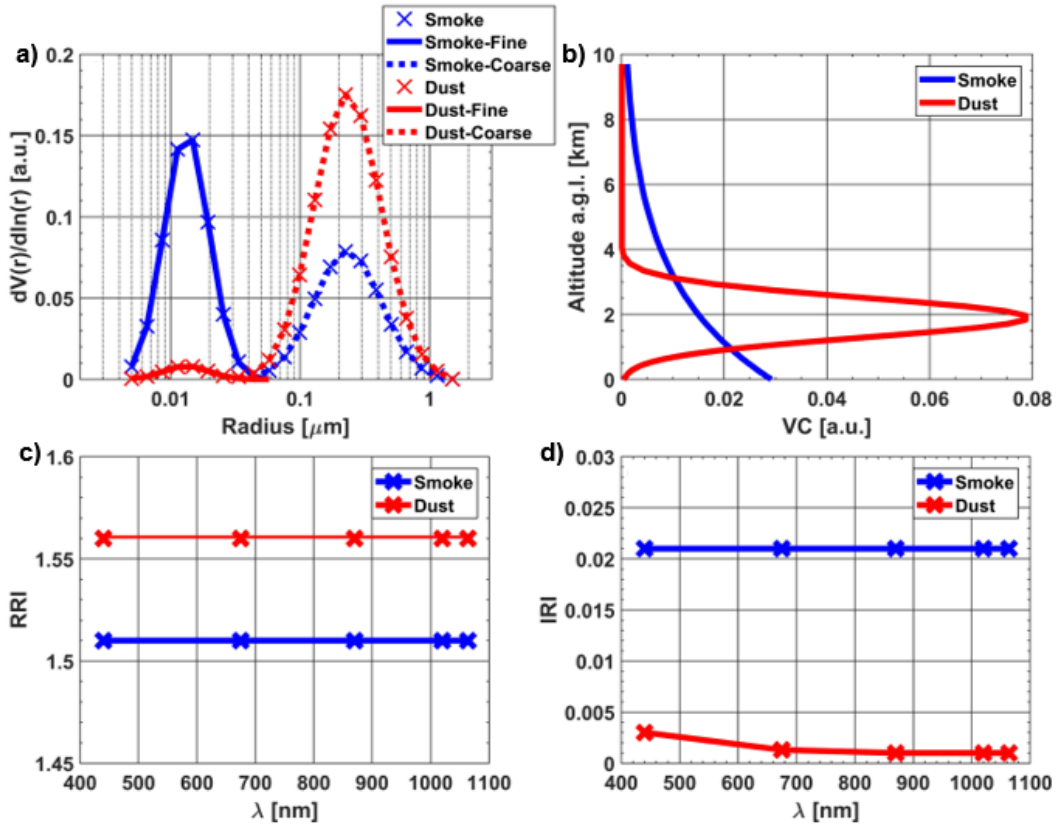

Figure 7.1. Microphysical and optical properties of the two aerosol models (Smoke and Dust) used to obtain synthetic data: particle size distribution (**a**); vertical volume concentration, VC, (**b**); real (**c**) and imaginary (**d**) refractive indices, RRI and IRI, respectively.

The PSD for each aerosol type (Figure 7.1a) is assumed as triangle binned and bimodal distribution: the fine mode is log-spaced in 10 radius bins (radius from 0.05 µm to 0.58 µm) and the coarse mode log-spaced in 15 bins (radius from 0.33 µm to 15 µm). Fine mode is predominant in Smoke aerosol with residual coarse mode, while for Dust the opposite occurs. For each scenario both fine and coarse mode have the same complex refractive indices, RRI being independent on wavelength with values of 1.51 and 1.56 for Smoke and Dust, respectively (Figure 7.1c). The IRI is wavelength independent for Smoke, with a value of 0.021, while for Dust it is assumed variable with wavelength varying from 0.003 at 440 nm to 0.001 at 1064 nm (Figure 7.1d). The vertical aerosol distribution has been assumed

as an exponential decay with altitude for Smoke, while this distribution has been considered as a Gaussian layer centred at 2000 m a.g.l. for Dust (Figure 7.1b).

Different synthetic scenarios are considered consisting to Smoke, Dust and mixtures among them. In the mixtures scenarios are assumed that fine mode has the intensive properties of Smoke while for coarse mode they are those of Dust. Fine mode of PSD is proportional to Smoke while that for coarse mode is proportional to Dust. Two different mixtures are considered, Mix-1 that imposes that AOD_{440} is equal for fine and coarse mode, and Mix-2 that imposes AOD at 1064 nm is equal for both modes. The difference between Mix-1 and Mix-2 is the larger volume concentration of fine particles in Mix-2 than in Mix-1. The PSD and the vertical concentration for these scenarios can be observed in the figures discussed in Section 7.1.2, labeled as "Original" in Figure 7.3 and 7.4, respectively. From all these scenarios, twelve (4 aerosol types x 3 AODs) synthetic data are computed from different AOD_{440} values: 0.1 (low aerosol load), 0.4 (minimum AOD_{440} used by AERONET to provide quality assured SSA, RRI and IRI in version 2 retrievals) and 1.0 (high aerosol load).

The GRASP forward model is used to compute the synthetic observations (spectral AOD, sky radiances and RCS at 1064 nm) for each of the twelve aerosol scenarios, and varying the SZA by 10º from 40º to 80º in order to test different sets of scattering angles. Note that in all simulations the ground is assumed as the sea level and the assumed BDRF parameters for these simulations are the climatological values (explained in subsection 4.2.2.3a) for Granada in summer. Later, using the GRASP forward model the required observations for GRASP are computed: AOD and sky radiances (26 values from 3.5º to 160º azimuth angles) at 440, 675, 870 and 1020 nm and RCS (60 heights) at 1064 nm.

The computed synthetic observations are not representative of real measurements unless instrument uncertainties are considered, which are ±0.01 for

AOD and ±5% for sky radiances according to AERONET standards [Holben et al., 1998]. Therefore, next step in the simulation scheme is to add uncertainties to the simulated AOD and sky radiances, which is done by adding random errors generated from random number that follows a normal distribution with standard deviation equal to the uncertainties. The addition of noise to the simulated ceilometer values is done assuming a constant uncertainty (K) on raw ceilometer signal and, therefore, the RCS uncertainty σ varies with the square of the distance (h) and at a level ' h' is given as:

$$(RCS_h) = K \cdot h^2 \qquad \text{Eq. 7.1}$$

where is the range corrected signal at h.

The calibration constant for Granada ceilometer obtained by Cazorla et al. [2017] for molecular (aerosol free) regions presents variations with standard deviation of approximately 30% (result not published). Thus, the uncertainty of ceilometer RCS could be assumed as a 30% at the reference height (h_{ref}) where only molecular backscatter is detected. Then the uncertainty of RCS at h_{ref} can be written as:

$$\sigma\left(RCS_{h=h_{ref}}\right) = 0.3 \cdot RCS_{h=h_{ref}} \qquad \text{Eq. 7.2}$$

and combining Equation 7.1 and Equation 7.2:

$$K = \frac{0.3}{{h_{ref}}^2} \cdot RCS_{h=h_{ref}} \qquad \text{Eq. 7.3}$$

Finally, if Equation 7.3 is put in Equation 7.1, the uncertainty of RCS at each height can be expressed as:

$$\sigma(RCS_z) = \frac{0.3}{h_{ref}^2} \cdot RCS_{h=h_{ref}} \cdot h^2 \qquad \text{Eq. 7.4}$$

The most frequent value of h_{ref} obtained by the method used in Cazorla et al. [2017] is about 4000 m a.g.l.; therefore, in this work, the uncertainty of ceilometer RCS is calculated by Equation 7.4 using 4000 m as h_{ref}. Once RCS uncertainty has been characterized, synthetic RCS is interpolated every 15 m, and for each RCS value at 15 m at each scenario, a pseudorandom number normally distributed is generated with a standard deviation equal to the uncertainty of this RCS value, and this random number is added to the previously simulated RCS.

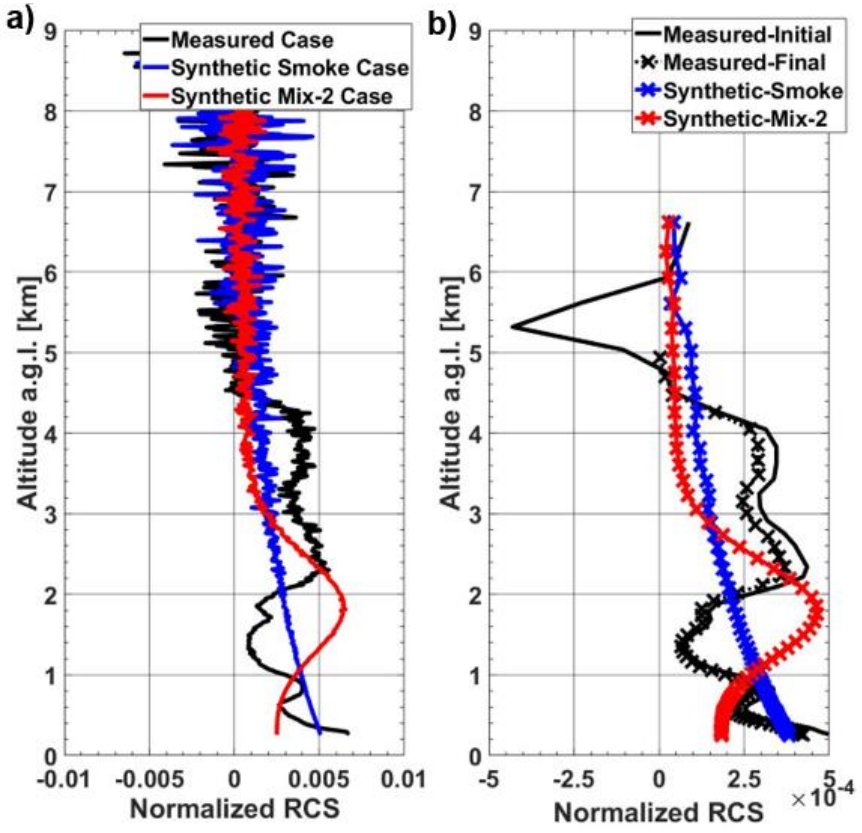

Figure 7.2. Range corrected signals (RCS) at 1064 nm, from 250 m to 9000 m every 15 m, normalized by the sum of all data (**a**) for three cases: half hour average of measured ceilometer signal on 17 June 2013, 07:40 UTC (AOD_{440}~0.21) (black line); synthetic and noisy signal of Smoke with AOD_{440} equal to 0.4 (blue line); and synthetic and noisy signal of "Mix-2" with AOD_{440} equal to 0.4 (red line). Panel **b** shows the RCS of panel **a**, but normalized to 60 log-spaced points following the criteria used for GRASP.

As an example, Figure 7.2 shows the synthetic RCS after adding uncertainties for the Smoke and Mix-2 scenarios with AOD_{440} equal to 0.4. In addition, a particular example of measured RCS in UGR station (dust case with AOD_{440} = 0.21) is included to illustrate the capabilities of the scheme to generate synthetic RCS with uncertainties. An iterative method to skip negative values in the measured RCS is applied to the initial values (Measured-Initial), that iteratively computes the 60 RCS log-spaced points decreasing 100 m the maximum altitude until all 60 values are positive, and it is observed as the final signal avoids negative values (Measured-Final). As can be observed the profiles look noisier at higher heights both for the synthetic and measured profiles. In fact, the shape of the added noise to the synthetic profiles is very similar to the one observed in the real measurements, which indicates that the obtained synthetic signal can be considered as realistic. The noise is higher for Smoke likely because for this scenario molecular zone is not completely well represented by the assumed h_{ref} equal to 4000 m a.g.l. Figure 7.2b shows the RCS of Figure 7.2a normalized to the 60 heights required as input in GRASP. It can be appreciated that noise is reduced by the averaging of RCS in log-scaled bins.

7.1.2. Analyses of retrieved parameters

Once the noisy synthetic observations are obtained for each aerosol scenario and SZA value, these data are used as input in GRASP. The differences, Δ_{fit}, between the synthetic observations used as input in GRASP and the observations generated by the retrieved aerosol scenario are calculated to quantify the fitness of each GRASP retrieval. Δ_{fit} is defined as:

$$\Delta_{fit}(k,n) = O_r(k,n) - O_i(k,n) \qquad \text{Eq. 7.5}$$

and in percentage as:

$$\Delta_{fit}(k,n)(\%) = 100 \cdot \frac{O_r(k,n) - O_i(k,n)}{O_i(k,n)} \qquad \text{Eq. 7.6}$$

where *O* represents an observation; the subscript *i* and *r* indicated if the observation is an input or a value obtained from the retrieved aerosol scenario, respectively; *k* determines the kind of observation (AOD, sky radiances or RCS) and *n* is the number of this kind of observation. The fitness of the retrieval can be quantified for each *k*-kind observation by the mean (MBE; mean bias error) and standard deviation (STD) of Δ_{fit} using all *n* available observations for the *k*-kind. MBE represents the accuracy between O_r and O_i, while STD indicates their precision. Following this method, MBE and STD for AOD (subscript *aod*), sky radiance (subscript *rad*) and RCS (subscript *rcs*) are calculated for all retrievals and they are shown in Table 7.1. MBE_{aod} and STD_{aod} are shown in absolute values while MBE and STD for sky radiance and RCS are in percentage. Scattering angle interval is also added in Table 7.1, reaching bigger angles when SZA increases. Table 7.1 reveals that MBE_{aod}, MBE_{rcs}, STD_{aod}, and STD_{rcs} are usually larger for retrievals with AOD_{440}=0.1; MBE_{rad} is usually within ±1% and STD_{rad} around 3%. In general, the fitness estimation does not show a clear dependence on aerosol type, SZA or AOD, which could indicate that differences in these values for different cases are mainly caused by the noise in the synthetic measurements since it is random.

Several aerosol GRASP products are obtained for each retrieval, but this work is mainly focus on columnar particle size distribution and especially on aerosol VC profiles. Figure 7.3 shows, for different aerosol types and loads, all the retrieved size distributions for various SZA values. It reminds that errors were added to input optical data. The original particle size distributions are also included. In general, the retrieved particle size distributions look qualitatively similar to the original ones, especially for the coarse mode, for all aerosol scenarios. Discrepancies on fine mode are more evident especially at low AODs. Worse agreement is expected for small SZA values since the scattering angle range is shorter, however it is not observed.

Table 7. 1. Mean bias error (MBE) of the GRASP retrievals of AOD, sky radiance, and lidar range-corrected signal under different aerosol scenarios. Standard deviation (STD) is in parenthesis.

Aerosol Type*	SZA (º)	Scattering Angle Range (º)	AOD_{440} = 0.1			AOD_{440} = 0.4			AOD_{440} = 1.0		
			MBE_{aod} (x1000)	MBE_{rad} (%)	MBE_{rcs} (%)	MBE_{aod} (x1000)	MBE_{rad} (%)	MBE_{rcs} (%)	MBE_{aod} (x1000)	MBE_{rad} (%)	MBE_{rcs} (%)
Smoke	40	2.3-78.6	5.3 (8.2)	-0.5 (3.0)	0.0 (1.3)	1.8 (3.0)	-0.1 (3.1)	0.2 (4.7)	-0.3 (0.4)	-0.2 (2.8)	0.1 (1.3)
	50	2.7-98.0	16.7 (19.7)	-0.3 (2.7)	0.4 (5.3)	-1.5 (3.0)	0.2 (2.9)	0.0 (0.4)	1.0 (1.5)	-0.5 (3.8)	0.2 (2.3)
	60	3.0-117.1	0.5 (0.7)	-0.1 (3.1)	0.1 (3.1)	0.4 (0.4)	-0.1 (2.8)	0.1 (1.6)	13.5 (17.4)	-1.7 (3.6)	-0.1 (2.7)
	70	3.3-135.5	3.8 (5.8)	-0.6 (3.0)	0.0 (2.0)	-1.1 (2.0)	-0.5 (3.6)	0.2 (3.4)	0.4 (0.2)	-0.1 (3.2)	0.1 (0.9)
	80	3.5-151.8	2.6 (3.7)	-0.6 (2.8)	0.1 (2.3)	1.7 (3.5)	-1.3 (3.0)	0.2 (0.7)	-0.1 (0.8)	-0.3 (3.3)	0.2 (2.5)
Dust	40	2.3-78.6	16.7 (30.4)	-2.9 (4.0)	7.2 (14.7)	-5.5 (8.6)	-1.1 (2.9)	0.5 (4.1)	9.4 (7.7)	-3.2 (4.0)	0.3 (2.6)
	50	2.7-98.0	3.2 (4.2)	-0.8 (3.0)	1.9 (5.4)	-5.1 (7.4)	0.8 (4.4)	0.1 (4.2)	11.6 (11.3)	1.5 (4.5)	1.3 (4.8)
	60	3.0-117.1	16.5 (31.3)	-0.2 (3.2)	0.7 (5.0)	-2.9 (4.7)	0.0 (3.3)	0.0 (2.3)	-3.0 (4.9)	1.1 (4.0)	0.5 (1.9)
	70	3.3-135.5	7.5 (14.3)	-0.6 (3.0)	0.3 (3.7)	-3.7 (6.5)	0.7 (3.4)	0.0 (1.7)	8.7 (6.2)	0.3 (3.6)	0.2 (2.9)
	80	3.5-151.8	-4.0 (7.5)	0.7 (3.2)	0.3 (1.1)	7.6 (10.3)	-0.3 (2.7)	0.2 (2.0)	3.6 (4.0)	0.2 (3.4)	0.2 (1.9)
Mix-1	40	2.3-78.6	4.1 (6.3)	-0.5 (2.8)	0.9 (3.1)	-3.0 (4.0)	-0.5 (3.4)	0.4 (1.7)	-5.9 (10.4)	0.1 (2.9)	-0.2 (1.9)
	50	2.7-98.0	-7.6 (13.5)	0.1 (3.6)	0.9 (2.3)	11.2 (16.7)	0.1 (3.3)	0.3 (6.8)	-0.4 (0.8)	0.2 (3.6)	-0.1 (2.8)
	60	3.0-117.1	-5.6 (7.6)	2.4 (5.6)	8.4 (11.8)	-2.1 (4.5)	2.3 (7.0)	0.0 (2.0)	-1.0 (1.3)	0.6 (3.1)	-0.2 (1.5)
	70	3.3-135.5	-2.8 (4.3)	0.4 (3.4)	1.2 (4.1)	-8.4 (16.4)	2.1 (4.7)	0.6 (2.7)	1.9 (3.0)	0.5 (3.4)	0.1 (1.1)
	80	3.5-151.8	-2.8 (8.0)	6.4 (8.0)	8.1 (11.1)	-2.2 (3.0)	1.7 (3.8)	-0.2 (1.6)	9.3 (12.5)	1.5 (4.6)	0.4 (3.9)
Mix-2	40	2.3-78.6	-3.3 (6.7)	-1.8 (3.5)	1.4 (5.1)	2.4 (3.7)	1.3 (5.1)	0.8 (8.3)	-0.1 (0.2)	-0.2 (3.3)	0.0 (1.1)
	50	2.7-98.0	-3.8 (6.0)	-2.0 (3.2)	1.1 (6.0)	0.7 (1.1)	-0.4 (3.1)	0.1 (2.0)	0.4 (1.2)	0.0 (2.9)	0.1 (5.4)
	60	3.0-117.1	1.1 (2.5)	-0.2 (3.4)	0.6 (3.6)	1.6 (2.6)	1.4 (4.9)	0.4 (3.2)	0.0 (0.4)	1.0 (3.5)	0.0 (0.9)
	70	3.3-135.5	1.9 (4.9)	-3.5 (4.4)	2.1 (9.7)	-0.4 (1.0)	-0.1 (2.6)	0.0 (1.0)	-0.8 (0.5)	0.1 (3.3)	0.0 (0.3)
	80	3.5-151.8	-0.7 (0.9)	-0.1 (2.5)	0.1 (2.6)	0.0 (1.1)	0.0 (3.5)	0.1 (1.4)	0.1 (0.1)	0.1 (2.4)	0.0 (1.4)

The differences between the original and retrieved size distributions are mostly related with Δ_{fit}. For example, the retrieved size distribution for Mix-1 type with AOD_{440}=0.4 differs more from the original at SZA equal to 60º than for the other angles; it should be caused by a worse fit between the inputs and the retrieved observations as it can be observed in Table 7.1, where MBE_{rad} and STD_{rad} reach their highest values (2.3% and 7.0%, respectively) for all retrievals with

AOD_{440}=0.4. It can also be appreciated in the Mix-1 type with AOD_{440}=1.0 and SZA of 80º.

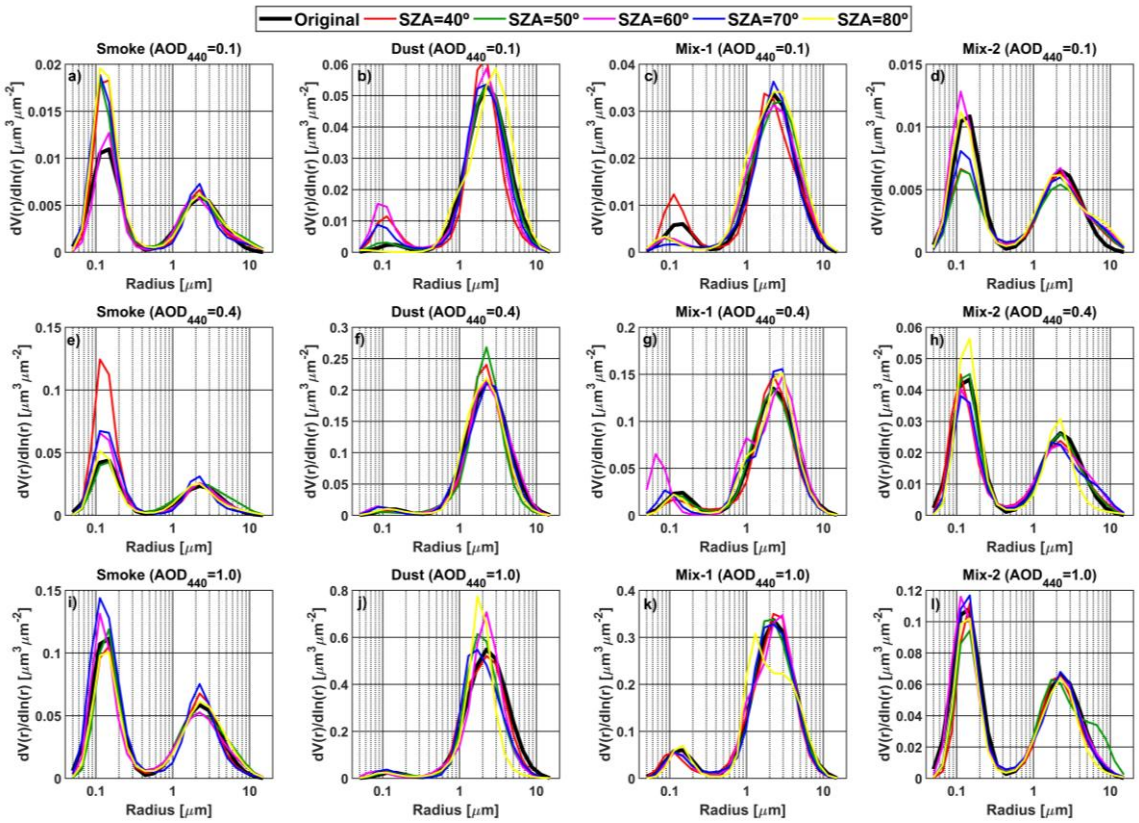

Figure 7.3. Original aerosol size distribution as retrieved by GRASP for different aerosol types (Smoke, Dust, Mix-1 and Mix-2) and loads (AOD440=0.1, 0.4 and 1.0), and at different solar zenith angles from 40° to 80°.

Figure 7.4 shows the VC profiles for the same data than in Figure 7.3. These profiles show a good agreement with the original ones when coarse mode predominates as can be observed for Dust and Mix-1 cases. The larger differences between retrieved and reference profiles are found for Smoke, being particularly noisy for heights above 2 km. This worse agreement for Smoke could be due to the use of RCS at 1064 nm, this wavelength being less sensitive to the fine particles like those prevailing in Smoke. The original Mix-2 profiles present two intense aerosol layers: dust around 2 km and smoke below 1 km; GRASP is able to detect both

aerosol layers, although it shows discrepancies compared with the reference. This can be explained by the limited information of using RCS at only one wavelength.

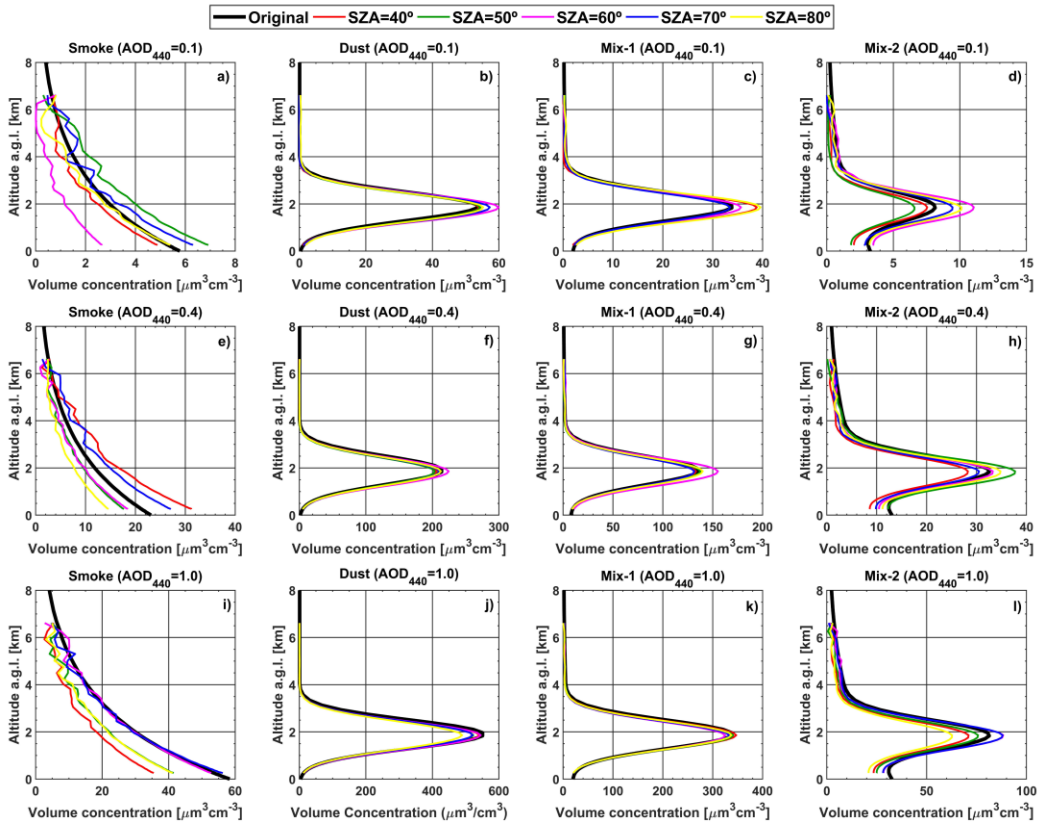

Figure 7.4. Original aerosol volume concentration vertical profile as retrieved by GRASP for different aerosol types (Smoke, Dust, Mix-1 and Mix-2) and loads (AOD_{440}=0.1, 0.4 and 1.0), and at different solar zenith angles from 40° to 80°.

Table 7.2. MBE and STD from the differences between the VC retrieved by GRASP and the original under different aerosol scenarios and SZA values. Original VC values below 1 $\mu m^3/cm^3$ have not been taken into account in the calculations. MBE and STD are given in % in parenthesis.

Aerosol Type*	SZA (°)	$AOD_{440} = 0.1$		$AOD_{440} = 0.4$		$AOD_{440} = 1.0$		All	
		MBE [$\mu m^3/cm^3$]	STD [$\mu m^3/cm^3$]	MBE [$\mu m^3/cm^3$]	STD [$\mu m^3/cm^3$]	MBE [$\mu m^3/cm^3$]	STD [$\mu m^3/cm^3$]	MBE [$\mu m^3/cm^3$]	STD [$\mu m^3/cm^3$]
Smoke	40	-0.5 (-15.5)	0.1 (8.4)	6.0 (39.2)	3.2 (17.1)	-12.7 (-38.2)	4.8 (6.5)	-2.5 (-4.5)	8.5 (35.0)
	50	1.2 (33.6)	0.3 (5.9)	-2.5 (-18.6)	1.0 (5.7)	-8.7 (-26.4)	3.2 (6.9)	-3.5 (-4.9)	4.5 (27.1)
	60	-2.0 (-57.9)	0.5 (9.4)	-2.2 (-18.7)	0.7 (11.0)	-0.5 (-1.8)	0.8 (9.0)	-1.6 (-25.2)	1.0 (25.2)
	70	0.6 (14.9)	0.3 (9.8)	3.6 (24.8)	1.8 (13.3)	0.6 (-0.7)	1.4 (8.4)	1.6 (12.9)	2.0 (15.1)
	80	-0.1 (-6.1)	0.2 (11.8)	-4.6 (-33.6)	1.8 (5.8)	-8.9 (-27.5)	3.1 (6.9)	-4.7 (-22.9)	4.2 (14.4)
	All	-0.2 (-6.2)	1.1 (32.3)	0.0 (-1.4)	4.4 (30.4)	-6.0 (-18.9)	6.0 (16.8)	-2.1 (-8.9)	5.2 (28.2)
Dust	40	0.3 (-1.5)	1.7 (13.1)	-2.0 (-2.7)	6.7 (12.4)	-3.1 (-1.4)	14.0 (11.3)	-1.6 (-1.9)	9.2 (12.2)
	50	0.5 (3.6)	1.6 (10.6)	-3.1 (-5.2)	7.2 (13.8)	-9.0 (-5.7)	16.2 (11.6)	-4.0 (-2.6)	11.1 (12.7)
	60	2.2 (11.5)	2.7 (10.9)	3.6 (5.4)	6.9 (12.7)	-1.9 (-1.5)	14.3 (12.5)	1.3 (5.0)	9.6 (13.1)
	70	1.3 (5.8)	2.1 (11.0)	-0.5 (2.1)	6.5 (12.1)	-10.1 (-7.2)	15.5 (11.4)	-3.2 (0.1)	11.1 (12.7)
	80	1.1 (15.5)	1.7 (18.2)	-0.3 (-1.0)	5.7 (11.8)	-20.1 (-11.8)	25.0 (10.9)	-6.6 (0.6)	17.8 (17.8)
	All	1.1 (7.0)	2.1 (14.3)	-0.5 (-0.3)	6.9 (13.0)	-8.8 (-5.5)	18.5 (12.1)	-2.8 (0.3)	12.4 (14.1)
Mix-1	40	1.4 (1.8)	2.1 (18.1)	-1.1 (-8.9)	3.4 (14.0)	0.9 (-6.1)	7.1 (13.9)	0.3 (-4.8)	4.9 (15.8)
	50	-0.1 (-1.5)	0.9 (8.2)	0.1 (-6.8)	3.3 (12.5)	-0.7 (-7.0)	7.9 (12.5)	-0.3 (-5.3)	5.1 (11.6)
	60	0.6 (2.1)	1.1 (9.3)	6.1 (18.6)	7.3 (17.9)	-5.0 (-9.7)	9.7 (12.1)	0.5 (3.7)	8.6 (18.2)
	70	-0.2 (-3.1)	0.9 (8.6)	-1.1 (-1.1)	3.7 (13.1)	-3.0 (-10.6)	8.8 (14.2)	-1.5 (-5.1)	5.8 (13.0)
	80	2.0 (14.9)	2.1 (8.7)	1.0 (-2.7)	3.5 (13.0)	-2.3 (-10.7)	6.0 (14.8)	0.1 (-0.4)	4.7 (16.3)
	All	0.7 (2.9)	1.8 (12.8)	1.0 (-0.2)	5.2 (17.2)	-2.0 (-8.8)	8.2 (13.6)	-0.2 (-2.4)	6.0 (15.6)
Mix-2	40	-0.8 (-24.5)	0.2 (13.2)	-3.1 (-28.2)	1.1 (14.1)	-6.7 (-23.7)	2.7 (11.3)	-3.7 (-25.6)	3.0 (13.0)
	50	-1.2 (-32.2)	0.2 (10.9)	1.2 (-1.2)	2.0 (21.4)	-4.6 (-18.0)	1.9 (12.1)	-1.6 (-16.1)	3.0 (20.1)
	60	1.1 (21.9)	0.9 (12.3)	-0.9 (-12.5)	1.0 (12.8)	0.4 (-3.2)	3.3 (12.6)	0.2 (0.8)	2.3 (18.9)
	70	0.3 (2.7)	0.6 (10.2)	-1.9 (-18.5)	0.8 (12.4)	0.2 (-4.2)	3.3 (12.7)	-0.5 (-7.3)	2.3 (14.7)
	80	0.7 (11.1)	0.7 (12.6)	-0.2 (-8.6)	1.3 (14.8)	-10.1 (-32.0)	4.8 (9.5)	-3.5 (-11.2)	5.8 (21.4)
	All	0.0 (-4.2)	1.1 (23.9)	-1.0 (-13.8)	2.0 (17.8)	-4.2 (-16.2)	5.2 (16.1)	-1.8 (-11.9)	3.8 (19.9)
All	40	0.1 (-10.1)	1.6 (17.1)	0.0 (0.0)	5.4 (29.1)	-5.5 (-18.0)	9.4 (18.3)	-1.9 (-9.4)	7.0 (23.5)
	50	0.1 (1.9)	1.3 (25.4)	-1.0 (-8.1)	4.3 (15.8)	-5.6 (-14.6)	9.4 (13.8)	-2.3 (-7.3)	6.6 (19.8)
	60	0.4 (-7.3)	2.2 (33.6)	1.6 (-2.2)	6.0 (20.3)	-1.7 (-4.1)	8.7 (12.0)	0.1 (-4.4)	6.5 (23.2)
	70	0.5 (5.3)	1.3 (11.9)	0.0 (1.8)	4.3 (20.2)	-2.8 (-5.6)	9.6 (12.4)	-0.8 (0.3)	6.4 (16.1)
	80	0.9 (8.4)	1.6 (15.9)	-1.1 (-12.0)	4.0 (17.7)	-10.0 (-20.8)	13.9 (14.4)	-3.6 (-8.9)	9.8 (20.0)
	All	0.4 (-0.4)	1.6 (23.3)	-0.1 (-4.1)	4.9 (21.7)	-5.1 (-12.6)	10.7 (15.8)	-1.7 (-5.9)	7.5 (21.0)

To quantify all the differences, it is defined Δ_{vc} as the difference between the retrieved and original VC profiles given by:

$$\Delta_{vc}(a,\theta,h) = VC_r(k,\theta,h) - VC_o(a,\theta,h) \quad \text{Eq. 7.7}$$

and in percentage as:

$$\Delta_{vc}(a,\theta,h)(\%) = 100 \cdot \frac{VC_r(a,\theta,h) - VC_o(a,\theta,h)}{VC_o(a,\theta,h)} \quad \text{Eq. 7.8}$$

where VC_r and VC_o represents the retrieved and original VC values, respectively; a determines the aerosol scenario (aerosol type and AOD_{440}), θ are the solar zenith angle and h being one of the 60 bins of the retrieved VC profiles. Table 7.2 shows the MBE and STD calculated as the mean and standard deviation, respectively, of the 60 Δ_{vc} values of each profile. The Δ_{vc} values with VC_o below 1 $\mu m^3/cm^3$ have been discarded in the MBE and STD calculation since they could provide extreme differences in percentage. The results of Table 7.2 are showed for each of the 12 different aerosol scenarios and for different SZA. MBE and STD of Table 7.2 do not show any dependence with SZA. The best agreements (minima MBE and STD) are found for Dust and Mix-1 scenarios, where coarse mode is predominant. In general, unsigned MBE increases with AOD_{440} while the precision of GRASP, given by STD, decreases in percentage with AOD_{440}. As a general result, for all scenarios together GRASP systematically underestimates VC showing a MBE of -5.9% and with an uncertainty, which is given by STD, of 21%. The lowest uncertainties of GRASP are for Dust aerosol (~14%) with bias close to zero, while the highest uncertainties are for the Smoke type (~28%).

Table 7.3. Percentage of differences between the VC retrieved by GRASP and the original that is below the uncertainty, σ_a, of VC given by GRASP, for different aerosol scenarios and SZA values. The same percentage but for differences below $2\sigma_a$ is also shown.

Aerosol Type	SZA (°)	$AOD_{440} = 0.1$		$AOD_{440} = 0.4$		$AOD_{440} = 1.0$		All	
		$\Delta_{vc}<\sigma_a$ (%)	$\Delta_{vc}<2\sigma_a$ (%)	$\Delta_{vc}<\sigma_a$ (%)	$\Delta_{vc}<2\sigma_a$ (%)	$\Delta_{vc}<\sigma_a$ (%)	$\Delta_{vc}<2\sigma_a$ (%)	$\Delta_{vc}<\sigma_a$ (%)	$\Delta_{vc}<2\sigma_a$ (%)
Smoke	40	95.0	100.0	8.3	98.3	1.7	1.7	35.0	66.7
	50	90.0	100.0	88.3	98.3	1.7	85.0	60.0	94.4
	60	1.7	1.7	81.7	93.3	95.0	98.3	59.4	64.4
	70	96.7	100.0	66.7	98.3	93.3	100.0	85.6	99.4
	80	91.7	95.0	3.3	68.3	0.0	85.0	31.7	82.8
	All	75.0	79.3	49.7	91.3	38.3	74.0	54.3	81.6
Dust	40	93.3	100.0	91.7	100.0	93.3	100.0	92.8	100.0
	50	90.0	100.0	80.0	91.7	86.7	98.3	85.6	96.7
	60	86.7	90.0	83.3	95.0	86.7	96.7	85.6	93.9
	70	78.3	85.0	80.0	95.0	85.0	96.7	81.1	92.2
	80	63.3	83.3	86.7	98.3	80.0	90.0	76.7	90.6
	All	82.3	91.7	84.3	96.0	86.3	96.3	84.3	94.7
Mix-1	40	81.7	83.3	85.0	95.0	85.0	98.3	83.9	92.2
	50	100.0	100.0	90.0	100.0	81.7	96.7	90.6	98.9
	60	100.0	100.0	91.7	98.3	80.0	96.7	90.6	98.3
	70	91.7	100.0	88.3	100.0	75.0	93.3	85.0	97.8
	80	98.3	100.0	88.3	100.0	81.7	98.3	89.4	99.4
	All	94.3	96.7	88.7	98.7	80.7	96.7	87.9	97.3
Mix-2	40	55.0	95.0	38.3	80.0	36.7	80.0	43.3	85.0
	50	40.0	90.0	91.7	93.3	61.7	93.3	64.4	92.2
	60	78.3	95.0	88.3	95.0	95.0	98.3	87.2	96.1
	70	95.0	95.0	66.7	86.7	96.7	98.3	86.1	93.3
	80	96.7	98.3	83.3	91.7	1.7	58.3	60.6	82.8
	All	73.0	94.7	73.7	89.3	58.3	85.7	68.3	89.9
All	40	81.3	94.6	55.8	93.3	54.2	70.0	63.7	86.0
	50	80.0	97.5	87.5	95.8	57.9	93.3	75.1	95.6
	60	66.7	71.7	86.3	95.4	89.2	97.5	80.7	88.2
	70	90.4	95.0	75.4	95.0	87.5	97.1	84.4	95.7
	80	87.5	94.2	65.4	89.6	40.8	82.9	64.6	88.9
	All	81.2	90.6	74.1	93.8	65.9	88.2	73.7	90.9

In order to observe if the obtained differences between the original VC and the retrieved by GRASP are within σ_a (the estimation of retrieval uncertainty provided by GRASP; see Equation 4.26), the percentage of unsigned Δ_{vc} values that are below σ_a and $2\sigma_a$ have been calculated and named as $\Delta_{vc}<\sigma_a$ and $\Delta_{vc}<2\sigma_a$, respectively. If $\Delta_{vc}<\sigma_a$ and $\Delta_{vc}<2\sigma_a$ are similar to 68% and 95%, respectively, σ_a

will represent the uncertainty in a good way indicating that Δ_{vc} is similar to a normal distribution with a standard deviation equal to σ_a. Table 7.3 shows the obtained results for each scenario shown in Table 7.2. $\Delta_{vc}<\sigma_a$ and $\Delta_{vc}<2\sigma_a$ do not show any dependence on SZA or AOD_{440}. Mix-2 aerosol scenario presents the $\Delta_{vc}<\sigma_a$ and $\Delta_{vc}<2\sigma_a$ values closer to 68% and 95%; Dust and Mix-1 show even higher values. Smoke aerosol shows the lowest values when all SZA and AOD_{440} values are taken into account, but it is mainly caused by various individual cases with SZA=60º and AOD_{440}=0.1 or SZA=40º and AOD_{440}=1.0. For the combination of all the different aerosol scenarios, $\Delta_{vc}<\sigma_a$ is 74% and $\Delta_{vc}<2\sigma_a$ is 91%, which are close values to the expected 68% and 95%, and therefore it can be concluded that GRASP reproduces well the VC profiles within the margins given by the uncertainty associated with the numerical inversion.

For backscatter and extinction coefficients at 1064 nm and column integrated intensive properties such as CRI, SSA and LR it also did the same computations as in Table 7.2 and Table 7.3. Combining all the data of the different aerosol scenarios MBE are -11% and -5% and STD equal to 31% and 21% for backscatter and extinction profiles, respectively. For the backscatter coefficient, MBE presents the largest values for Smoke and Mix-2, while Dust and Mix-2 show the largest STD values. In the case of the extinction coefficient, Dust and Mix-1 present the lowest STD (13% and 15%) and MBE (3% and 2%) values. Regarding the retrieved column-integrated SSA, considering the five wavelengths together, the retrieved SSA fits better the original values when AOD_{440} increases, MBE being equal to -0.02, 0.01 and 0.00 and STD equal to 0.08, 0.05, and 0.02 for AOD_{440} of 0.10, 0.4 and 1.0, respectively for all aerosol types and SZA values. The retrieved SSA also agrees better as SZA increases, indicating the importance of large scattering angles in this property as expected [Dubovik et al., 2000], but this dependence is only clear for AOD_{440}=0.4 and 1.0. Similar dependence on AOD_{440}, but not on SZA, appears for the retrieved LR. These LR retrievals agree with the references when all

scenarios are considered together (MBE and STD are 10% and 29%). This agreement is found particularly for the Smoke aerosol cases. MBE and STD are reduced to 1% and 26% when only cases with AOD_{440}=0.4 are selected. Finally, for RRI and IRI, good agreements with the reference values are found for high AOD_{440}. The last computations reveal that most of the differences between retrieved properties and the original ones are within σ_a; the obtained results indicate that σ_a of backscatter and extinction is representative of the real uncertainty for all AOD_{440} and SZA values. On the other hand, for SSA and LR the percentage of differences below σ_a is lower than the expected but showing an increase with AOD_{440}.

7.2. Applications to real observation

7.2.1. ChArMEx/ADRIMED campaign

GRASP has been applied to ceilometer and sun/sky photometer measurements collected at UGR station during the ChArMEx/ADRIMED field campaign in June 2013. This campaign and the flights which took place over Granada are described in detail in Chapter 5. As commented, during the campaign period, the study region was affected by Saharan dust outbreaks with transport of dust particles.

Figure 7.5 shows the ceilometer RCS for the period 16th-17th June 2013 where flights were done over Granada. Airplane spirals near the study region were done at 14:15-14:45 UTC and at 07:15-07:45 UTC on 16th and 17th June, respectively. The time of flights is marked with purple vertical lines, while photometer data used by GRASP are the closest sun/sky photometer measurements is indicated by black vertical lines. Ceilometer data used in GRASP is time centred on the photometer data.

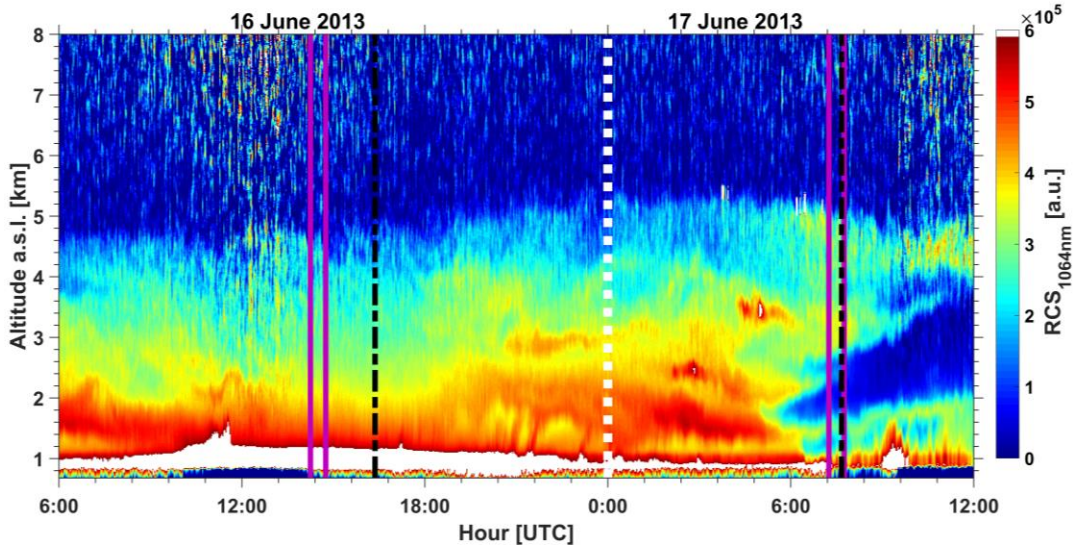

Figure 7.5. Ceilometer RCS at 1064 nm as a function of height and time from 16th, 6 UTC, to 17th June, 12 UTC, 2013. The times between vertical purple lines corresponds to the flights. Black vertical lines correspond in time with the sky radiance and AOD measurements (sun photometer) nearest to the flights.

Figure 7.6 shows the column-integrated PSD, SSA, and refractive indices obtained by GRASP and these provided by AERONET (level 1.5). Comparisons of size distributions reveal that they are very similar between both methodologies, being the differences within the GRASP uncertainties. The size distributions also indicate the predominance of the coarse mode as expected for Saharan dust outbreaks [Valenzuela et al., 2012c], and both retrievals point out a positive shift of the coarse mode concentration in the morning of 17th June.

It is corroborated by the effective radius of the coarse mode given by GRASP, which varied from 1.93 µm (Figure 7.6a) to 2.22 µm (Figure 7.6b). For SSA, Figure 7.6c and 7.6d reveal that values are very similar between GRASP and AERONET, and both retrievals show a spectral dependence typical of mineral dust [Dubovik et al. 2002a]. RRI from AERONET is slightly higher in both cases than from GRASP, but both retrievals show wavelength independence and a weak decrease from 16th to 17th June. Finally, for IRI again both AERONET and GRASP show similar patterns, typical for dust [Dubovik et al., 2002a], and differences

between methodologies are within the uncertainties. All these results point out that the column-integrated products from GRASP are in accordance with the ones provided by AERONET, at least in the analysed cases.

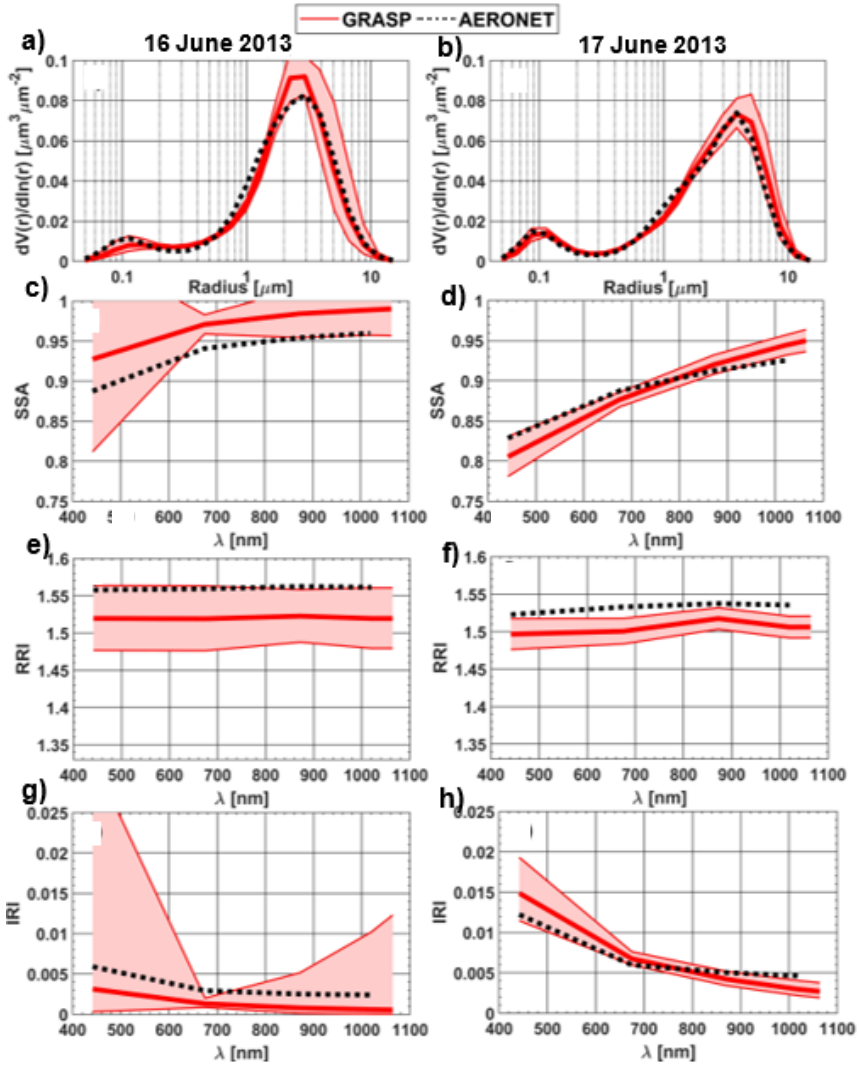

Figure 7.6. Particle size distribution (a, b), single scattering albedo (SSA; c, d), real refractive index (RRI, e, f) and imaginary refractive index (IRI; g, h) obtained by AERONET (black line) and GRASP (red line) on 16th June 2013 16:22 UTC (**a, c, e, g**) and 17th June 2013 07:40 UTC (**b, d, f, h**). Shadow band represents uncertainty in the GRASP retrieval.

Figure 7.7 shows vertically-resolved values of particle VC from GRASP (VC_{GRASP}) and the values obtained by airborne measurements ($VC_{Airborne}$). Generally

both methodologies present very similar profiles for the two cases. For the first flight, only one layer is observed with a slight and constant decrease up to 4.5 km approximately, while for the second flight three different layers are observed. Most of the differences are within the GRASP uncertainty, however, disagreements are found between retrievals and airplane measurements for altitudes below 1.5 km, which can be explained because of the orography and air-traffic restriction that did not allow the flight to perform spiral exactly above the station. This reasoning agrees with the largest aerosol VC values at the lowest layer observed by GRASP retrievals, which can be associated with pollution from the city.

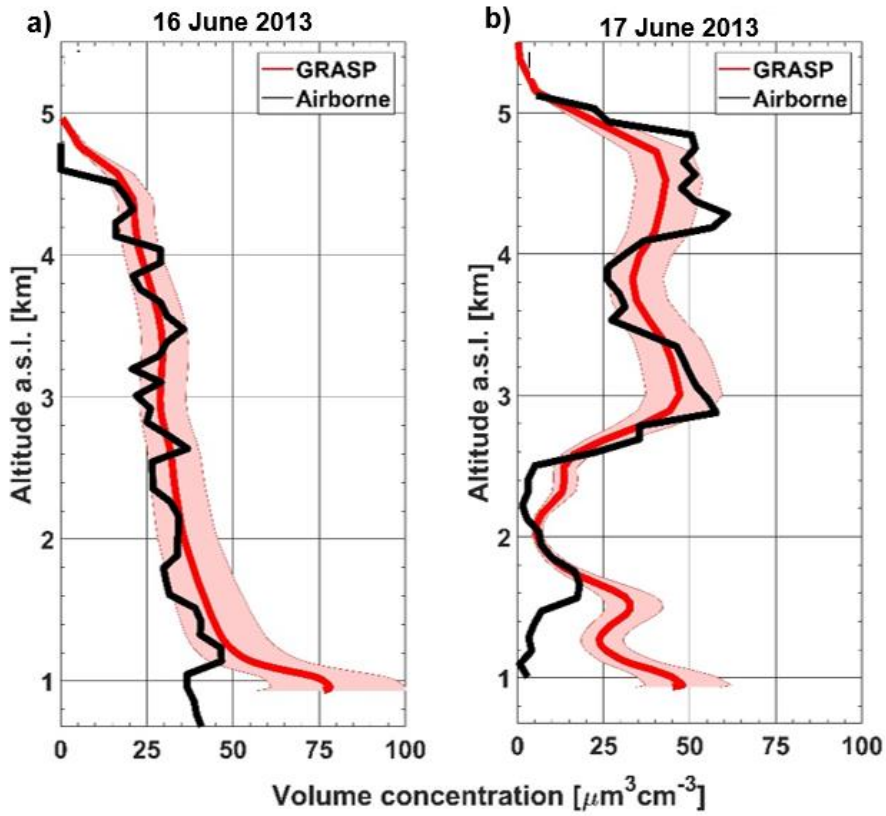

Figure 7.7. Profiles of aerosol volume concentration (VC) obtained by airborne instrumentation (black line) and GRASP (red line) on 16th (**a**) and 17th (**b**) June 2013. Shadow band represents uncertainty in the GRASP retrieval.

To quantify the differences between GRASP and airborne profiles, the VC from GRASP has been interpolated to the available heights of the airborne measurements. Point-by-point comparison between GRASP retrievals and airborne measurements are done. Linear interpolations of GRASP are done too for the same altitude than airborne measurements. Cases with very low aerosol load (VC<5 $\mu m^3/cm^3$) and measurements below 1.25 km a.s.l. (large disagreements in aerosol sampled between both techniques) are rejected in this comparison. Figure 7.8 shows particle VC obtained by GRASP versus airborne values. The correlation between both methodologies is high (correlation coefficient, *r*, higher than 0.80), and slightly better on 16th June. However, the slope of the least square fit indicates that GRASP underestimates the highest airborne measurements and the y-intercept points out that GRASP overestimates the lowest values. In addition, the differences, ΔVC, between VC values from GRASP and airborne have been calculated as follows:

$$\Delta VC = VC_{GRASP} - VC_{Airborne} \qquad \text{Eq. 7.9}$$

and in percentage as:

$$\Delta VC(\%) = 100 \cdot \frac{VC_{GRASP} - VC_{Airborne}}{VC_{Airborne}} \qquad \text{Eq. 7.10}$$

The histograms of ΔVC are shown in Figure 7.8d, 7.8e and 7.8f on 16th, 17th and both days, respectively. These graphs indicate that VC from GRASP agrees better with airborne measurements on 16th June, being the 37% of the absolute ΔVC values below 2.5 $\mu m^3/cm^3$ and 89% below 7.5 $\mu m^3/cm^3$. The ΔVC distribution on 17th June presents higher values but it is similar to a normal distribution, 61% of ΔVC absolute data being lower than 7.5 $\mu m^3/cm^3$; this percentage rises up to 75% when both flights are taken into account.

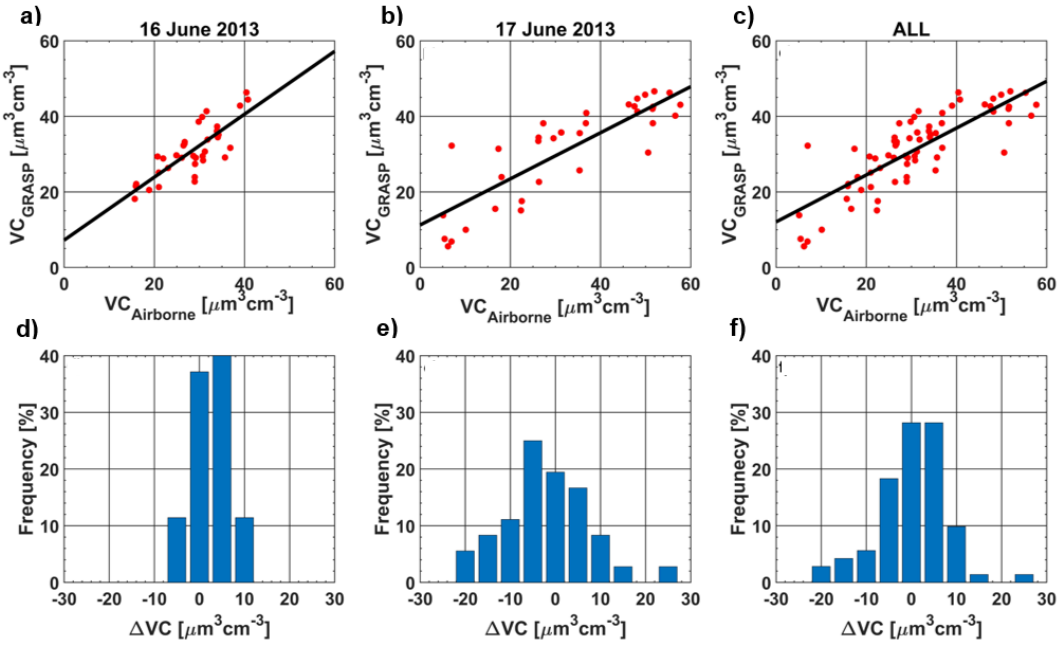

Figure 7.8. Aerosol volume concentration (VC) retrieved by GRASP as a function of the airborne measurements on 16th June (**a**), 17th June (**b**) and all (**c**). Histograms of the differences between the VC retrieved by GRASP and the VC from airborne on 16th June (**d**), 17th June (**e**) and all (**f**).

Table 7.4 shows the mean (MBE), mean of the absolute values (MABE) and standard deviation (STD) of ΔVC (Equation 9 and 10) for these three cases of Figure 7.8. GRASP slightly overestimates the $VC_{Airborne}$ values, showing MBE values of 10.5% and 12.9% on 16th and 17th June, respectively; however, the absolute MBE is close to 0 $\mu m^3/cm^3$. Assuming airborne measurements as a reference, the accuracy, given by MBE, of VC from GRASP is below 12% when both flights are taken into account. Regarding MABE, 17th June shows values around the double of that obtained on 16th June, which indicates that ΔVC differences are much higher in on 17th June, as STD confirms. The precision of GRASP using airborne measurements as a reference can be represented by STD, which presents a low value of 18.5% on 16th June, but this value on 17th June rises up to 70.8% due to the vertical shift of the lowest layer observed in Figure 7.7b. The STD for both flights together is 51.4%, but this value is still strongly affected by the differences on 17th June for low heights.

Table 7.4. Statistical estimators MBE, MABE and STD from ΔVC for the comparison of VC retrieved by GRASP and the airborne measured on 16th and 17th June 2013 and both days together. Values within parentheses are in %.

Flight	N	MBE [$\mu m^3/cm^3$]	MABE [$\mu m^3/cm^3$]	STD [$\mu m^3/cm^3$]	$\Delta VC<\sigma_a$ (%)	$\Delta VC<2\sigma_a$ (%)
16th June	35	2.5 (10.5)	4.1 (15.7)	4.4 (16.5)	77.1	100
17th June	36	-1.8 (12.9)	7.5 (33.9)	9.5 (70.8)	58.3	88.9
All	71	0.3 (11.7)	5.8 (24.9)	7.7 (51.4)	67.6	94.4

Finally, for both flights together, the percentage of ΔVC values which are below the uncertainty given by GRASP is 67.6%; this percentage is 94.4% when the double of the uncertainty is considered. These values are close to 68% and 95%, which points out that the uncertainty estimation provided by GRASP is representative of the real uncertainty of the retrieved VC.

7.2.2. SLOPE I campaign

In-situ VC measurements during SLOPE I field campaign at SNS station (VC_{SNS}) are used for evaluating retrieved values by GRASP at the same altitude. A detailed description of SLOPE I campaign is in Chapter 6. Ceilometer measurements used in GRASP are the averaged RCS values in a ± 15 min window centred on the sun/sky photometer time. In-situ instruments measured total particle VC in the radii range 0.05-10 μm, hence the GRASP retrieved values for this comparison have been integrated in the same range. From retrieved VC profiles, linear interpolations are done to have data at 2500 m a.s.l., which is the altitude of Sierra Nevada station. Figure 7.9 shows the temporal evolution of both in-situ and retrieved VC values for the entire period. While measurements of VC_{SNS} were continuous (24 hours per day), retrieved GRASP values are only available during some daytime points every day. The lack of VC_{SNS} data during some short periods were caused by instrumental failures. From Figure 7.9 can be observed that both measured and retrieved values

follow the same temporal evolution, with minimum values associated with clean atmosphere and extreme values associated mostly to Saharan dust arrivals. In fact, the largest values at Sierra Nevada were registered during the morning of 21st July, with in-situ measurements up to 269 $\mu m^3/cm^3$ and retrieved GRASP values from 279 to 364 $\mu m^3/cm^3$, and were associated with a strong Saharan dust episode that started on 20th July 2016.

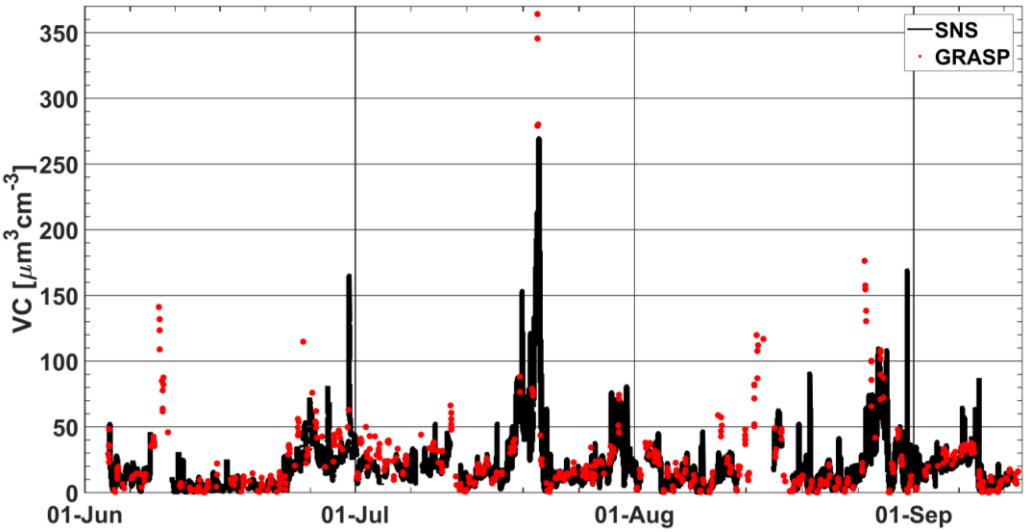

Figure 7.9. Temporal evolution of the aerosol volume concentration (VC) measured at SNS and the retrieved by GRASP at the same altitude.

Figure 7.10a shows a normalized number density plot of retrieved values by GRASP versus in-situ measurements (VC_{SNS}). Selected in-situ measurements are averaged during a time period of ±15 min from the retrieval time, which fits with the used ceilometer time range. Most of the VC values on Figure 7.10a are below 20 $\mu m^3/cm^3$, being 71% for VC_{SNS}. The linear fit reveals an overestimation of VC from GRASP to the VC_{SNS} values around 50%. The data for 26th August can be partially responsible of this overestimation with values ~150 $\mu m^3/cm^3$ while VC_{SNS} is ~50 $\mu m^3/cm^3$. These larger differences could be in part due to real differences in the aerosol over the Granada vertical and the aerosol at Sierra Nevada, since SNS could be affected by local effects and sources.

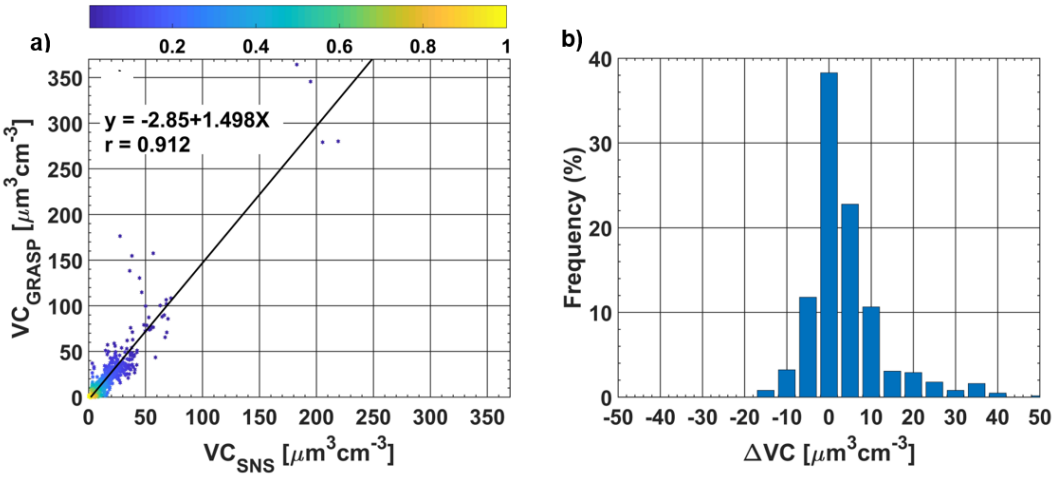

Figure 7.10. Aerosol volume concentration (VC) retrieved by GRASP at the Sierra Nevada Station (SNS) altitude as a function of the VC directly measured at SNS (**a**). Color of points represents the relative density of the points. Histograms of the differences between the VC retrieved by GRASP at SNS altitude and the VC directly measured at SNS (**b**).

Table 7.5. Statistical estimators for the comparison of VC retrieved by GRASP and the measured by in-situ instrumentation at SNS along SLOPE I campaign for different VC_{SNS} intervals. Values within parentheses are in %.

VC_{SNS} range [µm³/cm³]	N	MBE [µm³/cm³]	MABE [µm³/cm³]	STD [µm³/cm³]	$\Delta VC<\sigma_a$ [%]	$\Delta VC<2\sigma_a$ [%]
0-Max	619	5.5 (31.1)	7.7 (56.0)	16.6 (94.0)	37.6	68.2
5-Max.	493	6.3 (22.7)	8.9 (43.2)	18.2 (58.9)	40.0	72.0
0-5	126	2.3 (64.0)	3.2 (106.4)	5.9 (169.4)	28.6	53.2
5-10	132	0.7 (10.0)	3.6 (50.0)	4.3 (59.4)	27.3	59.8
10-20	184	3.1 (19.8)	5.9 (39.9)	8.1 (53.1)	45.1	75.0
20-30	97	8.8 (36.4)	9.9 (40.7)	16.7 (63.4)	45.4	80.4
30-50	58	11.2 (28.5)	15.1 (39.5)	25.6 (65.7)	55.2	79.3
50-100	18	27.1 (46.1)	29.0 (49.2)	24.1 (42.9)	11.1	66.7
100-Max.	4	116.7 (60.1)	116.7 (60.1)	58.6 (33.9)	0.0	50.0

The correlation between VC_{GRASP} and VC_{SNS} is high, being *r* equal to 0.91; this correlation coefficient is higher than the obtained between the ground measured AOD_{440} and VC_{SNS}, which is 0.79, and the correlation between the retrieved column-integrated VC and VC_{SNS}, which is 0.80. This result points out that the addition of ceilometer signal to the aerosol retrieval improves the capacity to estimate the aerosol vertical concentration. Figure 7.10b shows the differences ΔVC between VC_{GRASP} and the VC_{SNS}. This frequency histogram is similar to a normal distribution, the maximum being centred close to 0; however it is skewed to positive values. 38%, 73% and 87% of VC_{GRASP} shows absolute ΔVC differences lower than 2.5, 7.5 and 12.5 $\mu m^3/cm^3$, respectively.

Table 7.5 shows mean values and standard deviations of the differences ΔVC, for different VC_{SNS} ranges. The percentages of data when ΔVC is lower than the numerical uncertainty in the inversion, σ_a, are also included. From Table 7.5 when all ranges of VC are considered mean differences and standard deviations are 31% and 94%, both strongly affected by the low values of VC_{SNS}. In fact, MBE and STD are 64% and 169%, respectively, for VC_{SNS} values only below 5 $\mu m^3/cm^3$. However, if only data with VC_{SNS} above 5 $\mu m^3/cm^3$ are selected (493 in total), mean difference and standard deviations are reduced to 23% and 59%, respectively. In general, MBE increases with VC_{SNS} ranging from 10% to 60% if VC_{SNS} below 5 $\mu m^3/cm^3$ is not considered. MABE presents values around 40-50% for VC_{SNS} between 5 and 100 $\mu m^3/cm^3$. STD varies from 34 - 64%, showing the lowest values for highest concentrations. Regarding the ΔVC differences within the GRASP uncertainty estimation, Table 7.5 shows values below that expected, which indicates that the VC uncertainty estimation provided by GRASP could be not representative of the real uncertainty in this case. However, the obtained results could be affected by different factors, independent of GRASP, which yield a worse agreement than in the airborne comparison of Section 7.2.1. In this section the aerosol properties in the

free vertical atmosphere over Granada have been assumed equal to the properties at the surface on Sierra Nevada ground station, which could be affected by other aerosol sources and atmospheric conditions. Moreover, the instrumental uncertainty on VC_{SNS} could be also partially responsible of the observed differences.

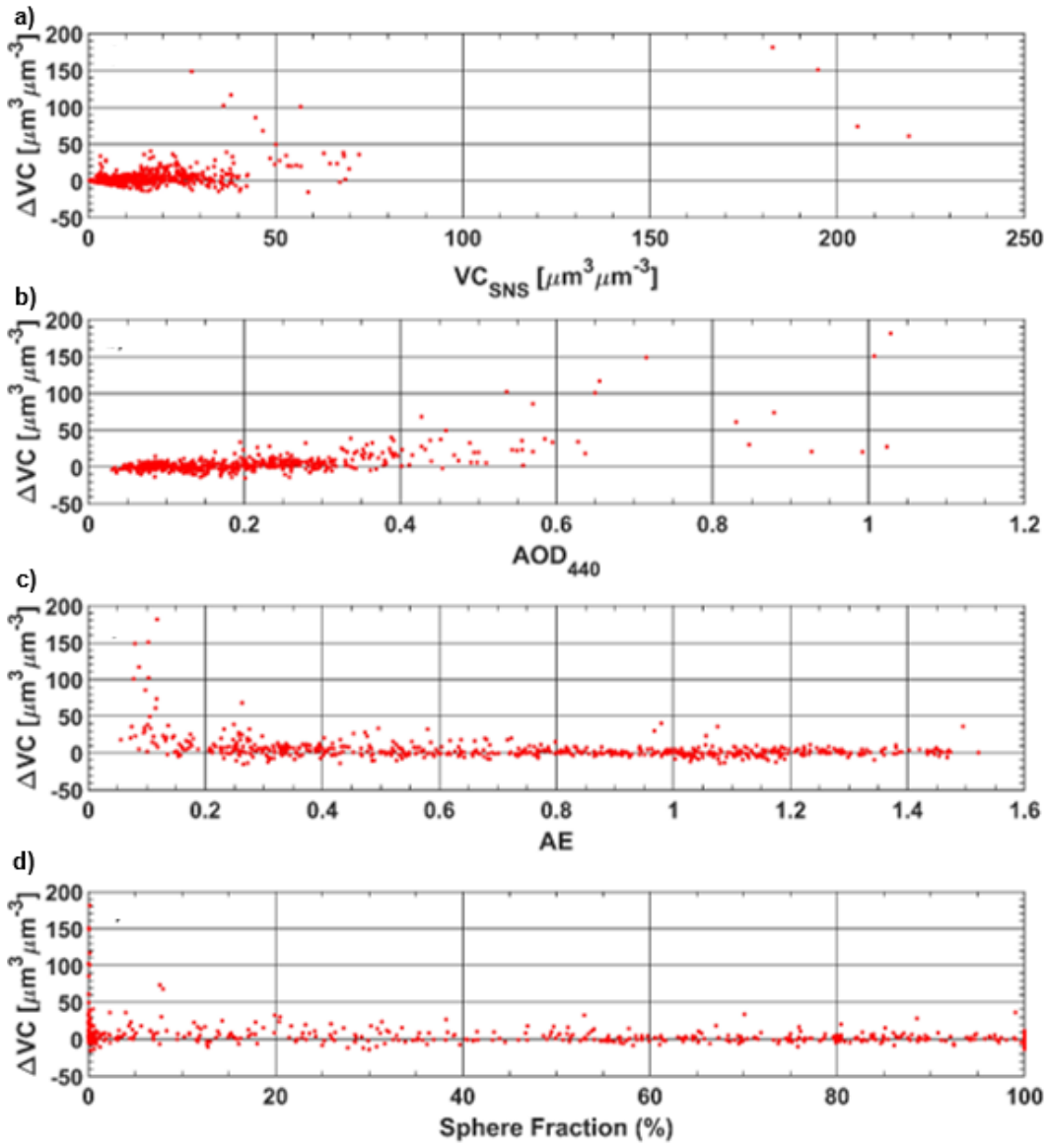

Figure 7.11. Differences between the aerosol volume concentration (VC) retrieved by GRASP at SNS altitude and the VC directly measured at SNS as a function of the VC at SNS (**a**), aerosol optical depth at 440 nm (**b**), Ångström Exponent (**c**) and sphere fraction (**d**).

Figure 7.11 shows the differences ΔVC as function of VC_{SNS} (Figure 7.11a), AOD_{440} (Figure 7.11b), Ångström Exponent (Figure 7.11c) and sphere fraction (Figure 7.11d). Generally it is observed that ΔVC increases with VC_{SNS}, however, some high ΔVC values appear for moderate VC_{SNS} values which correspond to the mentioned case of 26th August. ΔVC also increases with AOD_{440}, however high ΔVC values do not appear for moderate AOD_{440} and even low ΔVC values can be observed for high AOD_{440}. ΔVC does not show any clear dependence on AE and sphere fraction, except the highest ΔVC values for the lowest values of AE and sphere fraction, which mainly corresponds to dust particles during the mentioned strong dust episode of 20th -21st July 2016 (see Figure 7.9).

Finally, the same dust episode of 20th - 21st July 2016 studied in the Chapter 6 has been analysed as an illustration. Figure 7.12a and 7.12b show the retrieved VC profiles and the measured VC_{SNS} at Sierra Nevada on the afternoon of 20th July and on the morning of 21st July, respectively. The AOD_{440} from Granada was 0.85 and 0.83 for the Figure 7.12a and 7.12b, respectively, which indicates very similar aerosol load. It indicates that in columnar terms, both cases are similar, but if ceilometer measurements are added to the retrieval, the vertical distribution can be discerned; this is the case in Fig. 7.12, where the GRASP retrieval indicates that VC at SNS increased by about four times from 20th to 21st July, which was also appreciated in the measurements of VC_{SNS}. Then, thanks to ceilometer addition, it is known that the dust episode came 20th July in a strong layer located between 3.5-4.0 km a.s.l.. This layer went down providing extreme values at SNS height in the morning of 21st July, but also high dust concentrations in lower heights, which did not happen in the evening of 20th July. This cannot be appreciated using only the information from sun/sky photometer at UGR.

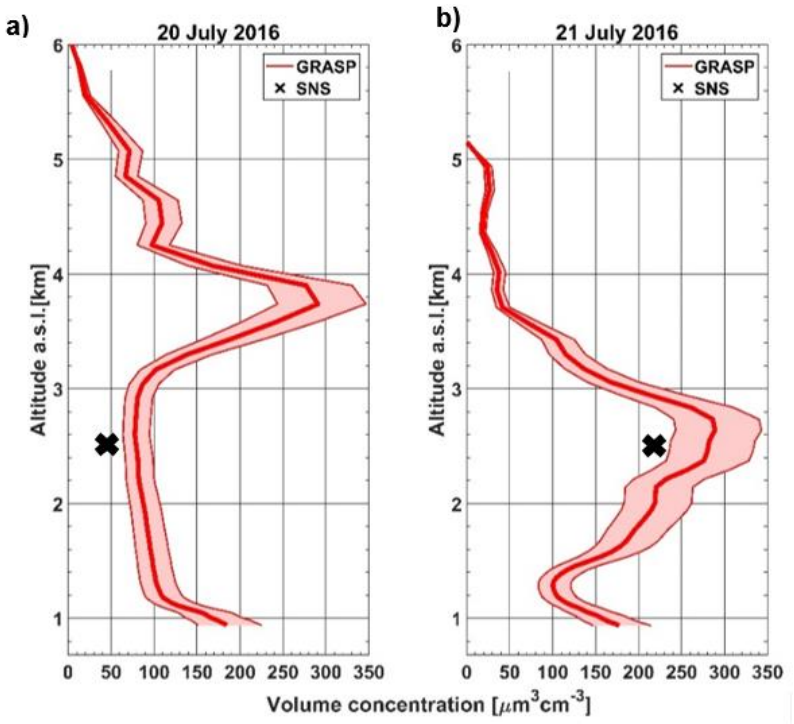

Figure 7.12. Profiles of aerosol volume concentration (VC) retrieved by GRASP at 20 July 2016, 18:12 UTC (**a**) and 21 July 2016, 09:32 UTC (**b**). VC measured at Sierra Nevada Station (SNS) is marked by a black cross. Shadow band represents uncertainty in the GRASP retrieval.

7.3. Conclusions

The results of the simulations have demonstrated good agreements for column-integrated size distributions and optical parameters such as CRI and SSA. For vertically-resolved aerosol properties, VC presents an accuracy of -6% and an uncertainty of 21%; this accuracy is -11% and 5% for β and α profiles at 1064 nm, being the uncertainty 31% and 21%, respectively. The mentioned analysis concludes that the uncertainty of these GRASP retrievals is representative of the real uncertainty of the retrieved parameters, except for column SSA and LR where the uncertainty given by GRASP is only representative when aerosol optical depth increases.

Differences in this concentration between GRASP retrievals and airborne measurements during ChArMEx/ADRIMED field campaign present a mean value below 12% and a standard deviation around 51%. All these differences are within the uncertainty estimations provided by the GRASP algorithm. Moreover, comparisons of the column-integrated retrieved parameters by the proposed scheme for GRASP versus AERONET retrievals have been done showing a good agreement between both techniques (differences were within uncertainties).

On the other hand, during the SLOPE I campaign, the in-situ VC at SNS station correlates better (r=0.91) with the aerosol VC obtained by GRASP at 2500 m a.s.l. than other variables like AOD at UGR station. Discarding the lowest concentration values, the mean differences between retrieved and the measured volume concentrations are of 23% with a standard deviation of 59%, which means that GRASP frequently overestimates the in-situ measurements at SNS station. However, part of these differences could be caused by uncertainties in the in-situ measurements and assumptions, and in the fact that the aerosol over Granada (where ceilometer monitoring was performed) could not be the same than the aerosol on Sierra Nevada, which could be affected by local dynamic and atmospheric effects, and also to local aerosol sources at the high mountains.

8. General conclusions and perspectives

Throughout the thesis the conclusions of each chapter have been presented. Thus, this section presents the main conclusions from this thesis, whose main objective was the characterization of atmospheric aerosol properties combining active and passive remote sensing measurements. These measurements were used as input in the Generalized Retrieval of Aerosol and Surface Properties algorithm (GRASP). This thesis explores the configuration of GRASP algorithm to use different synergistically combinations of measurements such as lidar signals and sun/sky/lunar photometer measurements at Andalusian Global ObseRvatory of the Atmosphere (AGORA), being possible to retrieve both vertically-resolved and column-integrated aerosol microphysical properties. Among the aerosol properties studied are the particle size distribution (PSD), real (RRI) and imaginary (IRI) refractive index, single-scattering albedo (SSA), extinction (α) and scattering (σ_{sca}) coefficients and volume concentration (VC).

The first study in this thesis was the evaluation of GRASP during ChArMEx/ADRIMED campaign in summer 2013 where correlative airborne measurements were acquired. GRASP was run with elastic lidar signals and with two sun/sky photometer measurements at different altitudes: one at the UGR station (37.16º N, 3.61º W, 680 m a.s.l.) with the instrument placed beside the lidar system, and the other one is placed at the surrounding mountain CP station (37.11º N, 3.49º W, 1820 m a.s.l.). This last set of measurements served to avoid issues of incomplete overlap of lidar signals. The analysis presented in this study was useful as a primary evaluation of the GRASP for the two configurations commented and revealed good agreements in the vertical-profiles between airborne and GRASP measurements, in spite of some outliers mostly associated with the differences in the areas sampled

between airplane and remote sensing measurements. Another important remark is the generally better results for the GRASP configuration located at CP, mostly associated with the lack of issues related with incomplete overlap. This indicates the need of accurate lidar measurements and of appropriate approaches for correcting overlap to retrieve accurate aerosol microphysical properties with GRASP. Nevertheless, all these analyses are for a short period of measurements and further evaluations need of a larger database.

The second part of the thesis focuses on night-time retrievals of vertically-resolved profiles and column-integrated retrievals of aerosol optical and microphysical properties combining active and passive remote sensing measurements in GRASP. Three different schemes have been tested by GRASP: N0 which assumes that there is no change in the aerosol column integrated properties along the night and uses as input data the night-time elastic lidar RCS measurements with the closest sun/sky measurements registered the day before or the day after; N1 which combines the night-time elastic lidar RCS measurements and night-time AOD retrieved from a lunar photometer but assumes the complex refractive index and sphericity; N2 which combines night-time elastic lidar RCS signals, AOD measurements retrieved from a lunar photometer and the relative sky radiances at the lunar aureole. All these measurements were acquired during an intense Saharan dust event (AOD_{440} ~1.0 on 20th - 21st July 2016) that took place during SLOPE I campaign at Granada (Spain) from 18th to 21st July 2016. This event was selected because intensive aerosol properties such as AE did not vary too much, with a value around 0.2 indicating large predominance of coarse particles. Also, this event was very intense with AOD reaching twice the typical values for Saharan dust outbreaks at Granada. Generally, a good continuity and coherence in the day-to-night evolution of aerosol microphysical properties is found, although noisier retrievals have been observed during night-time. This has been associated with the uncertainties in the passive remote sensing measurements such as in the case of the

sky radiances at lunar aureole from sky camera. Multiwavelength Raman lidar measurements during night-time allowed the evaluation of extinction coefficient obtained from GRASP using only elastic lidar signals and passive remote sensing measurements. This evaluation revealed GRASP and Raman agrees quite well, with differences below 30%. Nevertheless, these imply that some issues remain: The way of how the incomplete overlap area is analyzed in GRASP can yield to some incorrect values. Also, the uncertainties in IRI are behind these differences. On the other hand, evaluations versus in-situ measurements were possible thanks to the deployment of in-situ instrumentation at the high mountain site of SNS station (37.10º N, 3.39º W, 2500 m a.s.l.). Particularly, σ_{sca} and VC are evaluated. GRASP retrievals and in-situ measurements follow the same temporal evolution and are sensitive to the arrival of dust particles. Nevertheless, as commented above, night-time retrievals were noise and needs further evaluations.

Finally, it has been explored the use of ceilometer and collocated sun/sky photometer measurements in GRASP to retrieve column-integrated and vertically-resolved aerosol properties. Ceilometer works like an elastic lidar system emitting at 1064 nm, and the main advantage is that operate continuously in an unattended way. The capability to combining such set of measurements in GRASP has been studied through different sets of simulations using synthetic data for typical dust and biomass-burning aerosol placed at different altitudes as well as mixtures of both. In general, the proposed GRASP retrievals reproduce better aerosol properties for coarse particles, likely due to the operational long wavelength of the ceilometer at 1064 nm, and for high aerosol optical depth values. Overall, the obtained results indicate that the combination of sun/sky photometer and ceilometer measurements and their use as inputs in GRASP provides reliable products if the uncertainties are considered.

The studies developed here allowed the evaluation of GRASP retrievals versus the standard AERONET retrievals. The great novelty of GRASP is that the uses of additional elastic lidar signals have permitted separating refractive index between fine and coarse mode. Good agreement has been found between GRASP daytime retrievals and AERONET, both for ChArMEx/ADRIMED and SLOPE I field campaigns. Actually, for dust particles GRASP was capable of reproducing quite well the spectral dependence in IRI and SSA with enhanced absorption in the ultraviolet region, which is typical for mineral dust from western Sahara measured at Granada in previous studies [Valenzuela et al., 2014; Olmo et al., 2016]. However, for other aerosol types and mixtures – e.g. biomass-burning and pollution, the lack of data has no made possible further evaluations of GRASP algorithm.

Future research will be necessary in order to continue with the advancement in the aspects developed in this thesis, making emphasis in some topics:

- An important aspect for future research is the collaboration with lidar microphysical algorithms developers in order to improve the provided results and solve the remaining weak points.

- Try to combine one lidar with two sun/sky photometers at different heights to try improving the retrievals in the cases with different aerosol layers.

- Analysis of the data during SLOPE I and II intensive measurement period will be extended to study the absorption coefficient retrieved by GRASP which is a goal of ACTRIS.

- Evaluated the different schemes to retrieve night-time aerosol properties here presented on other types of aerosol. Also try to implement the multi-pixel scenario proposed by Dubovik et al. [2011] to retrieve the aerosol properties at night.

- Implement GRASP in the Iberian Ceilometer Network (ICENET) to retrieve the aerosol properties continuously.

- Finally, this thesis demonstrates that the Granada station provide valuable data to validate future satellite missions such as the 3MI polarimeter by EUMESAT or the HARP and PACE polarimeters in NASA missions.

Conclusiones generales y perspectivas

A lo largo de la tesis se han presentado las conclusiones de cada capítulo. Por lo que en esta sección se presentan las principales conclusiones que se han obtenido en esta tesis, cuyo principal objetivo fue la caracterización de las propiedades de los aerosoles atmosféricos mediante la combinación de medidas de teledetección activa y pasiva. Estas medidas se usan como entrada en el algoritmo GRASP (*Generalized Retrieval of Aerosol and Surface Properties*). En esta tesis se han explorado diferentes configuraciones de GRASP para obtener propiedades del aerosol atmosférico tanto en perfil como en columna. Para esto se han utilizado medidas de lidar y de fotómetros obtenidas en las estaciones de AGORA (*Andalusian Global ObseRvatory of the Atmosphere*). Entre las propiedades del aerosol estudiadas se encuentran la distribución del tamaño de partículas (PSD), la parte real (RRI) e imaginaria (IRI) del índice de refracción, el albedo de dispersión simple (SSA), los coeficientes de extinción (α) y de dispersión (σ_{sca}) y la concentración total en volumen (VC).

El primer estudio en esta tesis fue la evaluación de GRASP durante la campaña ChArMEx/ADRIMED en el verano de 2013, donde se realizaron un par de vuelos con instrumentación in situ a bordo. GRASP se evaluó combinando las medidas elásticas y las medidas de dos fotómetros solares a diferentes alturas: uno se encuentra en la estación UGR (37.16º N, 3.61º W, 680 m s.n.m.) junto al sistema lidar, y el segundo se encuentra en la estación de montaña CP (37.11º N, 3.49º W, 1820 m s.n.m.). Esta última combinación de medidas sirvió para evitar problemas de solapamiento incompleto de las señales lidar. El análisis presentado en este estudio es útil como una primera evaluación del GRASP para las dos configuraciones comentadas y revela buenos acuerdos en los perfiles verticales entre

las medidas del avión y GRASP, a pesar de algunas discrepancias asociadas principalmente a las diferencias entre las áreas muestreadas por el avión y las medidas realizadas en la estación AGORA. Otro resultado importante es el mejor acuerdo obtenido, en general, utilizando el fotómetro de la estación CP en lugar del de la estación UGR; esto puede ser debido a la ausencia de problemas relacionados con el solapamiento incompleto de la señal lidar. Esto señala la necesidad de utilizar medidas de lidar precisas y de enfoques apropiados para corregir el solapamiento para recuperar propiedades de aerosol más precisas con GRASP. Sin embargo, todos estos análisis son para un período corto de medidas y las evaluaciones adicionales necesitan una base de datos más amplia.

La segunda parte de la tesis combina las medidas de teledetección pasiva y activa en GRASP para obtener propiedades, tanto en columna como el perfil vertical, del aerosol durante la noche. Se han presentado tres esquemas distintos para las inversiones nocturnas: el primer esquema (N0) supone que no hay cambios en las propiedades integradas del aerosol en columna a lo largo de la noche y utiliza como datos de entrada las medidas nocturnas del lidar elástico y las medidas diurnas del fotómetro solar del día anterior o del día posterior a la medida lidar nocturna; el segundo esquema (N1) combina las medidas nocturnas del lidar y el espesor óptico obtenido del fotómetro lunar, y asume el índice de refracción y la esfericidad igual a las del día; el último esquema (N2) combina las medidas nocturnas del lidar, las medidas del espesor óptico con el fotómetro lunar y la radiancia relativa del cielo en la aureola lunar obtenida con una cámara de cielo. Todas estas medidas se adquirieron durante un intenso evento de polvo sahariano (AOD_{440} ~ 1.0 del 20 al 21 de julio de 2016) que tuvo lugar durante la campaña SLOPE I en Granada (España) del 18 al 21 de julio de 2016. Este evento se seleccionó debido a que las propiedades intensivas del aerosol como el AE no variaron demasiado, con un valor de alrededor de 0.2, el cual indica un gran predominio de partículas gruesas. Además, este evento fue muy intenso, ya que el AOD alcanzó el doble de los valores

típicos de los eventos de polvo sahariano registrados en Granada. En general, se encuentra una buena continuidad y coherencia en la evolución día-noche de las propiedades microfísicas de los aerosoles, aunque se han observado inversiones más ruidosas durante la noche. Esto se ha asociado con las incertidumbres en las medidas de teledetección pasiva, como en el caso de las radiaciones del cielo en la aureola lunar desde la cámara del cielo. Las medidas Raman del lidar durante la noche permitieron la evaluación del coeficiente de extinción obtenido por GRASP utilizando solo señales lidar elásticas y medidas de teledetección pasivas. Esta evaluación reveló que los resultados obtenidos con el algoritmo GRASP y por el método Raman están en concordancia, con diferencias por debajo del 30%. Sin embargo, algunos problemas se evidencian todavía: la forma en que se analiza el área de superposición incompleta en GRASP puede dar lugar a algunos valores incorrectos. Además, las incertidumbres en el IRI están parcialmente detrás de estas diferencias. Por otro lado, las comparaciones con medidas in situ fueron posibles gracias al despliegue de instrumentación in situ en la estación de alta montaña SNS (37.10º N, 3.39º W, 2500 m a.s.l.). Particularmente, se evalúan σ_{sca} y VC. Las inversiones de GRASP y las medidas in situ siguen la misma evolución temporal y son sensibles a la llegada de partículas de polvo. Sin embargo, como se comentó anteriormente, las inversiones nocturnas fueron ruidosas y necesitan más evaluaciones.

Finalmente, se ha explorado la combinación en GRASP de las medidas del ceilómetro y del fotómetro solar para obtener las propiedades de aerosol tanto en columna como en perfil. El ceilómetro funciona como un sistema lidar elástico que emite sólo a 1064 nm, y la principal ventaja es que opera de manera continua y sin supervisión. La capacidad de combinar dicho conjunto de medidas en GRASP se ha estudiado mediante diferentes conjuntos de simulaciones utilizando datos sintéticos típicos para el polvo y de quema de biomasa a diferentes alturas, así como mezclas de ambos. En general, las inversiones de GRASP propuestas reproducen mejores

propiedades de aerosol para partículas gruesas, probablemente debido a la longitud de onda de operación del ceilómetro, 1064 nm, y para valores altos de carga de aerosol. En general, los resultados obtenidos indican que la combinación de las medidas de fotómetro y ceilómetro y su uso como entradas en GRASP proporciona productos confiables si se tienen en cuenta las incertidumbres.

Los estudios desarrollados en esta tesis han permitido la evaluación de las inversiones de GRASP frente a las inversiones estándar de AERONET. La gran novedad de GRASP es el uso de señales lidar elásticas que han permitido separar el índice de refracción y la distribución de tamaños entre modo fino y el modo grueso. Se ha encontrado un buen acuerdo entre las inversiones diurnas de GRASP y AERONET, tanto para la campaña de campo ChArMEx/ADRIMED como para SLOPE I. En realidad, para partículas de polvo, GRASP fue capaz de reproducir bastante bien la dependencia espectral en IRI y SSA con una mayor absorción en la región ultravioleta; estos valores se han obtenido en estudios previos para el polvo mineral del Sahara occidental medido en Granada [Valenzuela et al., 2014; Olmo et al., 2016]. Sin embargo, la falta de datos para otros tipos de aerosoles y mezclas (quema de biomasa y otros), no ha permitido realizar evaluaciones adicionales del algoritmo GRASP.

Para continuar con el avance de los aspectos desarrollados en esta tesis, será necesario realizar en el futuro una investigación más exhaustiva de ciertos aspectos puestos de manifiesto en este estudio. Así

- Un aspecto importante para futuras investigaciones es la colaboración con los desarrolladores de algoritmos de inversión para mejorar los resultados obtenidos y resolver los puntos débiles de estos algoritmos.
- Intentar combinar las medidas lidar y de dos fotómetros solares a diferentes alturas para intentar mejorar las inversiones en los casos con diferentes capas de aerosol.

- Ampliar el análisis de los datos obtenidos durante las campañas de SLOPE-I y II. Centrándose en el coeficiente de absorción ya que es uno de los objetivos de ACTRIS.
- Evaluar los diferentes esquemas nocturnos que se han presentado utilizando otros tipos de aerosol. También intentar implementar el escenario "multi-pixel" propuesto por Dubovik et al. [2011] para poder obtener las propiedades del aerosol en la noche.
- Implementar GRASP en la *Iberian Ceilometer Network* (ICENET) para recuperar las propiedades del aerosol de forma continua.
- Finalmente, esta tesis demuestra que la estación de Granada proporciona datos valiosos para validar futuras misiones de satélites como el polarímetro 3MI de EUMESAT o los polarímetros HARP y PACE en misiones de la NASA.

List of Figures

List of Tables

List of Abbreviations

Abbreviation	Full name	Symbol
a.g.l.	above ground level	
a.s.l.	above sea level	
	absorption coefficient	σ_{abs}
	Absorption coefficient	σ_{abs}
APS	Aerodynamic Particle Sizer	
ADRIMED	Aerosol Direct Radiative Impact on the regional climate in the MEDiterranean region	
AOD	aerosol optical depth	τ
AERONET	AErosol RObotic NETwork	
aci	aerosol-cloud interactions	
ari	aerosol-radiation interactions	
ACTRIS	Aerosols, Clouds, and Trace gases Research InfraStructure Network	
AGORA	Andalusian Global ObseRvatory of the Atmosphere	
IISTA-CEAMA	Andalusian Institute for Earth System Research	
AE	Ångström exponent	
GFAT	Atmospheric Physics Group	
APD	avalanche photodiode	
	backscatter- Ångström exponent	AE_{β}
	backscatter coefficient	β

Abbreviation	Full name	Symbol
BRDF	Bidirectional Reflectance Distribution Function	
BC	black carbon	
CAPS	Cavity Attenuated Phase Shift	
CP	Cerro Poyos station	
CCD	charge-coupled device	
ChArMEx	Chemistry-Aerosol Mediterranean Experiment	
CALIPSO	Cloud-Aerosol Lidar and Infrared Pathfinder Satellite Observations	
CATS	Cloud-Aerosol Transport System	
CR	color ratio	
CRI	complex refractive index	m
CCN	condensation nuclei	
CPC	Condensation Particle Counter	
	correlation coefficient	r^2
	depolarization ratio	δ
	effective radius	r_{eff}
EARLINET	European Aerosol Research Lidar Network	
	extinction coefficient	α
FOV	field of view	
FSSP	Forward Scattering Spectrometer Probe	
GARRLiC	Generalized Aerosol Retrieval from Radiometer and Lidar Combined data algorithm	
GRASP	Generalized Retrieval of Aerosol and Surface Properties	
UGR	Granada station	

Abbreviation	Full name	Symbol
HDR	high dynamic range	
HSRL	High Spectral Resolution Lidar	
HYSPLIT	Hybrid Single-Particle Lagrangian Integrated Trajectory	
ICENET	Iberian CEilometer NETwork	
IN	ice forming nuclei	
IRI	imaginary part of the complex refractive index	κ
InGaAs	indium gallium arsenide	
IPCC	Intergovernmental Panel on Climate Change	
LALINET	Latin American LIdar NETwork	
LSM	least square method	
LIRIC	Lidar Radiometer Inversion Code	
LR	lidar ratio	
Lidar	light detection and ranging	
	maximum altitude	h_{max}
MBE	mean bias error	
MABE	mean of the absolute values	
SKYNET	MEXT Sky Radiometer Network	
MPLNET	Micro-Pulse Lidar Network	
	minimum altitude	h_{min}
	modelled vertical profiles of volume concentration	$c_k(h)$
MODIS	MODerate-Resolution Imaging Spectroradiometer	
MISR	Multi-angle Imaging SpectroRadiometer	
Nd:YAG	Neodymium-doped yttrium-aluminium-garnet	

Abbreviation	Full name	Symbol
NCR	normalized camera radiance	
$NRCS(h,\lambda)$	normalized range corrected signal	
	numeric size distribution	$\mathrm{n}(r)$
OT	optical thickness	
OC	organic carbon	
OMI	Ozone Monitoring Instrument	
PSD	particle size distribution	
	phase function	$P(\Theta)$
PLASMA	Photomètre Léger Aéroporté pour la Surveillance des Masses d'Air	
PMT	photomultiplier	
PARASOL	Polarization and Anisotropy of Reflectances for Atmospheric Science coupled with Observations from a Lidar	
POLDER	Polarization and Directionality of the Earth's Reflectance	
	radiance	L_λ
	random errors	σ_{rand}
RCS	range corrected signal	
RRI	real part of the complex refractive index	n
RIMA	Red Ibérica de Medida fotométrica de Aerosoles	
	relative optical air mass	m_0
RSR	relative sky radiance	
RMSE	root mean square error	
SMPS	Scanning Mobility Particle Sizer	

Abbreviation	Full name	Symbol
	scattering- Ångström exponent	AE_{sca}
	scattering coefficient	σ_{sca}
SLOPE I	Sierra Nevada Lidar AerOsol Profiling Experiment I	
SNS	Sierra Nevada station	
SSA	single-scattering albedo	ω_0
	size parameter	x
SZA	solar zenith angle	θ
	speed of light	c
STD	standard deviation	
	standard deviation of volume median radius	σ_v
	surface size distribution	$s(r)$
	systematic errors	σ_{bias}
TOA	top of atmosphere	
	total error estimate	σ_a
VC	total volume concentration	
UHSAS	Ultra-High Sensitivity Aerosol Spectrometer	
VC	Volume concentration	
	volume median radius	r_m
	volume size distribution	$v(r)$
	wavelength	λ

Bibliography

Alados-Arboledas, L., and Olmo, F. J.: Evolution of solar radiative effects of Mount Pinatubo at ground level, Tellus B, 49(2), 190-198, 1997.

Anderson, TL., and Ogren, J. A.: Determining aerosol radiative properties using the TSI 3563 integrating nephelometer, Aerosol Sci. Technol., 29, 57–69, 1998.

Andreae, M. O., Rosenfeld, D., Artaxo, P., Costa, A. A., Frank, G. P., Longo, K. M., and Silvas-Dias, M. A. F.: Smoking rain clouds over the Amazon, Science, 303, 1337–1342, 2004.

Ångström, A.: The parameters of atmospheric turbidity, Tellus, 16(1), 64-75, 1964.

Ansmann, A., Bösenberg, J., Chaikovsky, A., Comerón, A., Eckhardt, S., Eixmann, R., Freudenthaler, V., Ginoux, P., Komguem, L., and Linné, H.: Long-range transport of Saharan dust to northern Europe: The 11–16 October 2001 outbreak observed with EARLINET, Journal of geophysical research, 108(D24), 4783, 2003.

Ansmann, A., Riebesell, M, and Weitkamp, C.: Measurement of atmospheric aerosol extinction profiles with a Raman lidar, Optics Letters, 15(13), 746-748, 1990.

Baibakov, K., O´Neill, N.T., Ivanescu, L., Duck, T.J., Perro, C., Herber, A., Schulz, K.-H., and Schrems, O.: Synchronous starphotometry and lidar measurements at Eureka in High Canadian Arctic, Atmospheric Measurement Techniques, 8, 3789-3809, 2015.

Barreto, A., Cuevas, E., Damiri, B., Guirado, C., Berkoff, T., Berjón, A.J., Hernández, Y., Almansa, F., and Gil, M.: A new method for nocturnal aerosol measurements with a lunar photometer prototype, Atmospheric Measurement Techniques, 6, 585-598, 2013.

Barreto, Á., Cuevas, E., Granados-Muñoz, M. J., Alados-Arboledas, L., Romero, P. M., Gröbner, J., Kouremeti, N., Almansa, A. F., Stone, T., Toledano, C., Román, R., Sorokin, M., Holben, B., Canini, M., and Yela, M.: The new sun-skylunar Cimel CE318-T multiband photometer – a comprehensive performance evaluation, Atmos. Meas. Tech., 9, 631–654, https://doi.org/10.5194/amt-9-631-2016, 2016.

Barreto, Á., Román, R., Cuevas, E., Pérez-Ramírez, D., J. Berjón, A., Kouremeti, N., Kazadzis, S., Gröbner, J., Mazzola, M., Toledano, C., Benavent-Oltra, J. A., Doppler, L., Juryšek, J., Almansa, A. F., Victori, S., Maupin, F., Guirado-Fuentes, C., González, R., Vitale, V., Goloub, P., Blarel, L., Alados-Arboledas, L., Woolliams, E., Greenwell, C., Taylor, S., Antuña, J. C., and Yela, M.: Evaluation of night-time aerosols measurements and lunar irradiance models in the frame of the first multi-instrument nocturnal intercomparison campaign , Atmos. Environ., 202, 190-211, https://doi.org/10.1016/j.atmosenv.2019.01.006, 2019.

Barry, R. G., and Chorley, R. J.: Atmosphere, Weather, and Climate, Methuen, 1987.

Barth, C. A., Sanders, R. W., Thomas, R. J., Thomas, G. E., Jakosky, B. M., and West, R. A.: Formation of the El Chichon aerosol cloud, Geophysical Research Letters, 10(11), 993-996, 1983.

Baumgardner, D., Dye, J. E., Gandrud, B. W., and Knollenberg, R. G.: Interpretation of measurements made by the Forward Scattering Spectrometer Probe (FSSP-300) during the Airborne Arctic Stratospheric Expedition, J. Geophys. Res., 97, 8035-8046, DOI: 10.1029/91JD02728, 1992.

Bedoya-Velásquez, A. E., Navas-Guzmán, F., Granados-Muñoz, M. J., Titos, G., Román, R., Casquero-Vera, J. A., Ortiz-Amezcua, P., Benavent-Oltra, J. A., de Arruda Moreira, G., Montilla-Rosero, E., Hoyos, C. D., Artiñano, B., Coz, E., Olmo-Reyes, F. J., Alados-Arboledas, L., and Guerrero-Rascado, J. L.: Hygroscopic growth study in the framework of EARLINET during the SLOPE I campaign: synergy of remote sensing and in situ instrumentation, Atmos. Chem. Phys., 18, 7001-7017, https://doi.org/10.5194/acp-18-7001-2018, 2018.

Bergstrom, R. W., Pilewskie, P., Russell, P. B., Redemann, J., Bond, T. C., Quinn, P. K., and Sierau, B.: Spectral absorption properties of atmospheric aerosols, Atmos. Chem. Phys., 7, 5937-5943, doi:10.5194/acp-7-5937-2007, 2007.

Berkoff, T.A., Sorokin, M., Stone, T., Eck, T.F., Hoff, R., Welton, J.E., and Holben, B.: Nocturnal aerosol optical depth measurements with a small-aperture automated photometer using the moon as a light source. Journal of Atmospheric and Oceanic Technology, 8, 1297-1306, 2011.

Bluth, G. J. S., Rose, W. I., Sprod, I. E., and Krueger, A. J.: Stratospheric loading of sulfur from explosive volcanic eruptions, Journal of Geology, 105(6), 671-683, 1997.

Böckmann, C.: Hybrid regularization method for the ill-posed inversion of multiwavelength lidar data to determine aerosol size distributions, Appl. Optics, 40, 1329-1342, 2001.

Bodhaine, B. A., Wood, N. B., Dutton, E. G., and Slusser, J. R.: On Rayleigh optical depth calculations, J. Atm. Ocean Technol., 16, 1854–1861, 1999.

Bohren, C. F, and Huffman, D. R.: Absorption and Scattering of Light by Small Particles. New York (N.Y.): Wiley-Interscience, 1998.

Born, M. and Wolf, E.: Principles of optics: electromagnetic theory of propagation, interference and diffraction of light. Elsevier, 2013.

Boucher, O., Randall, D., Artaxo, P., Bretherton, C., Feingold, G., Forster, P., Kerminen, V.-M., Kondo, Y., Liao, H., Lohmann, U., Rasch, P., Satheesh, S. K., Sherwood, S., Stevens, B., and Zhang, X. Y.: Clouds and Aerosols, in: Climate Change 2013: The Physical Science Basis. Contribution of Working Group I to the Fifth Assessment Report of the Intergovernmental Panel on Climate Change, edited by: Stocker, T. F., Qin, D., Plattner, G.-K., Tignor, M., Allen, S. K., Boschung, J., Nauels, A., Xia, Y., Bex, V., and Midgley, P. M., Cambridge University Press, Cambridge, UK and New York, USA, 571–657, 2013.

Bovchaliuk, V., Goloub, P., Podvin, T., Veselovskii, I., Tanre, D., Chaikovsky, A., Dubovik, O., Mortier, A., Lopatin, A., Korenskiy, M., and Victori, S.: Comparison of aerosol properties retrieved using GARRLiC, LIRIC, and Raman algorithms applied to multi-wavelength lidar and sun/sky-photometer data, Atmos. Meas. Tech., 9, 3391-3405, doi:10.5194/amt-9-3391-2016, 2016.

Bravo-Aranda, J. A.: Lidar depolarization technique: assessment of the hardware polarizing sensitivity and applications. PhD Thesis, University of Granada, 2014.

Bucholtz, A.: Rayleigh-scattering calculations for the terrestrial atmosphere. Applied Optics, 34(15):2765–2773, 1995.

Cai, Y., Montague, D. C., Mooiweer-Bryan, W., and Deshler, T.: Performance characteristics of the ultra-high sensitivity aerosol spectrometer for particles between 55 and 800 nm: Laboratory and field studies, J. Aerosol Sci., 39, 759–769, 2008.

Carlson, T. N., and Benjamin, S. G.: Radiative heating rates of Saharan dust. J. Atmos. Sci.,37,193–213, 1980

Cazorla, A., Casquero-Vera, J.A., Román, R., Guerrero-Rascado, J.L., Toledano, C., Cachorro, V.E., Orza, J.A.G., Cancillo, M.L., Titos, G., Pandolfi, M., Alastuey, A., Hanrieder, N., Alados-Arboledas, L.: Near real time processing of ceilometer network data: characterizing an extraordinarty dust outbreak over the Iberian Peninsula. Atmos. Chem. Phys. 17, 11861–11876. http://dx.doi.org/10.5194/acp- 17-11861-2017, 2017.

Chaikovsky, A., Dubovik, O., Goloub, P., Balashevich, N., Lopatsin, A., Karol, Y., Denisov, S. and Lapyonok, T.: Software package for the retrieval of aerosol microphysical properties in the vertical column using combined lidar/photometer data (test version), Technical Report, Minsk, Belarus, Institute of Physics, National Academy of Sciences of Belarus, 2008.

Chaikovsky, A., Dubovik, O., Goloub, P., Tanré, D.,Pappalardo, G., Wandinger, U., Chaikovskaya, L., Denisov, S., Grudo, Y., Lopatsin, A., Karol, Y., Lapyonok, T., Korol, M., Osipenko, F., Savitski, D., Slesar, A., Apituley, A., Arboledas, L. A.,Binietoglou, I., Kokkalis, P., Granados Muñoz, M. J., Papayannis, A., Perrone, M. R., Pietruczuk, A., Pisani, G., Rocadenbosch, F., Sicard, M., De Tomasi, F., Wagner, J., and Wang, X.: Algorithm and software for the retrieval of vertical aerosol properties using combined lidar/radiometer data: dissemination in EARLINET, 26th International Laser and Radar Conference, Porto Heli, Greece, 2012.

Chaikovsky, A., Dubovik, O., Holben, B., Bril, A., Goloub, P., Tanré, D., Pappalardo, G., Wandinger, U., Chaikovskaya, L., Denisov, S., Grudo, J., Lopatin, A., Karol, Y., Lapyonok, T., Amiridis, V., Ansmann, A., Apituley, A., Allados-Arboledas, L., Binietoglou, I., Boselli, A., D'Amico, G., Freudenthaler, V., Giles, D., Granados-Muñoz, M. J., Kokkalis, P., Nicolae, D., Oshchepkov, S., Papayannis, A., Perrone, M. R., Pietruczuk, A., Rocadenbosch, F., Sicard, M., Slutsker, I., Talianu, C., De Tomasi, F., Tsekeri, A., Wagner, J., and Wang, X.: Lidar-Radiometer Inversion Code (LIRIC) for the retrieval of vertical aerosol properties from combined

lidar/radiometer data: development and distribution in EARLINET, Atmos. Meas. Tech., 9, 1181-1205, doi:10.5194/amt-9-1181-2016, 2016.

Chylek, P., and Wong, J.: Effect of absorbing aerosols on global radiation budget, Geophysical Research Letters, 22(8), 929-931, 1995.

Colarco, P.R., Nowottnick, E.P., Randles, C.A., Yi, B., Yang, P., Kim, K.-M., Smith, J.A., and Bardeen, C.: Impact of radiatively interactive dust aerosols in the NASA GEOS-5 climate model: Sensitivity to dust particle shape and refractive index. J. Geophys. Res., 119, 753-786, doi: 10.1002/2013JD020046. 2014.

de Arruda Moreira, G., Guerrero-Rascado, J. L., Benavent-Oltra, J. A., Ortiz-Amezcua, P., Román, R., E. Bedoya-Velásquez, A., Bravo-Aranda, J. A., Olmo Reyes, F. J., Landulfo, E., and Alados-Arboledas, L.: Analyzing the turbulent planetary boundary layer by remote sensing systems: the Doppler wind lidar, aerosol elastic lidar and microwave radiometer, Atmos. Chem. Phys., 19, 1263-1280, https://doi.org/10.5194/acp-19-1263-2019, 2019.

de Arruda Moreira, G., Guerrero-Rascado, J. L., Bravo-Aranda, J. A., Benavent-Oltra, J. A., Ortiz-Amezcua, P., Román, R., Bedoya-Velásquez, A. E., Landulfo, E., and Alados-Arboledas, L.: Study of the planetary boundary layer by microwave radiometer, elastic lidar and Doppler lidar estimations in Southern Iberian Peninsula, Atmos. Res., 213, 185–195, https://doi.org/10.1016/j.atmosres.2018.06.007, 2018.

Denjean, C., Cassola, F., Mazzino, A., Triquet, S., Chevaillier, S., Grand, N., Bourrianne, T., Momboisse, G., Sellegri, K., Schwarzenbock, A., Freney, E., Mallet, M., and Formenti, P.: Size distribution and optical properties of mineral dust aerosols transported in the western Mediterranean, Atmos. Chem. Phys., 16, 1081-1104, doi:10.5194/acp-16-1081-2016, 2016.

Denman, K. L., and Brasseur, G.: Couplings Between Changes in the Climate System and Biogeochemistry, Climate Change 2007: The Physical Science Basis, 499-587, 2007.

Dubovik, O.: Optimization of Numerical Inversion in Photopolarimetric Remote Sensing, in: Photopolarimetry in Remote Sensing, edited by: Videen, G., Yatskiv, Y., and Mishchenko, M., Kluwer Academic Publishers, Dordrecht, The Netherlands, 65–106, 2004.

Dubovik, O. and King, M.: A flexible inversion algorithm for retrieval of aerosol optical properties from Sun and sky radiance measurements, J. Geophys. Res., 105, 20673–20696, https://doi.org/10.1029/2000JD900282, 2000.

Dubovik, O., Smirnov, A., Holben, B. N., King, M., Kaufman, Y. J., Eck, T. F., and Slutsker, I.: Accuracy assessments of aerosol optical properties retrieved from Aerosol Robotic Network (AERONET) sun and sky radiance measurements, J. Geophys. Res., 105, 9791–9806, 2000.

Dubovik, O., Holben, B., Eck, T., Smirnov, A., Kaufman, Y., King, M., Tanre, D., and Slutsker, I.: Variability of absorption and optical properties of key aerosol types observed in worldwide locations, J. Atmos. Sci., 59, 590–608, 2002a.

Dubovik, O., Holben, B., Lapyonok, T., Sinyuk, A., Mishchenko, M., Yang, P., and Slutsker, I.: Non-spherical aerosol retrieval method employing light scattering by spheroids. Geophysical Research Letters, 29(10):54–1, 2002b.

Dubovik, O., Sinyuk, A., Lapyonok, T., Holben, B. N., Mishchenko, M., Yang, P., Eck, T. F., Volten, H., Munoz, O., Veihelmann, B., van der Zande, W. J., Leon, J.-F., Sorokin, M., and Slutsker, I.: Application of spheroid models to account for aerosol particle nonsphericity in remote sensing of desert dust, J. Geophys. Res., 111, D11208, doi:10.1029/2005JD006619, 2006.

Dubovik, O., Herman, M., Holdak, A., Lapyonok, T., Tanre, D., Deuze, J. L., Ducos, F., Sinyuk, A., and Lopatin, A.: Statistically optimized inversion algorithm for enhanced retrieval of aerosol properties from spectral multi-angle polarimetric satellite observations, Atmos. Meas. Tech., 4, 975–1018, doi:10.5194/amt-4- 975-2011, 2011.

Dubovik, O., Lapyonok, T., Litvinov, P., Herman, M., Fuertes, D., Ducos, F., Lopatin, A., Chaikovsky, A., Torres, B., Derimian, Y., Huang, X., Lopatin, A., Chaikovsky, A., Aspetsberger, M., and Federspiel, C.: Grasp: a versatile algorithm for characterizing the atmosphere. SPIE Newsroom, 25, 2014.

Dulac, F.: An overview of the Chemistry-Aerosol Mediterranean Experiment (ChArMEx), European Geosciences Union General Assembly, Geophysical Research Abstracts Vol. 16, EGU2014-11441, 27 April–2 May 2014, Vienna, Austria, 2014.

Ehn, M., Thornton, J. A., Kleist, E., Sipilä, M., Junninen, H., Pullinen, I., Springer, M., Rubach, F., Tillmann, R., Lee, B., Lopez-Hilfiker, F., Andres, S., Acir, I.-H., Rissanen, M., Jokinen, T., Schobesberger, S., Kangasluoma, J., Kontkanen, J., Nieminen, T., Kurtén, T., Nielsen, L. B., Jørgensen, S., Kjaergaard, H. G., Canagaratna, M., Maso, M. D., Berndt, T., Petäjä, T., Wahner, A., Kerminen, V.-M., Kulmala, M., Worsnop, D. R., Wildt, J., and Mentel, T. F.: A large source of low-volatility secondary organic aerosol, Nature, 506, 476, 2014.

Espinosa, W.R., Remer, L.A., Dubovik, O., Ziemba, L., Beyersdorf, A., Orozco, D., Schuster, G., Lapyonok, T., Fuertes, D., Martins, J.V., 2017. Retrievals of aerosol optical and microphysical properties from imaging polar nephelometer scattering measurements. Atmos. Meas. Tech. 10, 811–824.

Fedarenka, A., Dubovik, O., Goloub, P., Li, Z., Lapyonok, T., Litvinov, P., Blarel, L., Gonzalez, L., Podvin, T., Crozel, D., 2016. Utilization of AERONET polarimetric measurements for improving retrieval of aerosol microphysics: GSFC, Beijing and Dakar data analysis. J. Quant. Spectrosc. Radiat. Transf. 179, 72–97.

Fernald, F. G., Herman, B. M., and Reagan, J. A.: Determination of aerosol height distributions by lidar, J. Appl. Meteorol., 11, 482–489, 1972.

Fernald, F. G.: Analysis of atmospheric lidar observations- Some comments, App. Optics, 23, 652–653, 1984.

Flentje, H., Claude, H., Elste, T., Gilge, S., Köhler, U., Plass-Dülmer, C., Steinbrecht, W., Thomas, W., Werner, A., and Fricke, W.: The Eyjafjallajökull eruption in April 2010 – detection of volcanic plume using in-situ measurements, ozone sondes and lidar-

ceilometer profiles, Atmos. Chem. Phys., 10, 10085-10092, https://doi.org/10.5194/acp-10-10085-2010, 2010.

Gatebe, C. K., Dubovik, O., King, M. D., and Sinyuk, A.: Simultaneous retrieval of aerosol and surface optical properties from combined airborne- and ground-based direct and diffuse radiometric measurements, Atmos. Chem. Phys., 10, 2777–2794, doi:10.5194/acp-10-2777-2010, 2010.

Goudie, A. S., and Middleton, N. J.: Saharan dust storms: nature and consequences, Earth-Science Reviews, 56(1), 179-204, 2001.

Granados-Muñoz, M. J., Guerrero-Rascado, J. L., Bravo-Aranda, J. A., Navas-Guzmán, F., Valenzuela, A., Lyamani, H., Chaikovsky, A., Wandinger, U., Ansmann, A., Dubovik, O., Grudo, J., and Alados-Arboledas, L.: Retrieving aerosol microphysical properties by Lidar-Radiometer Inversion Code (LIRIC) for different aerosol types, J. Geophys. Res., 119, 4836–4858, doi:10.1002/2013JD021116, 2014.

Granados-Muñoz, M. J., Bravo-Aranda, J. A., Baumgardner, D., Guerrero-Rascado, J. L., Pérez-Ramírez, D., Navas-Guzmán, F., Veselovskii, I., Lyamani, H., Valenzuela, A., Olmo, F. J., Titos, G., Andrey, J., Chaikovsky, A., Dubovik, O., Gil-Ojeda, M., and Alados-Arboledas, L.: A comparative study of aerosol microphysical properties retrieved from ground-based remote sensing and aircraft in situ measurements during a Saharan dust event, Atmos. Meas. Tech., 9, 1113-1133, doi:10.5194/amt-9-1113-2016, 2016.

Guerrero-Rascado, J. L., Ruiz, B., and Alados Arboledas, L.: Multispectral Lidar characterization of the vertical structure of Saharan dust aerosol over southern Spain, Atmos. Environ., 42, 2668– 2681, https://doi.org/10.1016/j.atmosenv.2007.12.062, 2008.

Guerrero-Rascado, J. L., Olmo, F. J., Avilés-Rodríguez, I., Navas-Guzmán, F., Pérez-Ramírez, D., Lyamani, H., and Alados Arboledas, L.: Extreme Saharan dust event over the southern Iberian Peninsula in september 2007: active and passive remote sensing from surface and satellite, Atmos. Chem. Phys., 9, 8453-8469, doi:10.5194/acp-9-8453-2009, 2009.

Guerrero-Rascado, J.L., Landulfo, E., Antuña, J.C., Barbosa, H.M.J., Barja, B., Bastidas, A.E., Bedoya, A.E., da Costa, R.F., Estevan, R., Forno, R.N., Gouveia, D.A., Jimenez, C., Larroza, E.G., Lopes, F.J.S., Montilla-Rosero, E., Moreira, G.A., Nakaema, W.M., Nisperuza, D., Alegria, D., Múnera, M., Otero, L., Papandrea, S., Pawelko, E., Quel, E.J., Ristori, P., Rodrigues, P.F., Salvador, J., Sánchez, M.F., Silva, A.: Latin American Lidar Network (LALINET) for aerosol research: diagnosis on network instrumentation. J Atmos. Sol. Terr. Phys. 138–139, 112–120, 2016.

Hamonou, E., Chazette, P., Balis, D., Dulac, F., Schneider, X., Galani, E., Ancellet, G., and Papayannis, A.: Characterization of the vertical structure of Saharan dust export to the Mediterranean basin, Journal of Geophysical Research: Atmospheres (1984–2012), 104(D18), 22257-22270, 1999.

Haywood, J. M., and Shine, K. P.: The effect of anthropogenic sulfate and soot aerosol on the clear-sky planetary radiation budget, Geophysical Research Letters, 22(5), 603-606, 1995.

Haywood, J., and Boucher, O.: Estimates of the direct and indirect radiative forcing due to tropospheric aerosols: A review, Reviews of Geophysics, 38(4), 513-543, 2000.

Heese, B., Flentje, H., Althausen, D., Ansmann, A., and Frey, S.: Ceilometer lidar comparison: backscatter coefficient retrieval and signal-to-noise ratio determination, Atmos. Meas. Tech., 3, 1763-1770, https://doi.org/10.5194/amt-3-1763-2010, 2010.

Hegg, D. A., Ferek, R. J., and Hobbs, P. V.: Aerosol size distributions in the cloudy atmospheric boundary layer of the North Atlantic Ocean, Journal of Geophysical Research: Atmospheres (1984–2012), 98(D5), 8841-8846, 1993.

Heintzenberg, J., Raes, F., and Schwartz, S.: Atmospheric Chemistry in a Changing World: An Integration and Synthesis of a Decade of Tropospheric Chemistry Research: The International Global Atmospheric Chemisty Project of the International Geosphere-Biosphere Programme, Chapter 4: Tropospheric Aerosols, Springer Verlag, 2003.

Heintzenberg, J., Wiedensohler, A., Tuch, T. M., Covert, D. S., Sheridan, P., Ogren, J. A., Gras, J., et al.: Intercomparisons and aerosol calibrations of 12 commercial integrating nephelometers of three manufacturers, J. Atmos. Ocean. Tech., 23, 902–914, 2006.

Henyey, L.G. and Greenstein, J.L.: Diffuse Radiation in the Galaxy. Astrophysical Journal, 93, 70-83, 1941.

Holben, B. N., Eck, T. F., Slutsker, I., Tanre, D., Buis, J. P., Setzer, A., Vermote, E., Reagan, J. A., Kaufman, Y. J., Nakajima, T., Lavenu, F., Jankowiak, I., and Smirnov, A.: AERONET-a federated instrument network a data archive for aerosol characterization, Remote Sens. Environ., 66, 1–16, 1998.

Holben, B. N., Eck, T. F., Slutsker, I., Smirnov, A., Sinyuk, A., Schafer, J., Giles, D., and Dubovik, O.: AERONET's Version 2.0 quality assurance criteria, in: Remote Sensing of the Atmosphere and Clouds, edited by: Tsay, S., Nakajima, T., Singh, R., and Sridharan, R., vol. 6408 of Proc. SPIE, Q4080, conference on Remote Sensing of the Atmosphere and Clouds, Goa, INDIA, November 13–16, https://doi.org/10.1117/12.706524, 2006.

Horvath, H., Alados Arboledas, L., and Olmo Reyes, F. J.: Angular scattering of the Sahara dust aerosol, Atmos. Chem. Phys., 18, 17735-17744, https://doi.org/10.5194/acp-18-17735-2018, 2018.

IPCC, 2013: Climate Change 2013: The Physical Science Basis. Contribution of Working Group I to the Fifth Assessment Report of the Intergovernmental Panel on Climate Change [Stocker, T.F., D. Qin, G.-K. Plattner, M. Tignor, S.K. Allen, J. Boschung, A. Nauels, Y. Xia, V. Bex and P.M. Midgley (eds.)]. Cambridge University Press, Cambridge, United Kingdom and New York, NY, USA, 1535 pp.

Iqbal, M.: An introduction to solar radiation, Access Online via Elsevier, 1983.

Jenoptik, 2013. CHM15k – Nimbus Ceilometer User Manual. Revision P0, September 2013.

Karol, Y., Tanré, D., Goloub, P., Vervaerde, C., Balois, J. Y., Blarel, L., Podvin, T., Mortier, A., and Chaikovsky, A.: Airborne sun photometer PLASMA: concept, measurements, comparison of aerosol extinction vertical profile with lidar, Atmos. Meas. Tech., 6, 2383–2389, doi:10.5194/amt-6-2383-2013, 2013.

Kasten, F., and Young, A. T.: Revised optical air mass tables and approximation formula, Appl. Opt, 28(22), 4735-4738, 1989.

Kieffer, H. H. and Stone, T. C.: The Spectral Irradiance of the Moon, Astronom. J., 129, 2887–2901, https://doi.org/10.1086/430185, 2005.

Klett, J. D.: Stable analytical inversion solution for processing lidar returns, Appl. Optics, 20, 211–220, 1981.

Koepke, P., Hess, M., Schult, I., and Shettle, E. P.: Global aerosol data set. MPI Meteorologie Hamburg Rep. 243, 44 pp, 1997.

Kokhanovsky, A.A., Davis, A.B., Cairns, B., Dubovik, O., Hasekamp, O.P., Sano, I., Mukai, S., Rozanov, V.V., Litvinov, P., Lapyonok, T., Kolomiets, I.S., Oberemok, Y.A., Savenkov, S., Martin, W., Wasilewski, A., Di Noia, A., Stap, F.A., Rietjens, J., Xu, F., Natraj, V., Duan, M., Cheng, T., Munro, R., 2015. Space-based remote sensing of atmospheric aerosols: the multi-angle spectro-polarimetric frontier. Earth Sci. Rev. 145, 85–116.

Kovalev, V. and Eichinger, W.: Elastic Lidar, Wiley Online Library, John Wiley & Sons, Inc., Hoboken, NJ, USA, 2004.

Li, X., and Strahler, A.H.:Geometric-optical bidirectional reflectance modeling of the discrete crown vegetation canopy: effect of crown shape and mutual shadowing. IEEE Trans. Geosci. Remote Sens. 30 (2), 276–292, 1992.

Lopatin, A., Dubovik, O., Chaikovsky, A., Goloub, P., Lapyonok, T., Tanré, D., and Litvinov, P.: Enhancement of aerosol characterization using synergy of lidar and sun-photometer coincident observations: the GARRLiC algorithm, Atmospheric Measurement Techniques, 6, 2065–2088, doi:10.5194/amt-6-2065-2013, 2013.

Lopatin, A.: Enhanced Remote Sensing of atmospheric aerosol by joint inversión of active and passive remote sensing observations. PhD thesis, Lille 1, 2013.

Lyamani, H., Olmo, F. J., and Alados-Arboledas, L.: Saharan dust outbreak over southeastern Spain as detected by sun photometer, Atmos. Environ., 39, 7276–7284, doi:10.1016/j.atmosenv.2005.09.011, 2005.

Lyamani, H., Olmo, F.J., and Alados-Arboledas, L.: Physical and optical properties of aerosols over an urban location in Spain: seasonal and diurnal variability, Atmospheric Chemistry and Physics, 10, 239-254, 2010

Mallet, M., Dulac, F., Formenti, P., Nabat, P., Sciare, J., Roberts, G., Pelon, J., Ancellet, G., Tanré, D., Parol, F., Denjean, C., Brogniez, G., di Sarra, A., Alados-Arboledas, L., Arndt, J., Auriol, F., Blarel, L., Bourrianne, T., Chazette, P., Chevaillier, S.,

Claeys, M., D'Anna, B., Derimian, Y., Desboeufs, K., Di Iorio, T., Doussin, J.-F., Durand, P., Féron, A., Freney, E., Gaimoz, C., Goloub, P., Gómez-Amo, J. L., Granados-Muñoz, M. J., Grand, N., Hamonou, E., Jankowiak, I., Jeannot, M., Léon, J.-F., Maillé, M., Mailler, S., Meloni, D., Menut, L., Momboisse, G., Nicolas, J., Podvin, T., Pont, V., Rea, G., Renard, J.-B., Roblou, L., Schepanski, K., Schwarzenboeck, A., Sellegri, K., Sicard, M., Solmon, F., Somot, S., Torres, B., Totems, J., Triquet, S., Verdier, N., Verwaerde, C., Waquet, F., Wenger, J., and Zapf, P.: Overview of the Chemistry-Aerosol Mediterranean Experiment/Aerosol Direct Radiative Forcing on the Mediterranean Climate (ChArMEx/ADRIMED) summer 2013 campaign, Atmos. Chem. Phys., 16, 455-504, doi:10.5194/acp-16-455-2016, 2016.

Massoli, P., Kebabian, P. L., Onasch, T. B., Hills, F. B., and Freedman, A.: Aerosol light extinction measurements by Cavity Attenuated Phase Shift (CAPS) Spectroscopy: Laboratory validation and field deployment of a compact aerosol particle extinction monitor, Aerosol Sci. Tech., 44, 428–435, doi:10.1080/02786821003716599, 2010.

McHardy, T. M., Zhang, J., Reid, J. S., Miller, S. D., Hyer, E. J. and Kuehn, R. E.: An improved method for retrieving nighttimeaerosol optical thickness from the VIIRS Day/Night Band, At-mos. Meas. Tech., 8, 4773–4783, https://doi.org/10.5194/amt-8-4773-2015, 2015.

Meloni, D., di Sarra, A., Pace, G., and Monteleone, F.: Aerosol optical properties at Lampedusa (Central Mediterranean). 2. Determination of single scattering albedo at two wavelengths for different aerosol types, Atmos. Chem. Phys., 6, 715-727, https://doi.org/10.5194/acp-6-715-2006, 2006.

Mishchenko, M. I., Travis, L. D., Kahn, R. A., and West, R. A.: Modeling phase functions for dust like tropospheric aerosols using a shape mixture of randomly oriented polydisperse spheroids, J. Geophys. Res.-Atmos., 102, 16831–16847, https://doi.org/10.1029/96JD02110, 1997.

Mishchenko, M. I., Hovenier, J. W., and Travis, L. D.: Light scattering by nonspherical particles, Elsevier, New York, 2000.

Mishchenko, M. I., Travis, L. D., and Lacis, A. A.: Scattering, Absorption, and Emission of Light by Small Particles, Cambridge University Press, Cambridge, 1 Edn., 2002.

Müller, D., Wandinger, U., and Ansmann, A.: Microphysical particle parameters from extinction and backscatter lidar data by inversion with regularization: simulation, Appl. Opt. 38, 2358-2368, 1999.

Müller, T., Laborde, M., Kassell, G., and Wiedensohler, A.: Design and performance of a three-wavelength LED-based total scatter and backscatter integrating nephelometer, Atmos. Meas. Tech., 4, 1291–1303, doi:10.5194/amt-4-1291-2011, 2011.

Nakajima, T., Yoon, S. C., Ramanathan, V., Shi, G. Y., Takemura, T., Higurashi, A., Takamura, T., Aoki, K., Sohn, B. J., Kim, S. W., Tsuruta, H., Sugimoto, N., Shimizu, A., Tanimoto, H., Sawa, Y., Lin, N. H., Lee, C. T., Goto, D., and Schutgens, N.: Overview of the Atmospheric Brown Cloud East Asian Regional Experiment 2005

and a study of the aerosol direct radiative forcing in east Asia, J. Geophys. Res., 112, D24S91, doi:10.1029/2007JD009009, 2007.

Navas-Guzmán, F., Bravo-Aranda, J., Guerrero-Rascado, J., Granados-Muñoz, M., and Alados-Arboledas, L.: Statistical analysis of aerosol optical properties retrieved by Raman lidar over Southeastern Spain, Tellus B, 65, 21234, doi:10.3402/tellusb.v65i0.21234, 2013.

Navas-Guzmán, F., Guerrero-Rascado, J. L., and Alados-Arboledas, L.: Retrieval of the lidar overlap function using Raman signals, Opt. Pura Apl., 44, 71–75, 2011.

Nicolet, M.: On the molecular scattering in the terrestrial atmosphere: An empirical formula for its calculation in the homosphere, Planet. Space Sci., 32, 1467–1468, 1984.

Olmo, F. J., Quirantes, A., Alcantara, A., Lyamani, H., and Alados-Arboledas, L.: Preliminary results of a non-spherical aerosol method for the retrieval of the atmospheric aerosol optical properties,J. Quant. Spectrosc. Radiat. Transfer, 100, 305 –314, doi:10.1016/j.jqsrt.2005.11.047, 2006.

Pappalardo, G., Amodeo, A., Apituley, A., Comeron, A., Freudenthaler, V., Linné, H., Ansmann, A., Bösenberg, J., D'Amico, G., Mattis, I., Mona, L., Wandinger, U., Amiridis, V., Alados-Arboledas, L., Nicolae, D., and Wiegner, M.: EARLINET: towards an advanced sustainable European aerosol lidar network, Atmos. Meas. Tech., 7, 2389-2409, doi:10.5194/amt-7-2389-2014, 2014.

Patterson, E. M., Gillette, D. A., and Stockton, B. H.: Complex index of refraction between 300 and 700 for Saharan aerosols. J. Geophys. Res., 82, 3153–3160

Pérez-Ramírez, D., Aceituno, J., Ruiz, B., Olmo, F.J., and Alados-Arboledas, L.: Development and calibration of a star photometer to measure the aerosol optical depth: smoke observations at a high mountain site, Atmospheric Environment, 42, 2733-2738, 2008.

Pérez-Ramírez, D., Lyamani, H., Olmo, F.J., and Alados-Arboledas, L.: Improvements in star photometry for aerosol characterization, Journal of Aerosol Science, 42, 737-745, 2011.

Pérez-Ramírez, D., Lyamani, H., Olmo, F. J., Whiteman, D. N., and Alados-Arboledas, L.: Columnar aerosol properties from sun and- star photometry: statistical comparisons and day-to-night dynamic, Atmos. Chem. Phys., 12, 9719–9738, doi:10.5194/acp-12-9719-2012, 2012.

Pérez-Ramírez, D., Lyamani, H., Smirnov, A., O'Neill, N. T., Veselovskii, I., Whiteman, D. N., Olmo, F. J., Alados-Arboledas, L.: Statistical study of day and night hourly patterns of columnar aerosol properties using sun and star photometry, Proc. SPIE, 100001, 100010K, 2016.

Perrone, M. R., De Tomasi, F., and Gobbi, G. P.: Vertically resolved aerosol properties by multi-wavelength lidar measurements, Atmos. Chem. Phys., 14, 1185-1204, doi:10.5194/acp-14-1185-2014, 2014.

Pincus, R., and Baker, M. B.: Effect of Precipitation on the Albedo Susceptibility of Clouds in the Marine Boundary-Layer, Nature, 372(6503), 250-252, 1994.

Prata, A.J.: Satellite detection of hazardous volcanic clouds and the risk to global air traffic. Nat. Hazards 5, 303–324, 2009.

Prospero, J. M., Ginoux, P., Torres, O., Nicholson, S. E., and Gill, T. E.: Environmental characterization of global sources of atmospheric soil dust derived from the NIMBUS7 TOMS absorbing aerosol product, Rev, Citeseer, 2002.

Rodríguez, S., Alastuey, A., Alonso-Pérez, S., Querol, X., Cuevas, E., Abreu-Afonso, J., Viana, M., Pérez, N., Pandolfi, M., and de la Rosa, J.: Transport of desert dust mixed with North African industrial pollutants in the subtropical Saharan Air Layer, Atmos. Chem. Phys., 11, 6663-6685, https://doi.org/10.5194/acp-11-6663-2011, 2011.

Román, R., Torres, B., Fuertes, D., Cachorro, V.E., Dubovik, O., Toledano, C., Cazorla, A., Barreto, A., Bosch, J.L., Lapyonok,T, González, R., Goloub, P., Perrone, M.R., Olmo, F.J., de Frutos, A., Alados-Arboledas, L.: Remote sensing of lunar aureole with a sky camera: Adding information in the nocturnal retrieval of aerosol properties with GRASP code, Remote Sens. Environ., 196, 238-252, http://dx.doi.org/10.1016/j.rse.2017.05.013, 2017a.

Román, R., Cazorla, A., Toledano, C., Olmo, F.J., Cachorro, V.E., de Frutos, A., Alados-Arboledas, L.: Cloud cover detection combining high dynamic range sky images and ceilometer measurements. Atmos. Res. 196, 224–236, 2017b.

Ross, J.: The Radiation Regime and Architecture of Plant Stands. Dr. W. Junk Publ, The Hague, The Netherlands, 1981.

Sawamura, P., Vernier, J. P., Barnes, J. E., Berkoff, T. A., Welton, E. J., Alados-Arboledas, L., Navas-Guzmán, F., Pappalardo, G., Mona, L., and Madonna, F.: Stratospheric AOD after the 2011 eruption of Nabro volcano measured by lidars over the Northern Hemisphere, Environmental Research Letters, 7(3), 034013, 2012.

Schaaf, C.L.B., Liu, J., Gao, F., and Strahler, A.H.: MODIS Albedo and reflectance anisotropy products from Aqua and Terra. In: Ramachandran, B., Justice, C., Abrams, M. (Eds.), Land Remote Sensing and Global Environmental Change: NASA's Earth Observing System and the Science of ASTER and MODIS, Remote Sensing and Digital Image Processing Series, 11. 873 Springer-Cerlag, 2011.

Schnaiter, M., Horvath, H., M Qohler, O., Naumann, K.-H., Saatho, H., and Sch Qock, O.W.: UV-VIS-NIR spectral optical properties of soot and soot-containing aerosols. Journal of Aerosol Science, 34, 1421–1444, 2003.

Schuster, G. L., Dubovik, O., and Arola, A.: Remote sensing of soot carbon – Part 1: Distinguishing different absorbing aerosol species, Atmos. Chem. Phys., 16, 1565-1585, doi:10.5194/acp-16-1565-2016, 2016.

Seinfeld, J. H., and Pandis, S. N.: Atmospheric chemistry and physics, Wiley-Interscience, 1998.

Seinfeld, J.H. and Pandis, S.N.:Atmospheric Chemistry and Physics: From Air Pollution to Climate Change. 2nd Edition, John Wiley & Sons, New York, 2006.

Shettle, E. P., and Fenn, R. W.: Models of aerosols of lower troposphere and the effect of humidity variations on their optical properties. AFCRL Tech. Rep. 79 0214, Air Force Cambridge Research Laboratory, Hanscom Air Force Base, MA, 100 pp., 1979.

Shifrin, K. S.: Simple relationships for the Ångström parameter of disperse systems, Applied Optics, 34(21), 4480-4485, 1995.

Sinyuk, A., Dubovik, O., Holben, B., Eck, T. F., Bréon, F. M., Martonchik, J., Kahn, R., Diner, D. J., Vermote, E. F., Roger, J.-C., Lapyonok, T., and Slutsker, I.: Simultaneous retrieval of aerosol and surface properties from a combination of AERONET and satellite data, Remote Sens. Environ., 107, 90–108, doi:10.1016/j.rse.2006.07.022, 2007.

Sokolik, I. N., and Toon, O. B. Incorporation of mineralogical composition into models of the radiative properties of mineral aerosol from UV to IR wavelengths. J. Geophys. Res., 104, 9423–9444, 1999

Sokolik, I. N., Andronove, A., and Johnson, T. C.: Complex refractive index of atmospheric dust aerosols. Atmos. Environ., 27A, 2495–2502, 1993

Sorribas, M., Olmo, F.J., Quirantes, A., Lyamani, H., Gil-Ojeda, M., Alados-Arboledas, L., Horvath, H.: Role of spheroidal particles in closure studies for aerosol microphysical-optical properties. Quarterly Journal of the Royal Meteorological Society. 141 - 692, pp. 2700 -2707, 2015.

Stein, A.F., Draxler, R.R, Rolph, G.D., Stunder, B.J.B., Cohen, M.D., and Ngan, F.: NOAA's HYSPLIT atmospheric transport and dispersion modeling system, Bull. Amer. Meteor. Soc., 96, 2059-2077, 2015.

Stone, R. S., Herber, A., Vitale, V., Mazzola, M., Lupi, A., Schnell, R. C., Dutton, E. G., Liu, P. S. K., Li, S. M., Dethloff, K., Lampert, A., Ritter, C., Stock, M., Neuber, R., and Maturilli, M.: A three-dimensional characterization of Arctic aerosols from airborne Sun photometer observations: PAM-ARCMIP, April 2009, J. Geophys. Res., 115, D13203, https://doi.org/10.1029/2009JD013605, 2010.

Takamura, T., and Nakajima, T.: Overview of SKYNET and its activities, Opt. Pura Apl. 37, 3303-3308, 2004.

Thomas, G. E. and Stamnes, K.: Radiative transfer in the atmosphere and ocean, Cambridge University Press, 2002.

Titos, G., del Águila, A., Cazorla, A., Lyamani, H., Casquero- Vera, J. A., Colombi, C., Cuccia, E., Gianelle, V., Mocnik, G., Alastuey, A., Olmo, F. J., and Alados-Arboledas, L.: Spatial and temporal variability of carbonaceous aerosols: Assessing the impact of biomass burning in the urban environment, Sci. Total Environ., 578, 613–625, https://doi.org/10.1016/j.scitotenv.2016.11.007, 2017.

Toledano, C., Wiegner, M., Groß, S., Freudenthaler, V., Gasteiger, J., Müller, D., Müller, T., Schladitz, A., Weinzierl, B., Torres, B., and O'neill, N. T.: Optical properties of aerosol mixtures derived from sun-sky radiometry during SAMUM-2, Tellus B, 63, 635–648, doi:10.1111/j.1600-0889.2011.00573.x, 2011.

Tomasi, C., Kokhanovsky, A. A., Lupi, A., Ritter, C., Smirnov, A., O'Neill, N. T., Stone, R. S., Holben, B. N., Nyeki, S., Wehrli, C., Stohl, A., Mazzola, M., Lanconelli, C., Vitale, V., Stebel, K., Aaltonen, V., de Leeuw, G., Rodriguez, E., Herber, A. B., Radionov, V. F., Zielinski, T., Petelski, T., Sakerin, S. M., Kabanov, D. M., Xue, Y., Mei, L., Istomina, L., Wagener, R., McArthur, B., Sobolewski, P. S., Kivi, R., Courcoux, Y., Larouche, P., Broccardo, S., and Piketh, S. J.: Aerosol remote sensing in polar regions, Earth-Sci. Rev., 140, 108–157, https://doi.org/10.1016/j.earscirev.2014.11.001, 2015.

Torres, B., Dubovik, O., Toledano, C., Berjon, A., Cachorro, V. E., Lapyonok, T., Litvinov, P., and Goloub, P.: Sensitivity of aerosol retrieval to geometrical configuration of ground-based sun/sky radiometer observations, Atmos. Chem. Phys., 14, 847-875, doi:10.5194/acp-14-847-2014, 2014.

Torres, B., Dubovik, O., Fuertes, D., Schuster, G., Cachorro, V. E., Lapyonok, T., Goloub, P., Blarel, L., Barreto, A., Mallet, M., Toledano, C., and Tanré, D.: Advanced characterisation of aerosol size properties from measurements of spectral optical depth using the GRASP algorithm, Atmos. Meas. Tech., 10, 3743-3781, https://doi.org/10.5194/amt-10-3743-2017, 2017.

Tsekeri, A., Lopatin, A., Amiridis, V., Marinou, E., Igloffstein, J., Siomos, N., Solomos, S., Kokkalis, P., Engelmann, R., Baars, H., Gratsea, M., Raptis, P. I., Binietoglou, I., Mihalopoulos, N., Kalivitis, N., Kouvarakis, G., Bartsotas, N., Kallos, G., Basart, S., Schuettemeyer, D., Wandinger, U., Ansmann, A., Chaikovsky, A. P., and Dubovik, O.: GARRLiC and LIRIC: strengths and limitations for the characterization of dust and marine particles along with their mixtures, Atmos. Meas. Tech., 10, 4995-5016, https://doi.org/10.5194/amt-10-4995-2017, 2017.

Twomey, S.: Pollution and the planetary albedo, Atmospheric Environment, 8, 1251-1256, 1974.

Twomey, S.: The inuence of pollution on the shortwave albedo of clouds, Journal of the Atmospheric Sciences, 34, 1149-1152, 1977.

Valenzuela, A., Olmo, F. J., Lyamani, H., Antón, M., Quirantes, A., and Alados-Arboledas, L.: Classification of aerosol radiative properties during African desert dust intrusions over southeastern Spain by sector origins and cluster analysis, J. Geophys. Res., 117, D06214, doi:10.1029/2011JD016885, 2012a.

Valenzuela, A., Olmo, F. J., Lyamani, H., Antón, M., Quirantes, A., and Alados-Arboledas, L.: Analysis of the desert dust radiative properties over Granada using principal plane sky radiances and spheroids retrieval procedure, Atmos. Res., 104–105, 292–301, doi:10.1016/j.atmosres.2011.11.005, 2012b.

Valenzuela, A., Olmo, F.J., Lyamani, H., Antón, M., Quirantes, A., Alados-Arboledas, L.: Aerosol radiative forcing during African desert dust events (2005–2010) over Southeastern Spain. Atmos. Chem. Phys., 12, 21, 10331-10351, 2012c.

Valenzuela, A., Olmo, F.J., Lyamani, H., Granados-Muñoz, M.J., Antón, M., Guerrero-Rascado, J.L., Quirantes, A., Toledano, C., Pérez-Ramírez, D., and Alados-Arboledas, L.: Aerosol transport over the western Mediterranean basin: evidence of the contribution of fine particles to desert dust plumes over Alboran Island, Journal of Geophysical Research: Atmospheres, 119, 14028-14044, 2014.

Veselovskii, I., Kolgotin, A., Griaznov, V., Muller, D., Wandinger, U., Whiteman, D: Inversion with regularization for the retrieval of tropospheric aerosol parameters from multiwavelength lidar sounding. Applied Optics, 41, 3685-3699, 2002.

Veselovskii, I., Dubovik, O., Kolgotin, A., Lapyonok, T., Di Girolamo, P., Summa, D., Whiteman, D. N., Mishchenko, M., and Tanré, D.: Application of randomly oriented spheroids for retrieval of dust particle parameters from multi-wavelength lidar measurements, J. Geophys. Res., 115, D21203, doi:10.1029/2010JD014139, 2010.

Volten, H., Munoz, O., Rol, E., de Haan, J. F., Vassen, W., Hovenier, J. W., Muinonen, K., and Nousiainen, T.: Scattering matrices of mineral aerosol particles at 441.6 nm and 632.8 nm, Journal of Geophysical Research, 106, 17 375-17 401, 2001.

Wagner, R., Ajtai, T., Kandler, K., Lieke, K., Linke, C., Müller, T., Schnaiter, M., and Vragel, M.: Complex refractive indices of Saharan dust samples at visible and near UV wavelengths: a laboratory study, Atmos. Chem. Phys., 12, 2491–2512, https://doi.org/10.5194/acp-12-2491-2012, 2012.

Welton, E. J., Voss, K. J., Quinn, P. K., Flatau, P. J., Markowicz, K., Campbell, J. R., Spinhirne, J. D., Gordon, H. R., and Johnson, J. E.: Measurements of aerosol vertical profiles and optical properties during INDOEX 1999 using micropulse lidars, J. Geophys. Res., 107(D19), 8019, 18-1–18-20, 2002.

Whitby, K., and Cantrell, B.: Fine particles, in International Conference on Environmental Sensing and Assessment, Las Vegas, NV, Institute of Electrical and Electronic Engineers, 1976.

Wiedensohler, A., Birmili, W., Nowak, A., Sonntag, A., Weinhold,K., Merkel, M., Wehner, B., Tuch, T., Pfeifer, S., Fiebig, M.,Fjäraa, A. M., Asmi, E., Sellegri, K., Depuy, R., Venzac, H., Villani,P., Laj, P., Aalto, P., Ogren, J. A., Swietlicki, E., Williams,P., Roldin, P., Quincey, P., Hüglin, C., Fierz-Schmidhauser, R.,Gysel, M., Weingartner, E., Riccobono, F., Santos, S., Grüning,C., Faloon, K., Beddows, D., Harrison, R., Monahan, C., Jennings,S. G., O'Dowd, C. D., Marinoni, A., Horn, H.-G., Keck,L., Jiang, J., Scheckman, J., McMurry, P. H., Deng, Z., Zhao, C.S., Moerman, M., Henzing, B., de Leeuw, G., Löschau, G., andBastian, S.: Mobility particle size spectrometers: harmonization of technical standards and data structure to facilitate high quality long-term observations of atmospheric particle number sized distributions, Atmos. Meas. Tech., 5, 657–685, doi:10.5194/amt-5-657-2012, 2012.

Wiedensohler, A., Wiesner, A., Weinhold, K., Birmili, W., Hermann, M., Merkel, M., Müller, T., Pfeifer, S., Schmidt, A., Tuch, T., Velarde, F., Quincey, P., Seeger, S., and Nowak, A.: Mobility Particle Size Spectrometers: Calibration Procedures and Measurement Uncertainties, Aerosol Sci. Technol., https://doi.org/10.1080/02786826.2017.1387229, 2017.

Winker, D.M., Pelon, J., Coakley, J.A., Ackerman, S.A., Charlson, R.J., Colarco, P.R., Flamant, P., Fu, Q., Hoff, R.M., Kittaka, C.K., Kubar, T.L., Le Treut, H., McCormick, M.P., Mégie, G., Poole, L., Powel, K., Trepte, C., Vaughan, M.A., and Wielicki, B.A.: The CALIPSO mission: A global 3D view of aerosols and clouds, Bulletin of the American Meteorological Society, 1211-1229, 2010.

WMO: Radiation commission of IAMAP meeting of experts on aerosol and their climatic effects. World Meteorological Organization Rep. WCP55, 28–30, 1983.

Yorks, J.E., McGill, M.J., Palm, S.P., Hlavka, D.L., Selmer, P.A., Nowottnick, E.P., Vaughan, M.A., Rodier, S.D., and Hart, W.D.: An overview of the CATS level 1 processing algorithms and data products, Geophysical Research Letters, 43, 4632-4639, 2016

Zieger, P.: Effects of relative humidity on aerosol light scattering. PhD Thesis. Diss. ETH No. 19659, 2011.

Appendix A

Article published in *Atmospheric Measurement Techniques* (AMT) Journal.

Comparative assessment of GRASP algorithm for a dust event over Granada (Spain) during ChArMEx-ADRIMED 2013 campaign (https://doi.org/10.5194/amt-10-4439-2017, 2017)

Atmos. Meas. Tech., 10, 4439–4457, 2017
https://doi.org/10.5194/amt-10-4439-2017

Atmospheric Measurement Techniques
Open Access
EGU

Comparative assessment of GRASP algorithm for a dust event over Granada (Spain) during ChArMEx-ADRIMED 2013 campaign

Jose A. Benavent-Oltra[1,2], Roberto Román[1,2], María J. Granados-Muñoz[1,2], Daniel Pérez-Ramírez[1,2], Pablo Ortiz-Amezcua[1,2], Cyrielle Denjean[3], Anton Lopatin[4], Hassan Lyamani[1,2], Benjamin Torres[4,5], Juan L. Guerrero-Rascado[1,2], David Fuertes[5], Oleg Dubovik[4], Anatoli Chaikovsky[6], Francisco J. Olmo[1,2], Marc Mallet[3], and Lucas Alados-Arboledas[1,2]

[1]Department of Applied Physics, University of Granada, 18071 Granada, Spain
[2]Andalusian Institute for Earth System Research (IISTA-CEAMA), University of Granada, Autonomous Government of Andalusia, 18006 Granada, Spain
[3]CNRM, Centre National de la Recherche Météorologique (UMR3589, CNRS, Météo-France), Toulouse, France
[4]Laboratoire d'Optique Atmosphérique, Université de Lille 1, Villeneuve d'Ascq, France
[5]GRASP-SAS, Remote sensing developments, LOA/Université Lille-1, Villeneuve d'Ascq, France
[6]Institute of Physics, National Academy of Science, Minsk, Belarus

Correspondence to: Jose A. Benavent-Oltra (jbenavent@ugr.es)

Received: 19 June 2017 – Discussion started: 4 July 2017
Revised: 21 September 2017 – Accepted: 13 October 2017 – Published: 17 November 2017

Abstract. In this study, vertical profiles and column-integrated aerosol properties retrieved by the GRASP (Generalized Retrieval of Atmosphere and Surface Properties) algorithm are evaluated with in situ airborne measurements made during the ChArMEx-ADRIMED field campaign in summer 2013. In the framework of this campaign, two different flights took place over Granada (Spain) during a desert dust episode on 16 and 17 June. The GRASP algorithm, which combines lidar and sun–sky photometer data measured at Granada, was used to retrieve aerosol properties. Two sun-photometer datasets are used: one co-located with the lidar system and the other in the Cerro Poyos station, approximately 1200 m higher than the lidar system but at a short horizontal distance.

Column-integrated aerosol microphysical properties retrieved by GRASP are compared with AERONET products showing a good agreement. Differences between GRASP retrievals and airborne extinction profiles are in the range of 15 to 30 %, depending on the instrument on board the aircraft used as reference. On 16 June, a case where the dust layer was coupled to the aerosol layer close to surface, the total volume concentration differences between in situ data and GRASP retrieval are 15 and 36 % for Granada and Cerro Poyos retrievals, respectively. In contrast, on 17 June the dust layer was decoupled from the aerosol layer close to the surface, and the differences are around 17 % for both retrievals. In general, all the discrepancies found are within the uncertainly limits, showing the robustness and reliability of the GRASP algorithm. However, the better agreement found for the Cerro Poyos retrieval with the aircraft data and the vertical homogeneity of certain properties retrieved with GRASP, such as the scattering Ångström exponent, for cases with aerosol layers characterized by different aerosol types, shows that uncertainties in the vertical distribution of the aerosol properties have to be considered.

The comparison presented here between GRASP and other algorithms (i.e. AERONET and LIRIC) and with airborne in situ measurements shows the potential to retrieve the optical and microphysical profiles of the atmospheric aerosol properties. Also, the advantage of GRASP versus LIRIC is that GRASP does not assume the results of the AERONET inversion as a starting point.

1 Introduction

Atmospheric aerosols play an important role in the Earth–atmosphere radiative system due to their interaction with so-

lar and terrestrial radiation and their role in cloud development and precipitation (Boucher et al., 2013). Uncertainties associated with the interaction of atmospheric aerosols with radiation have been reduced in the last years, but there is still a need for improvement, mainly in those aspects related to their absorption properties (IPCC, 2013). The characterization of aerosol vertical distribution is another point of interest to reduce uncertainties associated with atmospheric aerosol particles, since they can be different near the surface, within the boundary layer and in the free troposphere.

Passive remote sensing offers large advances in aerosol characterization with global sun-photometry networks such as the Aerosol Robotic Network (AERONET; Holben et al., 1998) or lunar and/or star photometry measurements (Pérez-Ramírez et al., 2012; Barreto et al., 2016, 2017). In the last few years, several different inversion methods, based on spectral aerosol optical depth (AOD) measurements, were developed for the retrieval of aerosol microphysical properties such as effective radius (r_{eff}) and volume concentration (VC) (e.g. Pérez-Ramírez et al., 2015; Torres et al., 2017). Furthermore, other sophisticated algorithms that use sky radiance measurements were developed for the retrieval of aerosol microphysical properties as well as intensive properties such as single-scattering albedo (SSA), asymmetry parameter and aerosol refractive index (RI) (e.g. Nakajima et al., 1996; Dubovik and King, 2000; Olmo et al., 2006, 2008). Nevertheless, all these algorithms and measurements only provide column-integrated aerosol properties.

Since the 1970s, lidar systems have been widely used to characterize aerosol vertical distributions in order to contribute to reducing the radiative forcing uncertainties associated with the atmospheric aerosol. The most basic systems use only information about the elastic lidar signal to derive backscatter coefficient by aerosol particles but require an assumption about the extinction-to-backscatter ratio (lidar ratio, LR) (Fernald et al., 1972; Klett, 1981, 1985; Fernald, 1984). More advanced systems such as Raman (Ansmann et al., 1992; Whiteman et al., 1992) and HSRL (High Spectral Resolution Lidar) (Shipley et al., 1983; Grund and Eloranta, 1991) are able to provide independent measurements of backscatter and extinction coefficients (β and α, respectively) without LR assumption. Also, the depolarization measurements are a lidar improvement that provide information about the shape of aerosols and allow us to characterize the aerosol type (Murayama et al., 2004; Miffre et al., 2011; Bravo-Aranda et al., 2013). However, lidar observations dedicated to the aerosol characterization are very scarce compared to the sun-photometer measurements, and many international networks have emerged in the last decades to homogenize and explore such information. This is the case of the global NASA MPLNET network (Micro-Pulse Lidar Network; Lewis et al., 2016) developed for continuous measurements of aerosol and cloud vertical profiles at different sites in the world using standard instrument and data processing algorithms. The EARLINET (European Aerosol Research LIdar NETwork; Pappalardo et al., 2014) and LALINET (Latin American LIdar NETwork; Guerrero-Rascado et al., 2016) have also been established in order to provide long-term database for the vertical and temporal distribution of aerosols over Europe and Latin America, respectively.

The retrieval of particle vertical microphysical properties from multiwavelength lidar systems is possible by inverting measurements of three aerosol backscatter and two extinction coefficients, known as the $3\beta + 2\alpha$ configuration, using the algorithms developed by Müller et al. (1999), Böckmann (2001) and Veselovskii et al. (2002). However, $3\beta + 2\alpha$ measurements are scarce compared with the large database of elastic lidar measurements. In this sense, different inversion methods were recently developed within the framework of EARLINET in order to retrieve vertical profiles of aerosol microphysical properties using combined information of elastic lidar and sun-photometry measurements. These approaches were the LIdar-Radiometer Inversion Code (LIRIC; Chaikovsky et al., 2008, 2012, 2016), which provides vertical distribution of volume concentrations, and the Generalized Aerosol Retrieval from Radiometer and Lidar Combined data (GARRLiC; Lopatin et al., 2013), which also allows the retrieval of SSA and RI. Currently, GARRLiC algorithm is included in the Generalized Retrieval of Atmosphere and Surface Properties inversion code (GRASP; Dubovik et al., 2011). However, very few studies have attempted to evaluate this recently developed inversion algorithm (Lopatin et al., 2013; Bovchaliuk et al., 2016; Torres et al., 2017; Román et al., 2017), and therefore their evaluation under different atmospheric conditions is still necessary.

Field campaigns with state-of-the-art instrumentation offer unique possibilities for the evaluation of new retrievals techniques of particle microphysical and optical properties. Recently, the ADRIMED (Aerosol Direct Radiative Impact on the regional climate in the MEDiterranean region) field campaign, which was part of the international cooperative research program Chemistry-Aerosol Mediterranean Experiment (ChArMEx; Dulac, 2014), was carried out with the main objective of capturing the high complexity of the different aerosol types in the Mediterranean region (Mallet et al., 2016). Several in situ and remote sensing measurements both from surface and on airborne platforms were collected during this campaign using state-of-the-art instrumentation. The measurements were performed at different stations over the western Mediterranean region during summer 2013 to create an updated database of the physical, chemical and optical aerosol properties as well as the vertical distribution of the major "Mediterranean aerosols" (Mallet et al., 2016; Denjean et al., 2016). Data gathered during ChArMEx-ADRIMED campaign give us an excellent opportunity to evaluate the recently developed algorithms for retrieving aerosol microphysical and optical profiles.

In that framework, the main objective of this study is to evaluate the aerosol optical and microphysical proper-

ties obtained with GRASP during the ChArMEx-ADRIMED field campaign in Granada, Spain. The GRASP configuration evaluated in this study here is the one that combines lidar signals and sun–sky radiance measurements. The paper is structured as follows: Sect. 2 gives a brief description of the experimental site and the instrumentation employed in this study. GRASP and LIRIC codes are described in detail in Sect. 3. The results are discussed in Sect. 4 and, finally, the main conclusions are summarized in Sect. 5.

2 Site and instrumentation

2.1 Experimental site

The experimental measurements were obtained over Granada (Spain) at the Andalusian Institute for Earth System Research (IISTA-CEAMA) of the University of Granada, Spain (37.16° N, 3.61° W; 680 m a.s.l.), and at the remote high mountain site Cerro Poyos (37.11° N, 3.49° W; 1820 m a.s.l.) located at the Sierra Nevada mountain range, about 12 km away (horizontally) from IISTA-CEAMA station. Figure 1 shows a map illustrating the distance between the Granada and Cerro Poyos stations. The city of Granada is located in south-eastern Iberian Peninsula and is a non-industrialized medium-sized city with a population around 300 000 (twice including the metropolitan area). The city is sited in a natural basin surrounded by mountains with elevations between 1000 and 3500 m a.s.l. The area is approximately 200 km from the African continent and approximately 50 km from the western Mediterranean basin. In Granada, one main source of natural aerosol is the long-range transport of mineral dust particles from North Africa (e.g. Lyamani et al., 2005; Valenzuela et al., 2012a) that reaches the area in lofted layers (Müller et al., 2009; Guerrero-Rascado et al., 2008, 2009; Córdoba-Jabonero et al., 2011) before mixing with the atmospheric boundary layer (Bravo-Aranda et al., 2015) and been detected at the surface in precipitation samples (Calvo et al., 2010). Another natural source is biomass burning particles: fresh smoke (Alados-Arboledas et al., 2011) and long-range transported smoke (Ortiz-Amezcua et. al., 2014, 2017). While the main anthropogenic sources are pollution from Europe, the Iberian Peninsula and the Mediterranean Sea (Lyamani et al., 2006; Pérez-Ramírez et al., 2016), local sources are mainly road traffic and central heating systems (Lyamani et al., 2012; Titos et al., 2017).

2.2 Ground-based instrumentation

Columnar aerosol properties during daytime were obtained by CIMEL CE-318-4 (Cimel Electronique) sun–sky photometers at IISTA-CEAMA and Cerro Poyos sites. The sunphotometer instruments used in this study are operated in the framework of AERONET-RIMA network (Iberian Network for Aerosol Measurements, infrastructure of AERONET) (https://aeronet.gsfc.nasa.gov/). A complete description of

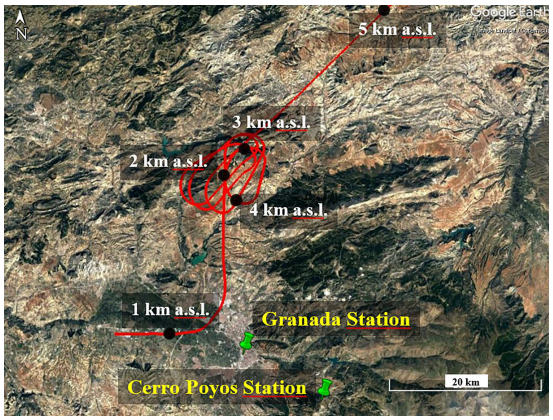

Figure 1. Map illustrating the Granada and Cerro Poyos stations. The red line indicates the trajectory and the black points show the altitude of the aircraft on 17 June.

the instrument can be found in Holben et al. (1998). Briefly, this instrument makes direct solar irradiance measurements at 340, 380, 440, 670, 870 and 1020 nm and sky radiance measurements at 440, 670, 870 and 1020 nm. Solar direct irradiance measurements are used to calculate the AOD at 340, 380, 440, 670, 870 and 1020 nm, with uncertainty of ± 0.01 for $\lambda > 400$ nm and of ± 0.02 for $\lambda < 400$ nm (Holben et al., 1998; Eck et al., 1999). Furthermore, the Ångström exponent (AE), a parameter that describes the spectral dependency of the AOD, is calculated in the range of 440–870 nm. The AE provides an indication of the particle size: small values (< 0.5) suggest a predominance of coarse particles, while large values (> 1.5) indicate a predominance of small particles (e.g. Dubovik et al., 2002). The solar direct irradiance and sky radiance measurements are used to retrieve aerosol optical and microphysical properties such as columnar particle size distribution (PSD), real and imaginary refractive indices (RRI and IRI) and SSA, using the algorithm of Dubovik et al. (2006). In addition, the inversion code provides other variables such as the VC, r_{eff} and standard deviation for fine and coarse modes of the retrieved PSD. The uncertainty of the AERONET inversion products is described by Dubovik et al. (2000). Briefly, the uncertainty in the retrieval of SSA is ± 0.03 for high aerosol load ($\text{AOD}_{440} > 0.4$) and solar zenith angle $> 50°$. For measurements with low aerosol load ($\text{AOD}_{440} < 0.2$), the retrieval accuracy of SSA (λ) drops down to 0.02–0.07 (Dubovik et al., 2000). For high aerosol load and solar zenith angle $> 50°$, errors are about 30–50 % for the imaginary part of the RI. For particles in the size range $0.1 < r < 7$ µm, errors in PSD retrievals are around 10–35 %, while for sizes lower than 1 µm and higher than 7 µm retrieval errors rise up to 80–100%. In this work, the AERONET Version 2 Level 2.0 data obtained at Granada and Cerro Poyos during

Table 1. Instruments on board the ATR-42 aircraft during F30 and F31 flights.

Parameter measured	Instrument	Abbreviation	Scientific objective	Nominal size range (μm)	Wavelength (nm)
Size distribution	Forward scattering spectrometer probe, model 300, Particle Measuring Systems	FSSP-300	Coarse mode concentration	0.28–20	632.8
	Sky optical particle counter, model 1.129, Grimm Technik	GRIMM	Coarse mode concentration	0.25–32	655
	Ultra high-sensitivity aerosol spectrometer, Droplet Measurement Technologies	UHSAS	Aiken + accumulation mode concentration	0.04–1	1054
	Scanning mobility particle sizer, custom-built	SMPS	Aiken + accumulation mode concentration	0.03–0.4	n/a*
Optical properties	3λ integrated nephelometer, model 3563, TSI	Nephelometer	Scattering coefficient	n/a*	450, 550, 700
	Cavity attenuated phase shift, Aerodyne Research Inc.	CAPS	Extinction coefficient	n/a*	530
	Photomètre Léger Aéroporté pour la Surveillance des Masses d'Air	PLASMA	Extinction coefficient, AOD	n/a*	340–2250

* Not applicable.

ChArMEx-ADRIMED 2013 are used. However, due to the strong limitations imposed by the AERONET inversion algorithm ($AOD_{440} > 0.4$ and solar zenith angle $> 50°$), there was no SSA and RI AERONET Level 2.0 retrievals during the campaign. Thus, for comparing AERONET SSA values with GRASP retrievals, the AERONET Level 1.5 cloud screened data corresponding to $AOD > 0.2$ and solar zenith angle $> 50°$ are used in this study.

The multiwavelength Raman lidar MULHACEN, based on a customized version of LR331D400 (Raymetrics S.A.), is used for obtaining vertical profiles of the atmospheric aerosol properties. This system, located at Granada, was incorporated to EARLINET in April 2005 and at present a contributing station to ACTRIS research infrastructure (Aerosols, Clouds, and Trace gases Research InfraStructure Network; http://actris2.nilu.no/). The system has a monostatic biaxial configuration alignment, pointing vertically to the zenith and uses a pulsed Nd:YAG laser with second- and third-harmonic generators, that emits simultaneously pulses at 1064, 532 and 355 nm. The receiving system consists of several detectors, which can split the radiation according to the three elastic channels at 355, 532 (parallel- and perpendicular-polarized; Bravo-Aranda et al., 2013) and 1064 nm; two nitrogen Raman channels at 387 and 607 nm (shifted signal from radiation at 355 and 532 nm, respectively); and a water vapour Raman channel at 408 nm (shifted signal from radiation at 355 nm; Navas-Guzmán et al., 2014). More information can be found in Guerrero-Rascado et al. (2008). The aerosol particle backscatter coefficient profiles obtained from the multiwavelength lidar were obtained by the Klett–Fernald method (Fernald et al., 1972; Fernald, 1984; Klett, 1981, 1985). Total uncertainty in the profiles obtained with Klett method is usually 20 % for β and 25–30 % for α profiles (Franke et al., 2001; Preißler et al., 2011). The procedure suggested by Wandinger and Ansmann (2002) was applied to the lidar data to correct the incomplete overlap. Without correction, the complete overlap for this instrument is above 1200 m a.g.l. (Navas-Guzmán et al., 2011).

2.3 Airborne measurements

During the period from 14 June to 4 July 2013, 16 flights were performed in the framework of ChArMEx-ADRIMED over the Mediterranean Basin with the ATR-42 aircraft of SAFIRE (French aircraft service for environmental research; http://www.safire.fr). These flights ascended or descended performing a spiral trajectory during 30 min. Two of these flights (flight number F30 and F31) took place over Granada on 16 and 17 June 2013, respectively. Figure 1 shows the spiral trajectory of F31 flight that is similar to that of F30, covering in both cases the same atmospheric column. Flight details are described by Mallet et al. (2016) and Denjean et al. (2016).

Table 1 summarizes the instrumentation on board the ATR-42 airplane used in this study. The scanning mobility particle sizer (SMPS) with an accuracy of 5 % (Wiedensohler et al., 2012) and the ultra high-sensitivity aerosol spectrometer (UHSAS) with an accuracy of 10 % (Cai et al., 2008) are used for measuring aerosol number size distribution in

Table 2. Input and output information used for LIRIC and GRASP retrievals.

	LIRIC		GRASP	
Input	Sun photometer* – AOD – VC – RRI and IRI – % sphericity	Lidar Elastic backscattered signal: – 355, 532 and 1064 nm – 532 cross-polarized signal	Sun photometer – AOT or AOD – Total scattered radiances At 440, 670, 870 and 1020 nm	Lidar Elastic backscattered signal: – 355, 532 and 1064 nm
Output	– VC profile for fine and coarse mode		Columnar (fine and coarse) – PSD – RRI and IRI – VC – r_{eff} – SSA – LR – % sphericity (total)	Vertical (fine and coarse) – VC – α and β – SSA

* AERONET product.

the submicron range. The wing-mounted Forward Scattering Spectrometer Probe (FSSP-300) with an accuracy of 30 % (Baumgardner et al., 1992) and the in-cabin GRIMM OPC (sky OPC 1.129) with an accuracy of 10 % (Denjean et al., 2016) were used to measure the optical size distributions in the diameter nominal size range between 0.28 and 20 µm and between 0.3 and 32 µm, respectively. The total particle volume concentrations in the diameter range 0.1–30 µm and volume concentrations of fine (0.1–1 µm) and coarse (1–30 µm) modes were calculated from the measured aerosol number size distributions, assuming that aerosol particles are spherical.

In addition, the nephelometer TSI (model 3563) was used to measure particle scattering coefficients at three wavelengths (450, 550 and 700 nm) with an accuracy of 5 % (Müller et al., 2011) and a cavity attenuated phase shift (CAPS) was employed to obtain particle extinction coefficient at 530 nm with an accuracy of 3 % (Massoli et al., 2010). Also, the PLASMA (Photomètre Léger Aéroporté pour la Surveillance des Masses d'Air) system, which is an airborne sun-tracking photometer, was used to obtain AOD with wide spectral coverage (15 channels between 0.34 and 2.25 µm) with an accuracy of approximately 0.01 (Karol et al., 2013), as well as the particle extinction vertical profiles (Torres et al., 2017).

3 GRASP and LIRIC inversion algorithms

The input information needed by the GRASP and LIRIC algorithms and the aerosol properties retrieved and used in this work are shown in Table 2. The LIRIC algorithm provides height-resolved aerosol VC data for the fine and coarse modes from combined lidar and sun–sky photometer information (Chaikovsky et al., 2008, 2012, 2016; Granados-Muñoz et al., 2014). For this, column-integrated aerosol properties provided by the AERONET code (Dubovik et al., 2002, 2006) are used as input, together with the lidar elastic backscatter signals at three different wavelengths (355, 532, and 1064 nm). These data are put through an iterative procedure based on the Levenberg–Marquardt method, which is described in detail in Chaikovsky et al. (2016). Besides the VC, the algorithm retrieves additional datasets, including profiles of particle α and β coefficients, and LR, among others. AERONET column-integrated products used as input are not modified by LIRIC during the retrieval process.

The GRASP inversion code (Dubovik et al., 2011; Lopatin et al., 2013) was developed at Laboratoire d'Optique Atmospherique (LOA) of the University of Lille. GRASP is based on a similar philosophy than LIRIC code but goes a step further since it simultaneously inverts both the coincident lidar and sun–sky photometer measurement, retrieving vertical, but also column, aerosol optical and microphysical properties for both fine and coarse modes. The simultaneous inversion of lidar and sun–sky photometer measurements is expected to improve the retrievals since the lidar data complement the sky photometer measurement at scattering angles of 180° and the photometer data provide the information (e.g. amount and type) required for lidar retrievals that otherwise would be assumed from climatological data (Bovchaliuk et al., 2016). Therefore, the column aerosol properties obtained by GRASP will differ from the AERONET ones. Additionally, it is worth to note that GRASP allows independently retrieving aerosol optical and microphysical properties for the two distinct aerosol modes, fine and coarse. The retrieval of height-dependent SSA data is an additional advantage of GRASP over LIRIC. GRASP also provides an estimation of the systematic and random errors for both the directly retrieved (PSD, RRI, IRI, SSA) and derived (α, β,

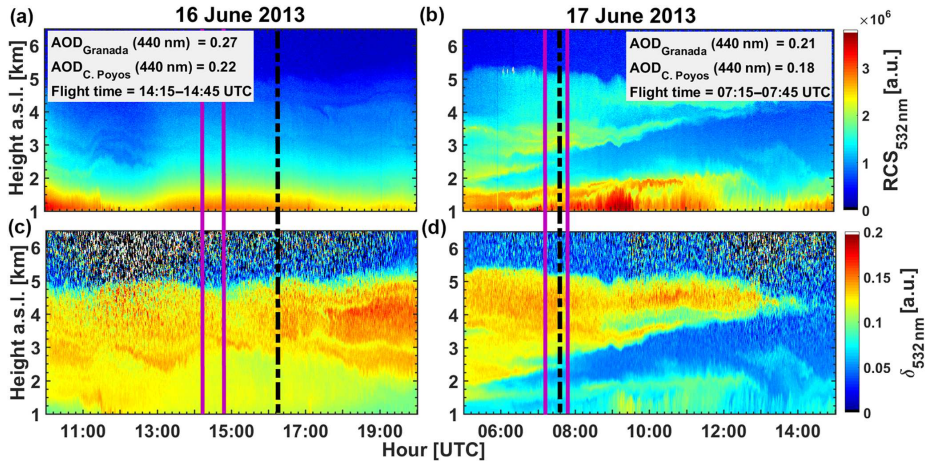

Figure 2. Temporal evolution of the lidar range-corrected signal **(a, b)** and the depolarization ratio **(c, d)** at 532 nm on 16 **(a, c)** and 17 **(b, d)** June 2013. The two purple lines indicate the lidar analysed interval. The black dashed line indicates the sun-photometer measurements.

VC profiles) aerosol properties. The SSA profiles errors are not shown because they are unfortunately not provided at the moment. Additional details on GRASP retrieval algorithm and its performance can be found in Lopatin et al. (2013) and Bovchaliuk et al. (2016).

4 Results

As previously mentioned, two of the ATR-42 flights performed in the framework of ChArMEx-ADRIMED campaign, F30 and F31, were carried out over Granada on 16 and 17 June 2013, respectively. Figure 2 shows the time series of the lidar range-corrected signal (RCS) and the depolarization ratio (δ) at 532 nm on both days measured at Granada station. The RCS is calculated as $P \cdot r^2$, where P is the lidar signal (corrected from background and dark current) and r is the altitude. On the first day, a homogeneous layer is observed from the surface up to 5 km a.s.l., with an elevated aerosol layer coupled to the superficial aerosol layer throughout the day. The next day this layer was decoupled from the aerosol layer close to surface and disappeared around 13:00 UTC; measurements of δ showed that there was an aerosol type below 2.7 km a.s.l. and another aerosol type above this altitude, up to 5.5 km a.s.l. On 16 June, the lidar measurements (marked with purple lines in Fig. 2) obtained during the first flight between 14:15 and 14:45 UTC and sun-photometer measurements collected at 16:22 UTC (black dashed line in Fig. 2) at Granada and Cerro Poyos were selected for further analysis. The selected sun-photometer measurement was the closest measurement available in time to the first flight. On 17 June, the lidar measurements obtained during the second flight (07:15 to 07:45 UTC) and sun–sky photometer measurements obtained at both stations at 07:40 UTC were selected for further analysis.

AERONET products during these flights indicate the presence of dust particles. In fact, on 16 June AOD_{440} at 14:15 UTC was around 0.26 and 0.19 for Granada and Cerro Poyos, respectively, and 0.27 and 0.22 at 16:22 UTC. On this day, the $AE_{440-870}$ was 0.30–0.26 (Granada–Cerro Poyos) at 14:30 UTC and 0.34–0.27 (Granada–Cerro Poyos) at 16:22 UTC, indicating moderate atmospheric aerosol load dominated by coarse particles. On 17 June, the AOD_{440} at 07:40 UTC was 0.21 and 0.18 and the $AE_{440-870}$ was 0.43 and 0.30 for Granada and Cerro Poyos, respectively, which also indicates the predominance of coarse particles on this day. The presence of mineral dust over Granada during both days is confirmed by the analysis of back-trajectory analysis (not shown) by HYSPLIT (Hybrid Single-Particle Lagrangian Integrated Trajectory; Stein et al., 2015; Rolph, 2016), which indicates that the relevant air masses came from the Saharan region, specifically from Algeria, at different heights.

4.1 Comparison of columnar properties retrieved by GRASP and AERONET algorithms

Some of the aerosol columnar properties obtained from AERONET and retrieved by GRASP (combining photometer and lidar measurements) on 16 and 17 June at Granada and Cerro Poyos stations are shown in Figs. 3–5 and summarized in Table 3.

Figure 3 shows the column-integrated PSD retrieved by both AERONET and GRASP algorithms on 16 and 17 June for Granada and Cerro Poyos stations. The retrieved PSD evidence the predominance of coarse mode particles, as expected for dust events (Lyamani et al., 2005; Guerrero-

Table 3. Columnar effective radius and particle volume concentration for coarse and fine particle modes retrieved by GRASP and AERONET algorithms.

			16 June 2013		17 June 2013	
			Granada	Cerro Poyos	Granada	Cerro Poyos
Effective radius (μm)	GRASP	fine	0.12	0.13	0.10	0.12
		coarse	2.2	2.2	2.4	2.2
	AERONET	fine	0.12	0.11	0.11	0.12
		coarse	1.9	1.9	2.1	1.9
Volume concentration ($\mu m^3\ \mu m^{-2}$)	GRASP	fine	0.018	0.017	0.018	0.011
		coarse	0.17	0.15	0.14	0.13
	AERONET	fine	0.015	0.015	0.016	0.010
		coarse	0.14	0.13	0.12	0.11

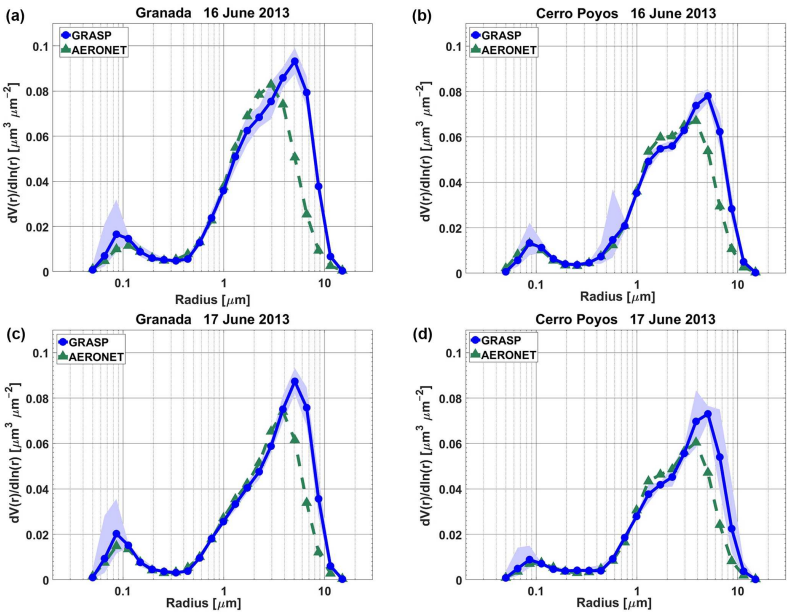

Figure 3. Size distribution retrieved by GRASP (blue) with its uncertainty (shaded area) and by AERONET (green) on 16 **(a, b)** and 17 **(c, d)** June 2013 at Granada **(a, c)** and Cerro Poyos **(b, d)**.

Rascado et al, 2009). Both AERONET and GRASP retrieved PSD present a bimodal behaviour, with the radius of fine mode below 0.5 μm and the radius of coarse mode above 0.5 μm. The differences between the PSD retrieved by GRASP and AERONET are mostly within uncertainties associated with both methods (±10–35 % for the size range from 0.1 to 7 μm and ±35–100 % outside this range; Dubovik et al., 2000) except for the size range 5–8.7 μm, where the differences are higher, especially at 6.64 μm (> 100 %). Furthermore, the coarse mode retrieved by GRASP over both sites shows a clear shift towards higher radii in comparison to the AERONET retrievals (Fig. 3). This shift was also observed by Lopatin et al. (2013) during dust and biomass burning events over Minsk, Belarus, and by Bovchaliuk et al. (2016) during dust events over Dakar, Senegal. These authors attributed this coarse mode shift towards higher radii to the use of the lidar data in the GRASP retrievals. The lidar data provide additional information at scattering angles of 180° and further wavelengths compared to the sun photometer, influencing the size distribution retrieved especially in the coarse mode.

Table 3 summarizes the columnar r_{eff} and VC of fine and coarse modes obtained at both stations by AERONET and GRASP algorithms on 16 and 17 June. The retrieved mi-

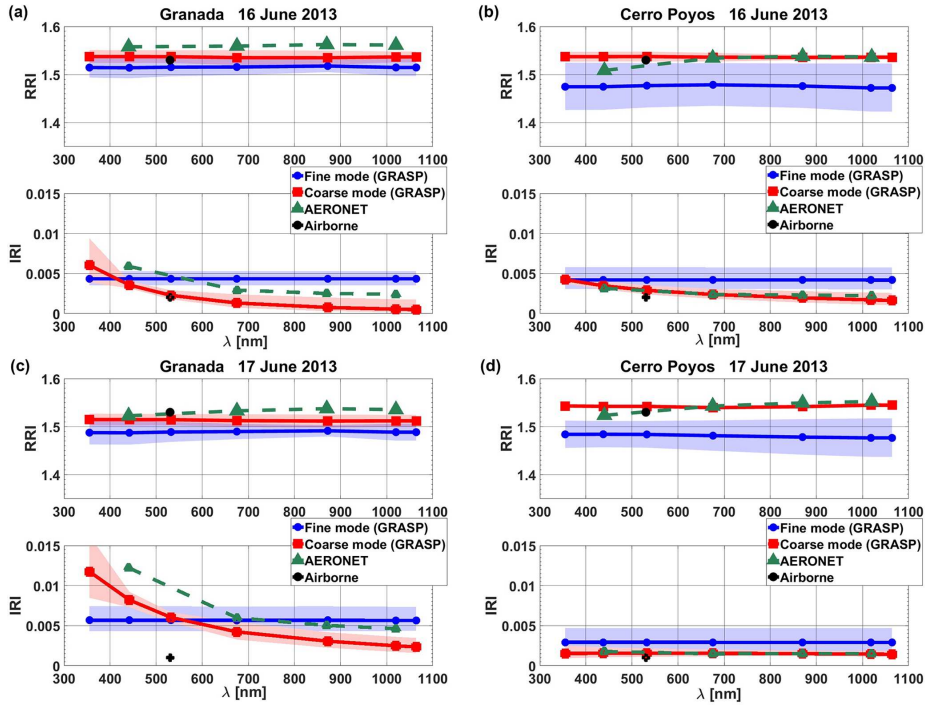

Figure 4. Spectral real (RRI) and imaginary (IRI) refractive indices retrieved by GRASP for the fine (blue) and coarse (red) modes with its uncertainty (shaded area), by AERONET (green) and by airborne measurement (black) on 16 **(a, b)** and 17 **(c, d)** June 2013 in Granada **(a, c)** and Cerro Poyos **(b, d)**.

crophysical properties are similar to those typically obtained during African desert dust events over Granada (Valenzuela et al., 2012b). The fine mode r_{eff} retrieved by both methods ranges between 0.10 and 0.13 µm. Differences between fine mode r_{eff} retrieved by GRASP and AERONET are below 0.02 µm, which are within the uncertainty of the inversions (Lopatin et al., 2013; Torres et al., 2014). For the coarse mode, the r_{eff} values obtained by GRASP were 0.03 µm higher than those retrieved by AERONET but the differences are within the uncertainty range. A similar behaviour is observed for the column-integrated VC, with slightly larger values provided by GRASP for the fine and coarse modes (0.016 ± 0.003 and $0.148 \pm 0.017\,\mu m^3\,\mu m^{-2}$) compared to AERONET ($0.014 \pm 0.003$ and $0.125 \pm 0.013\,\mu m^3\,\mu m^{-2}$), but differences are still within the uncertainties.

Figure 4 illustrates the retrieved columnar RRI and IRI for each day obtained by GRASP and AERONET at Granada and Cerro Poyos. Moreover, RRI and IRI at 530 nm estimated by Denjean et al. (2016) using airborne measurements over Granada on 16 and 17 June are included in the plot. AERONET provides RRI and IRI for the whole size distribution, while GRASP is able to provide RRI and IRI for fine and coarse modes separately. The RRI retrieved by GRASP and AERONET algorithms do not show any spectral wavelength variations, and the differences between RRI values retrieved by both inversion algorithms are within the uncertainties (differences below 5 %). Because of the predominance of the coarse mode during the analysed dust event, both the AERONET and airborne RRI values are close to the values retrieved by GRASP for the coarse mode, with differences < 0.03, on both days. In contrast, the IRI values retrieved by GRASP for the fine mode present a rather low spectral dependence while IRI values for the coarse mode presents a clear increase in the UV region. These results are coherent with those reported for different absorption species by Schuster et al. (2016) using AERONET data. At Cerro Poyos we did not find the spectral dependence of the IRI typically associated with mineral dust. The AOD at 440 nm was around 0.18–0.27 and we used AERONET Level 1.5 products; therefore, these values have large uncertainties (> 50 %; Dubovik et al., 2000). The lack of spectral dependence can be just an artifact of the inversion. However, it is worthy to note that at Cerro Poyos the PSD shows a mode in the coarse mode size range around 1 µm. As there is still discussion in the scientific community about dust RI and about the differences in dust particles between different sources (e.g. Colarco et al., 2014), results can suggest possible differences in dust RI between long-range transported and mixture

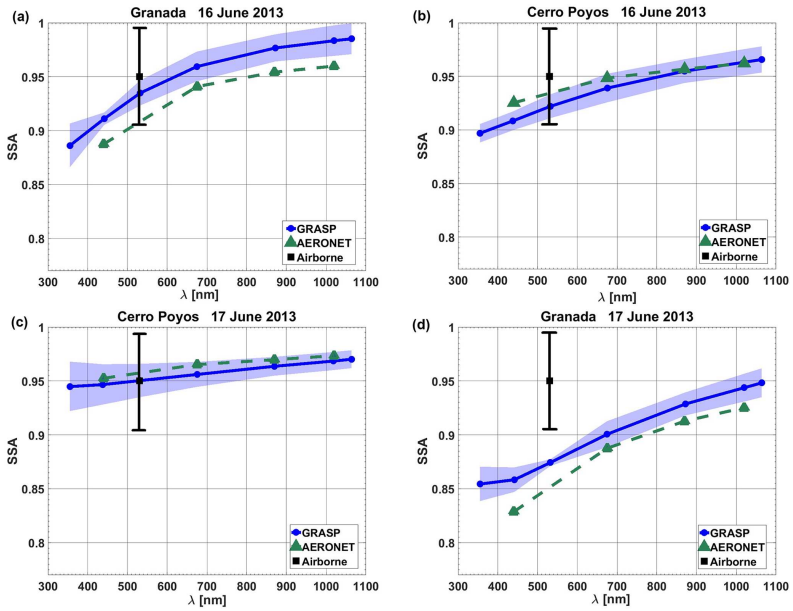

Figure 5. Single-scattering albedo retrieved by GRASP (blue) with its uncertainty (shaded area), by AERONET (green) and by airborne measurement (black) with its uncertainty on 16 **(a, b)** and 17 **(c, d)** June 2013 at Granada **(a, c)** and Cerro Poyos **(b, d)**.

with local dust injections (the area is very dry in summer, thus favouring local mineral dust resuspension) and local pollution. The RRI and IRI values provided by AERONET show good agreement with GRASP retrievals for the coarse mode, something expected due to the large predominance of dust particles. Better agreement between IRI retrieved by AERONET and by GRASP for the coarse mode was found for Cerro Poyos, with differences $\sim 10\,\%$, while for Granada these differences are between 35 and 80 % (larger differences at lower wavelengths). The high discrepancy between IRI retrieved by AERONET and by GRASP in the case of Granada can be explained by the uncertainty associated with the incomplete lidar overlap. Cerro Poyos station is located above the lidar incomplete overlap height, and thus the effect of the incomplete overlap on the retrieval is negligible. This is not the case for the retrieval from Granada station. On 16 June, IRI airborne values estimated at 530 nm are close to IRI retrieved by GRASP at 532 nm for the coarse mode, and the differences are within the associated uncertainties. In contrast, on 17 June, there are more differences between IRI values retrieved by GRASP at Granada station and those estimated from airborne measurement, with differences over 100 %, whereas for the Cerro Poyos retrievals the differences are 50 %.

Figure 5 shows the columnar SSA values retrieved by GRASP and AERONET on 16 and 17 June at Granada and Cerro Poyos. Moreover, the SSA value at 530 nm calculated by Denjean et al. (2016) for dust layers using airborne measurements during the campaign was 0.95 ± 0.04. SSAs retrieved by GRASP at 532 nm are close to the airborne value. Better agreement with this value is found for the retrievals from Granada on 16 June and at Cerro Poyos on 17 June. The differences from Granada on 17 June could be due to the fact that the in situ value was calculated for the dust layer whereas GRASP and AERONET use sun-photometer data, which measure the total atmospheric column. Furthermore, in the case of Granada station, these measurements could be influenced by injections of local pollution. The retrieved SSA values are in the range of 0.85–0.98 (355–1064 nm wavelength range), the typical values for dust aerosols (Dubovik et al., 2002; Toledano et al., 2011; Lopatin et al., 2013). Both AERONET and GRASP retrievals follow the same pattern with wavelength, with increasing SSA as wavelength increases, which is a typical characteristic of dust aerosols (Dubovik et al., 2002; Valenzuela et al., 2012b). Differences between SSA retrieved by AERONET and GRASP algorithms are below 0.03 at all wavelengths, within the uncertainties associated with each method. The discrepancies between SSA retrieved by AERONET and GRASP algorithms are obtained for Cerro Poyos station ($< 1\,\%$) at 1020 nm in particular, whereas for Granada retrievals the differences are bigger and the lowest discrepancies are obtained at 675 nm.

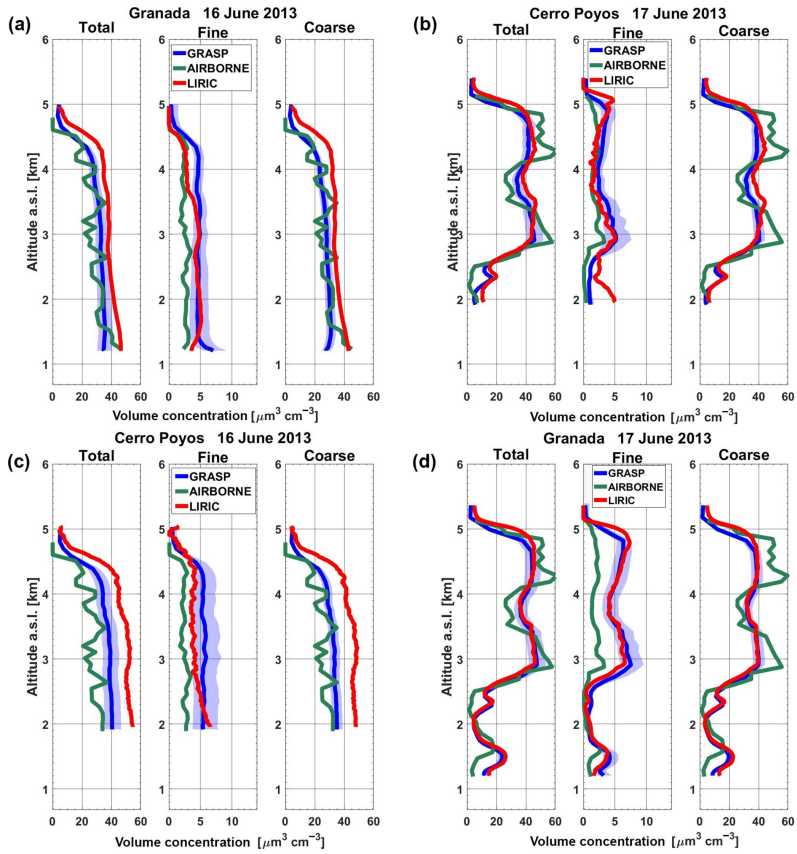

Figure 6. Volume concentration profile (total, fine and coarse mode) retrieved by GRASP (blue) with its uncertainty (shaded area), aircraft measurements (green) and LIRIC (red) on 16 **(a, b)** and 17 **(c, d)** June 2013 at Granada **(a, c)** and Cerro Poyos **(b, d)**.

4.2 Comparison of vertical properties retrieved by GRASP and LIRIC algorithms and in situ airborne measurements

Figure 6 shows particle VC profiles for the fine, coarse and total (fine + coarse) modes, retrieved by GRASP and LIRIC, together with the results obtained with airborne instrumentation. Generally, there is good agreement between the profiles retrieved by GRASP and LIRIC and those obtained by the airborne instrumentation, with both retrievals and the airborne data reproducing similar vertical structures on both days. The airborne data show a larger variability compared to GRASP and LIRIC mostly associated with their larger uncertainty and the fact that the airborne data are instantaneous measurements whereas the lidar data are on average over a 30 min period.

Table 4 summarizes the VC mean values and associated standard deviations retrieved from the in situ airborne measurements, GRASP and LIRIC profiles shown in Fig. 6. Data are analysed only for those layers with total VC above 20 μm^3 cm^{-3} to avoid undesirable outliers for low aerosol loads. Hence for 16 June we analyse the layer between 1.2 and 4.5 km a.s.l., and for 17 June the analysed layer is from 2.6 to 5.0 km a.s.l. There is a slight contribution of the fine mode in the dust layers on both days, with values between 3 μm^3 cm^{-3} for the airborne data and 5.3 μm^3 cm^{-3} for LIRIC. In general, it is observed that the coarse mode contributes the most to the total VC, which is expected due to the predominance of mineral dust. Coarse mode concentration values range between 28 ± 4 and 46 ± 4 μm^3 cm^{-3} on 16 June and 35 ± 5 and 42 ± 11 μm^3 cm^{-3} on 17 June, depending on the dataset considered. GRASP and LIRIC retrievals both overestimate the airborne data for the fine mode while they overestimate the total mode on 16 June and underestimate the total mode on 17 June using sun-photometer data at both Granada and Cerro Poyos stations. In the case of fine mode, the differences between the airborne and the retrievals are lower than 5 μm^3 cm^{-3} (about 80 %). The agree-

Table 4. Comparison of fine, coarse and total mean volume concentration ($\mu m^3\,cm^{-3}$) retrieved by GRASP, measured by airborne and retrieved by LIRIC for dust layers on 16 June (up to 4.5 km a.s.l.) and 17 June (from 2.6 to 5.0 km a.s.l.).

Volume concentration ($\mu m^3\,cm^{-3}$)		16 June 2013		17 June 2013	
		Granada	Cerro Poyos	Granada	Cerro Poyos
Fine	GRASP	4.7 ± 0.6	5.5 ± 0.3	5.5 ± 1.3	3.5 ± 1.0
	AIRBORNE	2.6 ± 0.4	2.6 ± 0.4	1.9 ± 0.6	1.9 ± 0.6
	LIRIC	4.2 ± 0.8	4.6 ± 1.0	5.3 ± 1.3	2.8 ± 1.1
Coarse	GRASP	28 ± 4	32 ± 4	35 ± 7	36 ± 5
	AIRBORNE	31 ± 8	27 ± 5	41 ± 11	41 ± 11
	LIRIC	37 ± 4	46 ± 4	35 ± 5	38 ± 6
Total	GRASP	33 ± 4	38 ± 4	40 ± 8	39 ± 6
	AIRBORNE	33 ± 8	28 ± 5	42 ± 11	42 ± 11
	LIRIC	41 ± 5	50 ± 4	40 ± 6	41 ± 6

ment for the coarse mode is high with differences lower than $6\,\mu m^3\,cm^{-3}$ (25 %), except for the LIRIC inversion from Cerro Poyos on 16 June, where the difference is $19\,\mu m^3\,cm^{-3}$ (around 80 %). Both algorithms show the largest differences for the retrievals from Cerro Poyos on 16 June, whereas the differences for the retrievals from Granada for total and coarse mode are around 15 and 25 % using GRASP and LIRIC, respectively. On 17 June for Granada retrieval, the differences between both algorithms and airborne data below 2 km a.s.l. could be explained because the flight was not exactly over Granada, as shown in Fig. 1, and differences are expected in the lower 2 km of the atmosphere because of the influence of the city. In the dust layer on 17 June, the differences are around 20 % for coarse and total VC by both algorithms for Granada and Cerro Poyos stations. Differences between GRASP and LIRIC retrievals are below 30 %, well within the combined uncertainty from both retrievals. There are no accurate calculations of the uncertainty associated with LIRIC profiles, but it is estimated to be around 50 % in cases of mineral dust (Granados-Muñoz et. al., 2016).

Figure 7 shows the aerosol β coefficient profiles at 355, 532 and 1064 nm retrieved by GRASP and the profiles calculated by Klett–Fernald method. The LR used in the Klett method is assumed constant for the entire profile and was computed by fitting the integral of the different extinction profiles to the measured AOD. However, GRASP uses both sun–sky radiances and the backscatter lidar data to provide LR values, both in column-integrated and vertical profiles. The GRASP LR values are close to the LR values used by Klett–Fernald method; these values are typical for Saharan dust measured over the south-eastern Spain (Guerrero-Rascado et al., 2009; Navas-Guzmán et al., 2013). Below 1.6 km, the Klett retrieval at 355 showed unrealistic values probably associated with instrumental problems. However, for GRASP this problem does not appear, probably due to the combined used of lidar and sun-photometer data. The GRASP algorithm underestimates the values obtained by the Klett–Fernald method, except for the Cerro Poyos retrieval on 17 June, with larger differences for Granada retrievals. Nevertheless, the differences are within the uncertainties claimed for our system (approximately 30 %). The differences at the ultraviolet channel reached 19 % and around 9 % for Granada and Cerro Poyos retrievals, respectively. The discrepancies between backscatter coefficient profiles at 532 nm retrieved by GRASP and Klett–Fernald are around 16 % for Granada retrieval on 16 June and 11 % on 17 June and for Cerro Poyos retrievals on both days. In the case of backscatter coefficient profiles at 1064 nm, the differences between both retrievals are close to 24 % for Granada on 16 June and Cerro Poyos on 17 June, while for the other two cases the differences are the lowest (6 %).

The comparison between aerosol α coefficient profiles retrieved by GRASP and those measured by airborne instruments (CAPS and PLASMA) is shown in Fig. 8. Profiles retrieved by GRASP show good agreement with the CAPS data (measurements only on 16 June at 532 nm), even with slightly higher values for GRASP of approximately $3 \pm 3\,Mm^{-1}$ (7 %) and $9 \pm 5\,Mm^{-1}$ (18 %) for the inversions from Granada and Cerro Poyos, respectively. GRASP extinction coefficient retrievals were larger than PLASMA measurements at all wavelengths, with larger differences at the ultraviolet channel (~ 50 %). On 16 June, the differences for the ultraviolet channel are $20 \pm 11\,Mm^{-1}$ (45 %) and for the visible and ultraviolet channels are $11 \pm 8\,Mm^{-1}$ (30 and 40 %, respectively). These differences were similar or lower than those obtained by Karol et al. (2013) when comparing PLASMA with lidar data. On 17 June, PLASMA and GRASP show the same layers, but their differences are larger, reaching 50 % for the visible channel and more than 60 % for the ultraviolet and infrared channels. As GRASP

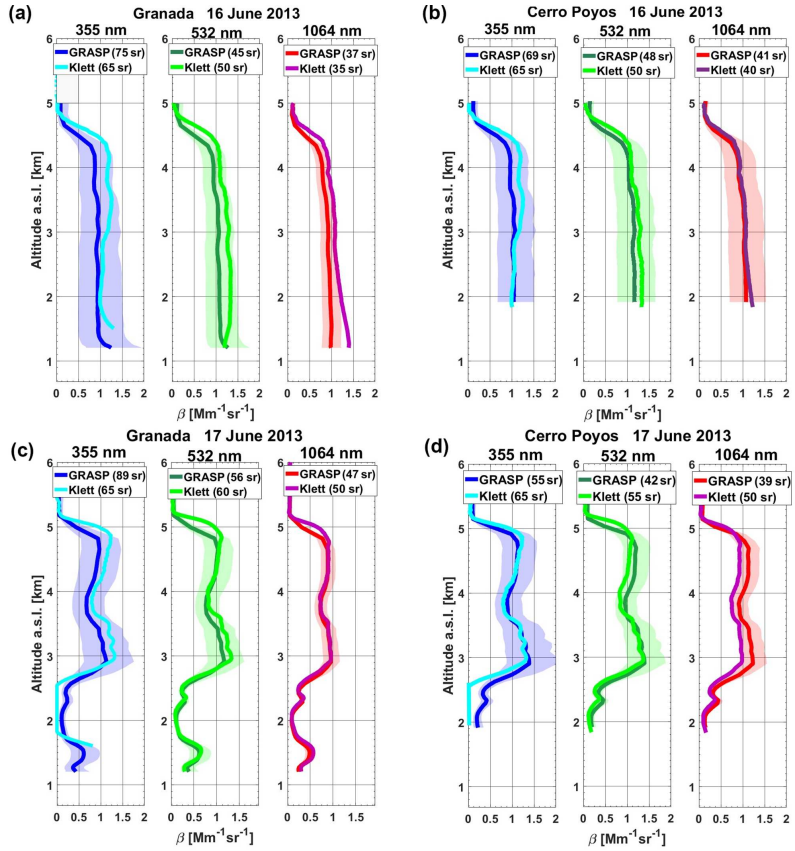

Figure 7. Aerosol backscatter coefficient profiles retrieved at 355, 532 and 1064 nm by GRASP with its uncertainty (shaded area) and Klett–Fernald on 16 **(a, b)** and 17 **(c, d)** June 2013 at Granada **(a, c)** and Cerro Poyos **(b, d)**.

and LIRIC reproduce the same layer structures for volume concentrations, these differences can be mainly associated with PLASMA.

Vertical profiles of SSA obtained by GRASP at Granada and Cerro Poyos station on 16 and 17 June are shown in Fig. 9. As SSA is an intensive aerosol parameter, only SSA values for the layers with large aerosol loads are represented. On 16 June, there are no remarkable changes in SSA with altitude, which agrees with the extinction and backscatter coefficients profiles and with the particle volume concentrations. For 17 June, vertical profiles of SSA are sensitive to the different aerosol layers with different aerosol types illustrating the capabilities of GRASP for detecting different aerosol layers with different composition. Nonetheless, the values of SSA are also within those associated with dust aerosol in previous studies (Dubovik et al., 2002; Toledano et al., 2011; Lopatin et al., 2013). Differences are observed again between the SSA profiles obtained at Granada and Cerro Poyos stations. On 16 June SSA differences between both retrievals are lower than 2 % while on 17 June differences reach up to 10 %. This result is again associated with overlap issues, although the influence of the city, i.e. injection of large amounts of particles confined below the altitude of Cerro Poyos, cannot be neglected in sky radiance measurements.

Figure 10 shows scattering AE computed between 450 and 700 nm, AE_{sca} (450–700), obtained by GRASP algorithm at Granada and Cerro Poyos stations together with those obtained from nephelometer airborne measurements. GRASP scattering coefficient profiles are calculated by multiplying the extinction coefficient by the SSA at the same wavelength. Despite the fact that the AE_{sca} (450–700) profiles from the airplane date are noisier than GRASP profiles, general good agreement is observed, with discrepancies within the uncertainties. In general, GRASP values are larger than the airborne data for altitudes above 2.5 km a.s.l. Above this altitude, the AE_{sca} (450–700) values are close to zero for the airborne data on both days, which is typical of aerosols dom-

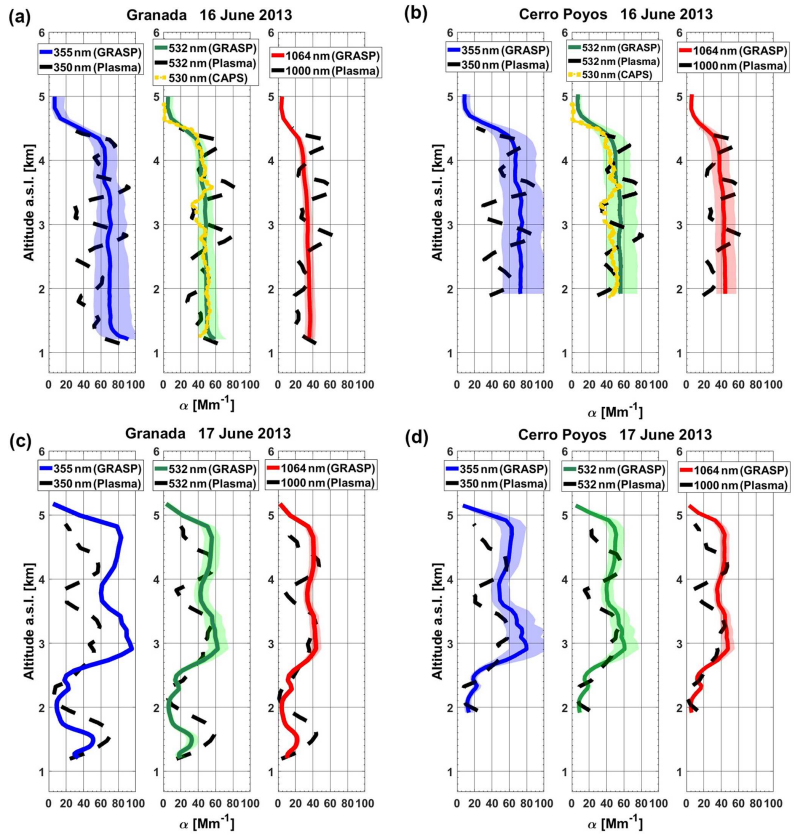

Figure 8. Aerosol extinction coefficient profiles retrieved by GRASP (355, 532 and 1064 nm) with its uncertainty (shaded area), PLASMA (350, 530 and 1000 nm) and CAPS (530 nm) on 16 **(a, b)** and 17 **(c, d)** June 2013 at Granada **(a, c)** and Cerro Poyos **(b, d)**.

inated by coarse particles (Bergstrom et al., 2007). However, in the lower part of the profiles AE_{sca} (450–700) values are larger (~ 0.7 and ~ 1.6 for the airborne data on 16 and 17 June, respectively) and GRASP profiles underestimate the airborne data. The values for these lower altitudes, including those retrieved by GRASP using the sun-photometer data measured at Granada and the airborne data, were similar to in situ measurements at IISTA-CEAMA, with values around 0.70 ± 0.10 and 1.67 ± 0.07 on 16 and 17 June, respectively. GRASP profiles have similar values above and below 2.5 km a.s.l. with better agreement between airborne data and Cerro Poyos retrieval. The Granada retrieval shows more differences on 17 June, the case with aerosol layers with different aerosol types. On 17 June, in the range of ~ 1.8–2.7 km a.s.l., the aerosol load was low ($\sim 5\ \mu m^3\ cm^{-3}$) and, hence, SSA and AE values could be less reliable in this layer. However, the layer up to 1.8 km a.s.l. showed a moderate concentration ($\sim 17\ \mu m^3\ cm^{-3}$) with a different composition from layers above 2.7 km a.s.l., as shown by the SSA and AE profiles (Figs. 9 and 10, respectively).

Table 5. Mean value of backscatter Ångström exponent ($\beta - AE$) and colour ratio (CR) between 532 and 1064 nm, retrieved by GRASP for dust layers on 16 and 17 June 2013.

	16 June 2013		17 June 2013	
	Granada	Granada	Granada	Granada
$\beta - AE$	0.65 ± 0.07	0.46 ± 0.05	0.63 ± 0.12	0.40 ± 0.10
CR	1.15 ± 0.05	1.13 ± 0.05	1.09 ± 0.09	1.08 ± 0.04

Finally, Table 5 shows the mean values with ± 1 SD (standard deviation) of $\beta - AE$ (532–1064) and colour ratio ($CR = \beta$ (532 nm)/β (1064 nm)) calculated by GRASP in the layer between 1.8 and 4.5 km a.s.l. and between 2.8 and 5.0 km a.s.l. on 16 and 17 June, respectively. The values of $\beta - AE$ and CR are 0.5 ± 0.2 and 1.3 ± 0.3, respectively, which is in the range of typical values for dust aerosols (Perrone et al., 2014).

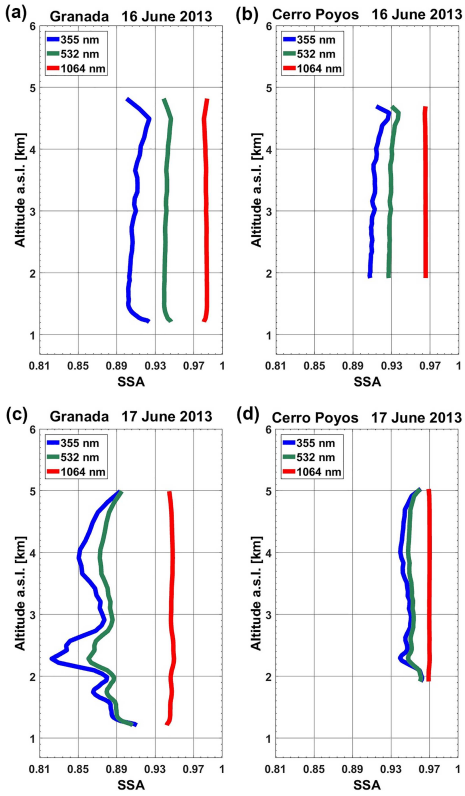

Figure 9. Single-scattering albedo profiles at 355, 532 and 1064 nm retrieved by GRASP on 16 **(a, b)** and 17 **(c, d)** June 2013 at Granada **(a, c)** and Cerro Poyos **(b, d)**.

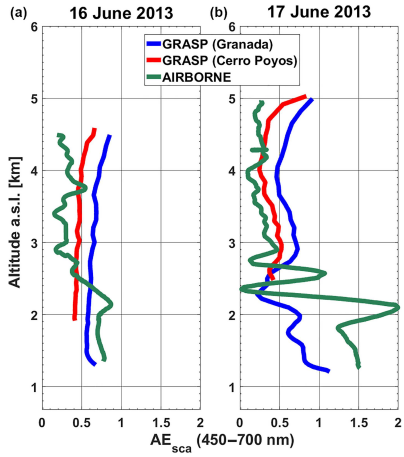

Figure 10. Scattering Ångström exponent (450–700 nm) retrieved by GRASP at Granada (blue) and Cerro Poyos (red) and aircraft measurements (green) on 16 **(a)** and 17 **(b)** June 2013.

5 Summary and conclusion

The GRASP algorithm is applied to lidar and sun–sky photometer measurements at Granada during the ChArMEx-ADRIMED campaign in summer 2013. Data from a second photometer at 1.2 km above the lidar system are also used, located above the lidar incomplete overlap height. This second sun photometer allows us to explore the effect of the lidar incomplete overlap on the retrievals and the influence of the aerosol vertical layering on the results, especially in cases of complex structures when different aerosol types are observed below and above Cerro Poyos. The optical and microphysical properties retrieved by GRASP using independent AERONET data have been compared with airborne measurements corresponding to two flights.

The flights took place on 16 and 17 June 2013, during dust events affecting Granada. The GRASP retrievals show a good agreement with AERONET products, with discrepancies well below the uncertainties. Total volume concentration profiles retrieved by GRASP and airborne measurements show a good agreement with differences around 15 % on 16 June using for the retrieval sun-photometer data measured at Granada and on 17 June using for the retrieval sun-photometer data measured at Cerro Poyos. The agreement for the aerosol backscatter profiles with respect to those obtained using only lidar data and Klett–Fernald algorithm are quite good using both station data, showing differences below 12 % at 355 and 532 nm for Cerro Poyos. In the case of the aerosol extinction profiles, good agreement was found between GRASP and the CAPS data (differences below 20 %), while the comparison with PLASMA data shows larger differences. The SSA profiles show values typical of dust aerosols and the differences between retrievals using sun-photometer data measured at Granada and Cerro Poyos are below 10 % at the lidar wavelengths. Other aerosol properties obtained with GRASP, like the colour ratio and the backscatter AE, also show similar values to those observed in the literature for dust aerosols.

GRASP algorithm is quite robust as shows the agreement between the optical and microphysical properties retrieved by AERONET products and airborne measurements. Results obtained here show that the combination of lidar and sun-photometer data can provide improved and more complete column-integrated data compared to AERONET retrieval. Reliable vertically resolved properties such as the SSA, extinction or volume concentration are also provided, improving the capabilities of previous algorithms such as LIRIC.

Nonetheless, the retrieved scattering AE profiles together with the better agreement found between Cerro Poyos retrievals and the aircraft compared to Granada retrievals indicate that GRASP vertical distribution of some of the aerosol properties is still affected by considerable uncertainties. This is an expected result because of the use of the column-integrated sun-photometer data.

The analysis presented here is useful as a primary evaluation of the GRASP algorithm using sun photometer and lidar signal to retrieve aerosol microphysical properties, both integrated along the vertical column and as vertical profiles, and also to obtain the fine and coarse mode aerosol RI and SSA, which is not possible with the current AERONET inversion. The use of a second sun photometer located over the local atmospheric boundary layer can be very relevant for the study of the properties of aerosol layers with features different than the atmospheric boundary layer aerosol. However, the presented analysis is representative of Saharan dust transport to southern Europe, and still it is necessary to test a more complete dataset that includes different aerosol loads and types. In future studies, we could try to combine one lidar with two sun–sky photometers at different heights to try improving the retrievals in the cases with different aerosol layers. In addition, in order to validate the presented GRASP scheme, in the future we plan to use a database from global aerosol models (e.g. GEOS-5) following an approach similar to Whiteman et al. (2018).

Data availability. The data from lidar system of the Granada station can be accessed through the EARLINET database (see http://access.earlinet.org/EARLINET/SearchPage.aspx). The data corresponding to column-integrated properties at Granada and Cerro Poyos can be obtained from the AERONET database (see https://aeronet.gsfc.nasa.gov/). The aircraft data are available on the ChArMEx database (http://mistrals.sedoo.fr/ChArMEx/). GRASP inversion algorithm software used in this work is free and publicly available at http://www.grasp-open.com.

Competing interests. The authors declare that they have no conflict of interest.

Special issue statement. This article is part of the special issue "CHemistry and AeRosols Mediterranean EXperiments (ChArMEx) (ACP/AMT inter-journal SI"). It is not associated with a conference.

Acknowledgements. This work was supported by the Andalusia Regional Government through project P12-RNM-2409, by the Spanish Ministry of Economy and Competitiveness through project CGL2013-45410-R and CGL2016-81092-R and through grant FPI (BES-2014-068893), by the "Juan de la Cierva-Formación" program (FJCI-2014-22052) and the Marie Skłodowska-Curie Individual Fellowships (IF) ACE_GFAT (grant agreement no. 659398), and by the University of Granada through "Plan Propio. Programa 9 Convocatoria 2013". The financial support for EARLINET in the ACTRIS Research Infrastructure Project by the European Union's Horizon 2020 research and innovation programme through project ACTRIS-2 (grant agreement no. 654109). The authors thankfully acknowledge the FEDER program for the instrumentation used in this work and the Sierra Nevada National Park, for its support for the operation of Cerro Poyos station.

This work is part of the ChArMEx project supported by ADEME, CEA, CNRS-INSU and Météo- France through the multidisciplinary programme MISTRALS (Mediterranean Integrated STudies at Regional And Local Scales). We thank the instrument scientists, pilots and ground crew of SAFIRE for facilitating the instrument integration and conducting flight operations. Finally, the authors would like to acknowledge the use of GRASP inversion algorithm software (http://www.grasp-open.com) in this work.

Edited by: François Dulac
Reviewed by: two anonymous referees

References

Alados-Arboledas, L., Müller, D., Guerrero-Rascado, J. L., Navas-Guzman, F., Pérez-Ramírez, D., and Olmo, F. J.: Optical and microphysical properties of fresh biomass burning aerosol retrieved by Raman lidar, and star-and sun-photometry, Geophys. Res. Lett., 38, L01807, https://doi.org/10.1029/2010gl045999, 2011.

Ansmann, A., Riebesell, M., Wandinger, U., Weitkamp, C., Voss, E., Lahmann, W., and Michaelis, W.: Combined Raman elastic backscatter LIDAR for vertical profiling of moisture, aerosol extinction, backscatter, and LIDAR ratio, Appl. Phys., B55, 18–28, https://doi.org/10.1007/BF00348608, 1992.

Barreto, Á., Cuevas, E., Granados-Muñoz, M.-J., Alados-Arboledas, L., Romero, P. M., Gröbner, J., Kouremeti, N., Almansa, A. F., Stone, T., Toledano, C., Román, R., Sorokin, M., Holben, B., Canini, M., and Yela, M.: The new sun-sky-lunar Cimel CE318-T multiband photometer – a comprehensive performance evaluation, Atmos. Meas. Tech., 9, 631–654, https://doi.org/10.5194/amt-9-631-2016, 2016.

Barreto, Á., Román, R., Cuevas, E., Berjón, A. J., Almansa, A. F., Toledano, C., González, R., Hernández, Y., Blarel, L., Goloub, P., Guirado, C., and Yela, M.: Assessment of nocturnal aerosol optical depth from lunar photometry at the Izaña high mountain observatory, Atmos. Meas. Tech., 10, 3007–3019, https://doi.org/10.5194/amt-10-3007-2017, 2017.

Baumgardner, D., Dye, J. E., Gandrud, B. W., and Knollenberg, R. G.: Interpretation of measurements made by the Forward Scattering Spectrometer Probe (FSSP-300) during the Airborne Arctic Stratospheric Expedition, J. Geophys. Res., 97, 8035–8046, https://doi.org/10.1029/91JD02728, 1992.

Bergstrom, R. W., Pilewskie, P., Russell, P. B., Redemann, J., Bond, T. C., Quinn, P. K., and Sierau, B.: Spectral absorption properties of atmospheric aerosols, Atmos. Chem. Phys., 7, 5937-5943, https://doi.org/10.5194/acp-7-5937-2007, 2007.

Böckmann, C.: Hybrid regularization method for the ill-posed inversion of multiwavelength lidar data to determine aerosol size distributions, Appl. Optics, 40, 1329–1342, 2001.

Boucher, O., Randall, D., Artaxo, P., Bretherton, C., Feingold, G., Forster, P., Kerminen, V.-M., Kondo, Y., Liao, H., Lohmann, U., Rasch, P., Satheesh, S. K., Sherwood, S., Stevens, B., and Zhang, X. Y.: Clouds and Aerosols, in: Climate Change 2013: The Physical Science Basis. Contribution of Working Group I to the Fifth Assessment Report of the Intergovernmental Panel on Climate Change, edited by: Stocker, T. F., Qin, D., Plattner, G.-K., Tig-

nor, M., Allen, S. K., Boschung, J., Nauels, A., Xia, Y., Bex, V., and Midgley, P. M., Cambridge University Press, Cambridge, UK and New York, USA, 571–657, 2013.

Bovchaliuk, V., Goloub, P., Podvin, T., Veselovskii, I., Tanre, D., Chaikovsky, A., Dubovik, O., Mortier, A., Lopatin, A., Korenskiy, M., and Victori, S.: Comparison of aerosol properties retrieved using GARRLiC, LIRIC, and Raman algorithms applied to multi-wavelength lidar and sun/sky-photometer data, Atmos. Meas. Tech., 9, 3391–3405, https://doi.org/10.5194/amt-9-3391-2016, 2016.

Bravo-Aranda, J. A., Navas-Guzmán, F., Guerrero-Rascado, J. L., Pérez-Ramírez, D., Granados-Muñoz, M. J., and Alados-Arboledas, L.: Analysis of lidar depolarization calibration procedure and application to the atmospheric aerosol characterization, Int. J. Remote Sens., 34, 3543–3560, 2013.

Bravo-Aranda, J. A., Titos, G., Granados-Muñoz, M. J., Guerrero-Rascado, J. L., Navas-Guzmán, F., Valenzuela, A., Lyamani, H., Olmo, F. J., Andrey, J., and Alados-Arboledas, L.: Study of mineral dust entrainment in the planetary boundary layer by lidar depolarization technique, Tellus B, 67, 26180, https://doi.org/10.3402/tellusb.v67.26180, 2015.

Cai, Y., Montague, D. C., Mooiweer-Bryan, W., and Deshler, T.: Performance characteristics of the ultra-high sensitivity aerosol spectrometer for particles between 55 and 800 nm: Laboratory and field studies, J. Aerosol Sci., 39, 759–769, 2008.

Calvo, A. I., Olmo, F. J., Lyamani, H., Alados-Arboledas, L., Castro, A., Fernández-Raga, M., and Fraile, R.: Chemical composition of wet precipitation at the background EMEP station in Víznar (Granada, Spain) (2002–2006), Atmos. Res., 96, 408–420, 2010.

Chaikovsky, A., Dubovik, O., Goloub, P., Balashevich, N., Lopatsin, A., Karol, Y., Denisov, S., and Lapyonok, T.: Software package for the retrieval of aerosol microphysical properties in the vertical column using combined lidar/photometer data (test version), Technical Report, Institute of Physics, National Academy of Sciences of Belarus, Minsk, Belarus, 2008.

Chaikovsky, A., Dubovik, O., Goloub, P., Tanré, D.,Pappalardo, G., Wandinger, U., Chaikovskaya, L., Denisov, S., Grudo, Y., Lopatsin, A., Karol, Y., Lapyonok, T., Korol, M., Osipenko, F., Savitski, D., Slesar, A., Apituley, A., Arboledas, L. A., Binietoglou, I., Kokkalis, P., Granados Muñoz, M. J., Papayannis, A., Perrone, M. R., Pietruczuk, A., Pisani, G., Rocadenbosch, F., Sicard, M., De Tomasi, F., Wagner, J., and Wang, X.: Algorithm and software for the retrieval of vertical aerosol properties using combined lidar/radiometer data: dissemination in EARLINET, 26th International Laser and Radar Conference, Porto Heli, Greece, 2012.

Chaikovsky, A., Dubovik, O., Holben, B., Bril, A., Goloub, P., Tanré, D., Pappalardo, G., Wandinger, U., Chaikovskaya, L., Denisov, S., Grudo, J., Lopatin, A., Karol, Y., Lapyonok, T., Amiridis, V., Ansmann, A., Apituley, A., Allados-Arboledas, L., Binietoglou, I., Boselli, A., D'Amico, G., Freudenthaler, V., Giles, D., Granados-Muñoz, M. J., Kokkalis, P., Nicolae, D., Oshchepkov, S., Papayannis, A., Perrone, M. R., Pietruczuk, A., Rocadenbosch, F., Sicard, M., Slutsker, I., Talianu, C., De Tomasi, F., Tsekeri, A., Wagner, J., and Wang, X.: Lidar-Radiometer Inversion Code (LIRIC) for the retrieval of vertical aerosol properties from combined lidar/radiometer data: development and distribution in EARLINET, Atmos. Meas. Tech., 9, 1181–1205, https://doi.org/10.5194/amt-9-1181-2016, 2016.

Colarco, P. R., Nowottnick, E. P., Randles, C. A., Yi, B., Yang, P., Kim, K.-M., Smith, J. A., and Bardeen, C.: Impact of radiatively interactive dust aerosols in the NASA GEOS-5 climate model: Sensitivity to dust particle shape and refractive index, J. Geophys. Res., 119, 753–786, https://doi.org/10.1002/2013JD020046, 2014.

Córdoba-Jabonero, C., Sorribas, M., Guerrero-Rascado, J. L., Adame, J. A., Hernández, Y., Lyamani, H., Cachorro, V., Gil, M., Alados-Arboledas, L., Cuevas, E., and de la Morena, B.: Synergetic monitoring of Saharan dust plumes and potential impact on surface: a case study of dust transport from Canary Islands to Iberian Peninsula, Atmos. Chem. Phys., 11, 3067–3091, https://doi.org/10.5194/acp-11-3067-2011, 2011.

Denjean, C., Cassola, F., Mazzino, A., Triquet, S., Chevaillier, S., Grand, N., Bourrianne, T., Momboisse, G., Sellegri, K., Schwarzenbock, A., Freney, E., Mallet, M., and Formenti, P.: Size distribution and optical properties of mineral dust aerosols transported in the western Mediterranean, Atmos. Chem. Phys., 16, 1081–1104, https://doi.org/10.5194/acp-16-1081-2016, 2016.

Dubovik, O. and King, M.: A flexible inversion algorithm for retrieval of aerosol optical properties from Sun and sky radiance measurements, J. Geophys. Res., 105, 20673–20696, https://doi.org/10.1029/2000JD900282, 2000.

Dubovik, O., Smirnov, A., Holben, B. N., King, M., Kaufman, Y. J., Eck, T. F., and Slutsker, I.: Accuracy assessments of aerosol optical properties retrieved from Aerosol Robotic Network (AERONET) sun and sky radiance measurements, J. Geophys. Res., 105, 9791–9806, 2000.

Dubovik, O., Holben, B., Eck, T., Smirnov, A., Kaufman, Y., King, M., Tanre, D., and Slutsker, I.: Variability of absorption and optical properties of key aerosol types observed in worldwide locations, J. Atmos. Sci., 59, 590–608, 2002.

Dubovik, O., Sinyuk, A., Lapyonok, T., Holben, B. N., Mishchenko, M., Yang, P., Eck, T. F., Volten, H., Munoz, O., Veihelmann, B., van der Zande, W. J., Leon, J.-F., Sorokin, M., and Slutsker, I.: Application of spheroid models to account for aerosol particle nonsphericity in remote sensing of desert dust, J. Geophys. Res., 111, D11208, https://doi.org/10.1029/2005JD006619, 2006.

Dubovik, O., Herman, M., Holdak, A., Lapyonok, T., Tanre, D., Deuze, J. L., Ducos, F., Sinyuk, A., and Lopatin, A.: Statistically-optimized inversion algorithm for enhanced retrieval of aerosol properties from spectral multi-angle polarimetric satellite observations, Atmos. Meas. Tech., 4, 975–1018, https://doi.org/10.5194/amt-4-975-2011, 2011.

Dulac, F.: An overview of the Chemistry-Aerosol Mediterranean Experiment (ChArMEx), European Geosciences Union General Assembly, Geophysical Research Abstracts Vol. 16, EGU2014-11441, 27 April–2 May 2014, Vienna, Austria, 2014.

Eck, T. F., Holben, B. N., Reid, J. S., Dubovik, O., Smirnov, A., O'Neill, N. T., Slutsker, I., and Kinne, S.: Wavelength dependence of the optical depth of biomass burning, urban, and desert dust aerosols, J. Geophys. Res., 104, 31333–31349, https://doi.org/10.1029/1999JD900923, 1999.

Fernald, F. G.: Analysis of atmospheric lidar observations – Some comments, Appl. Optics, 23, 652–653, 1984.

Fernald, F. G., Herman, B. M., and Reagan, J. A.: Determination of aerosol height distributions by lidar, J. Appl. Meteorol., 11, 482–489, 1972.

Franke, K., Ansmann, A., Müller, D., Althausen, D., Wagner, F., and Scheele, R.: One-year observations of particle lidar ratio over the tropical Indian Ocean with Raman lidar, Geophys. Res. Lett., 28, 4559–4562, https://doi.org/10.1029/2001GL013671, 2001.

Granados-Muñoz, M. J., Guerrero-Rascado, J. L., Bravo-Aranda, J. A., Navas-Guzmán, F., Valenzuela, A., Lyamani, H., Chaikovsky, A., Wandinger, U., Ansmann, A., Dubovik, O., Grudo, J., and Alados-Arboledas, L.: Retrieving aerosol microphysical properties by Lidar-Radiometer Inversion Code (LIRIC) for different aerosol types, J. Geophys. Res., 119, 4836–4858, https://doi.org/10.1002/2013JD021116, 2014.

Granados-Muñoz, M. J., Bravo-Aranda, J. A., Baumgardner, D., Guerrero-Rascado, J. L., Pérez-Ramírez, D., Navas-Guzmán, F., Veselovskii, I., Lyamani, H., Valenzuela, A., Olmo, F. J., Titos, G., Andrey, J., Chaikovsky, A., Dubovik, O., Gil-Ojeda, M., and Alados-Arboledas, L.: A comparative study of aerosol microphysical properties retrieved from ground-based remote sensing and aircraft in situ measurements during a Saharan dust event, Atmos. Meas. Tech., 9, 1113–1133, https://doi.org/10.5194/amt-9-1113-2016, 2016.

Guerrero-Rascado, J. L., Ruiz, B., and Alados Arboledas, L.: Multispectral Lidar characterization of the vertical structure of Saharan dust aerosol over southern Spain, Atmos. Environ., 42, 2668–2681, https://doi.org/10.1016/j.atmosenv.2007.12.062, 2008.

Guerrero-Rascado, J. L., Olmo, F. J., Avilés-Rodríguez, I., Navas-Guzmán, F., Pérez-Ramírez, D., Lyamani, H., and Alados Arboledas, L.: Extreme Saharan dust event over the southern Iberian Peninsula in September 2007: active and passive remote sensing from surface and satellite, Atmos. Chem. Phys., 9, 8453–8469, https://doi.org/10.5194/acp-9-8453-2009, 2009.

Guerrero-Rascado, J. L., Landulfo, E., Antuña, J. C., Barbosa, H. M. J., Barja, B., Bastidas, A. E., Bedoya, A. E., da Costa, R. F., Estevan, R., Forno, R. N., Gouveia, D. A., Jimenez, C., Larroza, E. G., Lopes, F. J. S., Montilla-Rosero, E., Moreira, G. A., Nakaema, W. M., Nisperuza, D., Alegria, D., Múnera, M., Otero, L., Papandrea, S., Pawelko, E., Quel, E. J., Ristori, P., Rodrigues, P. F., Salvador, J., Sánchez, M. F., and Silva, A.: Latin American Lidar Network (LALINET) for aerosol research: diagnosis on network instrumentation, J. Atmos. Sol.-Terr. Phy., 138–139, 112–120, 2016.

Grund, C. J. and Eloranta, E. W.: University of Wisconsin high spectral resolution lidar, Opt. Eng., 30, 6–12, https://doi.org/10.1117/12.55766, 1991.

Holben, B. N., Eck, T. F., Slutsker, I., Tanre, D., Buis, J. P., Setzer, A., Vermote, E., Reagan, J. A., Kaufman, Y. J., Nakajima, T., Lavenu, F., Jankowiak, I., and Smirnov, A.: AERONET-a federated instrument network a data archive for aerosol characterization, Remote Sens. Environ., 66, 1–16, 1998.

IPCC: Contribution of Working Group I to the Fifth Assessment Report of the Intergovernmental Panel on Climate Change, Summary for Policymakers in Climate Change, Stocker, Cambridge University Press, Cambridgen, 2013.

Karol, Y., Tanré, D., Goloub, P., Vervaerde, C., Balois, J. Y., Blarel, L., Podvin, T., Mortier, A., and Chaikovsky, A.: Airborne sun photometer PLASMA: concept, measurements, comparison of aerosol extinction vertical profile with lidar, Atmos. Meas. Tech., 6, 2383–2389, https://doi.org/10.5194/amt-6-2383-2013, 2013.

Klett, J. D.: Stable analytical inversion solution for processing lidar returns, Appl. Optics, 20, 211–220, 1981.

Klett, J. D.: Lidar inversion with variable backscatter/extinction ratios, Appl. Optics, 24, 1638–1643, 1985.

Lewis, J. R., Campbell, J. R., Welton, E. J., Stewart, S. A., and Haftings, P. C.: Overview of MPLNET version 3 cloud detection, J. Atmos. Ocean. Tech., 33, 2113–2134, 2016.

Lopatin, A., Dubovik, O., Chaikovsky, A., Goloub, P., Lapyonok, T., Tanré, D., and Litvinov, P.: Enhancement of aerosol characterization using synergy of lidar and sun-photometer coincident observations: the GARRLiC algorithm, Atmos. Meas. Tech., 6, 2065–2088, https://doi.org/10.5194/amt-6-2065-2013, 2013.

Lyamani, H., Olmo, F. J., and Alados-Arboledas, L.: Saharan dust outbreak over southeastern Spain as detected by sun photometer, Atmos. Environ., 39, 7276–7284, https://doi.org/10.1016/j.atmosenv.2005.09.011, 2005.

Lyamani, H., Olmo, F. J., Alcantara, A., and Alados-Arboledas, L.: Atmospheric aerosols during the 2003 heat wave in southeastern spain I: Spectral optical depth, Atmos. Environ., 40, 6453–6464, https://doi.org/10.1016/j.atmosenv.2006.04.048, 2006.

Lyamani, H., Fernández-Gálvez, J., Pérez-Ramírez, D., Valenzuela, A., Antón, M., Alados, I., Titos, G., Olmo, F. J., and Alados-Arboledas, L.: Aerosol properties over two urban sites in South Spain during an extended stagnation episode in winter season, Atmos. Environ., 62, 424–432, https://doi.org/10.1016/j.atmosenv.2012.08.050, 2012.

Mallet, M., Dulac, F., Formenti, P., Nabat, P., Sciare, J., Roberts, G., Pelon, J., Ancellet, G., Tanré, D., Parol, F., Denjean, C., Brogniez, G., di Sarra, A., Alados-Arboledas, L., Arndt, J., Auriol, F., Blarel, L., Bourrianne, T., Chazette, P., Chevaillier, S., Claeys, M., D'Anna, B., Derimian, Y., Desboeufs, K., Di Iorio, T., Doussin, J.-F., Durand, P., Féron, A., Freney, E., Gaimoz, C., Goloub, P., Gómez-Amo, J. L., Granados-Muñoz, M. J., Grand, N., Hamonou, E., Jankowiak, I., Jeannot, M., Léon, J.-F., Maillé, M., Mailler, S., Meloni, D., Menut, L., Momboisse, G., Nicolas, J., Podvin, T., Pont, V., Rea, G., Renard, J.-B., Roblou, L., Schepanski, K., Schwarzenboeck, A., Sellegri, K., Sicard, M., Solmon, F., Somot, S., Torres, B., Totems, J., Triquet, S., Verdier, N., Verwaerde, C., Waquet, F., Wenger, J., and Zapf, P.: Overview of the Chemistry-Aerosol Mediterranean Experiment/Aerosol Direct Radiative Forcing on the Mediterranean Climate (ChArMEx/ADRIMED) summer 2013 campaign, Atmos. Chem. Phys., 16, 455–504, https://doi.org/10.5194/acp-16-455-2016, 2016.

Massoli, P., Kebabian, P. L., Onasch, T. B., Hills, F. B., and Freedman, A.: Aerosol light extinction measurements by Cavity Attenuated Phase Shift (CAPS) Spectroscopy: Laboratory validation and field deployment of a compact aerosol particle extinction monitor, Aerosol Sci. Tech., 44, 428–435, https://doi.org/10.1080/02786821003716599, 2010.

Miffre, A., David, G., Thomas, B., and Rairoux, P.: Atmospheric non-spherical particles optical properties from UV-polarization lidar and scattering matrix, Geophys. Res. Lett., 38, L16804, https://doi.org/10.1029/2011GL048310, 2011.

Müller, D., Wandinger, U., and Ansmann, A.: Microphysical particle parameters from extinction and backscatter lidar data by in-

version with regularization: simulation, Appl. Optics, 38, 2358–2368, 1999.

Müller, D., Heinold, B., Tesche, M., Tegen, I., Althausen, D.: Amiridis, V., Amodeo, A., Ansmann, A., Alados-Arboledas, L., Balis, D., Comeron, A., D'Amico, G., Gerasopoulos, E., Guerrero-Rascado, J. L., Freudenthaler, V., Giannakaki, E., Heese, B., Iarlori, M., Mamouri, R. E., Mona, L., Papayannis, A., Pappalardo, G., Perrone, M. R., Pisani, G., Rizi, V., Sicard, M., Spinelli, N., and Tafuro, A.: EARLINET Observations of the 14–22-May long-range dust transport event during SAMUM 2006: Validation of results from dust transport modelling, Tellus B, 61, 325–339, https://doi.org/10.1111/j.1600-0889.2008.00400.x, 2009.

Müller, T., Laborde, M., Kassell, G., and Wiedensohler, A.: Design and performance of a three-wavelength LED-based total scatter and backscatter integrating nephelometer, Atmos. Meas. Tech., 4, 1291–1303, https://doi.org/10.5194/amt-4-1291-2011, 2011.

Murayama, T., Müller, D., Wada, K., Shimizu, A., Sekiguchi, M., and Tsukamoto, T.: Characterization of Asian dust and Siberian smoke with multiwavelength Raman lidar over Tokyo, Japan in spring 2003, Geophys. Res. Lett., 31, L23103, https://doi.org/10.1029/2004GL021105, 2004.

Nakajima, T., Tonna, G., Rao, R., Boi, P., Kaufman, Y., and Holben, B.: Use of sky brightness measurements from ground for remote sensing of particulate polydispersions, Appl. Optics, 35, 2672–2686, https://doi.org/10.1364/AO.35.002672, 1996.

Navas-Guzmán, F., Guerrero-Rascado, J. L., and Alados-Arboledas, L.: Retrieval of the lidar overlap function using Raman signals, Opt. Pura Apl., 44, 71–75, 2011.

Navas-Guzmán, F., Bravo-Aranda, J., Guerrero-Rascado, J., Granados-Muñoz, M., and Alados-Arboledas, L.: Statistical analysis of aerosol optical properties retrieved by Raman lidar over Southeastern Spain, Tellus B, 65, 21234, https://doi.org/10.3402/tellusb.v65i0.21234, 2013.

Navas-Guzmán, F., Fernández-Gálvez, J., Granados-Muñoz, M. J., Guerrero-Rascado, J. L., Bravo-Aranda, J. A., and Alados-Arboledas, L.: Tropospheric wáter vapour and relative humidity profiles from lidar and microwave radiometry, Atmos. Meas. Tech., 7, 1201–1211, https://doi.org/10.5194/amt-7-1201-2014, 2014.

Olmo, F. J., Quirantes, A., Alcántara, A., Lyamani, H., and Alados-Arboledas, L.: Preliminary results of a non-spherical aerosol method for the retrieval of the atmospheric aerosol optical properties, J. Quant. Spectrosc. Ra., 100, 305–314, https://doi.org/10.1016/j.jqsrt.2005.11.047, 2006.

Olmo, F. J., Quirantes, A., Lara, V., Lyamani, H., and Alados-Arboledas, L.: Aerosol optical properties assessed by an inversion method using the solar principal plane for non-spherical particles, J. Quant. Spectrosc. Ra., 109, 1504–1516, 2008.

Ortiz-Amezcua, P., Guerrero-Rascado, J. L., Granados-Muñoz, M. J., Bravo-Aranda, J. A., and Alados-Arboledas, L.: Characterization of atmospheric aerosols for a long range transport of biomass burning particles from Canadian forest fires over the southern Iberian Peninsula in July 2013, Óptica Pura y Aplicada, 47, 43-49, https://doi.org/10.1016/j.jqsrt.2007.12.019, 2014.

Ortiz-Amezcua, P., Guerrero-Rascado, J. L., Granados-Muñoz, M. J., Benavent-Oltra, J. A., Böckmann, C., Samaras, S., Stachlewska, I. S., Janicka, L., Baars, H., Bohlmann, S., and Alados-Arboledas, L.: Microphysical characterization of long-range transported biomass burning particles from North America at three EARLINET stations, Atmos. Chem. Phys., 17, 5931–5946, https://doi.org/10.5194/acp-17-5931-2017, 2017.

Pappalardo, G., Amodeo, A., Apituley, A., Comeron, A., Freudenthaler, V., Linné, H., Ansmann, A., Bösenberg, J., D'Amico, G., Mattis, I., Mona, L., Wandinger, U., Amiridis, V., Alados-Arboledas, L., Nicolae, D., and Wiegner, M.: EARLINET: towards an advanced sustainable European aerosol lidar network, Atmos. Meas. Tech., 7, 2389–2409, https://doi.org/10.5194/amt-7-2389-2014, 2014.

Pérez-Ramírez, D., Lyamani, H., Olmo, F. J., Whiteman, D. N., and Alados-Arboledas, L.: Columnar aerosol properties from sun and -star photometry: statistical comparisons and day-to-night dynamic, Atmos. Chem. Phys., 12, 9719–9738, https://doi.org/10.5194/acp-12-9719-2012, 2012.

Pérez-Ramírez, D., Veselovskii, I., Whiteman, D. N., Suvorina, A., Korenskiy, M., Kolgotin, A., Holben, B., Dubovik, O., Siniuk, A., and Alados-Arboledas, L.: High temporal resolution estimates of columnar aerosol microphysical parameters from spectrum of aerosol optical depth by linear estimation: application to long-term AERONET and star-photometry measurements, Atmos. Meas. Tech., 8, 3117–3133, https://doi.org/10.5194/amt-8-3117-2015, 2015.

Pérez-Ramírez, D., Lyamani, H., Smirnov, A., O'Neill, N. T., Veselovskii, I., Whiteman, D. N., Olmo, F. J., Alados-Arboledas, L.: Statistical study of day and night hourly patterns of columnar aerosol properties using sun and star photometry, Proc. SPIE, 100001, 100010K, 2016.

Perrone, M. R., De Tomasi, F., and Gobbi, G. P.: Vertically resolved aerosol properties by multi-wavelength lidar measurements, Atmos. Chem. Phys., 14, 1185–1204, https://doi.org/10.5194/acp-14-1185-2014, 2014.

Preißler, J., Wagner, F., Pereira, S. N., and Guerrero-Rascado, J. L.: Multiinstrumental observation of an exceptionally strong Saharan dust outbreak over Portugal, J. Geophys. Res., 116, D24204, https://doi.org/10.1029/2011JD016527, 2011.

Rolph, G. D.: Real-time Environmental Applications and Display sYstem (READY) Website (http://www.ready.noaa.gov), NOAA Air Resources Laboratory, College Park, MD, 2016.

Román, R., Torres, B., Fuertes, D., Cachorro, V. E., Dubovik, O., Toledano, C., Cazorla, A., Barreto, A., Bosch, J. L., Lapyonok, T., González, R., Goloub, P., Perrone, M. R., Olmo, F. J., de Frutos, A., Alados-Arboledas, L.: Remote sensing of lunar aureole with a sky camera: Adding information in the nocturnal retrieval of aerosol properties with GRASP code, Remote Sens. Environ., 196, 238–252, https://doi.org/10.1016/j.rse.2017.05.013, 2017.

Schuster, G. L., Dubovik, O., and Arola, A.: Remote sensing of soot carbon – Part 1: Distinguishing different absorbing aerosol species, Atmos. Chem. Phys., 16, 1565–1585, https://doi.org/10.5194/acp-16-1565-2016, 2016.

Shipley, S. T., Tracy, D. H., Eloranta, E. W., Trauger, J. T., Sroga, J. T., Roesler, F. L., and Weinman, J. A.: High Spectral Resolution-Lidar to Measure Optical-Scattering Properties of Atmospheric Aerosols, 1.Theory and Instrumentation, Appl. Optics, 22, 3716–3724, https://doi.org/10.1364/AO.22.003716, 1983.

Stein, A. F., Draxler, R. R, Rolph, G. D., Stunder, B. J. B., Cohen, M. D., and Ngan, F.: NOAA's HYSPLIT atmospheric transport and dispersion modeling system, B. Am. Meteorol. Soc., 96, 2059–2077, 2015.

Titos, G., del Águila, A., Cazorla, A., Lyamani, H., Casquero-Vera, J. A., Colombi, C., Cuccia, E., Gianelle, V., Močnik, G., Alastuey, A., Olmo, F. J., and Alados-Arboledas, L.: Spatial and temporal variability of carbonaceous aerosols: Assessing the impact of biomass burning in the urban environment, Sci. Total Environ., 578, 613–625, https://doi.org/10.1016/j.scitotenv.2016.11.007, 2017.

Toledano, C., Wiegner, M., Groß, S., Freudenthaler, V., Gasteiger, J., Müller, D., Müller, T., Schladitz, A., Weinzierl, B., Torres, B., and O'neill, N. T.: Optical properties of aerosol mixtures derived from sun-sky radiometry during SAMUM-2, Tellus B, 63, 635–648, https://doi.org/10.1111/j.1600-0889.2011.00573.x, 2011.

Torres, B., Dubovik, O., Toledano, C., Berjon, A., Cachorro, V. E., Lapyonok, T., Litvinov, P., and Goloub, P.: Sensitivity of aerosol retrieval to geometrical configuration of ground-based sun/sky radiometer observations, Atmos. Chem. Phys., 14, 847–875, https://doi.org/10.5194/acp-14-847-2014, 2014.

Torres, B., Dubovik, O., Fuertes, D., Schuster, G., Cachorro, V. E., Lapionak, T., Goloub, P., Blarel, L., Barreto, A., Mallet, M., Toledano, C., and Tanré, D.: Advanced characterisation of aerosol size properties from measurements of spectral optical depth using the GRASP algorithm, Atmos. Meas. Tech., 10, 3743–3781, https://doi.org/10.5194/amt-10-3743-2017, 2017.

Valenzuela, A., Olmo, F. J., Lyamani, H., Antón, M., Quirantes, A., and Alados-Arboledas, L.: Classification of aerosol radiative properties during African desert dust intrusions over southeastern Spain by sector origins and cluster analysis, J. Geophys. Res., 117, D06214, https://doi.org/10.1029/2011JD016885, 2012a.

Valenzuela, A., Olmo, F. J., Lyamani, H., Antón, M., Quirantes, A., and Alados-Arboledas, L.: Analysis of the desert dust radiative properties over Granada using principal plane sky radiances and spheroids retrieval procedure, Atmos. Res., 104–105, 292–301, https://doi.org/10.1016/j.atmosres.2011.11.005, 2012b.

Veselovskii, I., Kolgotin, A., Griaznov, V., Müller, D., Wandinger, U., and Whiteman, D. N.: Inversion with regularization for the retrieval of tropospheric aerosol parameters from multiwavelength lidar sounding, Appl. Optics, 41, 3685–3699, https://doi.org/10.1364/AO.41.003685, 2002.

Wandinger, U. and Ansmann, A.: Experimental Determination of the Lidar Overlap Profile with Raman Lidar, Appl. Optics, 41, 511–514, https://doi.org/10.1364/AO.41.000511, 2002.

Whiteman, D. N., Melfi, S. H., and Ferrare, R. A.: Raman lidar system for the measurement of water vapor and aerosols in the Earth's atmosphere, Appl. Optics, 31, 3068–3082, https://doi.org/10.1364/AO.31.003068, 1992.

Whiteman, D. N., Pérez-Ramírez, D., Veselovskii, I., Colarco, P., and Buchard, V.: Retrievals of aerosol microphysics from simulations of spaceborne multiwavelength lidar measurements, J. Quant. Spectrosc. Ra., 205, 27–39, https://doi.org/10.1016/j.jqsrt.2017.09.009, 2018.

Wiedensohler, A., Birmili, W., Nowak, A., Sonntag, A., Weinhold,K., Merkel, M., Wehner, B., Tuch, T., Pfeifer, S., Fiebig, M.,Fjäraa, A. M., Asmi, E., Sellegri, K., Depuy, R., Venzac, H., Villani,P., Laj, P., Aalto, P., Ogren, J. A., Swietlicki, E., Williams,P., Roldin, P., Quincey, P., Hüglin, C., Fierz-Schmidhauser, R.,Gysel, M., Weingartner, E., Riccobono, F., Santos, S., Grüning,C., Faloon, K., Beddows, D., Harrison, R., Monahan, C., Jennings, S. G., O'Dowd, C. D., Marinoni, A., Horn, H.-G., Keck,L., Jiang, J., Scheckman, J., McMurry, P. H., Deng, Z., Zhao, C. S., Moerman, M., Henzing, B., de Leeuw, G., Löschau, G., and Bastian, S.: Mobility particle size spectrometers: harmonization of technical standards and data structure to facilitate high quality long-term observations of atmospheric particle number sized distributions, Atmos. Meas. Tech., 5, 657–685, https://doi.org/10.5194/amt-5-657-2012, 2012.

Appendix B

Article published in *Atmospheric Research* Journal.

Retrieval of aerosol profiles combining sunphotometer and ceilometer measurements in GRASP code (https://doi.org/10.1016/j.atmosres.2018.01.021)

Atmospheric Research 204 (2018) 161–177

Contents lists available at ScienceDirect

Atmospheric Research

journal homepage: www.elsevier.com/locate/atmosres

Retrieval of aerosol profiles combining sunphotometer and ceilometer measurements in GRASP code

R. Román[a,b,c,*], J.A. Benavent-Oltra[a,c], J.A. Casquero-Vera[a,c], A. Lopatin[d], A. Cazorla[a,c], H. Lyamani[a,c], C. Denjean[e], D. Fuertes[d], D. Pérez-Ramírez[a,c], B. Torres[d,f], C. Toledano[b], O. Dubovik[f], V.E. Cachorro[b], A.M. de Frutos[b], F.J. Olmo[a,c], L. Alados-Arboledas[a,c]

[a] Department of Applied Physics, University of Granada, 18071 Granada, Spain
[b] Grupo de Óptica Atmosférica (GOA), Universidad de Valladolid. Paseo Belén, 7, 47011 Valladolid, Spain
[c] Andalusian Institute for Earth System Research (IISTA-CEAMA), University of Granada, Autonomous Government of Andalusia, 18006 Granada, Spain
[d] GRASP-SAS, Lille, France
[e] CNRM, Centre National de la Recherche Météorologique (UMR3589, CNRS, Météo-France), Toulouse, France
[f] Laboratoire d'Optique Atmosphérique, Université de Lille 1, Villeneuve d'Ascq, France

ARTICLE INFO

Keywords:
GRASP
Ceilometer
Aerosol
Profiling
Photometer
Aerosol volume concentration

ABSTRACT

In this paper we present an approach for the profiling of aerosol microphysical and optical properties combining ceilometer and sun/sky photometer measurements in the GRASP code (General Retrieval of Aerosol and Surface Properties). For this objective, GRASP is used with sun/sky photometer measurements of aerosol optical depth (AOD) and sky radiances, both at four wavelengths and obtained from AErosol RObotic NETwork (AERONET), and ceilometer measurements of range corrected signal (RCS) at 1064 nm. A sensitivity study with synthetic data evidences the capability of the method to retrieve aerosol properties such as size distribution and profiles of volume concentration (VC), especially for coarse particles. Aerosol properties obtained by the mentioned method are compared with airborne in-situ measurements acquired during two flights over Granada (Spain) within the framework of ChArMEx/ADRIMED (Chemistry-Aerosol Mediterranean Experiment/Aerosol Direct Radiative Impact on the regional climate in the MEDiterranean region) 2013 campaign. The retrieved aerosol VC profiles agree well with the airborne measurements, showing a mean bias error (MBE) and a mean absolute bias error (MABE) of 0.3 $\mu m^3/cm^3$ (12%) and 5.8 $\mu m^3/cm^3$ (25%), respectively. The differences between retrieved VC and airborne in-situ measurements are within the uncertainty of GRASP retrievals. In addition, the retrieved VC at 2500 m a.s.l. is shown and compared with in-situ measurements obtained during summer 2016 at a high-atitude mountain station in the framework of the SLOPE I campaign (Sierra Nevada Lidar AerOsol Profiling Experiment). VC from GRASP presents high correlation (r = 0.91) with the in-situ measurements, but overestimates them, MBE and MABE being equal to 23% and 43%.

1. Introduction

Aerosols are a key piece in the Earth climatic system because they can increase the cooling or warming of the Earth surface depending on their properties (Boucher et al., 2013). Hence, columnar and vertical aerosol properties must be appropriately known to better understand their impact in the Earth energy balance and therefore on the Earth climate. Furthermore aerosol profiling is also relevant in the management of aviation traffic (Prata, 2009; Flentje et al., 2010).

Column-integrated microphysical and optical aerosol properties are commonly retrieved by sun/sky photometer measurements. This is the case of AERONET (AErosol RObotic NETwork; Holben et al., 1998), that derives aerosol optical depth (AOD) from multiwavelength measurements of direct beam sun irradiance, and uses these AOD values in combination with sky radiances measurements for obtaining aerosol properties such as aerosol size distribution, refractive indices, single scattering albedo (SSA), and phase function (Dubovik and King, 2000; Dubovik et al., 2006). However, this kind of measurements does not provide information about the vertical profile of these aerosol properties.

Lidar systems are capable of measuring the atmospheric backscatter profile at several wavelengths. The lidar signals are used for profiling optical and even retrieving microphysical aerosol properties applying different methods. These methods depend on the available lidar signals:

* Corresponding author at: Grupo de Óptica Atmosférica (GOA), Universidad de Valladolid. Paseo Belén, 7, 47011 Valladolid, Spain.
E-mail address: robertor@goa.uva.es (R. Román).

https://doi.org/10.1016/j.atmosres.2018.01.021
Received 1 December 2017; Received in revised form 26 January 2018; Accepted 30 January 2018

elastic range corrected signal (RCS) is useful to provide aerosol backscatter (β) profiles (Klett, 1981, 1985; Fernald, 1984; Sasano, 1984); non-elastic (Raman) signal can be used for obtaining independent range-resolved extinction (α) and backscatter coefficients (Ansmann et al., 1990; Whiteman et al., 1992). Elastic and Raman lidar signals can be combined, usually by the so called 3β + 2α configuration, to obtain profiles of aerosol microphysical properties through different inversion techniques (e.g. Müller et al., 1999; Böckmann, 2001; Veselovskii et al., 2002, 2012; Chemyakin et al., 2016); many papers being already published for characterizing long-transport of biomass-burning (e.g. Veselovskii et al., 2015; Ortiz-Amezcua et al., 2017), volcanic aerosol (e.g. Navas-Guzmán et al., 2013), dust (e.g. Granados-Muñoz et al., 2016; Veselovskii et al., 2017) pollution (e.g. Wandinger et al., 2002; Noh et al., 2009; Veselovskii et al., 2013), and artic haze (Müller et al., 2004). In addition, linear particle depolarization ratio measurements allow the detection and assessment of non-spherical particles such as dust or volcanic aerosol (e.g. Ansmann et al., 2009, 2012; Tesche et al., 2009, 2011; Bravo-Aranda et al., 2013) and allows aerosol typing (e.g. Burton et al., 2012; Gross et al., 2013).

EARLINET (European Aerosol Research LIdar NETwork; Pappalardo et al., 2014), founded in 2000 and now part of ACTRIS (Aerosols, Clouds, and Trace gases Research InfraStructure; www.actris.eu/), does include nowadays 31 lidar stations, most of them operating multi-wavelength Raman lidars. However, most Raman measurements are sparse and mostly limited to night-time. To retrieve vertical profiles of aerosol microphysics, several inversion techniques were developed within EARLINET/ACTRIS combining backscattering lidar and collocated AERONET sun/sky photometers such as LIRIC (Lidar Radiometer Inversion Code; Chaikovsky et al., 2008, 2016) and GARRLiC (Generalized Aerosol Retrieval from Radiometer and Lidar Combined data; Lopatin et al., 2013). The LIRIC code uses AERONET column-integrated retrievals plus backscattering lidar signals as inputs to provide vertical-resolved aerosol volume concentration (VC), both at fine and coarse mode. However, GARRLiC uses as inputs measured optical depth and sky radiances and the multiwavelength RCS from lidar to provide vertical-resolved aerosol microphysical and optical properties, both at fine and coarse mode, and also improves the classical AERONET columnar retrievals by providing intensive aerosol properties, like refractive indices or SSA, of fine and coarse modes, separately.

The Generalized Retrieval of Aerosol and Surface Properties (GRASP; Dubovik et al., 2014) code uses the heritage of AERONET inversion scheme (e.g. Dubovik and King, 2000; Dubovik et al., 2006) and is a versatile and open-source algorithm capable to obtain optical and microphysical aerosol properties from different sources of measurements (www.grasp-open.com). Recently, aerosol properties have been retrieved by GRASP using, among other information sources, satellite images (Kokhanovsky et al., 2015), polar nephelometer data (Espinosa et al., 2017) and different combinations with sun/sky photometer measurements: only spectral AODs (Torres et al., 2017); spectral AODs, sky radiances and polarized sky radiances (Fedarenka et al., 2016); and spectral AODs and sky camera images (Román et al., 2017a). The incorporation of the GARRLiC scheme in GRASP allows to combine AODs, sky radiances and RCS lidar values to retrieve columnar and vertical-resolved aerosol properties discerning between fine and coarse modes (Lopatin et al., 2013; Bovchaliuk et al., 2016; Benavent-Oltra et al., 2017).

Although the combination of lidar and sun/sky photometer measurements using GRASP with the GARRLiC scheme is promising, lidar systems are generally expensive and require supervision, so few stations have the set of measurements required to this end. An alternative to multiwavelength lidar systems could be the use of ceilometers, which were originally designed for studying cloud heights but recent ceilometer models are able to detect aerosol layers at altitudes of up to 10 km. Ceilometers only measure at one wavelength and are less accurate than classic lidars, but they are cheaper and more operative than multiwavelength lidar systems and they also can work continuously unattended. In fact, ceilometers have been previously used to obtain aerosol properties as PM2.5 (Li et al., 2017), PM10 (Münkel et al., 2007), aerosol backscatter coefficients (Heese et al., 2010; Wiegner and Geiss, 2012; Wiegner et al., 2014; Madonna et al., 2015) or aerosol hygroscopic growth (Haeffelin et al., 2016). Moreover, there are some programs nowadays as *E*-PROFILE, a program of EUMETNET (European METeorological services NETwork), and the COST Action ES1303 TOPROF (TOwards operational ground based PROFiling with ceilometers, doppler lidars and microwave radiometers for improving weather forecasts) dealing with the harmonization and better characterization of ceilometer measurements and products; and there are also ceilometer networks, like the Iberian CEilometer NETwork (ICENET; Cazorla et al., 2017) among others (e.g., de Haij et al., 2007; Emeis et al., 2011), trying to provide ceilometer measurements in near-real time with devices every 100 km. These issues motivate to try to combine ceilometer measurements with sun/sky photometer in order to obtain some vertical aerosol information.

The main objective of this work is use for the first time the GRASP code to obtain aerosol vertical profiling of aerosol microphyscial properties combining AERONET sun/sky photometer measurements with the monochromatic RCS measured by a ceilometer at 1064 nm. The use of this proposed combination of measurements allows the retrievals of column-integrated aerosol microphysical properties, and we explore the possibility of obtaining vertically-resolved aerosol volume concentration. Another important goal is the quantification of the accuracy and uncertainty of all retrieved parameters through synthetic data and also by comparisons of retrieved parameters versus in-situ measurements.

This paper is structured as follows: Section 2 describes the used instrumentation during the different measurement field campaigns; Section 3 introduces the GRASP code and the methodology to retrieve the aerosol properties; a sensitivity study with synthetic measurements is developed in Section 4 in order to test the capability of the proposed GRASP scheme. Section 5 shows the main results about the comparison of the obtained aerosol retrievals against in-situ measurements and, finally, the main conclusions are summarized in Section 6.

2. Instrumentation and campaigns

2.1. Instrumentation at Granada station

Most of the instrumentation used in this work is installed on the rooftop of the "Andalusian Institute for Earth System Research" (IISTA-CEAMA) building at Granada, Spain (37.1638° N; 3.6051° W; 680 m a.s.l.). This instrumentation is managed by the Atmospheric Physics Group ("Grupo de Física de la Atmósfera"; GFAT) of University of Granada. Granada is a Spanish city located in the South-Eastern of the Iberian Peninsula, in a natural basin surrounded by –Sierra Nevada Mountains with peaks of up to 3300 m a.s.l., showing a Mediterranean climate (Csa in Köppen classification). The city is medium-size with a population about 235,000 inhabitants, which increases up to 530,000 including the metropolitan area, and non-industrialized being its main aerosol sources the domestic heating based on fuel oil combustion in winter and the heavy traffic along all year (Lyamani et al., 2010, 2011; Titos et al., 2012, 2014). Columnar aerosol pattern in the area is characterized by higher values in summer mostly associated with Saharan dust arrivals (Pérez-Ramírez et al., 2012; Mandija et al., 2016), while the lowest aerosol loads usually corresponds to the arrivals of Atlantic air-masses that clean the atmosphere (Pérez-Ramírez et al., 2016).

A CE318-T sun/sky/lunar (triple) photometer (*Cimel Electronique*) is operative on the mentioned station since March 2016 for providing day and night columnar aerosol optical properties (Barreto et al., 2013, 2016). GFAT also operates different sun/sky photometers (hereafter 'sunphotometers') which belong to AERONET and have participated in field campaigns in Spain, Brazil, Colombia and Bolivia, and have

allowed continuous operation of the site in Granada since the end of 2004. Both sunphotometer models take measurements of direct beam sun irradiance, which retrieve AOD, and sky radiance at several wavelengths, but only the channels of 440, 675, 870 and 1020 nm are chosen in this work because they are available in most AERONET sunphotometers. All sunphotometer data used have been obtained from version 2 of AERONET as level 1.5 data. Level 1.5 data are cloud-screened and have been chosen instead of quality assurance level 2.0 data due to the near-real time availability of these data, which can be used to calculate also other products in near-real time.

The mentioned Granada station also includes a "CHM-15 k Nimbus" ceilometer (*Lufft manufacturer*), which belongs to ICENET (Cazorla et al., 2017) and is detailed in Román et al. (2017b). This instrument works as a one-wavelength lidar which emits at 1064 nm (a pulsed Nd:YAG laser) and measures the backscattered signal by the atmosphere at different heights (up to 15,360 m a.g.l.) with 15 m resolution. According to the overlap function provided by the manufacturer, the overlap is 90% complete between 555 and 885 m a.g.l. (Cazorla et al., 2017). The firmware of the instrument directly provides NetCDF files with the RCS at 1064 nm which includes background and overlap corrections. In addition, these files include the cloud base height (CBH) product, which is estimated from ceilometer measurements due to the strong backscattered signal of clouds (Martucci et al., 2010). The data are recorded as time averaged data every 15 s. More information about this ceilometer and its products can be found in the Jenoptik CHM15k user manual (Jenoptik, 2013).

2.2. ChArMEx/ADRIMED 2013

One of the main objectives of the ChArMEx/ADRIMED campaign (Chemistry-Aerosol Mediterranean Experiment/Aerosol Direct Radiative Impact on the regional climate in the MEDiterranean region) during summer 2013 was to conduct an experimental campaign, based on surface and aircraft observations, for creating a rich 3-D database of physical, chemical and optical properties of the main Mediterranean aerosols (Mallet et al., 2016). To this end, 16 flights, ascending or descending in a spiral trajectory during 30 min, were performed over the Mediterranean Basin with the ATR-42 aircraft of SAFIRE (French aircraft service for environmental research; http://www.safire.fr) during the period from 14th June to 4th July 2013 (Mallet et al. 2016; Denjean et al., 2016). The two flights named F30 and F31 of this campaign were done over Granada city on 16th and 17th June 2013, respectively.

In both flights the ATR-42 airplane was equipped with different in-situ instrumentation, being used in this work the measurements of fine and coarse aerosol concentrations. For the aerosol concentration measurements in the submicron range: an UHSAS (Ultra-High Sensitivity Aerosol Spectrometer; *Droplet Measurement Technologies*) and a SMPS (Scanning Mobility Particle Sizer) with an accuracy of 10% (Cai et al., 2008) and 5% (Wiedensohler et al., 2012), respectively. For coarse particles the optical size distributions was measured by a FSSP-300 (a wing-mounted Forward Scattering Spectrometer Probe, model 300 from *Particle Measuring Systems*) and by the in-cabin GRIMM OPC (sky-optical particle counter; model 1.129 from *Grimm Technik*) in the diameter nominal size ranges of 0.28–20 μm and 0.25–32 μm, respectively. FSSP-300 and GRIMM have an accuracy of 30% (Baumgardner et al., 1992) and 10% (Denjean et al., 2016), respectively. Finally, the profiles of the total aerosol VC (for radius ranging between 0.05 and 15 μm) have been obtained with a resolution of 100 m as in Benavent-Oltra et al. (2017): combining all the measurements of aerosol number size distributions (SMPS, UHSAS, FSSP-300 and GRIMM OPC) and assuming that aerosol particles are spherical (Denjean et al., 2016).

2.3. SLOPE I

The SLOPE I campaign (Sierra Nevada Lidar AerOsol Profiling Experiment) was designed in order to measure relevant data for testing different retrieval schemes of aerosol microphysical and optical vertical-profiles from remote sensing observations. The campaign, developed during summer 2016, combined active and passive remote sensing of the vertical column with in-situ measurements at several levels in the northwestern slope of Sierra Nevada mountain range (Spain). In this framework, a new measurement station (SNS: Sierra Nevada Station) was set up in a high-altitude site at Sierra Nevada (37.0958° N; 3.3869° W; 2500 m a.s.l.). This new station is 20 km far from IISTA-CEAMA in horizontal distance and it was equipped with aerosol in-situ instrumentation since May 2016, providing 24-hour aerosol in-situ measurements such as scattering, absorption and extinction coefficients.

The in-situ aerosol volume concentration at SNS has been calculated combining SMPS (model 3938 from *TSI Inc.*) and APS (Aerodynamic Particle Sizer; model 3321 from *TSI Inc.*) measurements. This volume concentration has been obtained in the 0.05–10 μm radius range with 5 min time resolution. For that, Q-value = 1 is assumed for conversion from aerodynamic (APS) to mobility size distribution (Sorribas et al., 2015).

3. GRASP retrieval

3.1. Inputs

3.1.1. Sun/sky photometer data

CE318 sunphotometers are configured to take a sequence of sky radiance measurements in the almucantar plane (zenith angle equal to solar zenith angle, SZA) for several air masses. AERONET provides the sky radiance usually at the next almucantar azimuth angles (relative to sun): 2°, 2.5°, 3°, 3.5°, 4°, 5°, 6°, 7°, 8°, 10°, 12°, 14°, 16°, 18°, 20°, 25°, 30°, 35°, 40°, 45°, 50°, 60°, 70°, 80°, 90°, 100°, 120°, 140°, 160° and 180°. These angles are scanned clockwise and counter clockwise giving two measurements for each angle of symmetric points with respect to the sun position. In this work the sky radiance has been averaged between both points. The azimuth angles below 3.5° are rejected following the same criteria than the version 1 level 1.5 of AERONET (Holben et al., 2006). The angles showing differences above 20% between both almucantar branches are assumed as cloud contaminated and are also discarded as in level 1.5 of AERONET version 2 (Holben et al., 2006). The azimuth at 180° does not have a symmetric point which makes difficult its cloud-screening, and hence this angle is also rejected. These criteria provide, in the most favourable case, 26 sky radiance values at the four channels at 440 nm, 675 nm, 870 nm and 1020 nm.

After cloud-screening, the scattering angle criterion of Holben et al. (2006) for AERONET (version 2 level 1.5) is applied. This criterion considers that sky radiance distribution for each wavelength is representative if there is at least one measurement in four regions identified by the scattering angle: ≥3.2° to 6°; ≥6° to 30°; ≥30° to 80°; and ≥80°. In this work the scattering angle of 80° has been replaced in these bins by 78° in order to use almucantars with sun altitude up to 50º (SZA = 40°).

The GRASP retrievals are done for each available cloud-screened almucantar if it satisfies: (1) the number of sky radiance points at each wavelength is higher or equal than 10 (as in AERONET version 2 level 1.5); (2) at each wavelength there is at least one radiance value at the four mentioned bins, and (3) the closest AOD (level 1.5), also used in the retrieval, is within ± 16 min of almucantar measurement for the four wavelengths. Sky radiance data used as input in GRASP is previously normalized using the "2000 ASTM Standard Extraterrestrial Spectrum Reference E-490-00" (http://rredc.nrel.gov/solar/spectra/am0), again the same than in AERONET version 2 aerosol inversions. In order to include the filter response of the photometer, the extraterrestrial spectrum is convoluted for each channel by a 10 nm width square filter (similar to the real filters) centred in the effective wavelength of the real photometer filters.

3.1.2. Ceilometer data

For each almucantar dataset the correlative ceilometer RCS values measured without clouds (CBH provided by the instrument is null) are averaged in a ± 15 min window centred around the almucantar time. A minimum of 5 RCS cloud-free profiles is imposed for calculating the average and for consequently running GRASP. This requirement of at least 5 profiles is not too restrictive working with averaged 15-second profiles and could provide averaged profiles too noisy when the number of used profiles in the averaging is closer to (and above) 5, but most of them will be only taken into account up to low altitudes due to the used iterative method to reject noisy points that is explained below; this threshold may be increased in future works, but now it permits to obtain more retrievals. The time averaged RCS is vertically smoothed by a moving average of ± 105 m window in order to reduce noise, and later it is normalized at 60 log-spaced bins at different heights, as in Lopatin et al. (2013), being the minimum of these heights (z_{min}) equal to 250 m a.s.l. since the ceilometer shows frequently very noisy signal below this height due to the overlap correction. The maximum height (z_{max}) selected for the 60 log-spaced bins is 7000 m a.s.l. since aerosol layers are rarely detected above this height and the ceilometer signal is usually too noisy, due to the low power of ceilometer's laser. The RCS at these 60 log-spaced bins is normalized by dividing the average of RCS in each logarithmic height interval by the integrated RCS between z_{min} and z_{max} according to the following equation:

$$NRCS_h = \frac{\frac{1}{N}\sum_{z=h_1}^{z=h_N} RCS_z}{\int_{z_{min}}^{z_{max}} RCS_z\, dz} \quad (1)$$

where $NRCS_h$ is the normalized RCS at the h-bin (h ranges from 1 to 60), N is the number of available RCS values in the height interval given by the h-bin, and h_1, $h_{2, \ldots}$ and h_N represents the N heights of the available RCS that are inside the h-bin.

Due to the background correction and the noisy signal at high altitudes, the smooth and normalization process occasionally provides negative values of normalized RCS, which cannot be processed by GRASP due to the lack of physical sense. An iterative method has been applied to solve this issue: if any normalized RCS value is negative then the 60 log-spaced bins and normalized values are recalculated considering the maximum height 100 m below the last; this loop with z_{max} decreasing 100 m per iteration stops when all values of normalized RCS are positive.

3.1.3. BRDF data

A part of measured sky radiance has its source in the light reflected by the Earth surface; therefore, the Bidirectional Reflectance Distribution Function (BRDF) is used to take into account this phenomenon. The BRDF is introduced in GRASP through the BRDF parameters of the Li–Ross model (Ross, 1981; Li and Strahler, 1992). GRASP is capable to calculate BRDF parameters from satellite images (Dubovik et al., 2014) but the BRDF parameters used for this work are obtained from the V005 Collection MCD43C1 product (V005 MODIS Terra + Aqua BRDF/Albedo 16-Day L3 0.05Deg CMG) of MODIS (MODerate-resolution Imaging Spectroradiometer) with a spatial resolution of 0.05° (Schaff et al., 2011). This product is produced every 8 days with 16 days of acquisitions at seven narrow bands, which central wavelengths are 470, 555, 659, 858, 1240, 1640 and 2130 nm. The available MCD43C1 data at the Granada coordinates from 2000 to 2014 have been averaged obtaining a table of BRDF parameters every 8 days for one representative year. The BRDF parameters used in a particular GRASP retrieval are obtained from the mentioned table taken into account the date and linearly interpolating the central wavelengths of MCD43C1 product to 675, 870, 1020 and 1064 nm and extrapolating to 440 nm.

3.2. Inversion strategy, constraints and products

GRASP includes two independent modules, the first is the forward model based on radiative transfer and aerosol model, which is capable to generate the radiative measurements for a given aerosol scenario (Dubovik et al., 2014). This forward model is used in Section 4 to simulate synthetic data for different aerosol scenarios. The second module corresponds to the numerical inversion, which includes general mathematical operations, based on multi-term least square method (Dubovik and King, 2000), not related to the particular physical nature of the inverted data (Dubovik et al., 2014). This module, combined with the forward module, allows flexible and rigorous inversions of the various combinations of the independent multi-source measurements. Detailed description about how GRASP and its modules work using sunphotometer and RCS data was given by Lopatin et al. (2013), who explained the GARRLiC algorithm which nowadays is part of GRASP code.

The use of sunphotometer and ceilometer data proposed in this work cannot discern between different aerosol modes in the vertical because the ceilometer provides RCS profiles at only one wavelength. Hence, for the retrieval constraining intensive aerosol properties such as refractive indices, SSA, lidar ratio (LR) or effective radius are assumed equal for fine and coarse mode in the retrieval, which therefore implies that GRASP is not able to provide vertical profiles of these parameters. Column integrated retrieved parameter are aerosol size distribution (22 log-spaced triangle bins from 0.05 μm to 15 μm radius as in the operational AERONET retrievals) and fraction of spherical particles (also called sphere fraction). The scheme also provides column-integrated values of real refractive index (RRI), imaginary refractive index (IRI), SSA and LR at 5 wavelengths (440, 675, 870, 1020 and 1064 nm). However, the hypothesis of vertically constant aerosol intensive parameters allows changes in extensive properties and, therefore, vertical profiles of the 60 log-spaced bins of aerosol volume concentration and of extinction, backscatter, absorption and scattering coefficients at the mentioned 5 wavelengths are provided.

In the GRASP retrievals we assume: no changes in extensive vertical properties from ground to the z_{min}; and an exponential decrease in these properties above z_{max} as in Lopatin et al. (2013). GRASP needs an initial aerosol scenario, also known as initial guess (Torres et al., 2017), to initialize each retrieval. The initial guess of each parameter has been assumed the same for all retrievals except for the size distribution, which has been assumed as a trapezoidal distribution proportional to the measured AOD at 440 nm wavelength (AOD_{440}). Finally, GRASP also provides the uncertainty, σ_G, on the retrieved parameters (VC, SSA, etc.), which is calculated from the random and systematic errors estimated by the detailed methodology shown in Sections 2.3 and 2.4 of Dubovik et al. (2000). These products obtained by GRASP using the described methodology are labeled in this work as $GRASP_{pac}$, which sub-index makes reference to the combination of "photometer and ceilometer". $GRASP_{pac}$ retrievals not showing convergence are rejected. Only 2% of the retrievals obtained in Section 5.2 were discarded by the convergence criteria.

4. Retrieval sensitivity

4.1. Generation of synthetic data

A sensitivity study with synthetic data is done in order to observe the capability of the $GRASP_{pac}$. To this end, two kinds of aerosol are considered: Smoke and Dust, including different mixtures among them. Smoke and Dust typical size distributions and refractive indices are from Dubovik et al. (2002) for biomass burning in the African savanna (Zambia) and for desert dust at the Arabian Peninsula (Saudi Arabia), respectively. Fig. 1 shows the typical size distributions for these two aerosol types (Fig. 1a) and their vertical distribution (Fig. 1b), real refractive index (Fig. 1c), and imaginary refractive index (Fig. 1d)

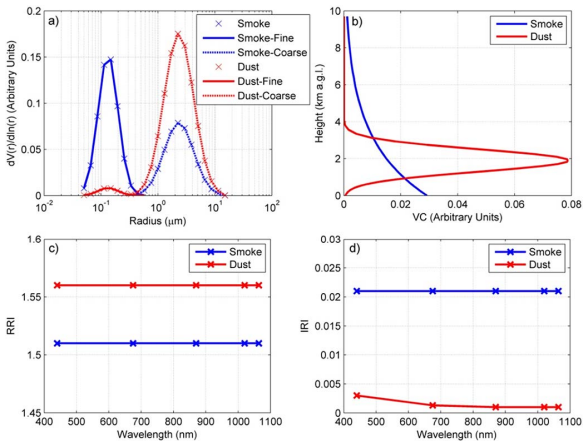

Fig. 1. Microphysical and optical properties of the two aerosol models (Smoke and Dust) used to obtain synthetic data: size distribution (panel a); vertical volume concentration, VC, (panel b); real (panel c) and imaginary (panel d) refractive indices, RRI and IRI, respectively.

according to values reported in the bibliography.

The size distribution for each aerosol type (Fig. 1a) are assumed as triangle binned and bimodal distribution: the fine mode is log-spaced in 10 radius bins (radius from 0.05 μm to 0.58 μm) and the coarse mode log-spaced in 15 bins (radius from 0.33 μm to 15 μm). Fine mode is predominant in Smoke aerosol with residual coarse mode, while for Dust the opposite occurs. We remember that for each scenario both fine and coarse mode have the same refractive indices, RRI being independent on wavelength with values of 1.51 and 1.56 for Smoke and Dust, respectively (Fig. 1c). The IRI is wavelength independent for Smoke, with a value of 0.021, while for Dust it is assumed variable with wavelength varying from 0.003 at 440 nm to 0.001 at 1064 nm (Fig. 1d). The vertical aerosol distribution has been assumed as an exponential decay with altitude for Smoke, while this distribution has been considered as a Gaussian layer centred at 2000 m a.g.l. for Dust (Fig. 1b).

Different synthetic scenarios are considered consisting to Smoke, Dust and mixtures among them. In the mixtures we assume that fine mode has the intensive properties of Smoke while for coarse mode they are those of Dust. Fine mode of size distribution is proportional to Smoke while that for coarse mode is proportional to Dust. Two different mixtures are considered, Mix-1 that imposes that AOD_{440} is equal for fine and coarse mode, and Mix-2 that imposes AOD at 1064 nm is equal for both modes. The difference between Mix-1 and Mix-2 is the larger volume concentration of fine particles in Mix-2 than in Mix-1. The size distribution and the vertical concentration for these scenarios can be observed in the figures discussed in Section 4.2, labeled as "Original" in Figs. 4 and 5, respectively. From all these scenarios, twelve (4 aerosol types × 3 AODs) synthetic data are computed from different AOD_{440} values: 0.1 (low aerosol load), 0.4 (minimum AOD_{440} used by AERONET to provide quality assured SSA, RRI and IRI in version 2 retrievals) and 1.0 (high aerosol load).

The GRASP forward model is used to compute the synthetic observations (spectral AOD, sky radiances and RCS at 1064 nm) following the conditions described in the flow diagram of Fig. 2 for each of the twelve aerosol scenarios, and varying the SZA by 10° from 40° to 80° in order to test different sets of scattering angles. Note that in all our simulations the ground is assumed as the sea level and the assumed BDRF parameters for these simulations are the climatological values (explained in Section 3.1.3) for Granada in summer. Later, using the GRASP forward model the required observations for $GRASP_{pac}$ are computed - AOD and sky radiances (26 values from 3.5° to 160° azimuth angles) at 440, 675, 870 and 1020 nm and RCS (60 heights) at 1064 nm.

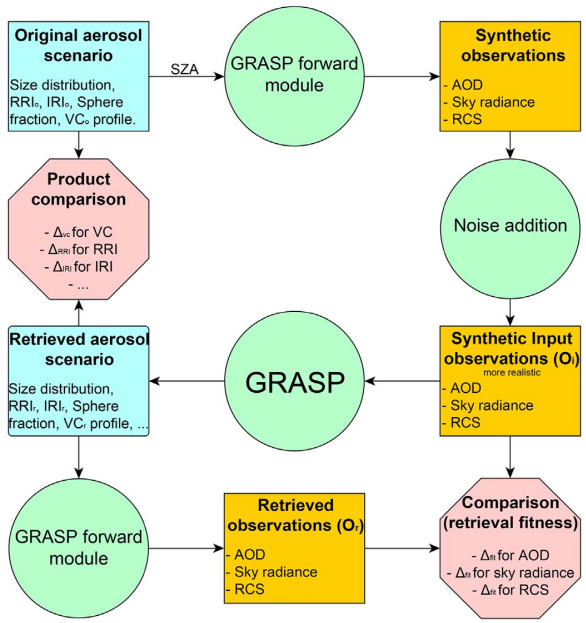

Fig. 2. Flow diagram about retrieval sensitivity study with synthetic data.

The computed synthetic observations are not representative of real measurements unless instrument uncertainties are considered, which are ± 0.01 for AOD and ± 5% for sky radiances according to AERONET standards (Holben et al., 1998). Therefore, next step in the simulation scheme of Fig. 2 is to add uncertainties to the simulated AOD and sky radiances, which is done by adding random errors generated from pseudorandom number that follows a normal distribution with standard deviation equal to the uncertainties. The addition of noise to the simulated RCS values is done assuming a constant uncertainty (K) on raw ceilometer signal and, therefore, the uncertainty σ(RCS) varies with the square of the distance (z) and at a level 'z' is given as:

$$\sigma(RCS_z) = Kz^2 \tag{2}$$

where RCS_z is the range corrected signal at z.

The calibration constant for Granada ceilometer obtained by Cazorla et al. (2017) for molecular (aerosol free) regions presents variations with standard deviation of approximately 30% (result not published). Thus, the uncertainty of ceilometer RCS could be assumed as a 30% at the reference height (z_{ref}) where only molecular backscatter is detected. Then the uncertainty of RCS at z_{ref} can be written as:

$$\sigma(RCS_{z=z_{ref}}) = 0.3 * RCS_{z=z_{ref}} \tag{3}$$

and combining Eq. (2) and Eq. (3):

$$K = \frac{0.3}{{z_{ref}}^2} RCS_{z=z_{ref}} \tag{4}$$

Finally, if Eq. (4) is put in Eq. (2), the uncertainty of RCS at each height can be expressed as:

$$\sigma(RCS_z) = \frac{0.3}{{z_{ref}}^2} RCS_{z=z_{ref}} * z^2 \tag{5}$$

The most frequent value of z_{ref} obtained by the method used in Cazorla et al. (2017) is about 4000 m a.g.l.; therefore, in this work, the uncertainty of ceilometer RCS is calculated by Eq. (5) using 4000 m as z_{ref}.

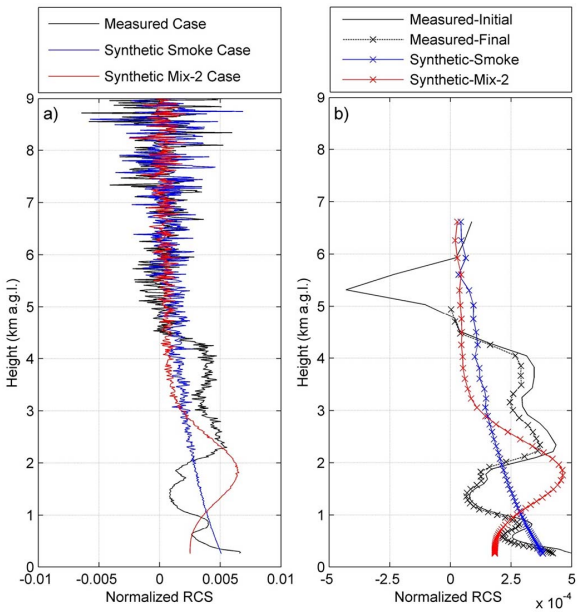

Fig. 3. Range corrected signals (RCS) at 1064 nm, from 250 m to 9000 m every 15 m, normalized by the sum of all data (panel a) for three cases: half hour average of measured ceilometer signal on 17 June 2013, 07:40 UTC (AOD_{440}~0.21) (black line); synthetic and noisy signal of Smoke with AOD_{440} equal to 0.4 (blue line); and synthetic and noisy signal of "Mix-2" with AOD_{440} equal to 0.4 (red line). Panel b shows the RCS of panel a, but normalized to 60 log-spaced points following the criteria used for $GRASP_{pac}$. (For interpretation of the references to colour in this figure legend, the reader is referred to the web version of this article.)

Once RCS uncertainty has been characterized, synthetic RCS is interpolated every 15 m, and for each RCS value at 15 m at each scenario, a pseudorandom number normally distributed is generated with a standard deviation equal to the uncertainty of this RCS value, and this random number is added to the previously simulated RCS.

As an example, Fig. 3a shows the synthetic RCS after adding uncertainties for the Smoke and Mix-2 scenarios with AOD_{440} equal to 0.4. In addition, a particular example of measured RCS in Granada (dust case with AOD_{440} = 0.21) is included to illustrate the capabilities of our scheme to generate synthetic RCS with uncertainties. The iterative method to skip negative values in the measured RCS is applied to the initial values (Measured-Initial) and it is observed as the final signal avoids negative values (Measured-Final). As can be observed the profiles look noisier at higher heights both for the synthetic and measured profiles. In fact, the shape of the added noise to the synthetic profiles is very similar to the one observed in the real measurements, which indicates that the obtained synthetic signal can be considered as realistic. The noise is higher for Smoke likely because for this scenario molecular zone is not completely well represented by the assumed z_{ref} equal to 4000 m a.g.l. Fig. 3b shows the RCS of Fig. 3a normalized to the 60 heights required as input in GRASP. It can be appreciated that noise is reduced by the averaging of RCS in log-scaled bins.

4.2. Analyses of retrieved parameters

As the diagram of Fig. 2 shows, once the noisy synthetic observations are obtained for each aerosol scenario and SZA value, these data are used as input in GRASP as explained in Section 3. The differences, Δ_{fit}, between the synthetic observations used as input in $GRASP_{pac}$ and the observations generated by the retrieved aerosol scenario are calculated to quantify the fitness of each $GRASP_{pac}$ retrieval (see Fig. 2). Δ_{fit} is defined as:

$$\Delta_{fit}(k,n) = O_r(k,n) - O_i(k,n) \quad (6)$$

and in percentage as:

$$\Delta_{fit}(k,n)(\%) = 100\% \frac{O_r(k,n) - O_i(k,n)}{O_i(k,n)} \quad (7)$$

where O represents an observation; the sub-index i and r indicated if the observation is an input or a value obtained from the retrieved aerosol scenario, respectively (see Fig. 2); k determines the kind of observation (AOD, sky radiances or RCS) and n is the number of this kind of observation. The fitness of the retrieval can be quantified for each k-kind observation by the mean (MBE; mean bias error) and standard deviation (STD) of Δ_{fit} using all n available observations for the k-kind. MBE represents the accuracy between O_r and O_i, while STD indicates their precision. Following this method, MBE and STD for AOD (sub-index *aod*), sky radiance (sub-index *rad*) and RCS (sub-index *rcs*) are calculated for all retrievals and they are shown in Table 1. MBE_{aod} and STD_{aod} are shown in absolute values while MBE and STD for sky radiance and RCS are in percentage. Scattering angle interval is also added in Table 1, reaching bigger angles when SZA increases. Table 1 reveals that MBE_{aod}, MBE_{rcs}, STD_{aod}, and STD_{rcs} are usually larger for retrievals with AOD_{440} = 0.1; MBE_{rad} is usually within ± 1% and STD_{rad} around 3%. In general, the fitness estimation does not show a clear dependence on aerosol type, SZA or AOD, which could indicate that differences in these values for different cases are mainly caused by the noise in the synthetic measurements since it is random.

Several aerosol $GRASP_{pac}$ products are obtained for each retrieval, but this work is mainly focus on columnar size distribution and especially on aerosol VC profiles. Fig. 4 shows, for different aerosol types and loads, all the retrieved size distributions for various SZA values. We remind that errors were added to input optical data. The original size distributions are also included. In general, the retrieved size distributions look qualitatively similar to the original ones, especially for the coarse mode, for all aerosol scenarios. Discrepancies on fine mode are more evident especially at low AODs. Worse agreement is expected for small SZA values since the scattering angle range is shorter, however it is not observed. The differences between the original and retrieved size distributions are mostly related with Δ_{fit}. For example, the retrieved size distribution for Mix-1 type with AOD_{440} = 0.4 differs more from the original at SZA equal to 60° than for the other angles; it should be caused by a worse fit between the inputs and the retrieved observations as it can be observed in Table 1, where MBE_{rad} and STD_{rad} reach their highest values (2.3% and 7.0%, respectively) for all retrievals with AOD_{440} = 0.4. It can also be appreciated in the Mix-1 type with AOD_{440} = 1.0 and SZA of 80°.

Fig. 5 shows the VC profiles for the same data than in Fig. 4. These profiles show a good agreement with the original ones when coarse mode predominates as can be observed for Dust and Mix-1 cases. The larger differences between retrieved and reference profiles are found for Smoke, being particularly noisy for heights above 2 km. This worse agreement for Smoke could be due to the use of RCS at 1064 nm, this wavelength being less sensitive to the fine particles like those prevailing in Smoke. The original Mix-2 profiles present two intense aerosol layers: dust around 2 km and smoke below 1 km; $GRASP_{pac}$ method is able to detect both aerosol layers, although it shows discrepancies compared with the reference. This can be explained by the limited information of using RCS at only one wavelength. To quantify all the differences we defined Δ_{vc}, as the difference between the retrieved and original VC profiles (see Fig. 2) given by:

$$\Delta_{vc}(a,SZA,z) = VC_r(a,SZA,z) - VC_o(a,SZA,z) \quad (8)$$

and in percentage as:

$$\Delta_{vc}(a,SZA,z)(\%) = 100\% \frac{VC_r(a,SZA,z) - VC_o(a,SZA,z)}{VC_o(a,SZA,z)} \quad (9)$$

where VC_r and VC_o represents the retrieved and original VC values,

Table 1
Mean bias error (MBE) of the $GRASP_{pac}$ retrievals (Δ_{fit} from Eqs. (6) and (7)) of AOD, sky radiance, and lidar range-corrected signal (aod, rad, and rcs respective index) under different aerosol scenarios. Standard deviation (STD) of Δ_{fit} is in parenthesis.

Aerosol type*	SZA (°)	Scattering Angle Range (°)	AOD_{440} = 0.1			AOD_{440} = 0.4			AOD_{440} = 1.0		
			MBE_{aod} (×1000)	MBE_{rad} (%)	MBE_{rcs} (%)	MBE_{aod} (×1000)	MBE_{rad} (%)	MBE_{rcs} (%)	MBE_{aod} (×1000)	MBE_{rad} (%)	MBE_{rcs} (%)
Smoke	40	2.3–78.6	5.3	−0.5	0.0	1.8	−0.1	0.2	−0.3	−0.2	0.1
			(8.2)	(3.0)	(1.3)	(3.0)	(3.1)	(4.7)	(0.4)	(2.8)	(1.3)
	50	2.7–98.0	16.7	−0.3	0.4	−1.5	0.2	0.0	1.0	−0.5	0.2
			(19.7)	(2.7)	(5.3)	(3.0)	(2.9)	(0.4)	(1.5)	(3.8)	(2.3)
	60	3.0–117.1	0.5	−0.1	0.1	0.4	−0.1	0.1	13.5	−1.7	−0.1
			(0.7)	(3.1)	(3.1)	(0.4)	(2.8)	(1.6)	(17.4)	(3.6)	(2.7)
	70	3.3–135.5	3.8	−0.6	0.0	−1.1	−0.5	0.2	0.4	−0.1	0.1
			(5.8)	(3.0)	(2.0)	(2.0)	(3.6)	(3.4)	(0.2)	(3.2)	(0.9)
	80	3.5–151.8	2.6	−0.6	0.1	1.7	−1.3	0.2	−0.1	−0.3	0.2
			(3.7)	(2.8)	(2.3)	(3.5)	(3.0)	(0.7)	(0.8)	(3.3)	(2.5)
Dust	40	2.3–78.6	16.7	−2.9	7.2	−5.5	−1.1	0.5	9.4	−3.2	0.3
			(30.4)	(4.0)	(14.7)	(8.6)	(2.9)	(4.1)	(7.7)	(4.0)	(2.6)
	50	2.7–98.0	3.2	−0.8	1.9	−5.1	0.8	0.1	11.6	1.5	1.3
			(4.2)	(3.0)	(5.4)	(7.4)	(4.4)	(4.2)	(11.3)	(4.5)	(4.8)
	60	3.0–117.1	16.5	−0.2	0.7	−2.9	0.0	0.0	−3.0	1.1	0.5
			(31.3)	(3.2)	(5.0)	(4.7)	(3.3)	(2.3)	(4.9)	(4.0)	(1.9)
	70	3.3–135.5	7.5	−0.6	0.3	−3.7	0.7	0.0	8.7	0.3	0.2
			(14.3)	(3.0)	(3.7)	(6.5)	(3.4)	(1.7)	(6.2)	(3.6)	(2.9)
	80	3.5–151.8	−4.0	0.7	0.3	7.6	−0.3	0.2	3.6	0.2	0.2
			(7.5)	(3.2)	(1.1)	(10.3)	(2.7)	(2.0)	(4.0)	(3.4)	(1.9)
Mix-1	40	2.3–78.6	4.1	−0.5	0.9	−3.0	−0.5	0.4	−5.9	0.1	−0.2
			(6.3)	(2.8)	(3.1)	(4.0)	(3.4)	(1.7)	(10.4)	(2.9)	(1.9)
	50	2.7–98.0	−7.6	0.1	0.9	11.2	0.1	0.3	−0.4	0.2	−0.1
			(13.5)	(3.6)	(2.3)	(16.7)	(3.3)	(6.8)	(0.8)	(3.6)	(2.8)
	60	3.0–117.1	−5.6	2.4	8.4	−2.1	2.3	0.0	−1.0	0.6	−0.2
			(7.6)	(5.6)	(11.8)	(4.5)	(7.0)	(2.0)	(1.3)	(3.1)	(1.5)
	70	3.3–135.5	−2.8	0.4	1.2	−8.4	2.1	0.6	1.9	0.5	0.1
			(4.3)	(3.4)	(4.1)	(16.4)	(4.7)	(2.7)	(3.0)	(3.4)	(1.1)
	80	3.5–151.8	−2.8	6.4	8.1	−2.2	1.7	−0.2	9.3	1.5	0.4
			(8.0)	(8.0)	(11.1)	(3.0)	(3.8)	(1.6)	(12.5)	(4.6)	(3.9)
Mix-2	40	2.3–78.6	−3.3	−1.8	1.4	2.4	1.3	0.8	−0.1	−0.2	0.0
			(6.7)	(3.5)	(5.1)	(3.7)	(5.1)	(8.3)	(0.2)	(3.3)	(1.1)
	50	2.7–98.0	−3.8	−2.0	1.1	0.7	−0.4	0.1	0.4	0.0	0.1
			(6.0)	(3.2)	(6.0)	(1.1)	(3.1)	(2.0)	(1.2)	(2.9)	(5.4)
	60	3.0–117.1	1.1	−0.2	0.6	1.6	1.4	0.4	0.0	1.0	0.0
			(2.5)	(3.4)	(3.6)	(2.6)	(4.9)	(3.2)	(0.4)	(3.5)	(0.9)
	70	3.3–135.5	1.9	−3.5	2.1	−0.4	−0.1	0.0	−0.8	0.1	0.0
			(4.9)	(4.4)	(9.7)	(1.0)	(2.6)	(1.0)	(0.5)	(3.3)	(0.3)
	80	3.5–151.8	−0.7	−0.1	0.1	0.0	0.0	0.1	0.1	0.1	0.0
			(0.9)	(2.5)	(2.6)	(1.1)	(3.5)	(1.4)	(0.1)	(2.4)	(1.4)

*See Section 4.1 for the aerosol models description.

respectively (see Fig. 2); *a* determines the aerosol scenario (aerosol type and AOD_{440}) and *z* being one of the 60 bins of the retrieved VC profiles.

Table 2 shows the MBE and STD calculated as the mean and standard deviation, respectively, of the 60 Δ_{vc} values (Eqs. (8) and (9)) of each profile. The Δ_{vc} values with VC_o below 1 $\mu m^3/cm^3$ have been discarded in the MBE and STD calculation since they could provide extreme differences in percentage. The results of Table 2 are showed for each of the 12 different aerosol scenarios and for different SZA. MBE and STD of Table 2 do not show any dependence with SZA. The best agreements (minima MBE and STD) are found for Dust and Mix-1 scenarios, where coarse mode is predominant. In general, unsigned MBE increases with AOD_{440} while the precision of $GRASP_{pac}$, given by STD, decreases in percentage with AOD_{440}. As a general result, for all scenarios together $GRASP_{pac}$ systematically underestimates VC showing a MBE of −5.9% and with an uncertainty, which is given by STD, of 21%. The lowest uncertainties of $GRASP_{pac}$ are for Dust aerosol (~14%) with bias close to zero, while the highest uncertainties are for the Smoke type (~28%).

In order to observe if the obtained differences between the original VC and the retrieved by $GRASP_{pac}$ are within σ_G (the estimation of retrieval uncertainty provided by $GRASP_{pac}$), the percentage of unsigned Δ_{vc} values (Eq. (8)) that are below σ_G and $2\sigma_G$ have been calculated and named as $\Delta_{vc} < \sigma_G$ and $\Delta_{vc} < 2\sigma_G$, respectively. If $\Delta_{vc} < \sigma_G$ and $\Delta_{vc} < 2\sigma_G$ are similar to 68% and 95%, respectively, σ_G will represent the uncertainty in a good way indicating that Δ_{vc} is similar to a normal distribution with a standard deviation equal to σ_G. Table 3 shows the obtained results for each scenario shown in Table 2. $\Delta_{vc} < \sigma_G$ and $\Delta_{vc} < 2\sigma_G$ do not show any dependence on SZA or AOD_{440}. Mix-2 aerosol scenario presents the $\Delta_{vc} < \sigma_G$ and $\Delta_{vc} < 2\sigma_G$ values closer to 68% and 95%; Dust and Mix-1 show even higher values. Smoke aerosol shows the lowest values when all SZA and AOD_{440} values are taken into account, but it is mainly caused by various individual cases with SZA = 60° and AOD_{440} = 0.1 or SZA = 40° and AOD_{440} = 1.0. For the combination of all the different aerosol scenarios, $\Delta_{vc} < \sigma_G$ is 74% and $\Delta_{vc} < 2\sigma_G$ is 91%, which are close values to the expected 68% and 95%, and therefore we can conclude that $GRASP_{pac}$ reproduces well the VC profiles within the margins given by the uncertainty associated with the numerical inversion.

For backscatter and extinction coefficients at 1064 nm and column integrated intensive properties such as complex refractive index, SSA and LR we also did the same computations (not shown) as in Table 2 and Table 3. Combining all the data of the different aerosol scenarios MBE are −11% and −5% and STD equal to 31% and 21% for backscatter and extinction profiles, respectively. For the backscatter coefficient, MBE presents the largest values for Smoke and Mix-2, while Dust and Mix-2 show the largest STD values. In the case of the extinction

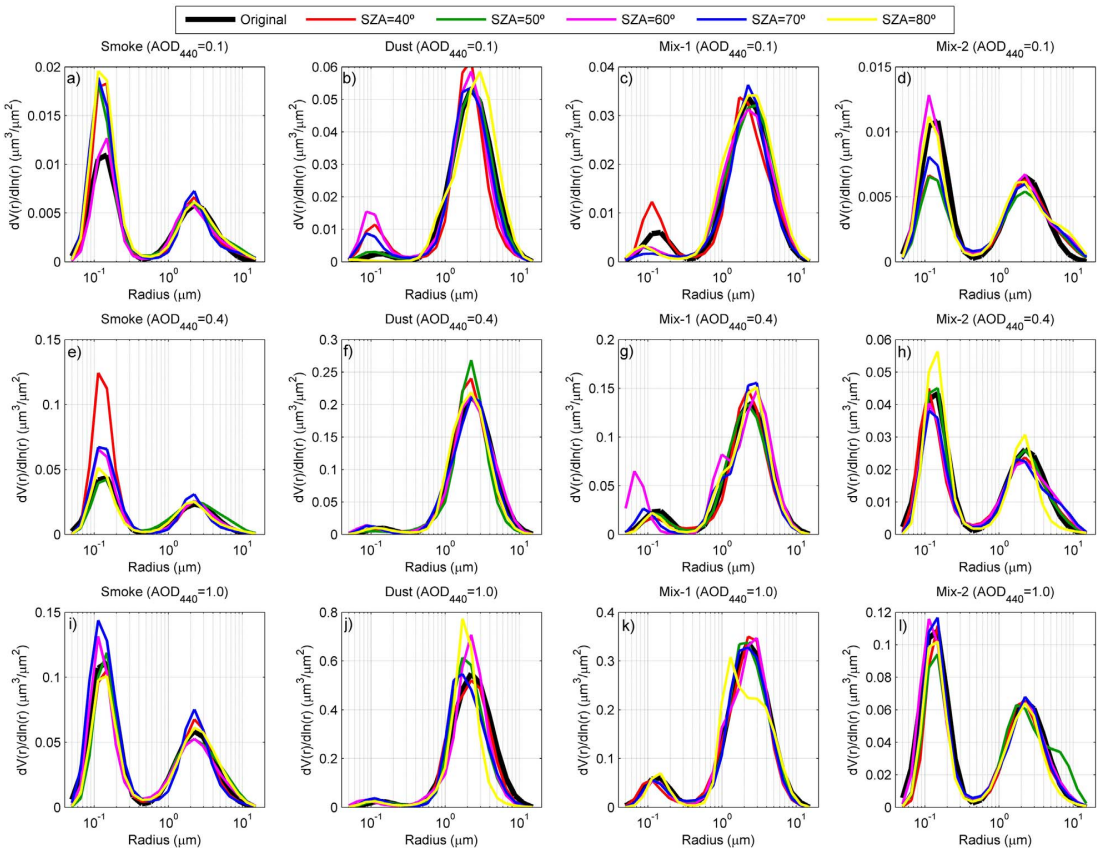

Fig. 4. Original aerosol size distribution as retrieved by $GRASP_{pac}$ for different aerosol types (Smoke, Dust, Mix-1 and Mix-2) and loads (AOD_{440} = 0.1, 0.4 and 1.0), and at different solar zenith angles (SZA) from 40° to 80°.

coefficient, Dust and Mix-1 present the lowest STD (13% and 15%) and MBE (3% and 2%) values. Regarding the retrieved column-integrated SSA, considering the five wavelengths together, the retrieved SSA fits better the original values when AOD_{440} increases, MBE being equal to −0.02, 0.01 and 0.00 and STD equal to 0.08, 0.05, and 0.02 for AOD_{440} of 0.10, 0.4 and 1.0, respectively for all aerosol types and SZA values. The retrieved SSA also agrees better as SZA increases, indicating the importance of large scattering angles in this property as expected (Dubovik et al., 2000), but this dependence is only clear for AOD_{440} = 0.4 and 1.0. Similar dependence on AOD_{440}, but not on SZA, appears for the retrieved LR. These LR retrievals agree with the references when all scenarios are considered together (MBE and STD are 10% and 29%). This agreement is found particularly for the Smoke aerosol cases. MBE and STD are reduced to 1% and 26% when only cases with AOD_{440} = 0.4 are selected. Finally, for RRI and IRI, good agreements with the reference values are found for high AOD_{440}. Our last computations reveal that the differences between retrieved properties and the original ones are within σ_G, the obtained results indicate that σ_G of backscatter and extinction is representative of the real uncertainty for all AOD_{440} and SZA values. On the other hand, for SSA and LR the percentage of differences below σ_G is lower than the expected and showing an increase with AOD_{440}.

5. Results from inversion of real observations

5.1. Airborne comparison

Fig. 6 shows the ceilometer RCS for the period 16-17th June 2013 where flights over Granada were done within the ChArMEx/ADRIMED field campaign. The largest RCS are observed below ~2 km a.s.l. that usually corresponds to aerosol in the planetary boundary layer (PBL). During this period, the study region was affected by Saharan dust outbreaks with transport of dust particles (Benavent-Oltra et al., 2017). The presence of long-range transported aerosol is clearly observed in Fig. 6 with significant signal up to 5 km a.s.l., approximately. Decoupled aerosol layers appeared from the 16th June evening to 17th morning, with aerosol entrainment in the PBL also observed, which is typically observed during Saharan dust arrivals at the study station (Bravo-Aranda et al., 2015). Signal decreases are observed from 17th morning, particularly strong at low levels, and explained by advection of clean air-masses at these levels. However, a high-altitude layer remained at 3–5 km a.s.l.. The averaged (± standard deviation) daytime AOD at 440 nm and Angström Exponent (AE; in this work calculated only with the AOD at 440 and 870 nm) were 0.26 ± 0.01 and 0.35 ± 0.04 (63 data), respectively, for 16th June and 0.20 ± 0.04 and 0.44 ± 0.04 for 17th June (19 data); the low AE values indicate the presence of coarse particles. Five-day back-trajectories analyses using HYSPLIT model (Stein et al., 2015) (not shown) point out that the air masses came at Granada from the Saharan desert, which agrees with the presence of coarse particles as Saharan mineral dust.

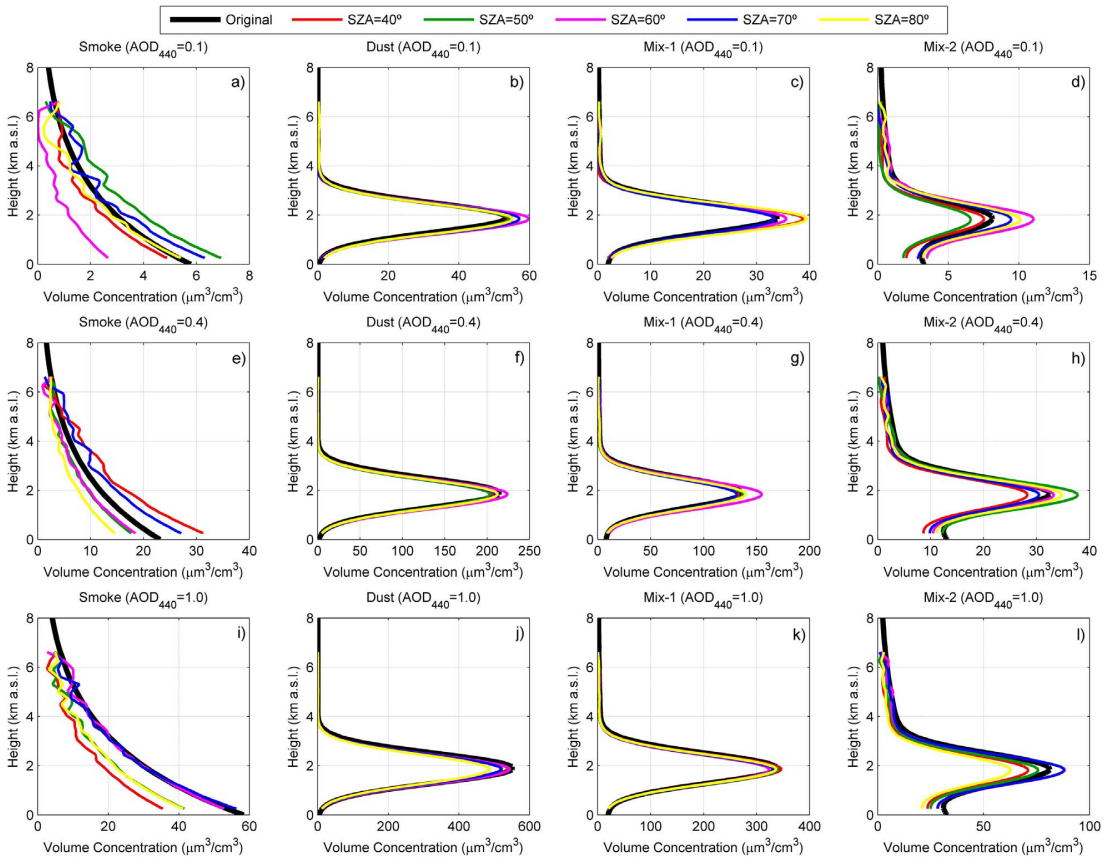

Fig. 5. Original aerosol volume concentration (VC) vertical profile as retrieved by $GRASP_{pac}$ for different aerosol types (Smoke, Dust, Mix-1 and Mix-2) and loads (AOD_{440} = 0.1, 0.4 and 1.0), and at different solar zenith angles (SZA) from 40° to 80°.

Airplane spirals near the study region were done at 14:15–14:45 UTC (denoted as F30) and at 07:15–07:45 UTC (F31). F31 trajectory (similar to F30) is shown in Benavent-Oltra et al. (2017) and it shows that airborne measurements were done around 20 km far from Granada station. The time of both flights are marked in Fig. 6 with black vertical lines while the closest $GRASP_{pac}$ retrieval to each flight is indicated by two green vertical lines, with AOD_{440} of 0.27 and 0.21, respectively. The time difference of 2 h between F30 flight and the closest $GRASP_{pac}$ retrieval is because limitations in SZA (at the exact time of the flight SZA was very small and become larger than 40° from 16:22 UTC). However, stable AOD measurements suggest not big aerosol variations during this 2 h period.

Fig. 7 shows the column-integrated size distribution, SSA, and refractive indices obtained by $GRASP_{pac}$ and these provided by AERONET (level 1.5). Comparisons of size distributions reveal that they are very similar between both methodologies, being the differences within the $GRASP_{pac}$ uncertainties. The size distributions also indicate the predominance of the coarse mode as expected for Saharan dust outbreaks (Valenzuela et al., 2012), and both retrievals point out a positive shift of the coarse mode concentration in the morning of 17th June. It is corroborated by the effective radius of the coarse mode given by $GRASP_{pac}$, which varied from 1.93 μm (Fig. 6a) to 2.22 μm (Fig. 6b). For SSA, Fig. 7c and d reveal that values are very similar between $GRASP_{pac}$ and AERONET, and both retrievals show a spectral dependence typical of mineral dust (Dubovik et al., 2002). RRI from AERONET is slightly higher in both cases than from $GRASP_{pac}$, but both retrievals show wavelength independence and a weak decrease from 16th to 17th June.

Finally, for IRI again both AERONET and $GRASP_{pac}$ show similar patterns, typical for dust (Dubovik et al., 2002), and differences between methodologies are within the uncertainties. All these results point out that the column-integrated products from $GRASP_{pac}$ are in accordance with the ones provided by AERONET, at least in the analysed cases.

Fig. 8 shows vertically-resolved values of particle VC from $GRASP_{pac}$ ($VC_{GRASP_{pac}}$) and the values obtained by airborne measurements ($VC_{Airborne}$). Generally both methodologies present very similar profiles for the two cases. For the flight F30, only one layer is observed with a slight and constant decrease up to 4.5 km approximately, while for F31 three different layers are observed. Most of the differences are within the $GRASP_{pac}$ uncertainty, however, disagreements are found between retrievals and airplane measurements for altitudes below 1.5 km, which can be explained because of the orography and air-traffic restriction that did not allow the flight to perform spiral exactly above the station. This reasoning agrees with the largest aerosol VC values at the lowest layer observed by GRASP retrievals, which can be associated with pollution from the city.

To quantify the differences between $GRASP_{pac}$ and airborne profiles, the VC from $GRASP_{pac}$ has been interpolated to the available heights of the airborne measurements. Point-by-point intercomparison between GRASP retrievals and airborne measurements are done. Linear interpolations of $GRASP_{pac}$ are done too for the same altitude than airborne measurements. Cases with very low aerosol load ($VC < 5\,\mu m^3/cm^3$) and measurements below 1.25 km a.s.l. (large disagreements in aerosol sampled between both techniques) are rejected in this comparison. Fig. 9 shows particle VC obtained by GRASP versus airborne values. The

Table 2
MBE and STD from the differences between the VC retrieved by $GRASP_{pac}$ and the original VC (Δ_{vc} from Eqs. (8) and (9)) under different aerosol scenarios and SZA values. Original VC values below 1 $\mu m^3/cm^3$ have not been taken into account in the calculations. MBE and STD are given in % in parenthesis.

Aerosol type*	SZA (°)	AOD_{440} = 0.1		AOD_{440} = 0.4		AOD_{440} = 1.0		All	
		MBE ($\mu m^3/cm^3$)	STD ($\mu m^3/cm^3$)	MBE ($\mu m^3/cm^3$)	STD ($\mu m^3/cm^3$)	MBE ($\mu m^3/cm^3$)	STD ($\mu m^3/cm^3$)	MBE ($\mu m^3/cm^3$)	STD ($\mu m^3/cm^3$)
Smoke	40	−0.5 (−15.5)	0.1 (8.4)	6.0 (39.2)	3.2 (17.1)	−12.7 (−38.2)	4.8 (6.5)	−2.5 (−4.5)	8.5 (35.0)
	50	1.2 (33.6)	0.3 (5.9)	−2.5 (−18.6)	1.0 (5.7)	−8.7 (−26.4)	3.2 (6.9)	−3.5 (−4.9)	4.5 (27.1)
	60	−2.0 (−57.9)	0.5 (9.4)	−2.2 (−18.7)	0.7 (11.0)	−0.5 (−1.8)	0.8 (9.0)	−1.6 (−25.2)	1.0 (25.2)
	70	0.6 (14.9)	0.3 (9.8)	3.6 (24.8)	1.8 (13.3)	0.6 (−0.7)	1.4 (8.4)	1.6 (12.9)	2.0 (15.1)
	80	−0.1 (−6.1)	0.2 (11.8)	−4.6 (−33.6)	1.8 (5.8)	−8.9 (−27.5)	3.1 (6.9)	−4.7 (−22.9)	4.2 (14.4)
	All	−0.2 (−6.2)	1.1 (32.3)	0.0 (−1.4)	4.4 (30.4)	−6.0 (−18.9)	6.0 (16.8)	−2.1 (−8.9)	5.2 (28.2)
Dust	40	0.3 (−1.5)	1.7 (13.1)	−2.0 (−2.7)	6.7 (12.4)	−3.1 (−1.4)	14.0 (11.3)	−1.6 (−1.9)	9.2 (12.2)
	50	0.5 (3.6)	1.6 (10.6)	−3.1 (−5.2)	7.2 (13.8)	−9.0 (−5.7)	16.2 (11.6)	−4.0 (−2.6)	11.1 (12.7)
	60	2.2 (11.5)	2.7 (10.9)	3.6 (5.4)	6.9 (12.7)	−1.9 (−1.5)	14.3 (12.5)	1.3 (5.0)	9.6 (13.1)
	70	1.3 (5.8)	2.1 (11.0)	−0.5 (2.1)	6.5 (12.1)	−10.1 (−7.2)	15.5 (11.4)	−3.2 (0.1)	11.1 (12.7)
	80	1.1 (15.5)	1.7 (18.2)	−0.3 (−1.0)	5.7 (11.8)	−20.1 (−11.8)	25.0 (10.9)	−6.6 (0.6)	17.8 (17.8)
	All	1.1 (7.0)	2.1 (14.3)	−0.5 (−0.3)	6.9 (13.0)	−8.8 (−5.5)	18.5 (12.1)	−2.8 (0.3)	12.4 (14.1)
Mix-1	40	1.4 (1.8)	2.1 (18.1)	−1.1 (−8.9)	3.4 (14.0)	0.9 (−6.1)	7.1 (13.9)	0.3 (−4.8)	4.9 (15.8)
	50	−0.1 (−1.5)	0.9 (8.2)	0.1 (−6.8)	3.3 (12.5)	−0.7 (−7.0)	7.9 (12.5)	−0.3 (−5.3)	5.1 (11.6)
	60	0.6 (2.1)	1.1 (9.3)	6.1 (18.6)	7.3 (17.9)	−5.0 (−9.7)	9.7 (12.1)	0.5 (3.7)	8.6 (18.2)
	70	−0.2 (−3.1)	0.9 (8.6)	−1.1 (−1.1)	3.7 (13.1)	−3.0 (−10.6)	8.8 (14.2)	−1.5 (−5.1)	5.8 (13.0)
	80	2.0 (14.9)	2.1 (8.7)	1.0 (−2.7)	3.5 (13.0)	−2.3 (−10.7)	6.0 (14.8)	0.1 (−0.4)	4.7 (16.3)
	All	0.7 (2.9)	1.8 (12.8)	1.0 (−0.2)	5.2 (17.2)	−2.0 (−8.8)	8.2 (13.6)	−0.2 (−2.4)	6.0 (15.6)
Mix-2	40	−0.8 (−24.5)	0.2 (13.2)	−3.1 (−28.2)	1.1 (14.1)	−6.7 (−23.7)	2.7 (11.3)	−3.7 (−25.6)	3.0 (13.0)
	50	−1.2 (−32.2)	0.2 (10.9)	1.2 (−1.2)	2.0 (21.4)	−4.6 (−18.0)	1.9 (12.1)	−1.6 (−16.1)	3.0 (20.1)
	60	1.1 (21.9)	0.9 (12.3)	−0.9 (−12.5)	1.0 (12.8)	0.4 (−3.2)	3.3 (12.6)	0.2 (0.8)	2.3 (18.9)
	70	0.3 (2.7)	0.6 (10.2)	−1.9 (−18.5)	0.8 (12.4)	0.2 (−4.2)	3.3 (12.7)	−0.5 (−7.3)	2.3 (14.7)
	80	0.7 (11.1)	0.7 (12.6)	−0.2 (−8.6)	1.3 (14.8)	−10.1 (−32.0)	4.8 (9.5)	−3.5 (−11.2)	5.8 (21.4)
	All	0.0 (−4.2)	1.1 (23.9)	−1.0 (−13.8)	2.0 (17.8)	−4.2 (−16.2)	5.2 (16.1)	−1.8 (−11.9)	3.8 (19.9)
All	40	0.1 (−10.1)	1.6 (17.1)	0.0 (0.0)	5.4 (29.1)	−5.5 (−18.0)	9.4 (18.3)	−1.9 (−9.4)	7.0 (23.5)
	50	0.1 (1.9)	1.3 (25.4)	−1.0 (−8.1)	4.3 (15.8)	−5.6 (−14.6)	9.4 (13.8)	−2.3 (−7.3)	6.6 (19.8)
	60	0.4 (−7.3)	2.2 (33.6)	1.6 (−2.2)	6.0 (20.3)	−1.7 (−4.1)	8.7 (12.0)	0.1 (−4.4)	6.5 (23.2)
	70	0.5 (5.3)	1.3 (11.9)	0.0 (1.8)	4.3 (20.2)	−2.8 (−5.6)	9.6 (12.4)	−0.8 (0.3)	6.4 (16.1)
	80	0.9 (8.4)	1.6 (15.9)	−1.1 (−12.0)	4.0 (17.7)	−10.0 (−20.8)	13.9 (14.4)	−3.6 (−8.9)	9.8 (20.0)
	All	0.4 (−0.4)	1.6 (23.3)	−0.1 (−4.1)	4.9 (21.7)	−5.1 (−12.6)	10.7 (15.8)	−1.7 (−5.9)	7.5 (21.0)

*See Section 4.1 for the aerosol models description.

correlation between both methodologies is high (correlation coefficient, *r*, higher than 0.80), and slightly better for F30 flight. However, the slope of the least square fit indicates that $GRASP_{pac}$ underestimates the highest airborne measurements and the abscissa intercept points out that $GRASP_{pac}$ overestimates the lowest values. In addition, the differences, ΔVC, between VC values from $GRASP_{pac}$ and airborne have been calculated as follows:

$$\Delta VC = VC_{GRASP_{pac}} - VC_{Airborne} \quad (10)$$

and in percentage as:

$$\Delta VC\,(\%) = 100\% \frac{VC_{GRASP_{pac}} - VC_{Airborne}}{VC_{Airborne}} \quad (11)$$

The histograms of ΔVC (Eq. (10)) are shown in Fig. 9d, e and f for F30, F31 and both flights, respectively. These graphs indicate that VC from $GRASP_{pac}$ agrees better with airborne measurements for F30 flight, being the 37% of the absolute ΔVC values below 2.5 $\mu m^3/cm^3$ and 89% below 7.5 $\mu m^3/cm^3$. The ΔVC distribution for F31 flight presents higher values but it is similar to a normal distribution, 61% of ΔVC absolute data being lower than 7.5 $\mu m^3/cm^3$; this percentage rises up to 75% when both flights are taken into account. Table 4 shows the mean (MBE), mean of the absolute values (MABE) and standard deviation (STD) of ΔVC (Eqs. (10) and (11)) for these three cases of Fig. 9. $GRASP_{pac}$ slightly overestimates the $VC_{Airborne}$ values, showing MBE values of 10.5% and 12.9% for F30 and F31 flights, respectively; however, the absolute MBE is close to 0 $\mu m^3/cm^3$. Assuming airborne measurements as a reference, the accuracy, given by MBE, of VC from $GRASP_{pac}$ is below 12% when both flights are taken into account. Regarding MABE, F31 flight shows values around the double of that obtained from F30, which indicates that ΔVC differences are much higher in the F31 case, as STD confirms. The precision of $GRASP_{pac}$ using airborne measurements as a reference can be represented by STD, which presents a low value of 18.5% in the F30 case, but this value for F31 rises up to 70.8% due to the vertical shift of the lowest layer observed in Fig. 8b. The STD for both flights together is 51.4%, but this value is still strongly affected by the differences in F31 flight for low heights. Finally, for both flights together, the percentage of ΔVC values which are below the uncertainty given by $GRASP_{pac}$ is 67.6%; this percentage is 94.4% when the double of the uncertainty is considered. These values are close to 68% and 95%, which points out that the uncertainty estimation provided by $GRASP_{pac}$ is representative of the real uncertainty of the retrieved VC.

5.2. High altitude station comparison

In-situ VC measurements during SLOPE I field campaign at SNS (VC_{SNS}) are used for evaluating retrieved values by $GRASP_{pac}$ at the same altitude. In-situ measurements measured total particle VC in the range 0.05–10 μm and the $GRASP_{pac}$ retrieved values are integrated in the same range. From retrieved VC profiles, linear interpolations are done to have data at 2500 m a.s.l., which is the altitude of SNS. Fig. 10 shows the temporal evolution of in-situ and retrieved VC values for the entire period. While measurements of VC_{SNS} were continuous (24 h per day), retrieved $GRASP_{pac}$ values are only available during some daytime points every day. The lack of VC_{SNS} data during some short periods were caused by instrumental failures. From Fig. 10 can be observed that both measured and retrieved values follow the same temporal evolution, with minimum values associated with clean atmosphere and extreme values associated mostly to Saharan dust arrivals. In fact, the largest values at Sierra Nevada were registered during the morning of 21st July, with in-situ measurements up to 269 $\mu m^3/cm^3$ and retrieved $GRASP_{pac}$ values from 279 to 364 $\mu m^3/cm^3$, and were associated with a

Table 3
Percentage of differences between the VC retrieved by $GRASP_{pac}$ and the original VC (Δ_{vc} from Eq. (8)) that is below the uncertainty, σ_G, of VC given by $GRASP_{pac}$, for different aerosol scenarios and SZA values. The same percentage but for differences below $2\sigma_G$ is also shown.

Aerosol type*	SZA (°)	AOD_{440} = 0.1		AOD_{440} = 0.4		AOD_{440} = 1.0		All	
		$\Delta_{vc} < \sigma_G$ (%)	$\Delta_{vc} < 2\sigma_G$ (%)	$\Delta_{vc} < \sigma_G$ (%)	$\Delta_{vc} < 2\sigma_G$ (%)	$\Delta_{vc} < \sigma_G$ (%)	$\Delta_{vc} < 2\sigma_G$ (%)	$\Delta_{vc} < \sigma_G$ (%)	$\Delta_{vc} < 2\sigma_G$ (%)
Smoke	40	95.0	100.0	8.3	98.3	1.7	1.7	35.0	66.7
	50	90.0	100.0	88.3	98.3	1.7	85.0	60.0	94.4
	60	1.7	1.7	81.7	93.3	95.0	98.3	59.4	64.4
	70	96.7	100.0	66.7	98.3	93.3	100.0	85.6	99.4
	80	91.7	95.0	3.3	68.3	0.0	85.0	31.7	82.8
	All	75.0	79.3	49.7	91.3	38.3	74.0	54.3	81.6
Dust	40	93.3	100.0	91.7	100.0	93.3	100.0	92.8	100.0
	50	90.0	100.0	80.0	91.7	86.7	98.3	85.6	96.7
	60	86.7	90.0	83.3	95.0	86.7	96.7	85.6	93.9
	70	78.3	85.0	80.0	95.0	85.0	96.7	81.1	92.2
	80	63.3	83.3	86.7	98.3	80.0	90.0	76.7	90.6
	All	82.3	91.7	84.3	96.0	86.3	96.3	84.3	94.7
Mix-1	40	81.7	83.3	85.0	95.0	85.0	98.3	83.9	92.2
	50	100.0	100.0	90.0	100.0	81.7	96.7	90.6	98.9
	60	100.0	100.0	91.7	98.3	80.0	96.7	90.6	98.3
	70	91.7	100.0	88.3	100.0	75.0	93.3	85.0	97.8
	80	98.3	100.0	88.3	100.0	81.7	98.3	89.4	99.4
	All	94.3	96.7	88.7	98.7	80.7	96.7	87.9	97.3
Mix-2	40	55.0	95.0	38.3	80.0	36.7	80.0	43.3	85.0
	50	40.0	90.0	91.7	93.3	61.7	93.3	64.4	92.2
	60	78.3	95.0	88.3	95.0	95.0	98.3	87.2	96.1
	70	95.0	95.0	66.7	86.7	96.7	98.3	86.1	93.3
	80	96.7	98.3	83.3	91.7	1.7	58.3	60.6	82.8
	All	73.0	94.7	73.7	89.3	58.3	85.7	68.3	89.9
All	40	81.3	94.6	55.8	93.3	54.2	70.0	63.7	86.0
	50	80.0	97.5	87.5	95.8	57.9	93.3	75.1	95.6
	60	66.7	71.7	86.3	95.4	89.2	97.5	80.7	88.2
	70	90.4	95.0	75.4	95.0	87.5	97.1	84.4	95.7
	80	87.5	94.2	65.4	89.6	40.8	82.9	64.6	88.9
	All	81.2	90.6	74.1	93.8	65.9	88.2	73.7	90.9

*See Section 4.1 for the aerosol models description.

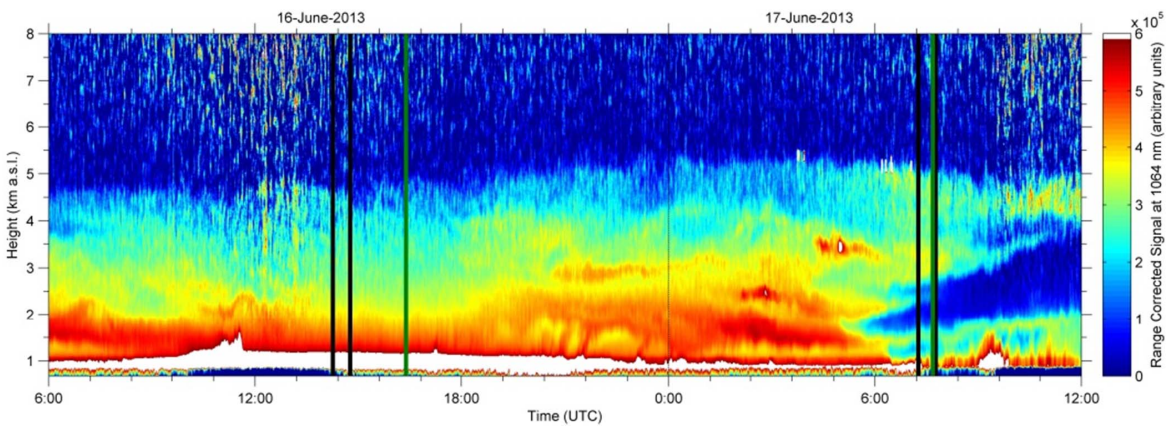

Fig. 6. Ceilometer range corrected signal at 1064 nm as a function of height and time from 16th, 6 UTC, to 17th June, 12 UTC, 2013. White colour represents all values above 6E5 arbitrary units. The times between vertical black lines corresponds to the F30 and F31 flights. Green vertical lines corresponds in time with the sky radiance and AOD measurements (sun photometer) nearest to the flights. (For interpretation of the references to colour in this figure legend, the reader is referred to the web version of this article.)

strong Saharan dust episode that started on 20th July 2016.

Fig. 11a shows a normalized number density plot of retrieved values by $GRASP_{pac}$ versus in-situ measurements (VC_{SNS}). Selected in-situ measurements are averaged during a time period of ± 15 min from the retrieval time. Most of the VC values on Fig. 11a are below 20 $\mu m^3/cm^3$, being 71% for VC_{SNS}. The linear fit reveals an overestimation of VC from $GRASP_{pac}$ to the VC_{SNS} values around 50%. The data for 26th August can be partially responsible of this overestimation with $VC_{GRASP_{pac}}$ values ~150 $\mu m^3/cm^3$ while VC_{SNS} is ~50 $\mu m^3/cm^3$. These larger differences could be in part due to real differences in the aerosol over the Granada vertical and the aerosol at Sierra Nevada, since SNS could be affected by local effects and sources.

The correlation between $VC_{GRASP_{pac}}$ and VC_{SNS} is high, being r equal to 0.91; this correlation coefficient is higher than the obtained between the ground measured AOD_{440} and VC_{SNS}, which is 0.79, and the correlation between the retrieved column-integrated VC and VC_{SNS}, which is 0.80. This result points out that the addition of ceilometer signal to the aerosol retrieval improves the capacity to estimate the aerosol vertical concentration.

As in Section 5.1, the differences ΔVC between $VC_{GRASP_{pac}}$ and the in-

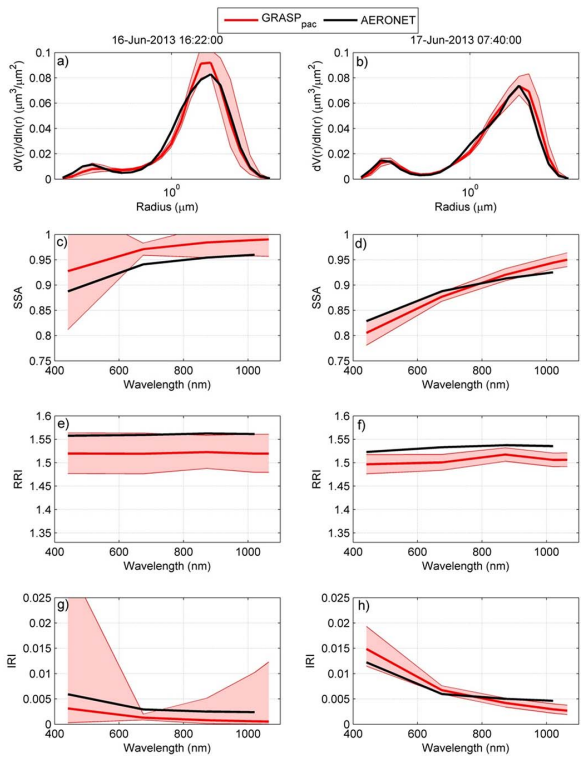

Fig. 7. Columnar size distribution (panels a and b), single scattering albedo (SSA; panels c and d), real refractive index (RRI, panels e and f) and imaginary refractive index (IRI; panels g and h) obtained by AERONET (black line) and GRASP (red line) at 16 June 2013 16:22 UTC (left panels) and 17 June 2013 07:40 UTC (right panels). Shadow band represents uncertainty in the GRASP$_{pac}$ retrieval. (For interpretation of the references to colour in this figure legend, the reader is referred to the web version of this article.)

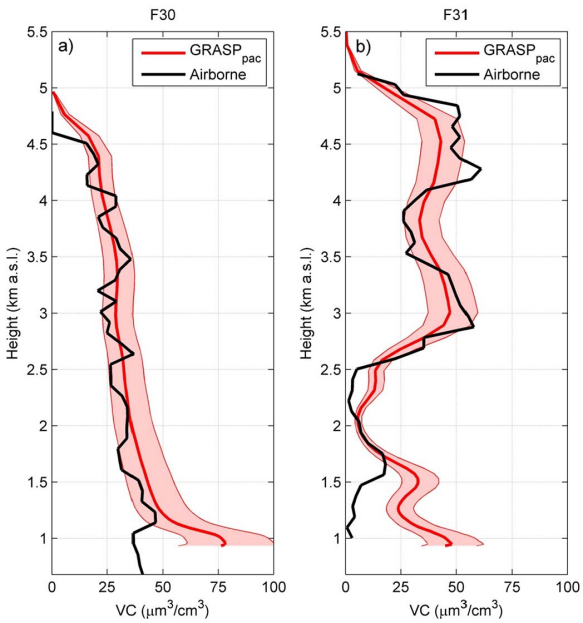

Fig. 8. Profiles of aerosol volume concentration (VC) obtained by airborne instrumentation (black line) and GRASP$_{pac}$ (red line) at the flights F30 (panel a) and F31 (panel b). Shadow band represents uncertainty in the GRASP$_{pac}$ retrieval. (For interpretation of the references to colour in this figure legend, the reader is referred to the web version of this article.)

situ measurements, in this case VC_{SNS}, have been calculated. ΔVC can be expressed as:

$$\Delta VC = VC_{GRASP_{pac}} - VC_{SNS} \tag{12}$$

and in percentage as:

$$\Delta VC\,(\%) = 100\% \frac{VC_{GRASP_{pac}} - VC_{SNS}}{VC_{SNS}} \tag{13}$$

Fig. 11b shows the ΔVC (Eq. (12)) distribution. This frequency histogram is similar to a normal distribution, the maximum being centred close to 0; however it is skewed to positive values. 38%, 73% and 87% of $VC_{GRASP_{pac}}$ shows absolute ΔVC differences lower than 2.5, 7.5 and 12.5 μm^3/cm^3, respectively.

Table 5 shows mean values and standard deviations of the differences ΔVC, from Eqs. (12) and (13), for different VC_{SNS} ranges. The percentages of data when ΔVC is lower than the numerical uncertainty in the inversion, σ_G, are also included. From Table 5 when all ranges of VC are considered mean differences and standard deviations are 31% and 94%, both strongly affected by the low values of VC_{SNS}. In fact, MBE and STD are 64% and 169%, respectively, for VC_{SNS} values only below 5 μm^3/cm^3. However, if only data with VC_{SNS} above 5 μm^3/cm^3 are selected (493 in total), mean difference and standard deviations are reduced to 23% and 59%, respectively. In general, MBE increases with VC_{SNS} ranging from 10% to 60% if VC_{SNS} below 5 μm^3/cm^3 is not considered. MABE presents values around 40–50% for VC_{SNS} between 5 and 100 μm^3/cm^3. STD varies from 34 to 64%, showing the lowest values for highest concentrations. Regarding the ΔVC differences within the GRASP$_{pac}$ uncertainty estimation, Table 5 shows values below that expected, which indicates that the VC uncertainty estimation provided by GRASP$_{pac}$ could be not representative of the real uncertainty in this case. However, the obtained results could be affected by different factors, independent of GRASP$_{pac}$, which yield a worse agreement than in the airborne comparison of Section 5.1. In this section the aerosol properties in the free vertical atmosphere over Granada have been assumed equal to the properties at the surface on Sierra Nevada ground station, which could be affected by other aerosol sources and atmospheric conditions. Moreover, the instrumental uncertainty on VC_{SNS} could be also partially responsible of the observed differences.

Fig. 12 shows the differences ΔVC of Eq. (12) as function of VC_{SNS} (Fig. 12a), AOD_{440} (Fig. 12b), Angström Exponent (Fig. 12c) and sphere fraction (Fig. 12d). Generally it is observed that ΔVC increases with VC_{SNS}, however, some high ΔVC values appear for moderate VC_{SNS} values which correspond to the mentioned case of 26th August. ΔVC also increases with AOD_{440}, however high ΔVC values do not appear for moderate AOD_{440} and even low ΔVC values can be observed for high AOD_{440}. ΔVC does not show any clear dependence on AE and sphere fraction, except the highest ΔVC values for the lowest values of AE and sphere fraction, which mainly corresponds to dust particles during the mentioned strong dust episode of 20th–21st July 2016 (see Fig. 10).

Finally, a case of study based on the dust episode of 20th–21st July 2016 has been analysed as an illustration. Fig. 13a and b show the retrieved VC profiles and the measured VC_{SNS} at Sierra Nevada on the afternoon of 20th July and on the morning of 21st July, respectively. The AOD_{440} from Granada was 0.85 and 0.83 for the Fig. 13a and b, respectively, which indicates very similar aerosol load. It indicates that in columnar terms, both cases are similar, but if ceilometer measurements are added to the retrieval, the vertical distribution can be discerned; this is the case in Fig. 13, where the GRASP$_{pac}$ retrieval indicates that VC at SNS increased by about four times from 20th to 21st July, which was also appreciated in the measurements of VC_{SNS}. Then, thanks to ceilometer addition, it is known that the dust episode came

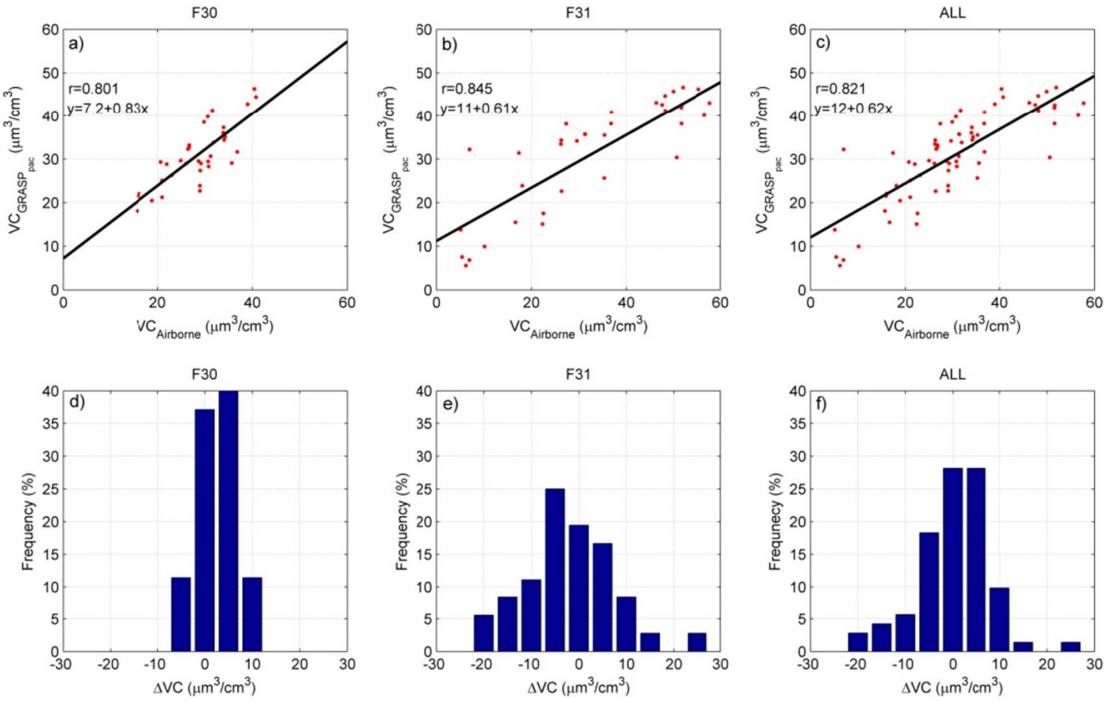

Fig. 9. Aerosol volume concentration (VC) retrieved by $GRASP_{pac}$ as a function of the airborne measurements for the flights F30 (panel a), F31 (panel b) and all (panel c). Histograms of the differences between the VC retrieved by GRASP and the VC from airborne (ΔVC from Eq. (10)) for the flights F30 (panel d), F31 (panel e) and all (panel f).

Table 4
Statistical estimators MBE, MABE and STD from ΔVC (Eq. (10)) for the comparison of VC retrieved by $GRASP_{pac}$ and the airborne measured for the F30, F31 and both flights together. Values within parentheses are in % (from Eq. (11)).

Flight	N	MBE ($\mu m^3/cm^3$)	MABE ($\mu m^3/cm^3$)	STD ($\mu m^3/cm^3$)	$\Delta VC < \sigma_G$ (%)	$\Delta VC < 2\sigma_G$ (%)
F30	35	2.5 (10.5)	4.1 (15.7)	4.4 (16.5)	77.1	100
F31	36	−1.8 (12.9)	7.5 (33.9)	9.5 (70.8)	58.3	88.9
All	71	0.3 (11.7)	5.8 (24.9)	7.7 (51.4)	67.6	94.4

20th July in a strong layer located between 3.5 and 4.0 km a.s.l. This layer went down providing extreme values at SNS height in the morning of 21st July, but also high dust concentrations in lower heights, which did not happen in the evening of 20th July.

6. Conclusions

In this work we have explored the use of collocated sun/sky photometer and ceilometer measurements in the General Retrieval of Aerosol and Surface Properties (GRASP) code to retrieve column-integrated and vertically-resolved optical and microphysical aerosol properties such as backscatter and extinction coefficients and volume concentration, among others. The capability to combining such set of measurements and using them in GRASP has been studied through different sets of simulations for typical dust and biomass-burning

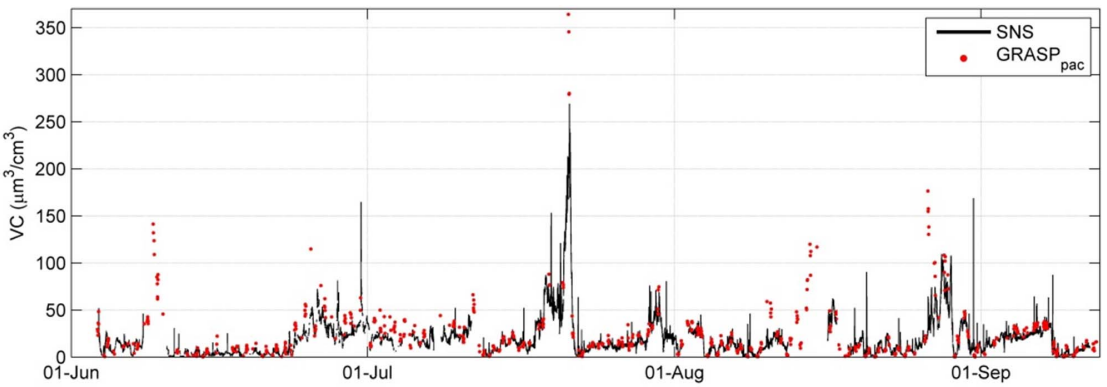

Fig. 10. Temporal evolution of the aerosol volume concentration (VC) measured at the Sierra Nevada Station (SNS) and the retrieved by $GRASP_{pac}$ at the same altitude.

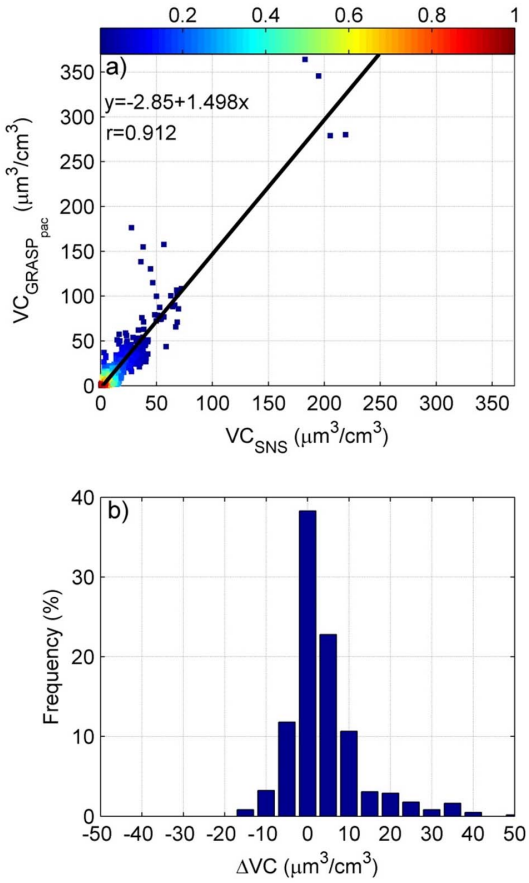

Fig. 11. Aerosol volume concentration (VC) retrieved by $GRASP_{pac}$ at the Sierra Nevada Station (SNS) altitude as a function of the VC directly measured at SNS (panel a). Colour of points represents the relative density of the points. Histograms of the differences (ΔVC from Eq. (12)) between the VC retrieved by $GRASP_{pac}$ at SNS altitude and the VC directly measured at SNS (panel b).

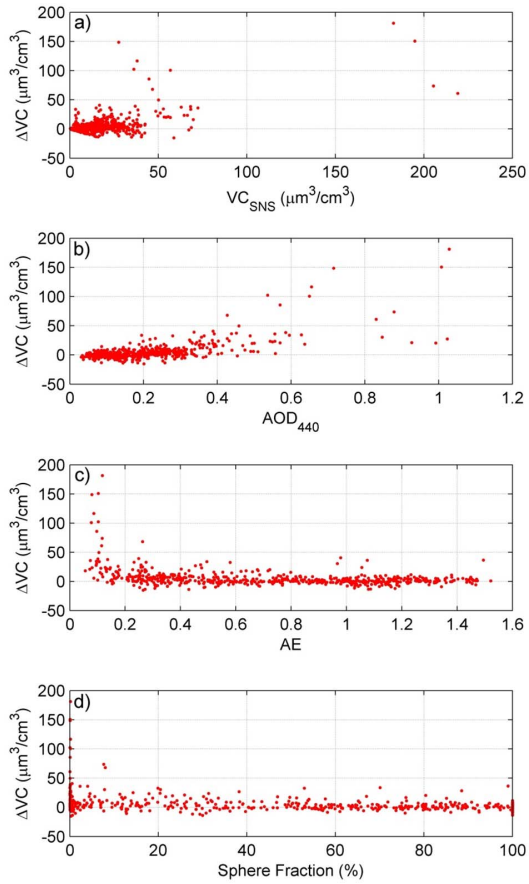

Fig. 12. Differences between the aerosol volume concentration (VC) retrieved by $GRASP_{pac}$ at Sierra Nevada Station (SNS) altitude and the VC directly measured at SNS (ΔVC from Eq. (12)) as a function of the VC at SNS (panel a), aerosol optical depth at 440 nm (panel b), Angström Exponent (panel c) and sphere fraction (panel d).

aerosol located at different altitudes as well as mixtures of both. In general, the proposed GRASP retrievals reproduce better aerosol properties for coarse particles, likely due to the operational long wavelength of the ceilometer at 1064 nm, and for high aerosol optical depth values. The results of the simulations have demonstrated good agreements for column-integrated size distributions and optical parameters such as complex refractive indices and single scattering albedo. For vertically-resolved aerosol properties, volume concentration presents an accuracy of −6% and an uncertainty of 21%; this accuracy is −11% and 5% for backscatter and extinction profiles at 1064 nm, being the uncertainty 31% and 21%, respectively. The mentioned analysis concludes that the uncertainty of these GRASP retrievals is representative of the real uncertainty of the retrieved parameters, except for column single scattering albedo and lidar ratio where the uncertainty given by GRASP is only representative when aerosol optical depth increases.

Two case studies from mid-June 2013 documented during the ChArMEx/ADRIMED field campaign have allowed the comparison of retrieved vertical profiles versus airborne in-situ measurements. The

Table 5
Statistical estimators for the comparison of VC retrieved by $GRASP_{pac}$ and the measured by in-situ instrumentation at SNS (ΔVC from Eq. (12)) along SLOPE I campaign for different VC_{SNS} intervals. Values within parentheses are in % (from Eq. (13)).

VC_{SNS} range	N	MBE ($\mu m^3/cm^3$)	MABE ($\mu m^3/cm^3$)	STD ($\mu m^3/cm^3$)	$\Delta VC < \sigma_G$ (%)	$\Delta VC < 2\sigma_G$ (%)
0-Max. $\mu m^3/cm^3$	619	5.5 (31.1)	7.7 (56.0)	16.6 (94.0)	37.6	68.2
5-Max. $\mu m^3/cm^3$	493	6.3 (22.7)	8.9 (43.2)	18.2 (58.9)	40.0	72.0
0–5 $\mu m^3/cm^3$	126	2.3 (64.0)	3.2 (106.4)	5.9 (169.4)	28.6	53.2
5–10 $\mu m^3/cm^3$	132	0.7 (10.0)	3.6 (50.0)	4.3 (59.4)	27.3	59.8
10–20 $\mu m^3/cm^3$	184	3.1 (19.8)	5.9 (39.9)	8.1 (53.1)	45.1	75.0
20–30 $\mu m^3/cm^3$	97	8.8 (36.4)	9.9 (40.7)	16.7 (63.4)	45.4	80.4
30–50 $\mu m^3/cm^3$	58	11.2 (28.5)	15.1 (39.5)	25.6 (65.7)	55.2	79.3
50–100 $\mu m^3/cm^3$	18	27.1 (46.1)	29.0 (49.2)	24.1 (42.9)	11.1	66.7
100-Max. $\mu m^3/cm^3$	4	116.7 (60.1)	116.7 (60.1)	58.6 (33.9)	0.0	50.0

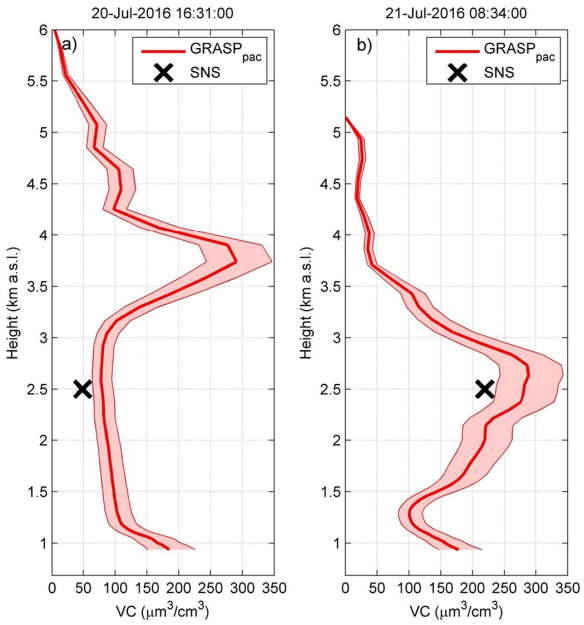

Fig. 13. Profiles of aerosol volume concentration (VC) retrieved by $GRASP_{pac}$ at 20 July 2016, 18:12 UTC (panel a) and 21 July 2016, 09:32 UTC (panel b). VC measured at Sierra Nevada Station (SNS) is marked by a black cross. Shadow band represents uncertainty in the $GRASP_{pac}$ retrieval.

aerosol volume concentration obtained by GRASP presents high correlation with the measured one during the two flights. Differences in this concentration between GRASP retrievals and airborne measurements present a mean value below 12% and a standard deviation around 51%. All these differences are within the uncertainty estimations provided by the GRASP code. Moreover, comparisons of the column-integrated retrieved parameters by the proposed scheme for GRASP versus AERONET retrievals have been done showing a good agreement between both techniques (differences were within uncertainties).

Data acquired during the SLOPE I field campaign (summer 2016) at the high mountain Sierra Nevada station, located at 2500 m a.s.l, were used to evaluate the retrieved aerosol volume concentration at a certain altitude. The in-situ volume concentration at a mountain station in Sierra Nevada correlates better ($r = 0.91$) with the aerosol volume concentration obtained by GRASP at 2500 m a.s.l. than other variables like aerosol optical depth at Granada (ground station). Discarding the lowest concentration values, the mean differences between retrieved and the measured volume concentrations are of 23% with a standard deviation of 59%, which means that GRASP frequently overestimates the in-situ measurements at Sierra Nevada. However, part of these differences could be caused by uncertainties in the in-situ measurements and assumptions, and in the fact that the aerosol over Granada (where ceilometer monitoring was performed) could not be the same than the aerosol on Sierra Nevada, which could be affected by local dynamic and atmospheric effects, and also to local aerosol sources at the high mountains.

Overall, the obtained results indicate that the combination of sun/sky photometer and ceilometer measurements and their use as inputs in GRASP provides reliable products if the uncertainties are considered. Nevertheless, the experimental data obtained were mostly representative of dust and clean conditions, and more evaluations are required for very polluted environment and intense biomass-burning. Therefore, as outlook, the method could be applied in different places, using networks like ICENET, and in long time series in order to characterize the regional and temporal changes on vertical aerosol extensive properties.

Acknowledgements

This work was supported by the Andalusia Regional Government (project P12-RNM-2409) and by the "Consejería de Educación" of "Junta de Castilla y León" (project VA100U14); the Spanish Ministry of Economy and Competitiveness under the projects, CMT2015-66742-R, CGL2016-81092-R and "Juan de la Cierva-Formación" program (FJCI-2014-22052); and the European Union's Horizon 2020 research and innovation programme through project ACTRIS-2 (grant agreement no 654109) and the Marie Curie Rise action GRASP-ACE (grant agreement no 778349). The authors thankfully acknowledge the FEDER program for the instrumentation used in this work. COST Action TOPROF (ES1303), supported by COST (European Cooperation in Science and Technology), is also acknowledged. The authors acknowledge the use of GRASP inversion algorithm (www.grasp-open.com). The MODIS MCD43C1 data product was retrieved from the online Data Pool, courtesy of the NASA Land Processes Distributed Active Archive Center (LP DAAC), USGS/Earth Resources Observation and Science (EROS) Center, Sioux Falls, South Dakota, https://lpdaac.usgs.gov/data_access/data_pool. This work contributes to WP4 on aerosol-radiation-climate interaction of the ChArMEx project supported by ADEME, CEA, CNRS-INSU and Météo-France through the multidisciplinary programme MISTRALS (Mediterranean Integrated Studies at Regional And Local Scales). We thank the instrument scientists, pilots and ground crew of SAFIRE for facilitating the instrument integration and conducting flight operations.

References

Ansmann, A., Riebesell, M., Weitkamp, C., 1990. Measurement of atmospheric aerosol extinction profiles with a Raman lidar. Opt. Lett. 15, 746–748.

Ansmann, A., Baars, H., Tesche, M., Müller, D., Althausen, D., Engelmann, R., Pauliquevis, T., Artaxo, P., 2009. Dust and smoke transport from Africa to South America: lidar profiling over Cape Verde and the Amazon rainforest. Geophys. Res. Lett. 36 (11), L11802. http://dx.doi.org/10.1029/2009GL037923.

Ansmann, A., Seifert, P., Tesche, M., Wandinger, U., 2012. Profiling of fine and coarse particle mass: case studies of Saharan dust and Eyjafjallajökull/Grimsvötn volcanic plumes. Atmos. Chem. Phys. 12 (20), 9399–9415.

Barreto, A., Cuevas, E., Damiri, B., Berkoff, T., Berjón, A.J., Hernández, Y., Almansa, F., Gil, M., 2013. A new method for nocturnal aerosol measurements with a lunar photometer prototype. Atmos. Meas. Tech. 6, 585–598.

Barreto, A., Cuevas, E., Granados-Muñoz, M.J., Alados-Arboledas, L., Romero, P.M., Gröbner, J., Kouremeti, N., Almansa, A.F., Stone, T., Toledano, C., Román, R., Sorokin, M., Holben, B., Canini, M., Yela, M., 2016. The new sun-sky-lunar Cimel CE318-T multiband photometer – a comprehensive performance evaluation. Atmos. Meas. Tech. 9, 631–654. http://dx.doi.org/10.5194/amt-9-631-2016.

Baumgardner, D., Dye, J.E., Gandrud, B.W., Knollenberg, R.G., 1992. Interpretation of measurements made by forward scattering probe (FSSP-300) during the airborne arctic stratospheric expedition. J. Geophys. Res. 97, 8035–8046. http://dx.doi.org/10.1029/91JD02728.

Benavent-Oltra, J.A., Román, R., Granados-Muñoz, M.J., Pérez-Ramírez, D., Ortiz-Amezcua, P., Denjean, C., Lopatin, A., Lyamani, H., Torres, B., Guerrero-Rascado, J.L., Fuertes, D., Dubovik, O., Chaikovsky, A., Olmo, F.J., Mallet, M., Alados-Arboledas, L., 2017. Comparative assessment of GRASP algorithm for a dust event over Granada (Spain) during ChArMEx-ADRIMED 2013 campaign. Atmos. Meas. Tech. 10, 4439–4457. http://dx.doi.org/10.5194/amt-2017-200.

Böckmann, C., 2001. Hybrid regularization method for the ill-posed inversion of multi-wavelenght lidar data to determine aerosol size distributions. Appl. Opt. 40, 1329–1342.

Boucher, O., Randall, D., Artaxo, P., Bretherton, C., Feingold, G., Forster, P., Kerminen, V.-M., Kondo, Y., Liao, H., Lohmann, U., Rasch, P., Satheesh, S.K., Sherwood, S., Stevens, B., Zhang, X.Y., 2013. Clouds and aerosols. In: Climate change 2013: the physical science basis. Contribution of Working Group I to the Fifth Assessment Report of the Intergovernmental Panel on Climate Change. Cambridge University Press, United Kingdom and New York, NY, USA, pp. 571–657.

Bovchaliuk, V., Goloub, P., Podvin, T., Veselovskii, I., Tanre, D., Chaikovsky, A., Dubovik, O., Mortier, A., Lopatin, A., Korenskiy, M., Victori, S., 2016. Comparison of aerosol properties retrieved using GARRLiC, LIRIC, and Raman algorithms applied to multi-wavelength LIDAR and sun/sky-photometer data. Atmos. Meas. Tech. 9, 3391–3405. http://dx.doi.org/10.5194/amt-9-3391-2016.

Bravo-Aranda, J.A., Navas-Guzmán, F., Guerrero-Rascado, J.L., Pérez-Ramírez, D., Granados-Muñoz, M.J., Alados-Arboledas, L., 2013. Analysis of lidar depolarization calibration procedure and application to the atmospheric aerosol characterization. Int. J. Remote Sens. 34 (9–10), 3543–3560.

Bravo-Aranda, J.A., Titos, G., Granados-Muñoz, M.J., Guerrero-Rascado, J.L., Navas-Guzmán, F., Valenzuela, A., Lyamani, H., Olmo, F.J., Andrey, J., Alados-Arboledas, L., 2015. Study of mineral dust entrainment in the planetary boundary layer by lidar depolarisation technique. Tellus B 67 (1), 26180. http://dx.doi.org/10.5194/amt-9-3391-2016.

Burton, S.P., Ferrare, R.A., Hostetler, C.A., Hair, J.W., Rogeres, R.R., Obland, M.D., Obland, M.D., Butler, C.F., Cook, A.L., Harper, D.B., Froyd, K.D., 2012. Aerosol classification using airborne high spectral resolution lidar measurements - methodology and examples. Atmos. Meas. Tech. 5, 73–98.

Cai, Y., Montague, D.C., Mooiweer-Bryan, W., Deshler, T., 2008. Performance characteristics of the ultra high sensitivity aerosol spectrometer for particles between 55 and 800 nm: laboratory and field studies. J. Aerosol Sci. 39, 759–769. http://dx.doi.org/10.1016/j.jaerosci.2008.04.007.

Cazorla, A., Casquero-Vera, J.A., Román, R., Guerrero-Rascado, J.L., Toledano, C., Cachorro, V.E., Orza, J.A.G., Cancillo, M.L., Titos, G., Pandolfi, M., Alastuey, A., Hanrieder, N., Alados-Arboledas, L., 2017. Near real time processing of ceilometer network data: characterizing an extraordinarty dust outbreak over the Iberian Peninsula. Atmos. Chem. Phys. 17, 11861–11876. http://dx.doi.org/10.5194/acp-17-11861-2017.

Chaikovsky, A., Dubovik, O., Goloub, P., Balashevich, N., Lopatsin, A., Karol, Y., Denisov, S., Lapyonok, T., 2008. Software Package for the Retrieval of Aerosol Microphysical Properties in the Vertical Column Using Combined Lidar/Photometer Data (Test Version), Technical Report. Institute of Physics, National Academy of Sciences of Belarus, Minsk, Belarus.

Chaikovsky, A., Dubovik, O., Holben, B., Bril, A., Goloub, P., Tanré, D., Pappalardo, G., Wandinger, U., Chaikovskaya, L., Denisov, S., Grudo, J., Lopatin, A., Karol, Y., Lapyonok, T., Amiridis, V., Ansmann, A., Apituley, A., Allados-Arboledas, L., Binietoglou, I., Boselli, A., D'Amico, G., Freudenthaler, V., Giles, D., Granados-Muñoz, M.J., Kokkalis, P., Nicolae, D., Oshchepkov, S., Papayannis, A., Perrone, M.R., Pietruczuk, A., Rocadenbosch, F., Sicard, M., Slutsker, I., Talianu, C., De Tomasi, F., Tsekeri, A., Wagner, J., Wang, X., 2016. Lidar-radiometer inversion code (LIRIC) for the retrieval of vertical aerosol properties from combined lidar/radiometer data: development and distribution in EARLINET. Atmos. Meas. Tech. 9, 1181–1205. http://dx.doi.org/10.5194/amt-9-1181-2016.

Chemyakin, E., Burton, S., Kolgotin, A., Müller, D., Hostetler, C., Ferrare, R., 2016. Retrieval of aerosol parameters from multiwavelength lidar: investigation of the underlying inverse mathematical problem. Appl. Opt. 55, 2188–2202.

De Haij, M., Wauben, W., Baltink, H.K., 2007. Continuous Mixing Layer Height Determination Using the LD-40 Ceilometer: A Feasibility Study. KNMI Report WR-2007-01. KNMI, De Bilt, The Netherlands.

Denjean, C., Cassola, F., Mazzino, A., Triquet, S., Chevaillier, S., Grand, N., Bourrianne, T., Momboisse, G., Sellegri, K., Schwarzenbock, A., Freney, E., Mallet, M., Formenti, P., 2016. Size distribution and optical properties of mineral dust aerosols transported in the western Mediterranean. Atmos. Chem. Phys. 16, 1081–1104. http://dx.doi.org/10.5194/acp-16-1081-2016.

Dubovik, O., King, M.D., 2000. A flexible inversion algorithm for retrieval of aerosol optical properties from sun and sky radiance measurements. J. Geophys. Res. Atmos. 105, 20673–20696.

Dubovik, O., Smirnov, A., Holben, B.N., King, M.D., Kaufman, Y.J., Eck, T.F., Slutsker, I., 2000. Accuracy assessments of aerosol optical properties retrieved from aerosol Robotic network (AERONET) sun and sky radiance measurements. J. Geophys. Res. 105 (D8), 9791–9806. http://dx.doi.org/10.1029/2000JD900040.

Dubovik, O., Holben, B., Eck, T.F., Smirnov, A., Kaufman, Y.J., King, M.D., Tanre, D., Slutsker, I., 2002. Variability of absorption and optical properties of key aerosol types observed in worldwide locations. J. Atmos. Sci. 59, 590–608.

Dubovik, O., Sinyuk, A., Lapyonok, T., Holben, B.N., Mishchenko, M., Yang, P., Eck, T., Volten, H., Munoz, O., Veihelmann, B., Van Der Zande, W.J., Leon, J., Sorokin, M., Slutsker, I., 2006. Application of spheroid models to account for aerosol particle nonsphericity in remote sensing of desert dust. J. Geophys. Res. Atmos. 111, D11208. http://dx.doi.org/10.1029/2005JD006619.

Dubovik, O., Lapyonok, T., Litvinov, P., Herman, M., Fuertes, D., Ducos, F., Lopatin, A., Chaikovsky, A., Torres, B., Derimian, Y., Huang, X., Aspetsberger, M., Federspiel, C., 2014. GRASP: A Versatile Algorithm for Characterizing the Atmosphere. SPIE Newsroomhttp://dx.doi.org/10.1117/2.1201408.005558.

Emeis, S., Forkel, R., Junkermann, W., Schafer, K., Flentje, H., Gilge, S., Fricke, W., Wiegner, M., Freudenthaler, V., Gross, S., Ries, L., Meinhardt, F., Birmili, W., Munkel, C., Obleitner, F., Suppan, P., 2011. Measurement and simulation of the 16/17 April 2010 Eyjafjallajökull volcanic ash layer dispersion in the northern Alpine region. Atmos. Chem. Phys. 11, 2689–2701.

Espinosa, W.R., Remer, L.A., Dubovik, O., Ziemba, L., Beyersdorf, A., Orozco, D., Schuster, G., Lapyonok, T., Fuertes, D., Martins, J.V., 2017. Retrievals of aerosol optical and microphysical properties from imaging polar nephelometer scattering measurements. Atmos. Meas. Tech. 10, 811–824.

Fedarenka, A., Dubovik, O., Goloub, P., Li, Z., Lapyonok, T., Litvinov, P., Blarel, L., Gonzalez, L., Podvin, T., Crozel, D., 2016. Utilization of AERONET polarimetric measurements for improving retrieval of aerosol microphysics: GSFC, Beijing and Dakar data analysis. J. Quant. Spectrosc. Radiat. Transf. 179, 72–97.

Fernald, F.G., 1984. Analysis of atmospheric lidar observations: some comments. Appl. Opt. 23, 652–653.

Flentje, H., Claude, H., Elste, T., Gilge, S., Köhler, U., Plass-Dülmer, C., Steinbrecht, W., Thomas, W., Werner, A., Fricke, W., 2010. The Eyjafjallajökull eruption in April 2010–detection of volcanic plume using in-situ measurements, ozone sondes and lidar-ceilometer profiles. Atmos. Chem. and Phys. 10, 10085–10092. http://dx.doi.org/10.5194/acp-10-10085-2010.

Granados-Muñoz, M.J., Bravo-Aranda, J.A., Baumgardner, D., Guerrero-Rascado, J.L., Pérez-Ramírez, D., Navas-Guzmán, F., Veselovskii, I., Lyamani, H., Valenzuela, A., Olmo, F.J., Titos, G., Andrey, J., Chaikovsky, A., Dubovik, O., Gil-Ojeda, M., Alados-Arboledas, L., 2016. A comparative study of aerosol microphysical properties retrieved from ground-based remote sensing and aircraft in situ measurements during a Saharan dust event. Atmos. Meas. Tech. 9, 1113–1133. http://dx.doi.org/10.5194/amt9-1113-2016.

Gross, S., Esselborn, M., Weinzierl, B., Wirth, M., Fix, A., Petzold, A., 2013. Aerosol classification by airborne high spectral resolution lidar observations. Atmos. Chem. Phys. 13 (5), 2487–2505.

Haeffelin, M., Laffineur, Q., Bravo-Aranda, J.-A., Drouin, M.-A., Casquero-Vera, J.-A., Dupont, J.-C., De Backer, H., 2016. Radiation fog formation alerts using attenuated backscatter power from automatic lidars and ceilometers. Atmos. Meas. Tech. 9, 5347–5365. http://dx.doi.org/10.5194/amt-9-5347-2016.

Heese, B., Flentje, H., Althausen, D., Ansmann, A., Frey, S., 2010. Ceilometer lidar comparison: backscatter coefficient retrieval and signal-to-noise ratio determination. Atmos. Meas. Tech. 3 (6), 1763–1770.

Holben, B.N., Eck, T.F., Slutsker, I., Tanré, D., Buis, J.P., Setzer, A., Vermote, E., Reagan, J.A., Kaufman, Y.J., Nakajima, T., Lavenu, F., Jankowiak, I., Smirnov, A., 1998. AERONET – a federated instrument network and data archive for aerosol characterization. Remote Sens. Environ. 66, 1–16.

Holben, B.N., Eck, T.F., Slutsker, I., Smirnov, A., Sinyuk, A., Schafer, J., Giles, D., Dubovik, O., 2006. AERONET's Version 2.0 Quality Assurance Criteria. Proc. SPIE 6408, Remote Sensing of the Atmosphere and Clouds, 64080Q (November 28, 2006). http://dx.doi.org/10.1117/12.706524.

Jenoptik, 2013. CHM15k – Nimbus Ceilometer User Manual. Revision P0, September 2013.

Klett, J.D., 1981. Stable analytical inversion solution for processing lidar returns. Appl. Opt. 20, 211–220.

Klett, J.D., 1985. Lidar inversion with variable backscatter/extinction ratios. Appl. Opt. 24, 1638–1643.

Kokhanovsky, A.A., Davis, A.B., Cairns, B., Dubovik, O., Hasekamp, O.P., Sano, I., Mukai, S., Rozanov, V.V., Litvinov, P., Lapyonok, T., Kolomiets, I.S., Oberemok, Y.A., Savenkov, S., Martin, W., Wasilewski, A., Di Noia, A., Stap, F.A., Rietjens, J., Xu, F., Natraj, V., Duan, M., Cheng, T., Munro, R., 2015. Space-based remote sensing of atmospheric aerosols: the multi-angle spectro-polarimetric frontier. Earth Sci. Rev. 145, 85–116.

Li, X., Strahler, A.H., 1992. Geometric-optical bidirectional reflectance modeling of the discrete crown vegetation canopy: effect of crown shape and mutual shadowing. IEEE Trans. Geosci. Remote Sens. 30 (2), 276–292.

Li, S., Everette, J., Min, Q., Yin, B., Sakai, R., Payne, M.K., 2017. Remote sensing of PM2.5 during cloudy and nighttime periods using ceilometer backscatter. Atmos. Meas. Tech. 10, 2093–2104.

Lopatin, A., Dubovik, O., Chaikovsky, A., Goloub, P., Lapyonok, T., Tanré, D., Litvinov, P., 2013. Enhancement of aerosol characterization using synergy of lidar and sun-photometer coincident observations: the GARRLiC algorithm. Atmos. Meas. Tech. 6, 2065–2088. http://dx.doi.org/10.5194/amt-6-2065-2013.

Lyamani, H., Olmo, F.J., Alados-Arboledas, L., 2010. Physical and optical properties of aerosols over an urban location in Spain: seasonal and diurnal variability. Atmos. Chem. Phys. 10, 239–254.

Lyamani, H., Olmo, F.J., Foyo, I., Alados-Arboledas, L., 2011. Black carbon aerosols over an urban area in south-eastern Spain: changes detected after the 2008 economic crisis. Atmos. Environ. 45, 6423–6432.

Madonna, F., Amato, F., Vande Hey, J., Pappalardo, G., 2015. Ceilometer aerosol profiling versus Raman lidar in the frame of the INTERACT campaign of ACTRIS. Atmos. Meas. Tech. 2207–2223.

Mallet, M., Dulac, F., Formenti, P., Nabat, P., Sciare, J., Roberts, G., Pelon, J., Ancellet, G., Tanré, D., Parol, F., Denjean, C., Brogniez, G., di Sarra, A., Alados-Arboledas, L., Arndt, J., Auriol, F., Blarel, L., Bourrianne, T., Chazette, P., Chevaillier, S., Claeys, M., D'Anna, B., Derimian, Y., Desboeufs, K., Di Iorio, T., Doussin, J.-F., Durand, P., Féron, A., Freney, E., Gaimoz, C., Goloub, P., Gómez-Amo, J.L., Granados-Muñoz, M.J., Grand, N., Hamonou, E., Jankowiak, I., Jeannot, M., Léon, J.-F., Maillé, M., Mailler, S., Meloni, D., Menut, L., Momboisse, G., Nicolas, J., Podvin, T., Pont, V., Rea, G., Renard, J.-B., Roblou, L., Schepanski, K., Schwarzenboeck, A., Sellegri, K., Sicard, M., Solmon, F., Somot, S., Torres, B., Totems, J., Triquet, S., Verdier, N., Verwaerde, C., Waquet, F., Wenger, J., Zapf, P., 2016. Overview of the chemistry-aerosol Mediterranean experiment/aerosol direct radiative forcing on the Mediterranean climate (ChArMEx/ADRIMED) summer 2013 campaign. Atmos. Chem. Phys. 16, 455–504. http://dx.doi.org/10.5194/acp-16-455-2016.

Mandija, F., Sicard, M., Comerón, A., Alados-Arboledas, L., Guerrero-Rascado, J.L., Barragan, R., Bravo-Aranda, J.A., Granados-Muñoz, M.-J., Lyamani, H., Muñoz Porcar, C., Rocadenbosch, F., Rodríguez, A., Valenzuela, A., García Vizcaíno, D., 2016. Origin and pathways of the mineral dust transport to two Spanish EARLINET sites: effect on the observed columnar and range-resolved dust optical properties. Atmos. Res. 187, 69–83. http://dx.doi.org/10.1016/j.atmosres.2016.12.002.

Martucci, G., Milroy, C., O'Dowd, C.D., 2010. Detection of cloud-base height using Jenoptik CHM15K and Vaisala CL31 ceilometers. J. Atmos. Ocean. Tech. 27 (2), 305–318.

Müller, D., Wandinger, U., Ansmann, A., 1999. Microphysical particle parameters from extinction and backscatter lidar data by inversion with regularization: simulation. Appl. Opt. 38, 2358–2368.

Müller, D., Mattis, I., Ansmann, A., Wehner, B., Althausen, D., Wandinger, U., Dubovik, O., 2004. Closure study on optical and microphysical properties of a mixed urban and Arctic haze air mass observed with Raman lidar and sun photometer. J. Geophys. Res. 109, D13206.

Münkel, C., Eresmaa, N., Räsänen, J., Karppinen, A., 2007. Retrieval of mixing height and dust concentration with lidar ceilometer. Bound.-Layer Meteorol. 124 (1), 117–128.

Navas-Guzmán, F., Müller, D., Bravo-Aranda, J.A., Guerrero-Rascado, J.L., Granados-

Muñoz, M.J., Pérez-Ramírez, D., Olmo, F.J., Alados-Arboledas, L., 2013. Eruption of the Eyjafjallajökull Volcano in spring 2010: multiwavelength Raman lidar measurements of sulphate particles in the lower troposphere. J. Geophys. Res. 118, 1804–1813.

Noh, Y.M., Müller, D., Shin, D.H., Lee, H., Jung, J.S., Lee, K.H., Cribb, M., Li, Z., Kim, Y.J., 2009. Optical and microphysical properties of severe haze and smoke aerosol measured by integrated remote sensing techniques in Gwangju, Korea. Atmos. Environ. 43, 879–888.

Ortiz-Amezcua, P., Guerrero-Rascado, J.L., Granados-Muñoz, M.J., Benavent-Oltra, J.A., Böckmann, C., Samaras, S., Stachlewska, I.S., Janicka, Ł., Baars, H., Bohlmann, S., Alados-Arboledas, L., 2017. Microphysical characterization of long-range transported biomass burning particles from North America at three EARLINET stations. Atmos. Chem. Phys. 17, 5931–5946. http://dx.doi.org/10.5194/acp-17-5931-2017.

Pappalardo, G., Amodeo, A., Apituley, A., Comeron, A., Freudenthaler, V., Linne, H., Ansmann, A., Bosenberg, J., D'Amico, G., Mattis, I., Mona, L., Wandinger, U., Amiridis, V., Alados-Arboledas, L., Nicolae, D., Wiegner, M., 2014. EARLINET: towards an advanced sustainable European aerosol lidar network. Atmos. Meas. Tech. 7, 2389–2409. http://dx.doi.org/10.5194/amt7-2389-2014.

Pérez-Ramírez, D., Lyamani, H., Olmo, F.J., Whiteman, D.N., Alados-Arboledas, L., 2012. Columnar aerosol properties from sun-and-star photometry: statistical comparisons and day-to-night dynamic. Atmos. Chem. Phys. 12, 9719–9738.

Pérez-Ramírez, D., Lyamani, H., Smirnov, A., O'Neill, N.T., Veselovskii, I., Whiteman, D.N., Olmo, F.J., Alados-Arboledas, L., 2016. Statistical study of day and night hourly patterns of columnar aerosol properties using sun and star photometry. Proc. of SPI Vol. 10001, 100010K. In: Comeron, Adolfo, Kassianov, Evgueni I., Schafer, Klaus, Jack, James W., Picard, Richard H., Weber, Konradin (Eds.), Remote Sensing of Clouds and the Atmosphere XXI.

Prata, A.J., 2009. Satellite detection of hazardous volcanic clouds and the risk to global air traffic. Nat. Hazards 5, 303–324.

Román, R., Torres, B., Fuertes, D., Cachorro, V.E., Dubovik, O., Toledano, C., Cazorla, A., Barreto, A., Bosch, J.L., Lapyonok, T., González, R., Goloub, P., Perrone, M.R., Olmo, F.J., de Frutos, A., Alados-Arboledas, L., 2017a. Remote sensing of lunar aureole with a sky camera: adding information in the nocturnal retrieval of aerosol properties with GRASP code. Remote Sens. Environ. 196, 238–252. http://dx.doi.org/10.1016/j.rse.2017.05.013.

Román, R., Cazorla, A., Toledano, C., Olmo, F.J., Cachorro, V.E., de Frutos, A., Alados-Arboledas, L., 2017b. Cloud cover detection combining high dynamic range sky images and ceilometer measurements. Atmos. Res. 196, 224–236.

Ross, J., 1981. The Radiation Regime and Architecture of Plant Stands. Dr. W. Junk Publ, The Hague, The Netherlands.

Sasano, Y., Nakane, H., 1984. Significance of the extinction/backscatter ratio and the boundary value term in the solution for the two-component lidar equation. Appl. Opt. 23, 11–13.

Schaaf, C.L.B., Liu, J., Gao, F., Strahler, A.H., 2011. MODIS Albedo and reflectance anisotropy products from Aqua and Terra. In: Ramachandran, B., Justice, C., Abrams, M. (Eds.), Land Remote Sensing and Global Environmental Change: NASA's Earth Observing System and the Science of ASTER and MODIS, Remote Sensing and Digital Image Processing Series, 11. 873 Springer-Cerlag.

Sorribas, M., Ogren, J.A., Olmo, F.J., Quirantes, A., Fraile, R., Gil-Ojeda, M., Alados-Arboledas, L., 2015. Assessment of African desert dust episodes over the southwest Spain at sea level using in situ aerosol optical and microphysical properties. Tellus B 67 (1), 27482.

Stein, A.F., Draxler, R.R., Rolph, G.D., Stunder, B.J., Cohen, M.D., Ngan, F., 2015. NOAA's HYSPLIT atmospheric transport and dispersion modeling system. Bull. Am. Meteorol. Soc. 96 (12), 2059–2077.

Tesche, M., Ansmann, A., Müller, D., Althausen, D., Mattis, I.N.A., Heese, B., Freudenthaler, V., Wiegner, M., Esselborn, M., Pisani, G., Knippertz, P., 2009. Vertical profiling of Saharan dust with Raman lidars and airborne HSRL in southern Morocco during SAMUM. Tellus B 61 (1), 144–164.

Tesche, M., Gross, S., Ansmann, A., Müller, D., Althausen, D., Freudenthaler, V., Esselborn, M., 2011. Profiling of Saharan dust and biomass-burning smoke with multiwavelength polarization Raman lidar at Cape Verde. Tellus B 6 (4), 649–676.

Titos, G., Foyo-Moreno, I., Lyamani, H., Querol, X., Alastuey, A., Alados-Arboledas, L., 2012. Optical properties and chemical composition of aerosol particles at an urban location: an estimation of the aerosol mass scattering and absorption efficiencies. J. Geophys. Res. 117, D04206. http://dx.doi.org/10.1029/2011JD016671.

Titos, G., Lyamani, H., Pandolfi, M., Alastuey, A., Alados-Arboledas, L., 2014. Identification of fine (PM1) and coarse (PM10-1) sources of particulate matter in an urban environment. Atmos. Environ. 89, 593–602.

Torres, B., Dubovik, O., Fuertes, D., Lapyonok, T., Toledano, C., Schuster, G.L., Goloub, P., Blarel, L., Barreto, A., Mallet, M., Tanré, D., 2017. Advanced characterization of aerosol properties from measurements of spectral optical depth using the GRASP algorithm. Atmos. Meas. Tech. 10, 3743–3781. http://dx.doi.org/10.5194/amt-10-3743-2017.

Valenzuela, A., Olmo, F.J., Lyamani, H., Antón, M., Quirantes, A., Alados-Arboledas, L., 2012. Aerosol radiative forcing during African desert dust events (2005–2010) over Southeastern Spain. Atmos. Chem. Phys. 12 (21), 10331–10351.

Veselovskii, I., Kolgotin, A., Griaznov, V., Müller, D., Wandinger, U., Whiteman, D.N., 2002. Inversion with regularization for the retrieval of tropospheric aerosol parameters from multiwavelength lidar sounding. Appl. Opt. 41, 3685–3699. http://dx.doi.org/10.1364/AO.41.003685.

Veselovskii, I., Whiteman, D.N., Korenskiy, M., Kolgotin, A., Dubovik, O., Perez-Ramirez, D., Suvorina, A., 2013. Retrieval of spatio-temporal distributions of particle parameters from multiwavelength lidar measurements using the linear estimation technique and comparison with AERONET. Atmos. Meas. Tech. 6, 2671–2682.

Veselovskii, I., Whiteman, D.N., Korenskiy, M., Suvorina, A., Kolgotin, A., Lyapustin, A., Wang, Y., Chin, M., Bian, H., Kucsera, T.L., Pérez-Ramírez, D., Holben, B., 2015. Characterization of forest fire smoke event near Washington, DC in summer 2013 with multi-wavelength lidar. Atmos. Chem. Phys. 15, 1647–1660.

Veselovskii, I., Goloub, P., Podvin, T., Tanre, D., da Silva, A., Colarco, P., Castellanos, P., Korenskiy, M., Hu, Q., Whiteman, D.N., Perez-Ramirez, D., Augustin, P., Fourmentin, M., Kolgotin, A., 2017. Characterization of smoke/dust episode over West Africa: comparison of MERRA-2 modeling with multiwavelength Mie-Raman lidar observations. Atmos. Meas. Tech. Discuss. http://dx.doi.org/10.5194/amt-2017-342.

Wandinger, U., Müller, D., Bockman, C., Althausen, D., Matthias, V., Bosenberg, J., WeiB, V., Fiebig, M., Wendisch, M., Stohl, A., Ansmann, A., 2002. Optical and microphysical characterization of biomass-burning and industrial-pollution aerosols from multiwavelength lidar and aircraft measurements. J. Geophys. Res. 107 (D21), 8125. http://dx.doi.org/10.1029/2000JD000202.

Whiteman, D.N., Melfi, S.H., Ferrare, R.A., 1992. Raman lidar system for the measurement of water vapor and aerosol in the Earth's atmosphere. Appl. Opt. 31, 3061–3082. http://dx.doi.org/10.1364/AO.31.003068.

Wiedensohler, A., Birmili, W., Nowak, A., Sonntag, A., Weinhold, K., Merkel, M., Wehner, B., Tuch, T., Pfeifer, S., Fiebig, M., Fjäraa, A.M., Asmi, E., Sellegri, K., Depuy, R., Venzac, H., Villani, P., Laj, P., Aalto, P., Ogren, J.A., Swietlicki, E., Williams, P., Roldin, P., Quincey, P., Hüglin, C., Fierz-Schmidhauser, R., Gysel, M., Weingartner, E., Riccobono, F., Santos, S., Grüning, C., Faloon, K., Beddows, D., Harrison, R., Monahan, C., Jennings, S.G., O'Dowd, C.D., Marinoni, A., Horn, H.-G., Keck, L., Jiang, J., Scheckman, J., McMurry, P.H., Deng, Z., Zhao, C.S., Moerman, M., Henzing, B., de Leeuw, G., Löschau, G., Bastian, S., 2012. Mobility particle size spectrometers: harmonizationof technical standards and data structure to facilitate high quality long-term observations of atmospheric particle number sized distributions. Atmos. Meas. Tech. 5, 657–685. http://dx.doi.org/10.5194/amt-5-657-2012.

Wiegner, M., Geiss, A., 2012. Aerosol profiling with the Jenoptik ceilometer CHM15kx. Atmos. Meas. Tech. 5 (8), 1953–1964. http://dx.doi.org/10.5194/amt-5-1953-2012.

Wiegner, M., Madonna, F., Binietoglou, I., Forkel, R., Gasteiger, J., Geiß, A., Pappalardo, G., Schäfer, K., Thomas, W., 2014. What is the benefit of ceilometers for aerosol remote sensing? An answer from EARLINET. Atmos. Meas. Tech. 7, 1979–1997.